

© Copyright by David Nicholas Olivieri 1996

All Rights Reserved

**FERMILAB
LIBRARY**

AAE5152 8/68

A DYNAMIC MOMENTUM COMPACTION FACTOR LATTICE FOR
IMPROVEMENTS TO STOCHASTIC COOLING IN STORAGE RINGS

A Dissertation Presented
by
DAVID NICHOLAS OLIVIERI

Approved as to style and content by:



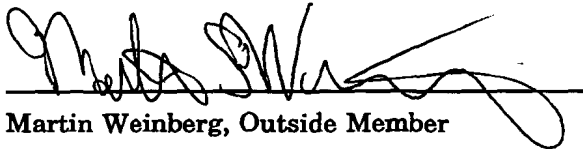
Monroe Rabin, Co-chair



Michael Church, Co-Chair



William Gerace, Member



Martin Weinberg, Outside Member



John F. Dubach, Department Head
Department of Physics and Astronomy

For my parents
Gasper J. and Elena M. Olivieri

for my brother
Steven A. Olivieri

&

for my dear friend
Eva Dobarro Peña

ACKNOWLEDGMENTS

To my family, I owe infinite gratitude. Without the constant encouragement, love, and support from my parents, Gasper and Elena, my years at the University of Massachusetts Amherst and Fermilab would not have been possible. Their commitment and selfless dedication, throughout these years, to my education and well-being, have been fundamental to any of my accomplishments. From them, and from their example, I have never stopped learning.

To my brother, Steven A. Olivieri, I owe countless thanks for his patience, encouragement, and constant reassurance regarding the relevance of my endeavors. Not only have I been able to rely upon him through thick and thin, but his vivacious intellectual interests, encompassing everything from vascular surgery, to fly-fishing, to RF engineering, constantly keeps me on my toes. Special thanks also, to René Olivieri for her friendship and encouragement.

To Eva Dobarro Peña, my gratitude is without bound. Through her undying friendship, love, and keen insights, I have found the will and energy to run faster and reach further. Also through her, I am continually reminded that the world is larger and more fascinating than I previously had imagined.

At Fermilab there have been countless people, from whom I have had the opportunity to learn much physics. In particular, I want to extend my gratitude to my advisor Dr. Michael Church. His deep insights, experience, and instincts regarding the physics of the Antiproton Source proved invaluable to my work pertaining to the dynamic γ_t project.

Many thanks are due to Dr. Monroe Rabin at the University of Massachusetts Amherst for being a steady voice and providing unending encouragement, especially in the critical moments.

To Mr. James Morgan, I am indebted for making my thesis work at Fermilab enjoyable. His interest, experience with the operation of the Antiproton Source, and his constant enthusiasm were fundamental to the successful commissioning of the γ_t project.

From Dr. Michael Martens, I have learned quite a lot of physics through our many discussions, and much more about literature, politics, economics, and friendship. His dedication, pursuit of excellence in whatever he undertakes, and his kind nature have been a tremendous source of inspiration for me.

I owe countless thanks to Mr. Howard Pfeffer for all the power supply regulation efforts, and what became our daily early morning review of the experimental analysis after endless owl shifts.

I am convinced that without his experience, clairvoyance, patience, and honest assessment of the data, many of the power supply problems would have gone unsolved. To him, I am also indebted for assuring that I did not blow up any of the Debuncher power supplies during Run 1B - at least not seriously! Thanks are also due to Mr. Robert Oberholtzer, Mr. Bernard Wisner and Mr. Thomas Miller for their generous help and efforts associated with the electronic hardware.

I want to extend my gratitude to Dr. Steven Werkema for many fruitful discussions about stochastic cooling, beam transfer functions, numerical methods, and perhaps most important, the various techniques for improving one's golf score.

Much of my interest in collective beam effects, and in particular, mathematical aspects of the Fokker Planck equation, developed and was sustained through my many discussions with Dr. Patrick Colestock. I am also indebted to him for his many efforts in helping me choose a future career path.

I owe a great deal of thanks to Dr. Leo Michelotti and Dr. James Holt for their help in getting me started and hooked on C++. Use of their accelerator physics computational tools allowed me to break the bonds of stodgy input files, thus providing the ability to study dispersion waves with more freedom.

I want to thank Dr. Gerald Jackson for bringing me out to Fermilab and introducing me to the exciting field of accelerator physics. His constant interest in my work and progress proved instrumental during the days when machine study time was an expensive commodity.

The many other people at Fermilab I would like to extend my thanks to include: Dr. David Finley, Dr. John Peoples, Dr. Steven O'Day, Dr. Ralph Pasquinelli, Dr. David McGinnis, Mr. Kenneth Fullet, Mr. David Peterson, Dr. Peter Bagley, Dr. John Marriner, Mr. Elvin Harms, Dr. Kirk Bertsche, Dr. Frank Bieniosik Dr. Shekhar Shukla, and Mr. Eric Colby.

The commissioning of the dynamic γ_t project would not have been possible without the concerted commitment of the entire Fermilab Operations Department. In particular, thanks are due to Mr. Dean Still, Mr. Todd Sullivan, Mr. Stan Johnson, Mr. Tom Meyer, and especially to Mr. David Vander Meulen, Mr. Kent Triplett, Mr. Kieth Engell, and Mr. William Pellico.

From the early days at the University of Massachusetts Amherst, I owe much thanks to Dr. William Gerace. Through him, I learned a tremendous amount about how to learn and think.

To Dr. James Walker, I am indebted for all his efforts in establishing and flawlessly main-

taining the bureaucratic connection between Fermilab and UMass.

Also from the University of Massachusetts Amherst, special thanks are due to Dr. William Mullin, Dr. Arthur Swift, Dr. Martin Weinberg, Dr. Gerald Peterson, Dr. Rory Miskimen, Dr. Po-zen Wong, Dr. William Leonard, and my good friend Dr. Sudip Bhattacharjee.

From my early days in graduate school, I want to extend a special thanks to my dear friend Dr. Galathara L. Kahanda. His encouragement and constant belief in me has never wavered since our days back in the Condensed Matter laboratory.

David Nicholas Olivieri, May 1996

Fermi National Accelerator Laboratory

University of Massachusetts Amherst

ABSTRACT

A DYNAMIC MOMENTUM COMPACTION FACTOR LATTICE FOR IMPROVEMENTS TO STOCHASTIC COOLING IN STORAGE RINGS

MAY 1996

DAVID NICHOLAS OLIVIERI, B.S., UNIVERSITY OF MASSACHUSETTS AMHERST

M.S., UNIVERSITY OF MASSACHUSETTS AMHERST

Ph.D., UNIVERSITY OF MASSACHUSETTS AMHERST

Directed by: Professor Michael Church and Professor Monroe Rabin

A dynamic momentum compaction factor, also referred to as a dynamic $\Delta\gamma_t$, lattice for the FNAL Antiproton Source Debuncher Storage Ring is studied, both theoretically and experimentally, for the purpose of improving stochastic precooling, and hence, improving the global antiproton production and stacking performance. A dynamic $\Delta\gamma_t$ lattice is proposed due to the competing requirements inherent within the Debuncher storage ring upon γ_t . Specifically, the Debuncher storage ring performs two disparate functions, (i) accepting and debunching a large number of \bar{p} s/pulse at the outset of the production cycle, which would perform ideally with a large value of γ_t , and (ii) subsequently employing stochastic cooling throughout the remainder of the \bar{p} production cycle for improved transfer and stacking efficiency into the Accumulator, for which a small value γ_t is ideal in order to reduce the diffusive heating caused by the mixing factor. In the initial design of the Debuncher optical lattice, an intermediate value of γ_t was chosen as a compromise between the two functional requirements. The goal of the thesis is to improve stochastic precooling by changing γ_t between two desired values during each \bar{p} production cycle. In particular, the dynamic $\Delta\gamma_t$ lattice accomplishes a reduction in γ_t , and hence the mixing factor, through an uniform increase to the dispersion throughout the arc sections of the storage ring. Experimental measurements of cooling rates and system performance parameters, with the implementation of the dynamic $\Delta\gamma_t$ lattice, are in agreement with theoretical predictions based upon a detailed integration of the stochastic cooling Fokker Planck equations. Based upon the consistency between theory and experiment, predictions of cooling rates are presented for future operational parameters of the Antiproton Source with the dynamic $\Delta\gamma_t$.

TABLE OF CONTENTS

ACKNOWLEDGMENTS	v
ABSTRACT	viii
LIST OF TABLES	xiv
LIST OF FIGURES	xvi
LIST OF SYMBOLS	xxi
GLOSSARY	xxiii
CHAPTER 1 Prologue: Introductory Concepts	1
1.1 Introduction - The Debuncher Dynamic $\Delta\gamma_t$ Project	1
1.2 Some Elementary Definitions and Physical Relations	1
1.3 Changing the Dispersion in the FNAL Debuncher	2
1.4 Resonance Issues	3
1.5 Stochastic Cooling and the Mixing Factor	4
1.6 Implications of Improved Precooling for the Antiproton Source	6
1.7 Structure of Thesis	7
CHAPTER 2 The $\gamma_t^{(f)}$ Lattice Design: Fundamentals	9
2.1 Introduction	9
2.2 The Function of the FNAL Debuncher	9
2.3 The Nominal FNAL Debuncher Lattice	11
2.3.1 Characterizing the Lattice	14
2.3.1.1 Predictions/Measurements of the β Functions	15
2.3.1.2 Predictions/Measurements of Chromaticity ξ	16
2.3.1.3 Predictions/Measurements of the dispersion, $D(s)$	18
2.3.1.4 Predictions/Measurement of the Slip Factor, η	20
2.4 $\Delta\gamma_t$ Lattice Design	21
2.4.1 Early motivations and historical review	22
2.4.1.1 Historical Perspective	23
2.4.2 Some comments on designing the dynamic γ_t lattice	24
2.4.3 $\Delta\gamma_t$ with localized dispersion waves	25
2.4.4 Introduction to π^- Doublets in the Debuncher Ring	26

2.4.4.1	Analytic expression for the $\Delta\gamma_t$ of a π doublet	27
2.4.4.2	First order expression for $\Delta\gamma_t$	27
2.4.4.3	Harmonic content of π - Doublet	29
2.4.4.4	Evaluation of $\Delta\gamma_t^{(1)}$	31
2.4.4.5	Maximum π - doublet filling of the arc sections	32
2.5	Specification for a complete $\Delta\gamma_t^f$ design	33
2.5.1	Introduction: The problem of minimizing tune shift	34
2.5.2	Details for a complete γ_t^f design	35
2.5.2.1	Hardware for the $\Delta\gamma_t^f$ design	39
2.5.3	Experimental Results of γ_t^f	40
2.5.3.1	Predictions/Measurements of the dispersion, $D(s)$	41
2.5.3.2	Predictions/Measurements of the slip factor η_f	43
2.5.4	Measurements of Resonances for $\Delta\gamma_t$ lattice	44
2.5.4.1	Resonances structure of $\gamma_t^{(i)}$ and $\gamma_t^{(f)}$	45
2.6	Chapter Summary	46
CHAPTER 3	The Dynamic $\Delta\gamma_t$ Lattice	47
3.1	Introduction	47
3.2	Ideal $\Delta\gamma_t^{(f)}$ Ramp	47
3.3	Actual $\Delta\gamma_t^f/\Delta t$ Ramp	48
3.3.1	The Power Supply/Magnet/Current-Bypass Shunt Model	49
3.3.2	Feedforward Correction: Introduction	51
3.3.3	The Feedforward Electronics System	53
3.3.4	Details of the Active Feedforward Circuit	55
3.3.5	The Magnet Current Bypass Shunt Circuit	57
3.4	Analysis of the $\Delta\gamma_t^{(f)}/300\text{msec}$ Case	58
3.4.1	Current Errors in Power Supplies: $\Delta\gamma_t^{(f)}/300$ msec case	58
3.4.2	Future Engineering Considerations	61
3.4.3	Tune Excursion: $\Delta\gamma_t^{(f)}/300$ msec case	63
3.4.4	Tune Excursion: Contribution from Each Device	64
3.4.5	Summary: Effects of Errors to $\Delta\gamma_t^{(f)}/300\text{msec}$ Tune Excursion	66

3.4.5.1	Tolerances of each Constituent Quadrupole System	67
3.4.6	Chromaticity Measurements for $\Delta\gamma_t^{(f)}/300\text{msec}$ Case	68
3.5	Chapter Summary	70
CHAPTER 4	The Debuncher Stochastic Cooling Model	72
4.1	Introduction	72
4.2	Historical Development	72
4.3	Stochastic Cooling: Definitions	73
4.3.1	Basic Physical Processes	75
4.3.2	Macroscopic Quantities and Simple Systems	76
4.3.2.1	Longitudinal system	76
4.3.2.2	The transverse cooling system:	78
4.3.3	Brief Description of Stochastic Cooling Hardware	79
4.4	Longitudinal Stochastic Cooling in the Debuncher	81
4.4.1	The Fokker Planck Description	81
4.4.2	Schottky Signals at Microwave Frequencies	83
4.4.3	Longitudinal thermal noise: $\mathcal{U}_{\text{therm}}^{\parallel}$	85
4.4.3.1	The Fits	86
4.4.4	Signal Suppression $\epsilon_{\parallel}(x)$ & $\langle G_{\parallel} \rangle$	89
4.4.4.1	Experimental Extraction of G_{\parallel}	91
4.4.4.2	Fits and Results	92
4.4.5	Longitudinal Open-loop transfer function measurements	95
4.4.5.1	Experimental Results	97
4.5	Transverse Stochastic Cooling	103
4.5.1	Schottky signals & $\mathcal{U}_{\perp}(q_m\omega)$	104
4.5.2	Signal Suppression $\epsilon_{\perp}(\omega)$ & $\langle g_{\perp} \rangle$	107
4.5.3	Open-loop Transfer Function & $\langle \tilde{g}_{\perp} \rangle$	109
4.6	Computational Results	111
4.6.1	Longitudinal system: cooling, diffusion, optimal gain and comparisons . . .	112
4.6.1.1	Longitudinal cooling term: $S_1(x, t)$	113
4.6.1.2	Longitudinal heating term	115

4.6.1.3	Comparison of $S_1(x, t)$ and $S_2(x, t)$	116
4.6.1.4	Model comparison to longitudinal cooling measurements	117
4.6.1.5	Transverse model comparison with cooling rate measurement	118
4.7	Chapter summary	120
CHAPTER 5	The Stochastic Cooling Results with a Dynamic $\Delta\gamma_t$	123
5.1	Introduction	123
5.1.1	Beam Loss Normalization: T_γ	123
5.1.2	The Measurements	124
5.2	Indirect Experimental Results: The performance parameters	125
5.2.1	The early data: $\frac{1}{3}\Delta\gamma_t^f$	126
5.2.2	$\frac{4}{5}\Delta\gamma_t^{(f)}/300\text{msec}$ and $\Delta\gamma_t^{(f)}/300\text{msec}$: Performance Parameters	128
5.2.2.1	Particle Number as a function of T_γ	131
5.3	Direct Cooling Measurements and Debuncher Cooling Model	132
5.3.1	Theory: The Debuncher Stochastic Cooling Model	133
5.3.2	The full results as function of T_γ	133
5.3.2.1	The $\frac{4}{5}\gamma_t/300\text{msec}$ Results	134
5.3.2.2	The $\Delta\gamma_t^{(f)}/300\text{msec}$ Results	135
5.4	Summary $\Delta\gamma_t^f$ versus T_γ : Indirect and Direct	137
5.5	Chapter Summary	138
CHAPTER 6	Stochastic Cooling Extrapolations and General Conclusions	139
6.1	Introduction	139
6.2	Projections of the Debuncher stochastic cooling model	140
6.2.1	Longitudinal Rates with present system gain	140
6.2.2	Longitudinal rates with increased gain	142
6.2.3	Dependence of the transverse rates with η	144
6.2.4	Summary of the cooling rate extrapolations	146
6.3	Final Comments regarding a dynamic $\Delta\gamma_t$	146
APPENDIX A	Some Notes Relevant to the $\Delta\gamma_t/\Delta t$ Optimization Problem	148
A.1	Introduction	148
A.2	General Comments	148

A.2.1	Classical Methods Optimization methods	148
A.2.2	Simulated Annealing Optimization	149
A.3	Optimization with a second order model	150
A.4	Conclusion: Optimization within Lattice Calculation	154
APPENDIX B	Numerical Integration for the Longitudinal Cooling Model	156
B.1	Introduction	156
B.2	Analytic Methods	156
B.2.1	Method of Characteristics for Cooling	156
B.2.1.1	Linear Diffusion Green Function	158
B.3	Numerical Finite Difference Methods	159
B.3.1	Explicit Methods	159
B.3.1.1	Euler Method	159
B.3.1.2	General Two Step Lax-Wendroff	159
B.3.2	Implicit Methods: Linear Diffusion	160
B.4	Tests of the Finite Difference Equations	161
BIBLIOGRAPHY		162

LIST OF TABLES

2.1	I versus K cubic fitting parameters a_j for the three types of quadrupole magnets in the Debuncher.	15
2.2	Comparison between measured and predicted β function values at the location of four quadrupoles in the Debuncher.	16
2.3	Result of chromaticity measurement for $\eta = .006$	16
2.4	Details of Lattice Parameters for the γ_t^f design	37
2.5	Types of quadrupole current changes in arcs sections for the $\gamma_t^{(f)}$ design.	38
2.6	The straight section quadrupole current shunt settings for the nominal γ_t and $\gamma_t^{(f)}$ lattices.	38
2.7	A comparison between the <i>measured</i> percentage beam loss amongst the dominant transverse resonances for the nominal lattice and the γ_t^f lattice design.	45
3.1	Resistance and Inductance values of magnets for each power supply system used in the simple model for calculation of the required constant current power supply voltage $V(t)$ during ramps.	51
3.2	The currents ΔI for $\frac{4}{5}\Delta\gamma_t^{(f)}/300\text{msec}$ associated with each device.	52
3.3	Result of residuals $\langle\mathcal{R}_x\rangle \times 10^{-2}$ and $\langle\mathcal{R}_y\rangle \times 10^{-2}$ for each device.	66
3.4	The percentage contribution of errors, $\langle\mathcal{R}_j\rangle/\sum_k\langle\mathcal{R}_k\rangle$, from each device.	67
3.5	Current tolerance, $\partial\nu/\partial I_j$, for the j th device.	67
4.1	Summary of fitted parameters for $\mathcal{U}_{\text{therm}}^{\parallel}(\mathbf{x}, t)$	88
4.2	Experimental Fits to $\langle G_{\parallel} \rangle$	95
4.3	Summary of the open loop network analyzer fits to $\langle G_{\parallel} \rangle$	102
4.4	$\mathcal{U}^{\perp}(q_m\omega)$ Result of measurements across the microwave band at the beginning of cycle ($\Delta t = 0.1\text{sec}$ after injection).	105
4.5	$\mathcal{U}^{\perp}(q_m\omega)$ for 2.2GHz as a function of time.	107
4.6	Experimental fits to transverse signal suppression, ϵ_m^{\perp} across the microwave bandwidth, at the beginning of the cycle $\Delta t = .1\text{sec}$	108
4.7	Experimental fits to transverse signal suppression, ϵ_m^{\perp} at 2.2GHz as a function of time. Values for $\mathcal{P}_{\text{open}}$ and $\mathcal{P}_{\text{closed}}$ are obtained from fits to data in Figure 4.24.	109

4.8	Summary of the open loop network analyzer fits to $\langle g_{\perp} \rangle$	111
A.1	Jacobian matrix elements for the tune optimization problem free parameters - the quadrapoles in the straight sections quadrapoles.	150
A.2	Hessian matrix elements for the tune optimization problem free parameters - the quadrapoles in the straight sections quadrapoles.	151
A.3	Test of the quadratic model with Jacobian and Hessian given in Tables A.1 and A.2, respectively, against the actual lattice calculation. The comparison is used to quantify the accuracy of the quadratic model for calculating the tune shifts $\Delta\nu$	153

LIST OF FIGURES

1.1	A diagram of a small region of transverse tune space indicating the dominant resonances leading to beam loss.	4
1.2	Debuncher to Accumulator (D/A) transfer efficiency and transverse emittance as a function of the duration of the production cycle.	7
2.1	A diagram of the FNAL Antiproton Source Debuncher/Accumulator storage rings. .	10
2.2	An optical element diagram of a representative sector in the Debuncher ring.	12
2.3	The nominal Debuncher lattice parameters for $\eta = 0.006$ from MAD calculation. . .	14
2.4	Chromaticity data with associated linear least square fit.	17
2.5	Representative measurements from the BPM data as a function of $\Delta p/p$	18
2.6	A Comparison of the predicted and measured dispersion for the $\eta = 0.006$ nominal lattice.	19
2.7	Power density (dB/Hz) versus energy difference $x = E - E_o$ of the longitudinal Schottky signal (126th harmonic) for obtaining the synchrotron frequency f_s	20
2.8	Measurements of the synchrotron frequency (f_s^2) as a function of the rf- cavity voltage on DRF3 (\tilde{V}_{rf}).	21
2.9	Illustration of a localized dispersion function created by a π Doublet.	26
2.10	Illustration optics for one sector of the Debuncher ring indicating the location of a π doublet formed with $Q13 \Leftrightarrow Q17$ quadrupoles used in the numerical example.	29
2.11	Fourier spectra, $\Delta\tilde{\beta}_\pi(\omega)$, for the single π doublet (formed with $Q13 \Leftrightarrow Q17$).	30
2.12	Calculation of $\Delta\gamma_t$, and η for a π doublet as a function of $\Delta I(\delta k)$ [Amps].	32
2.13	Illustration of maximum π doublet filling in the arc sections.	33
2.14	The complete $\gamma_t^{(f)}$ design for a sector of the Debuncher lattice indicating each ΔI . .	36
2.15	Comparison of the dispersion functions for γ_t^f ($\eta_f = 0.0094$), the nominal lattice γ_t^i , and a design for a <i>large</i> γ_t ($\eta = .0028$)	36
2.16	The Debuncher lattice parameters for $\gamma_t^{(f)}$ ($\eta = 0.0093$) from a BEAMLIN (or MAD) calculation.	39
2.17	A diagram of a sector in the Debuncher indicating the location of the new magnet shunts to be used for the $\Delta\gamma_t^{(f)}$	40

4.22	Measurements of the transverse signal/noise at (a) 0.1sec, and (b) 0.5sec, into the cooling cycle.	106
4.23	Measurements of the transverse signal/noise at (a) 1.5sec, and (b) 2.2sec, into the cooling cycle.	106
4.24	Transverse signal suppression measurements at $f = 2.2\text{GHz}$ for (a) 0.5sec and (b) 1.0sec into the cooling cycle.	108
4.25	Transverse open loop measurements at the 3.1GHz sideband.	110
4.26	Transverse $ (S_{\perp}^m)_{21} $ measurements at 2.1GHz and 3.8GHz.	111
4.27	Comparison of $S_1(x, t = 0)$ and $S_2(x, t = 0)$ with and without signal suppression and with $\langle G \rangle = 8.0 \times 10^{-4} \text{ Mev/sec}$, $\tau = 2.5 \times 10^{-2} \text{ MeV}^{-1}$	117
4.28	Comparison of beam width to model prediction with $\langle G \rangle = 7.5 \times 10^{-4} \text{ Mev/sec}$, $\tau_c = 2.5 \times 10^{-2} \text{ MeV}^{-1}$	118
4.29	A comparison of the <i>measured integrated power</i> within the 127th harmonic vertical Schottky sideband as a function of time against the transverse cooling calculation. $\langle g_{\perp} \rangle = 7.0 \times 10^{-3}$	119
4.30	A comparison of the measured integrated vertical Schottky power obtained with Gaussian fits and the cooling model with $\langle g_{\perp} \rangle = 7.0 \times 10^{-3}$	120
5.1	Time line and trigger events for defining T_{γ} during \bar{p} production cycle.	124
5.2	The performance parameters (a) yield, and (b) D/A Efficiency, as a function of T_{γ} for $\frac{1}{3}\Delta\gamma_t/300\text{msec}(\eta = .007)$	126
5.3	The performance parameters (a) Accumulator efficiency and (b) stack rate, as a function of T_{γ} for $\frac{1}{3}\Delta\gamma_t/300\text{msec}(\eta = .007)$	127
5.4	The performance parameters for $\frac{4}{5}\Delta\gamma_t^{(f)}/300\text{msec}(\eta = 0.0085)$	128
5.5	The performance parameters for $\frac{4}{5}\Delta\gamma_t^{(f)}/300\text{msec}(\eta = 0.0085)$	129
5.6	The performance parameters for $\Delta\gamma_t^{(f)}/300\text{msec}(\eta \approx 0.0093)$	130
5.7	The performance parameters for $\Delta\gamma_t^{(f)}/300\text{msec}(\eta \approx 0.0093)$	130
5.8	The measured zeroth moment of the longitudinal distribution <i>versus</i> T_{γ} for $\frac{4}{5}\gamma_t^f$ ($\eta = 0.0085$).	131
5.9	The measured zeroth moment of the longitudinal distribution <i>versus</i> T_{γ} for γ_t^f ($\eta = 0.009$).	132

5.10	The measured longitudinal widths <i>versus</i> T_γ for $\frac{4}{5}\gamma_t^f/300$ msec ($\eta = 0.0085$) together with results of the longitudinal stochastic cooling model, with inputs to the cooling model, $\langle G \rangle = 2.5 \times 10^{-4}$ MeV/sec and $\tau_c = .02051/\text{MeV}$	134
5.11	Transverse Schottky sideband power <i>versus</i> T_γ for $\frac{4}{5}\gamma_t^f/300$ msec ($\eta = .0085$) at the beginning and the end of the cycle.	135
5.12	The measured longitudinal widths <i>versus</i> T_γ for $\Delta\gamma_t^{(f)}/300$ msec ($\eta = 0.0094$) together with cooling model results for inputs: $\langle G \rangle = 2.5 \times 10^{-4}$ and $\tau_c = .0205$	136
5.13	Transverse Schottky sideband power <i>versus</i> T_γ for $\Delta\gamma_t^{(f)}/300$ msec ($\eta = .0094$) at the beginning and the end of the cycle.	136
5.14	Experimentally determined dependence of T_γ upon the the Debuncher/Accumulator efficiency and the stack rate for three values of η	137
6.1	Comparisons of σ_o/σ_f as a function of N and η for the present values $G_\parallel = 7.5 \times 10^{-4}$ MeV and $\tau = 2.5 \times 10^{-2}$ MeV $^{-1}$	141
6.2	Comparisons of σ_o/σ_f as a function of N and η for the present values but without thermal noise $\mathcal{U} = 0$, $G_\parallel = 7.5 \times 10^{-4}$ MeV, and $\tau = 2.5 \times 10^{-2}$ MeV $^{-1}$	141
6.3	Comparisons of σ_o/σ_f as a function of N and η for $G_\parallel = 11.25 \times 10^{-4}$ MeV and $\tau = 2.5 \times 10^{-2}$ MeV $^{-1}$	142
6.4	Comparisons of σ_o/σ_f as a function of N and η for the present values but without thermal noise $\mathcal{U} = 0$, $G_\parallel = 7.5 \times 10^{-4}$ MeV, and $\tau = 2.5 \times 10^{-2}$ MeV $^{-1}$	143
6.5	Comparison of longitudinal cooling rates for several values of η and compared against the present experimental rate.	144
6.6	Comparisons of $\varepsilon_o/\varepsilon_f$ as a function of N and η	145
6.7	Plots of $\varepsilon(t = 0; N, \eta)/\varepsilon(t = t_f; N, \eta)$ as a function of η for different values of gain and number of particles N	145
A.1	A simulated annealing results for the 6 parameter quadratic model.	154

LIST OF SYMBOLS

SYMBOLS RELATED TO BEAM OPTICS

<i>Symbol</i>	<i>Name</i>
$\beta(s)$	betatron function
$\mu(s)$	betatron phase advance
ν	betatron tune
$\Delta\nu$	betatron tune deviation
Q	fractional tune
α	momentum compaction factor
η	slip factor
$\Delta p/p$	momentum spread
ε_{\perp}	transverse emittance
$D(s)$	dispersion function
$\Delta D(s, s_i)$	dispersion wave at s_i
$D_{\pi}(s)$	π doublet dispersion
$\Delta D_{\pi}(s; s_1, s_2)$	π doublet dispersion wave
π_f	focusing π doublet label
π_d	defocusing π doublet label
$\Delta \mathbf{x}(s)$	closed orbit
$\Delta\varphi_{\text{pu} \rightarrow \text{k}}$	pickup-kicker betatron phase advance
$\gamma_t^{(i)}$	nominal transition energy
$\gamma_t^{(f)}$	final design value of transition energy
$\Delta\gamma_t/\Delta t$	dynamic γ_t slew rate
T_{γ}	variable timing event
δ_{foc}	focusing quadrupole strength
δ_{def}	defocusing quadrupole strength
$\beta_{x,y}^{\text{foc}}$	β focusing quad.
$\beta_{x,y}^{\text{def}}$	β defocusing quad.
$D_{x,y}^{\text{foc}}$	dispersion at focusing quad.
$D_{x,y}^{\text{def}}$	dispersion at defocusing quad.
ξ	chromaticity
ξ_o	natural chromaticity
J_n	β fourier Component
$\tilde{\beta}_i$	Fourier spectra of nominal lattice
$\tilde{\beta}_{\pi}$	Fourier spectra with a π doublet
$\Delta\tilde{\beta}_{\pi}$	Residual Fourier spectra for π doublet

SYMBOLS RELATED TO THE TUNE EXCURSION PROBLEM

<i>Symbol</i>	<i>Name</i>
$\min\{\mathcal{F}(\nu)\}$	minimization of object function
$V^k(t)$	voltage on the k th power supply
$\Upsilon_{\text{total}}(t)$	total tune footprint
$\Upsilon_j(t)$	tune footprint for errors in j th device
$ \mathcal{R}_j $	residual associated with $\Upsilon_j(t)$
$ \langle\mathcal{R}\rangle $	total residual in tune footprint

SYMBOLS RELATED TO STOCHASTIC COOLING

<i>Symbol</i>	<i>Name</i>
$\langle G_{\parallel} \rangle$	longitudinal cooling system gain
$G_{\Re}^{(m)}$ and $G_{\Im}^{(m)}$	Real and Imaginary longitudinal gain
$\mathcal{U}_{\text{therm}}^{\parallel}(x, t)$	longitudinal thermal noise/signal
$\langle g_{\perp} \rangle$	transverse cooling system gain
$\mathcal{U}_{\text{therm}}^{\perp}(\omega, t)$	transverse thermal noise/signal
$M_m(\omega)$	mixing factor
W	Cooling system bandwidth
$\bar{k} = \beta^2 E / [\eta f_o]$	energy - frequency proportionality constant
$\bar{\kappa} = N \pi \beta^2 E / \eta f_o$	energy - frequency conversion factor
$(\epsilon_m)_{\parallel}$	longitudinal signal suppression
$\epsilon_{\Re}^{(m)}$ and $\epsilon_{\Im}^{(m)}$	real and imaginary signal suppression
$(\epsilon_m)_{\perp}$	transverse signal suppression
$M(\omega)$	transverse mixing factor
$N(\Delta E)$	longitudinal notch filter response
$P_{\parallel}(\Delta E)$	longitudinal pickup response
$K_{\parallel}(\Delta E)$	longitudinal kicker response
g_e	electronic gain constant
$x = \beta^2 E df / f / [\eta f_o]$	energy difference
$\Psi(x, t)$	longitudinal distribution function
$\psi(x, t)$	number independent longitudinal dist. function
$\phi(x, t)$	conserved flux
$\Gamma[f]$	collision operator
$(S_{\parallel}^m)_{21}(x)$	longitudinal S_{21} parameter
$B(x)$	longitudinal beam transfer function
$S_1(x)$ and $S_2(x)$	longitudinal cooling and heating term
$\varsigma(z)$	digamma function
$(S_{\perp}^m)_{21}(\omega)$	transverse S_{21} parameter
$Y(\omega)$	transverse beam response function
σ_o / σ_f	initial/final beam width
ϵ_o / ϵ_f	initial/final transverse emittance
Δ_{σ}	fractional change in beam width
Δ_{ϵ}	fractional change in beam emittance

GLOSSARY

-A-

The Accumulator Storage Ring The Accumulator is one of the two storage rings of the FNAL Antiproton Source with the purpose of collecting and storing antiprotons.

Accumulator Efficiency: The Accumulator efficiency is the total beam power on the Accumulator injection orbit, which is averaged over a super-cycle, divided by the average number of antiprotons stacked, ie. accumulator efficiency $\sim A:FFTTOT/A:STCKRT$

FNAL Antiproton Source Debuncher: The primary purpose of the Fermilab Debuncher ring is twofold; to accept approximately $6.5\mu A$ /pulse. (there are 80 pulses which make up the incoming beam with a time structure of 1.5 [nsec]) of 8.9 GeV antiprotons (\bar{p}) downstream from the production target and to subsequently reduce the momentum spread from $\Delta p/p \sim 4\%$ to $\sim .2\%$, and transverse emittance, from $\epsilon \sim 20\pi$ mm-mrad to $\sim 5\pi$ mm-mrad, for improved transfer and stacking performance in the Antiproton Accumulator ring.

-B-

Bunch rotation: A bunch of particles is defined as the collection of particle sharing the area in phase space within the separatrix, referred to as the bucket. Thus, bunch rotation refers to the collective circulation of particles in phase space along phase stable orbits.

BEAMLIN: A collection of C++ objects for the purpose of calculating linear and nonlinear lattice parameters with results identical to MAD.

betatron phase advance $\mu(s)$: is given by the phase in the solution for the particle trajectory through the accelerator $\mu(s) = \int ds/\beta(s)$

Betatron Function $\beta(s)$: Given the homogeneous Hill differential equation, $x'' + K(s)x = 0$, the betatron function is defined as the amplitude through $x(s) = \sqrt{\epsilon\beta} \cos \int ds/\beta(s)$. Thus, the betatron function must satisfy

$$2\beta\beta'' - \beta'^2 + 4\beta^2K = 4$$

Cockroft-Walton: An electrostatic preaccelerator which provides negative hydrogen ions at 750kV. The large potentials are possible based upon the principle of charging capacitors in parallel and discharging them in series.

-D-

Debuncher/Accumulator Transfer Efficiency: The ratio of the amount of beam which is transferred into the Accumulator from the total integrated Schottky power (A:FFTTOT), divided by the total Schottky power (D:FFTTOT) in the Debuncher is referred to as the Debuncher/Accumulator transfer efficiency.

Dispersion: The dispersion function $D(s)$ describes the local (at arc length s in the storage ring) transverse distance between the orbits of off-momentum particles and the design orbit. Thus, a definition of the dispersion function is $\Delta x(s) = D(s)\Delta p/p$, for which $\Delta x(s)$ is the difference in the transverse excursion between the off- and on-momentum particles.

Dispersion Killers: A dispersion killer is created at the interface between an arc section and a long straight section by creating a FODO cell with *missing* dipoles. The choice of a missing magnet dispersion killer forces the betatron phase to be $\pi/3$.

π Doublets: A π doublet refers to the perturbation of a pair of quadrupoles separated by π in betatron phase, and for which a localized dispersion wave is created between the two quadrupoles.

-E-

Emittance The emittance is the phase space area occupied by the beam. Moreover, for the solution to the Hill equation x and x' , the phase area occupied by the beam is bound by the ellipse given by

$$\frac{\epsilon}{\pi} = \gamma x^2 + 2\alpha x x' + \beta x'^2$$

For a Gaussian distribution, the emittance may be written in terms of the phase space that contains a fraction of the beam. For the present case, the emittance is defined as that which contains 95% of the beam and is given by $\epsilon = 6\pi\sigma^2/\beta$.

-F-

Feedforward electronics: In general, *feedforward* is a technique for increasing the *effective bandwidth* of a control system, such as the power supply voltage regulator circuit, by supplying the proper error signal without feedback. Thus, the feedforward signal is known or derivable prior to application to the control system.

FODO cell: The FODO cell is the basic optical arrangement of quadrupoles in an alternating gradient synchrotron, which provides strong focusing.

Fokker Planck Equation: The general character of a Fokker-Planck equation results from an *approximation* of the Master equation, which describes stochastic processes.

-H-

HP 8990 Vector Signal Analyzer: The HP8990 is a digital instrument which combines features of a wide-band super-heterodyne spectrum analyzer with the resolution of a dynamic signal analyzer.

-L-

Localized Dispersion Waves: The notion of localized dispersion waves is predicated upon the the periodicity of the inhomogeneous Hill differential equation. Thus, for a given accelerator lattice with variable *spring constant* $K(s)$, the Hill differential equation for the dispersion is

$$D'' + K(s)D - \frac{1}{\rho} \frac{p_o}{p}$$

In terms of the solution to the Hill equation for transverse betatron motion, $\beta(s)$, an integral representation of the dispersion function is given by

$$D(s) = \int \frac{\sqrt{\beta(s')\beta(s)}}{2 \sin \pi Q} K(s') \cos(\pi Q - |\mu(s') - \mu(s)|) ds' \quad (0.1)$$

where Q is the fractional tune, $\beta(s')$ and $\beta(s)$ are the beta functions at the locations s' and s , respectively, and $|\mu(s') - \mu(s)|$ is the betatron phase difference between s' and s .

-M-

Magnet current bypass - shunt circuits: The active electronics for bypassing current from individual quadrupoles are referred to as magnet current bypass - shunt circuits.

MAD: The *Methodical Accelerator Design* program is the *industry* standard lattice calculational tool and has originated and maintained at CERN.

Main Injector Project: The Main Injector Project represents the first stage of the future *luminosity upgrades* at Fermilab within the immediate future. With respect to the operation of the Antiproton Source Debuncher, the predominant parameters represented by the Main Injector project are: (i) a faster repetition rate for producing \bar{p} s and a larger intensity (3.2×10^{12} protons/pulse $\rightarrow 5 \times 10^{12}$), and (ii) a modification of the Debuncher yield of $6.7 \times 10^7 \bar{p}$ /pulse $\rightarrow 8.9 \times 10^7 [\bar{p}/\text{pulse}]$, thus a factor of 1.32 above the present number of particles. With the incorporation of beam sweeping and a Li lens upgrades, the increase of antiprotons into the Debuncher shall be expected to increase from $6.7 \times 10^7 [\bar{p}/\text{pulse}] \rightarrow 18.5 \times 10^7 [\bar{p}/\text{pulse}]$, yielding a factor of 2.7 more particles than with present scenarios.

Mixing Factor: A quantity which is a *measure of the number of revolution periods it takes for a sample of particles to mix with an adjacent sample* is the mixing factor, M . For a coasting beam with (i) a Gaussian transverse density distribution ψ , (ii) a momentum spread given by σ_p/p , and (iii) a cooling system bandwidth W , an expression for the mixing factor is given by $M = \psi_0 / [2W|\eta|\sqrt{\pi}\sigma_p/p]$.

Maximum π Doublet Filling: A complete design of $\gamma_i^{(f)}$ consists of *maximally filling the arc sections* with π doublets, for the purpose of minimizing the maximum current changes (ΔI_{\max}) required.

Momentum Compaction Factor: The momentum compaction factor is the circumference difference ΔC , between the orbits of particles having different momenta, often referred to as *off-momentum*, from the orbit of the design particle. Thus, $\Delta C/C = \alpha \Delta p/p$, for which $\alpha = 1/C \oint D(s)/\rho(s) ds$.

Momentum Spread: The momentum spread $\Delta p/p$, shall refer to the full width containing 95% of the beam.

-P-

Performance Parameters: (i) Debuncher \bar{p} yield (YIELD), (ii) the Debuncher to Accumulator transfer efficiency (DAE), (iii) the Accumulator stacking efficiency (ASE), and perhaps most important, (iv) the average stack rate (SR).

Pickup & Kicker electrodes: The pickup and kicker electrodes utilized in the Debuncher stochastic cooling system are electromagnetic loop couplers.

\bar{p} production cycle: At the FNAL Tevatron complex, the \bar{p} production cycle corresponds to the ~ 2.4 sec time in which protons are used to create antiprotons, the antiprotons are then collimated, collected, and stored in the Antiproton Source.

-S-

Separatrix: The well defined boundary in phase space between stable and unstable motion is referred to as the separatrix.

Stochastic cooling: Stochastic cooling is the damping of transverse betatron oscillations and longitudinal momentum spread or synchrotron oscillations of a particle beam by a feedback system. In its simplest form, a pick-up electrode (sensor) detects the transverse positions or momenta and longitudinal momentum deviation of particles in a storage ring and the signal produced is amplified and applied downstream to a kicker electrode, which produces electromagnetic fields that deflect the particles, in general, in all three directions. The time delay of the cable and electronics is designed to match the transit time of particles along the arc of the storage ring between the pick-up and kicker so that an individual particle receives the amplified version of the signal it produced at the pick-up [22].

Stack Rate: The stack rate is the total antiproton beam current, averaged over one *super-cycle* ($200\text{sec}/2.4\text{sec} = 83$ production cycles).

SEM grids: Secondary emission monitors used for obtaining the beam size.

Simulated Annealing Optimization: The monte carlo optimization technique of simulated annealing has been introduced with particular emphasis upon large large combinatoric and *non*-smooth problems, such as the traveling salesman problem. Thus, given an object function, and a fundamental parameter, such as *temperature*, which is a measure of the energy of the system, relative to the ground state minimum, the global features of the object function may be probed at the beginning of the search since the system may search large areas of the object function without encountering barriers due to local minima. The temperature parameter plays the key role in deciding in a probabilistic manner, whether to accept movement to some point in the configuration space which does not decrease the object function. As the system anneals, the sampled configuration space should reside close to the minima.

Signal Suppression: An expression for the signal suppression factor $\epsilon_m(x, t)$, is given by the dispersion relation:

$$\epsilon_m(x, t) = 1 + \frac{N\pi}{m} \frac{\beta^2 E}{2\eta f_o} G_m(x) \int \frac{\partial \psi(x', t)}{\partial x'} \frac{dx'}{(x - x') + i\eta}$$

-T-

Tune Footprint: The tune footprint is the path in the ν_x, ν_y plane as a function of time, during the $\Delta\gamma_t/\Delta t$ ramp.

Tune footprint $\Upsilon_{total}(t)$: The footprint excursion due to the total current errors during the $\Delta\gamma_t/\Delta t$ ramp, is given by $\Upsilon_{total}(t)$.

Tune footprint $\Upsilon_j(t)$: The footprint excursion due to current errors in all devices during the $\Delta\gamma_t/\Delta t$ ramp except for the j th device, is referred to as $\Upsilon_{total}(t)$.

transverse tune ν : The transverse tune is defined as the total number of betatron oscillations per turn in the accelerator ring, and is given by

$$\nu = \frac{1}{2\pi C} \int^C \frac{ds}{\beta(s)}$$

Transition energy (initial) $\gamma_t^{(i)}$: The value of the transition energy for the *nominal* Debuncher lattice is denoted by $\gamma_t^{(i)}$. In the dynamic $\Delta\gamma_t$ project $\gamma_t^{(i)} = 7.6$ (corresponding to $\eta = 0.0062$) is the *initial* lattice configuration.

Transition energy (final) $\gamma_t^{(f)}$: The value of the transition energy for the *final* lattice configuration, designed to improve stochastic cooling is denoted by $\gamma_t^{(f)}$. In the dynamic $\Delta\gamma_t$ project, $\gamma_t^{(f)} = 7.0$ (corresponding to $\eta = 0.0093$).

Timing Event T_γ : A variable time corresponding to the interval in the cooling cycle at which the lattice attains the constant value $\gamma_i^{(f)}$ for improved cooling performance. Operationally, the time corresponds to the on an \$82 variable TEV TCLK trigger event for returning to the initial lattice for the beginning of the next cycle.

-Y-

Antiproton Debuncher Yield: The *yield* is obtained by measuring the total Schottky power obtained from the longitudinal monitor in the Debuncher, divided by the amount of beam current targeted from a measure of the injection line toroid (M:TOR109).

CHAPTER 1

PROLOGUE: INTRODUCTORY CONCEPTS

1.1 Introduction - The Debuncher Dynamic $\Delta\gamma_t$ Project

The primary purpose of the Fermilab Debuncher ring is twofold; to accept approximately $6.5\mu\text{A}/\text{pulse}^1$ of 8.9 GeV antiprotons (\bar{p}) downstream from the production target and to subsequently reduce the momentum spread², from $\Delta p/p \sim 4\%$ to $\sim .2\%$, and transverse emittance, from $\epsilon \sim 20\pi$ mm-mrad to $\sim 5\pi$ mm-mrad, for improved transfer and stacking performance in the Antiproton Accumulator ring³. To accomplish this objective, rf- cavities are used to rotate and adiabatically debunch the beam on the time scale of ~ 40 msec, after which stochastic cooling systems, both transverse and longitudinal, are used to reduce the transverse emittance and longitudinal momentum spread throughout the remainder of the $\sim 2.4\text{sec}$ \bar{p} production cycle.

In the initial design of the Debuncher ring, the momentum compaction factor (α), or equivalently the slip factor, $\eta = \alpha - 1/\gamma^2$, was chosen to have a value which is a compromise between the two competing functions of the ring; accepting and debunching a large number of \bar{p} s/pulse, which requires a large γ_t (η small), and subsequently employing stochastic precooling, which requires a small value of γ_t (η large), prior to extraction. The goal of this experiment is to reconcile this compromise by changing η between two desired values during each \bar{p} production cycle.

1.2 Some Elementary Definitions and Physical Relations

The momentum compaction factor is the circumference difference ΔC , between the orbits of particles having momenta different, often referred to as *off- momentum* from the orbit of the design particle. Thus, $\Delta C/C = \alpha \Delta p/p$, for which $\alpha = 1/C \oint D(s)/\rho(s)ds$. In this expression for α , the dispersion function $D(s)$ describes the local (at arc length s in the storage ring) transverse distance between the orbits of off- momentum particles and the design orbit. Thus, a definition of

¹There are 80 pulses which make up the incoming beam with a time structure of 1.5 [nsec].

² $\Delta p/p$ shall refer to the full width containing 95% of the beam.

³The predominant difficulty in \bar{p} production for high energy physics is with scale of the increase in phase space density which must be attained. For each $\sim 3 \times 10^{12}$ protons on target, approximately $6.5 \times 10^7 \bar{p}$ s with $\Delta p/p \sim .3\%$ and $\epsilon_{\perp} \sim 17\pi$ are accepted into the Debuncher ring. The final requirements before \bar{p} s are ready for injection into the Tevatron for $p\bar{p}$ physics, are that $N \sim 10^{12}$ with $\epsilon_{\perp} \sim 1\pi$ and $\Delta p/p \sim .1\%$. Such an increase in particle number and phase space density spans 7 orders of magnitude.

the dispersion function is $\Delta x(s) = D(s)\Delta p/p$, for which $\Delta x(s)$ is the difference in the transverse excursion between the off- and on- momentum particles. In order to increase the momentum compaction factor for an existing storage ring, the equations just defined suggest that it is sufficient to increase the dispersion function.

A convenient definition for the momentum compaction factor is through the transition energy γ_t . Since the transit time of a particle is given by $\tau = C/c\beta$, then $\Delta\tau/\tau = \Delta C/C - \Delta\beta/\beta$. Utilizing the relations: $\Delta C/C = \alpha\Delta p/p$, and for a circular ring $\Delta f/f = -\Delta\tau/\tau$ then the following expression may be written

$$df/f = [\gamma^{-2} - \alpha]dp/p = \eta dp/p$$

The quantity $\gamma_t = 1/\sqrt{\alpha}$ is defined as the transition energy. The physical implication of the transition energy follows from the fact that particles above transition ($\gamma > \gamma_t$) require a longer time for one revolution compared with the ideal particle, because of the larger average radius defined through the dispersion function.

1.3 Changing the Dispersion in the FNAL Debuncher

The Debuncher ring has a circumference of 505 m and is composed of a sixfold symmetric separated function optical lattice. The basic arrangement of the ring consists of three long straight sections together with arc sections consisting of 57 regular FODO achromats in total. The lattice is designed to produce zero dispersion within the long straight sections in order to accommodate rf-cavities for adiabatic debunching and stochastic cooling devices for precooling in all three dimensions. As a result of the optical scheme chosen for producing zero dispersion straight sections⁴, each regular FODO cell has a betatron phase advance of $\pi/3$. Furthermore, the ring operates above the transition energy with large dispersion in the arc sections, thus limiting the momentum acceptance upon injection. The dispersion function in the arc sections reaches a maximum value of 2.4 m and the maximum transverse beta functions are approximately 14 m with tunes typically operated at 9.79 horizontal, and 9.77 vertical.

To accomplish the task of uniformly changing the dispersion function in the arc sections, while maintaining a large number of practical constraints, interleaved localized dispersion waves were

⁴The method used for producing zero dispersion in the straight sections is referred to as a *missing magnet dispersion killer*. The importance of the special FODO cell is that boundary conditions upon the dynamical equations which describe the lattice parameters dictate the betatron phase advance must be $\pi/3$.

created by perturbing the field strengths (through changes in the currents) of judiciously chosen quadrupole pairs, which are separated by π in nominal betatron phase ($\Delta\varphi$), and are referred to as π doublets. Amongst the stringent constraints which the final design satisfied are the requirements that: (i) current changes, ΔI , to any quadrupole do not exceed $\approx \pm 20$ Amps due to the power supply limitations and present design of the current shunt devices used for individual focusing adjustments, (ii) the tunes shift between the initial and final γ_t is minimized such that $\Delta\nu_{x,y} \sim \pm .005$ to avoid transverse resonance crossing resulting in beam loss, (iii) the dispersion function remains strictly zero in the straight sections due to the location of stochastic cooling devices and rf-cavities, (iv) the β functions do not exceed 10% of their nominal values ⁵, and (v) the betatron phase advance between the stochastic cooling pickup and kicker $\Delta\varphi_{PU \rightarrow K} \approx 0$ to avoid heating effects due to poor phasing.

1.4 Resonance Issues

A change in dispersion function with interleaved π -doublets in the arc sections is accompanied with relatively large tune shifts, which must be removed through adjustments of the quadrupole magnet strengths located within the zero dispersion straight sections. While perfect ($\Delta\gamma_t/\Delta t$) ramps may be designed which produce a zero tune shift, the actual implementation must consider practical engineering issues such as the finite bandwidth of power supplies. Thus, in the actual dynamic $\Delta\gamma_t$ system, slew rates are restricted completely by hardware limitations.

Since the magnet current errors during the $\Delta\gamma_t/\Delta t$ ramps accounted for the major obstacles in avoiding beam loss due to tune shift, the dominant transverse resonances which lead to measurable beam loss are given in Figure 1.1 of the transverse tune plane. The lines in the figure correspond to the resonance condition ⁶ $m\nu_x + k\nu_y = i$ (m and $k \pm$ integers). Experimentally, the *strength* and *width* of the resonances were quantified by (i) moving the operating tunes (ν_x, ν_y), with adjustment of quadrupole field strengths in the zero dispersion straight sections, to values satisfying the resonance equation, and (ii) observing the beam loss through yield measurements at or near the resonance lines. From the results of the measurements, the following resonances cause beam loss: (i) the 3rd order sum resonances with $(k, m, i) = (1, 2, 3), (0, 3, 3), (3, 0, 3)$ (with a stopband width of $\Delta\nu \sim .006$), (ii)

⁵In actuality, larger β functions at the location of the pickup and kicker tanks would enhance the signal gain/length, thereby improving cooling performance. The difficulty in shaping the β functions in this manner, however, is a result of the location of these devices. Chapter 6 describes some possible schemes for future consideration.

⁶In the resonance condition equation $m\nu_x + k\nu_y = i$, i is the order of the resonance

the 4th order sum resonances with $(k, m, i) = (\pm 2, \pm 2, 4)$, (with stopband width of $\Delta\nu = .003$), and (iii) the 5th order *sum* resonance with $(k, m, i) = (1, 4, 5), (2, 3, 5), (3, 2, 5), (4, 1, 5)$, (with an associated stopband width of $\Delta\nu = .002$). Avoiding these resonances placed considerable constraints upon the dynamic $\Delta\gamma_t$ project.

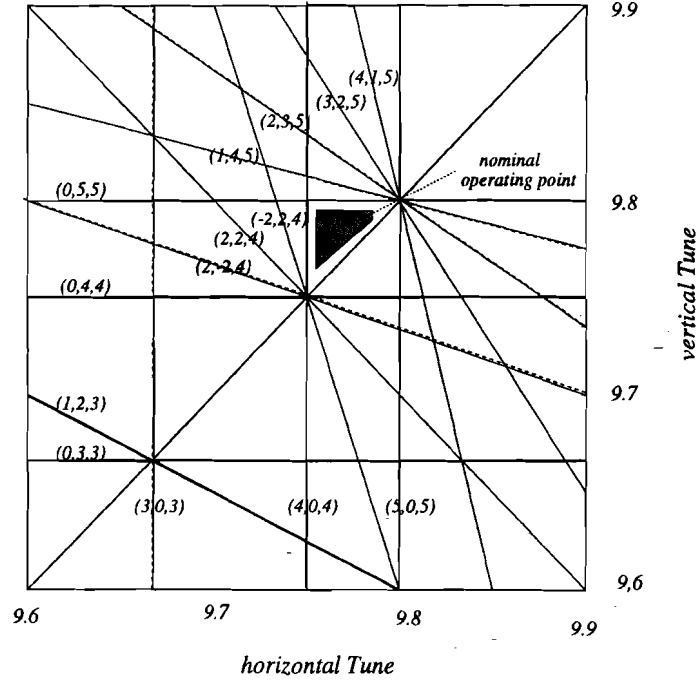


Figure 1.1: A diagram of a small region of transverse tune space indicating the dominant resonances leading to beam loss.

1.5 Stochastic Cooling and the Mixing Factor

Stochastic cooling is the damping of transverse oscillations and longitudinal momentum spread of a particle beam by a feedback system. With each revolution, the signal from a given distribution of particles is detected at a sampling rate given by the bandwidth of the feedback system. The sampled beam signal is subsequently applied back upon the same sample of particles downstream from the pickup. If there existed a spread in revolution frequencies amongst the particle distribution, due to a finite dispersion and momentum spread, then particles of nearby samples will *mix* during subsequent revolutions through the ring. The effect of *mixing*, or equivalently, producing more statistically independent sampling processes, *increases* the stochastic cooling rates.

A quantity which is a *measure of the number of revolution periods it takes for a sample of particles to mix with an adjacent sample* is the mixing factor, M . For a coasting beam with (i) a Gaussian transverse density distribution ψ , (ii) a momentum spread given by σ_p/p , and (iii) a cooling system bandwidth W , an expression for the mixing factor is given by $M = \psi_0/[2W|\eta|\sqrt{\pi}\sigma_p/p]$. From this expression, an increase in the slip factor η decreases the mixing factor.

Based upon the theory of stochastic cooling, the role of the mixing factor M is more apparent from the equation describing the time evolution of the transverse emittance ⁷ ε_\perp :

$$-\frac{1}{\varepsilon_\perp} \frac{d\varepsilon_\perp}{dt} = \frac{W}{N} \sum_{m=-\infty}^{\infty} \left[\text{Real}[g_m(\omega_l)T(\omega_l)] - \frac{\pi N}{\Omega} |g_l(\omega_l)T(\omega_l)|^2 [M(\omega_l) + \mathcal{U}(\omega_l)] \right] \quad (1.1)$$

In Equation (1.1) for ε_\perp , the sum is over all sidebands of the m -revolution harmonic corresponding to a frequency $\omega_m = (m \pm \nu)f_0$. Although the cooling system has nonzero gain $g_m(\omega_m)$ only within the frequency band W from 2GHz - 4GHz, the sum over m is finite. Furthermore, the *open loop gain* is modified by the closed loop feedback system through the quantity $T_m(\omega_m)$, referred to as the *signal suppression factor*. The first term of Equation (1.1) represents the cooling interaction, while the diffusive heating is described by the second term, which is proportional to (i) the mixing factor at each m th harmonic $M_m(\omega_m)$, and (ii) thermal noise/signal ratio at the m th harmonic $\mathcal{U}_m(\omega_m)$.

Since the cooling term in Equation (1.1) is proportional to $\text{Real}[g_m(\omega_m)]$ and the diffusion term is proportional to $|g_m(\omega_m)|^2$, it is possible to define an *optimal gain* g_{opt} which maximizes the cooling rate of Equation (1.1): $1/\varepsilon_\perp [d\varepsilon_\perp/dt]$. Because the stochastic cooling systems in the Debuncher are noise dominated, the systems operate far below the optimal gain. For improvements to the stochastic cooling performance, Equation (1.1) obviates the requirement to decrease the strength of the heating term through $M_m(\omega_m)$ and $\mathcal{U}_m(\omega_m)$. In a future Antiproton Source upgrade project, the reduction of the thermal noise/signal term $\mathcal{U}_m(\omega_m)$ shall be accomplished with the implementation of liquid helium cryogenic systems for eliminating thermal noise within the front end electronics⁸. Another approach for decreasing the strength of diffusive heating, and thus improving stochastic cooling, is by reducing $M_m(\omega_m)$. *The goals of this thesis for a dynamic $\Delta\gamma_t$ lattice are tantamount to reducing the mixing factor $M_m(\omega_m)$.*

Together with transverse stochastic cooling systems, the Debuncher also performs longi-

⁷D. Möhl, *Stochastic Cooling*, from CERN Accelerator School Proceedings 1987 CERN 87-03, Vol. II,(453)

⁸Amongst the Antiproton Source upgrade projects for the Main Injector project, a direct reduction in the noise/signal ratio (\mathcal{U}) is scheduled with the replacement of liquid nitrogen cooling with liquid helium cooling ($\sim 5K$) of the front end pickup arrays and pre-amplifiers. For reference, see *The Main Injector technical design handbook*, Batavia IL, Fermilab Main Injector Dept. 1994

tudinal (momentum) stochastic cooling. An increase in η (decrease in γ_t) shall also increase the momentum cooling rate due to the reduction of a diffusion term. Thus, increased precooling in all dimensions was predicted for the dynamic $\Delta\gamma_t$ project. Since the mixing factor $M \sim 1/[\eta(\Delta p/p)]$, there exists a subtle competition between an increase in longitudinal cooling rate to the increase in transverse cooling rate. Thus, in order to predict the cooling rates for the dynamic $\Delta\gamma_t$ project, a full integration of the Fokker Planck transport equation was required. Based upon the successful comparisons between the predicted and experimental cooling rates, extrapolations have been performed for the higher beam fluxes anticipated with the operation of the Main Injector. Moreover, it is with this extrapolation that the dynamic $\Delta\gamma_t$ project is expected to have significant cost/benefits performance improvements.

1.6 Implications of Improved Precooling for the Antiproton Source

Improved stochastic precooling in the Debuncher has direct benefits for the stacking of antiprotons in the Accumulator. Figure 1.2 is the result of an experimental study to quantify improvements to the Debuncher to Accumulator (D/A) transfer efficiency with smaller transverse emittances. The smaller emittances ε_{\perp} were obtained by extending the production cycle, and hence allowing longer cooling times. Measurements of the transverse beam size were obtained with SEM grids within the transfer channel, and the D/A efficiency was measured by taking the ratio of the total current in the Debuncher to that measured upon injection into the Accumulator. The results of the measurements indicate that a reduction of the emittance by a factor of 2 translates to an increase of the D/A efficiency by $\sim 12\%$. Although this particular study could not predict the effect upon stack rate, since the longer cooling times result in *less* particles available for stacking, independent measurements suggest such an increase in the D/A transfer efficiency translates to a increase in the stacking rate by approximately 6%.

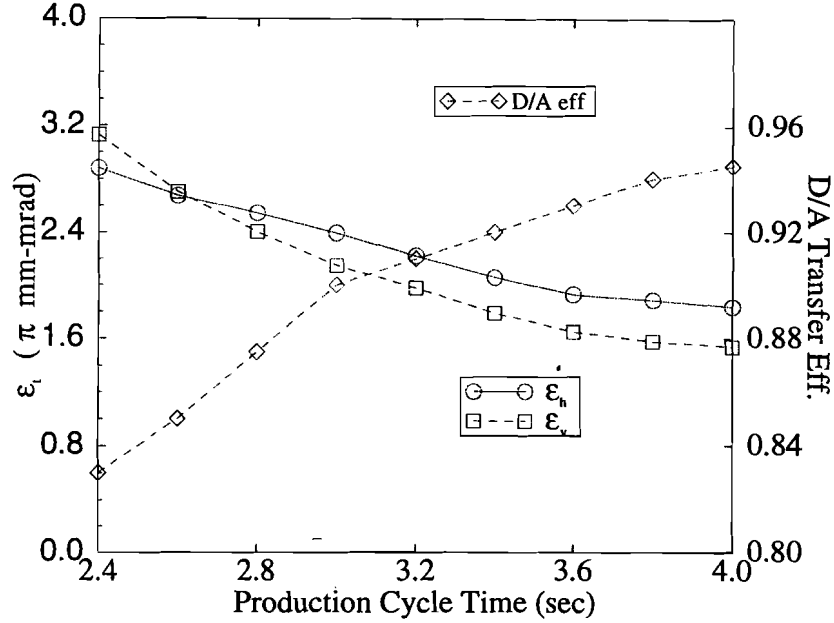


Figure 1.2: Debuncher to Accumulator (D/A) transfer efficiency and transverse emittance as a function of the duration of the production cycle.

1.7 Structure of Thesis

The specific structure of this thesis is intended to facilitate, from several levels, a discussion of the technical challenges inherent within the dynamic $\Delta\gamma_t$ project. First, details associated with designing a stable lattice with the required $\gamma_t^{(f)}$ from the modification of an existing lattice design are presented. Together with design methodology inherent in the original Debuncher design and that for a dynamic $\Delta\gamma_t$, various theoretical underpinnings, historical perspectives, and measurements of the relevant lattice parameters shall be presented.

A major ingredient associated with accelerator lattice design is often the need to solve a difficult constrained optimization problem. This was particularly true for the dynamic $\Delta\gamma_t$ project, since the design was required to embody the original lattice concepts and constraints, while making dramatic changes to the dispersion. Standard optimization theory/techniques are discussed in the first chapter with specific application to the Debuncher dynamic $\Delta\gamma_t$ lattice design. As a comparison to *classical* optimization algorithms, the method of simulated annealing is shown to be a possible

candidate for implementing difficult accelerator lattice design constraints.

In the second chapter, details of the fast $\Delta\gamma_t/\Delta t$ ramps (*current slew*) rates are presented and discussed through: (i) experimental examples and associated calculations illustrating the resulting transverse tunes as a function of time, (ii) engineering solutions to power supply regulation problems, and (iii) a complete characterization of the special case $\Delta\gamma_t^{(f)}/300\text{msec}$.

Together with hardware and regulation issues, questions about the generation of higher multipoles during the $\Delta\gamma_t/\Delta t$ ramps are addressed in chapter 2. Through comparison of the measured and calculated tune footprints, the beam may be used to assess whether the quadrupole focusing field is distorted by rapidly changing magnetic fields on the relevant time scales. Furthermore, the generation of sextupole components in the γ_t^f design is investigated through measurements of the chromaticity as function of time through the $\Delta\gamma_t^{(f)}/\Delta t$ ramps.

Issues related to stochastic cooling are introduced in chapter 3. Prior to investigating the effects of $\Delta\gamma_t$, however, the cooling feedback system is described through experimental measurements which are used to extract inputs for a comprehensive computer model. Comparisons between the results of the computer calculation and the experimental cooling data are presented.

The full results of the Debuncher dynamic γ_t project are given in the final chapter. Predictions from the stochastic cooling computer model, which is described in detail in chapter 3, are compared against experimental results. Based upon the success of the model, projections are made for the performance of stochastic cooling with a dynamic $\Delta\gamma_t$ lattice with Main Injector beam parameters.

CHAPTER 2

THE $\gamma_t^{(f)}$ LATTICE DESIGN: FUNDAMENTALS

2.1 Introduction

To optimize the performance of stochastic precooling within the Antiproton Debuncher Ring, while not degrading other functional requirements, an option is to change γ_t between two values; the original design value $\gamma_t = 7.63188(\eta_i = 0.006155)$ at injection, to the final value $\gamma_t^{(f)} = 7.02655(\eta_f = 0.00924)$ throughout the remainder of the production cycle, in order to increase the mixing amongst particles (a decrease in the mixing factor M). This chapter shall address the following issues: (i) the results from computational models of the nominal design lattice together with comparisons with experimental measurements of selected lattice functions, (ii) the theoretical underpinnings involved with decreasing $\gamma_t^{(i)} \rightarrow \gamma_t^{(f)}$ through localized dispersion waves produced with quadrupole π -doublets, (iii) the optimization problem for producing zero tune shift ($\Delta\nu \approx 0$) between $\gamma_t^{(i)}$ and $\gamma_t^{(f)}$, (iii) the complete specifications for a $\gamma_t^{(f)}$ design, which includes comparisons to experimental measurements and hardware requirements, and (iv) the transverse resonances in the Debuncher relevant to the dynamic $\Delta\gamma_t$ project.

2.2 The Function of the FNAL Debuncher

The fundamental role of the Antiproton Debuncher ring is predicated upon solving many difficulties involved with \bar{p} production [26]. For the luminosity objectives of the Tevatron project [32], it is such that *an increase in antiproton number and phase space density must span 7 orders of magnitude*. The obdurate technical challenges inherent in \bar{p} production are overcome at Fermilab in several stages and through a complex choreography amongst several different accelerators and storage rings.

Figure 2.1 is a simplified illustration of the Fermilab complex layout. Antiproton (\bar{p}) production begins with acceleration of protons through a potential created by an electrostatic Cockroft-Walton magnetron (negative ion) source. Bunches of H^- ions are accelerated through a linear accelerator (the *LINAC*) to 400 MeV and injected into a rapid cycling accelerator, the *Booster*. The energy of the protons is increased to 8 GeV in the Booster at which point they are injected into the *Main Ring*. 82 bunches of protons are accelerated to 120 GeV in the *Main Ring* and may be used

for producing antiprotons. As described in the Tevatron I Design Report, the proton energy of 120 GeV was selected for two reasons: (i) the \bar{p} yield per unit volume per unit time does not increase appreciably beyond 150 GeV yet the operating costs increase dramatically beyond 120 GeV, and (ii) specific engineering issues of Main Ring dictate 120 GeV is the maximum energy which can be extracted from F17 straight section. The \bar{p} production momentum was chosen to be 8 GeV off the target, which was governed by (i) the fact that the \bar{p} yield displays a plateau from 8-13 GeV/c, and (ii) the antiproton source matches the maximum energy of the Booster synchrotron.

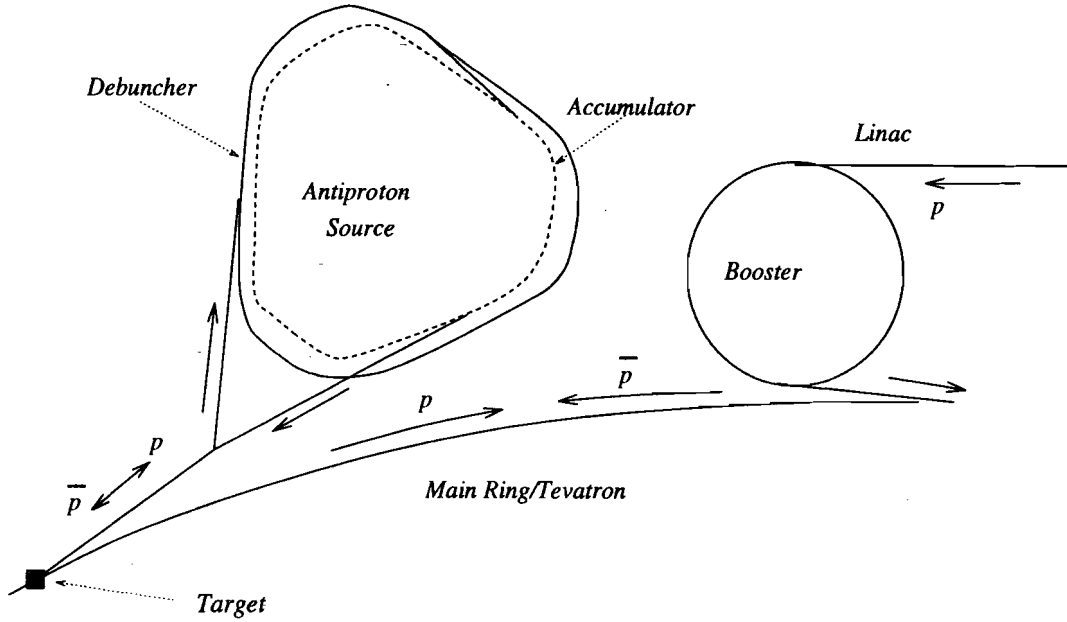


Figure 2.1: A diagram of the FNAL Antiproton Source Debuncher/Accumulator storage rings.

Based upon yield measurements in the Debuncher, for every 10^6 protons incident upon the production target, 18 antiprotons are accepted into the Debuncher¹. Since for the Main Ring beam current $N \sim 3 \times 10^{12}$ protons, this corresponds to $\sim 6\mu\text{Amps} - \bar{p}/\text{pulse}$, or $N \sim 6 \times 10^7$ antiprotons.

Thus, for the purpose of obtaining the luminosities required of $p\bar{p}$ high energy physics, it is necessary to build up a collection of antiprotons over several hours of production operation. For the purpose of producing, collimating, cooling and storing antiprotons, the Antiproton Source utilizes two storage rings - the Debuncher and the Accumulator.

With each production cycle, the Debuncher ring accepts 80 \bar{p} bunches having a time structure

¹The \bar{p} accounting may be broken down further: (i) a total of 4×10^5 protons absorbed into the target, (ii) 300 \bar{p} are created within the AP2/Debuncher momentum aperture, (iii) -70 \bar{p} absorbed in target and lens, (iv) -130 \bar{p} miss lens, and (v) -82 fall outside the transverse aperture of the AP2/Debuncher \rightarrow 18 \bar{p} are accepted. Special thanks to Frank Bieniosik for supplying these estimates based on his work with the target sweeping project.

of 1.5nsec, an intensity of approximately $7\mu\text{A}/\text{pulse}$, an energy of 8.9 GeV, a momentum spread $\Delta p/p \sim 4\%$ (95% FW) , and a transverse emittance $\epsilon \sim 20\pi$ mm-mrad. Since the time structure of the antiprotons reflects the time structure of the targeted protons², the separate pulses are captured with rf-cavity voltage, which are frequency matched to the Main Ring. By allowing the particles to exchange energy with the applied rf electric field, the time structure of the antiprotons can be removed in a process referred to as *bunch rotation*. Within the $\Delta E - \Delta t$ phase space, the rotation of the bunch of particles with a narrow time structure Δt is exchanged for a narrow energy structure ΔE . Bunch rotation is accomplished in the Antiproton Debuncher with 8 rf- cavities, which produce a total initial voltage of 5MV (the rotation stage $\sim 100\mu\text{s}$) which is rapidly reduced to $\sim 120\text{kV}$ in order to slow the particles from rotating through more of the synchrotron phase. The voltage is then *adiabatically* reduced to zero with $\sim 10\text{msec}$ and the rf- structure of the beam is removed.

Stochastic cooling feedback systems in the Debuncher ring are used to precool the injected antiproton beam for improved stacking performance by the Accumulator. The details of the cooling systems are discussed at length in chapter 3.

2.3 The Nominal FNAL Debuncher Lattice

The FNAL Antiproton Source Debuncher is a sixfold symmetric, triangular shaped storage ring with an average radius of 80.42m. The shape of the storage ring was chosen for the purpose of obtaining maximum *real estate* for locating RF cavities and stochastic cooling devices within the optical lattice. The beam energy is $\gamma = 9.52978$ ($T = 8.0\text{GeV}$ and $\beta = .99448$), with a revolution period of $\tau = 1.6948\mu\text{sec}$. For a bending radius of $\rho = 17.44\text{m}$, the magnetic rigidity is $B\rho = 296.5\text{kG-m}$ and the average dipole field strength is 1.7T for dipoles with an effective length of 1.6604m. The location of the Antiproton Source and Debuncher ring, relative to the other accelerators has been given in Figure 2.1.

Within the long straight sections of the Debuncher (labeled $D10$, $D30$ and $D50$) , there are (i) RF cavities for performing phase space rotation and subsequent adiabatic debunching of injected

²Prior to targeting, bunch rotation is performed in the Main Ring to produce a narrow time structure in favor of a large ΔE . Increasing ΔE prior to targeting *maximizes* the number of antiprotons which are accepted into the Debuncher (since the momentum acceptance is a constant $\Delta p/p = 4\%$)

antiprotons³, (ii) stochastic cooling pickup and kicker tanks⁴, and (iii) diagnostic beam sensing devices. By comparison, the arc sections are rather simple, consisting of regular FODO cells⁵ with sextupole chromatic correctors located at the entrance and exit of each quadrupole.

A simplified illustration of the optical/electrical power configuration for one sector of the Debuncher is given in Figure 2.2. Represented in Figure 2.2 are: (i) the quadrupoles, by convex (*focusing* - odd numbered lenses) and concave (*defocusing* - even numbered lenses) thin lenses, (ii) the dipoles, by inverted triangles, (iii) although sextupoles are omitted from the diagram, they exist on either side of quadrupoles with alternating polarity, and (iv) the electrical power supply connections: D:QSS, the straight section power supply for Q1 through Q5 with associated magnet current shunts, D:QF, the supply for the *focusing* odd numbered quadrupoles Q7 through Q19, and D:QD, the power supply for the even numbered quadrupoles Q6 through Q20. Also indicated in Figure 2.2 are the two general divisions of the lattice; the long *dispersion free* straight section - composed of quadrupoles $\frac{1}{2}$ Q1 through Q6, and the arc section - consisting of quadrupoles Q7 through $\frac{1}{2}$ Q20, and dipoles D7 through D19.

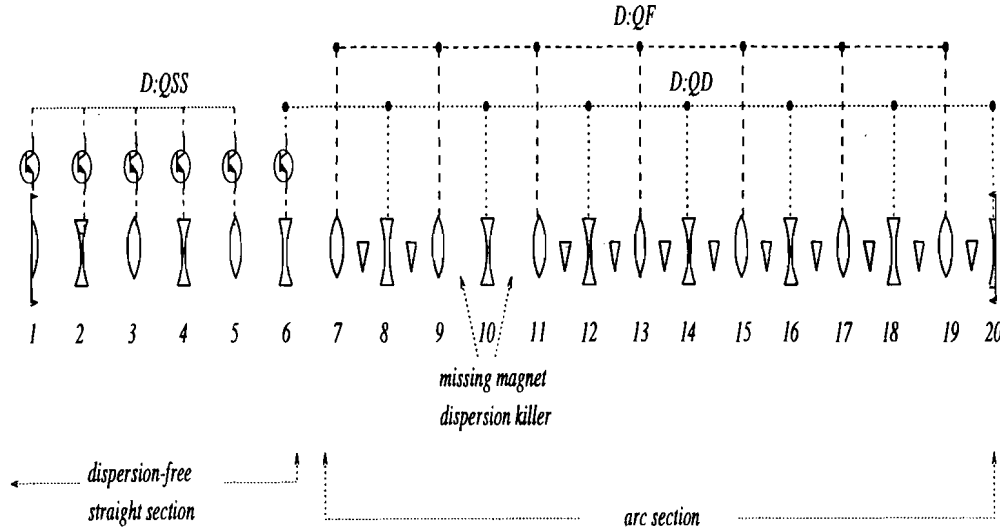


Figure 2.2: An optical element diagram of a representative sector in the Debuncher ring.

For the purpose of obtaining zero dispersion in the long straight sections, FODO cells,

³There are a total of 8 RF cavities (denoted DRF1 - DRF8). Six of these cavities achieve a maximum voltage gain per turn of 5MV over approximately 50μsec, while the remaining two cavities adiabatically reduce the voltage from 120 kV to less than 5kV in ~ 10msec.

⁴Tanks refers to 4 sets of 32 pickup pairs (and kickers) which are installed in the D10 straight section (D30 straight section). The number of pickup pairs is a multiple of 2 and as large as possible to get the maximum gain per length

⁵A FODO cell refers to the standard strong focusing arrangement of alternating gradient accelerators, having the structure: *focusing* (F) - *drift* (O) - *defocusing* (D) - *drift* (O).

referred to as dispersion killers [11], [12], [13], which omit dipole bending magnets, are located at each of the interfaces of the arc sections and the straight sections. In Figure 2.2 the location of the FODO cell with missing dipole magnets is illustrated between Q9-Q10, and Q10-Q11.

As a result of specific design choice of the missing magnet dispersion killer, the boundary conditions required for matching lattice parameters across the FODO cells *imply*⁶ the betatron phase advance per FODO cell be $\Delta\varphi = \pi/3$.

Thin lens formulas may be used to obtain approximate values of the lattice parameters at the locations of the focusing and defocusing quadrupoles for a simple FODO cell [102]. For the given thin lens strengths⁷ in the Debuncher arc section FODO cells, $\delta_{\text{foc}} = 0.337267\text{m}^{-1}$ and $\delta_{\text{def}} = 0.33014\text{m}^{-1}$ and FODO cell length $L = 8.865\text{m}$, the phase advance in each transverse dimension μ_x , and μ_y , respectively, may be obtained with Equations (2.1)

$$\delta_{\text{def}}\delta_{\text{foc}} = -\frac{\cos \mu_x + \cos \mu_y - 2}{L^2} \quad \delta_{\text{foc}} - \delta_{\text{def}} = \frac{\cos \mu_y - \cos \mu_x}{L} \quad (2.1)$$

With $\mu_x \approx \mu_y = \pi/3$, approximate expressions for the lattice functions, β and D , at the location of the focusing and defocusing quadrupoles may be obtained. The betatron function at the location of focusing quadrupole in the standard arc section FODO cell is given by:

$$\beta_{x,y}^{\text{foc}} = \frac{L}{\sin \mu_{x,y}} [1 \pm L\delta_d/6] = \begin{cases} 15.2[\text{m}] \\ 5.2[\text{m}] \end{cases} \quad (2.2)$$

which is approximately equivalent to the results at the defocusing quadrupoles, $\beta_{y,x}^{\text{def}}$. Expressions for the dispersion may be obtained at the center of the focusing and defocusing quadrupoles of a FODO cell in the thin lens approximation, and are given by D^{foc} and D^{def} , respectively,

$$D^{\text{foc}} = \frac{L\Phi[\delta_d L + 8]}{8(1 - \cos \mu_x)} \quad D^{\text{def}} = \frac{L\Phi[\delta_d + \delta_f]}{2\delta_d(1 - \cos \mu_x)} - \frac{\Phi}{\delta_d} \quad (2.3)$$

$$(2.4)$$

for which $\Phi = L_{\text{dipole}}/\rho \approx 0.092$ is the bending angle of the sector dipole magnet. Thus, with $\mu_{x,y} \approx \pi/3$, and $L = 8.865\text{m}$ the values of the dispersion are $D^{\text{foc}} = 2.1\text{m}$, and $D^{\text{def}} = 1.55\text{m}$.

⁶The fact that the phase advance per FODO cell *must* be $\pi/3$ may be derived by elementary methods demanding the mapping across FODO cells obey a unitary transformation [89], [90], [93]. Given the transfer matrix M across one FODO cell and a lattice function ξ , then the symplectic condition demands: $\xi M = \xi$. One then writes the transfer map for a FODO cells with and without dipoles, e.g. M_1 and M_2 respectively, constructs $M = M_1 M_2$, and then solves the symplectic condition. The result is that the only manner in which the symplectic condition would be satisfied is if the β - phase advance, $\varphi = \pi/3$

⁷The thin lens strengths δ_j correspond to the inverse of the focal length, or $B'/[B\rho]$.

Furthermore, the thin lens approximation for the transition energy due to a single FODO cell, is given by

$$\frac{1}{\gamma_t^2} = \frac{\Phi^2}{48} \left[\frac{5 \cos \mu_x - 3 \cos \mu_y + 46}{(1 - \cos \mu_x)} \right] \quad (2.5)$$

The numerical value of γ_t obtained with the approximate FODO cell thin lens equation, and which assumes the entire storage is filled with regular cells, is given by $\gamma_t \approx 7.76$. This value compares well with the exact value of $\gamma_t = 7.631$.

Utilizing a standard linear lattice model, *Methodical Accelerator Design* [43] (MAD), the lattice parameters may be calculated at all points in the storage ring. The dispersion and transverse β functions of nominal lattice in the Debuncher from a calculation with MAD is given in Figure 2.3.

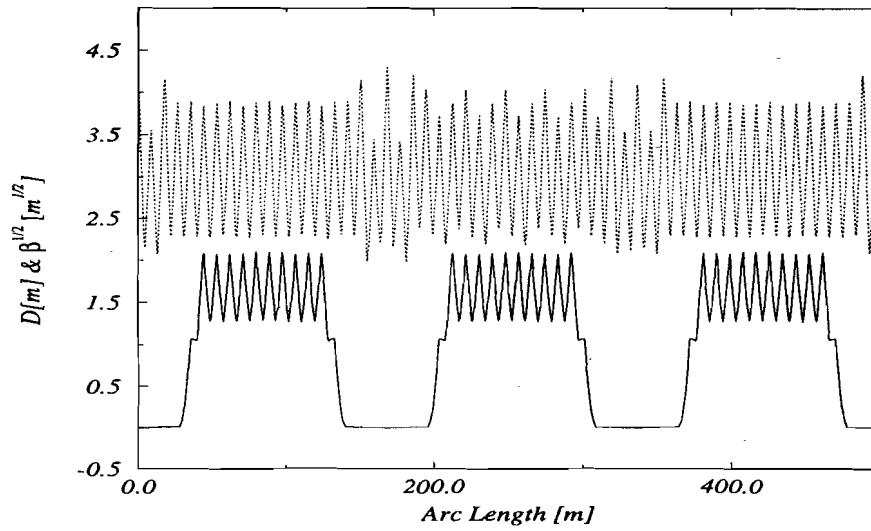


Figure 2.3: The nominal Debuncher lattice parameters for $\eta = 0.006$ from MAD calculation.

2.3.1 Characterizing the Lattice

In this section, the general notions about the optics in the Debuncher are developed further through comparisons between experiments and the results from computer models. Moreover, these comparisons may be used to benchmark predictions for the design of $\gamma_t^{(f)}$ in order to gain an appreciation for the associated errors between simple linear lattice calculations and the actual Debuncher

optics. Specifically, measurements and calculations shall be described for the following quantities: (a) the β functions, (b) the chromaticity ξ , (c) the dispersion, $D(s)$, and (d) the transition energy γ_t , or equivalently, the slip factor $\eta = 1/\gamma_t^2 - 1/\gamma^2$.

2.3.1.1 Predictions/Measurements of the β Functions

The transverse betatron functions, β_x and β_y were measured at the location of four quadrupoles equipped with power supply shunt circuits. Since the first order transverse tune shift, $\Delta\nu^{(1)}$, is proportional to the perturbed quadrupole strength ΔK , the beta function are easily extracted. Specifically, the first order tune shift due to a change in the quadrupole field gradient is $\Delta\nu^{(1)} = \frac{1}{4\pi} \oint \beta(s) \Delta K(s) ds \simeq \frac{1}{4\pi} \beta_i(s) \int_{s_0}^{s_0+L} \Delta K(s) ds$, for which β_i is the beta function at the i -th quadrupole. Utilizing I versus K magnet data, a parameterization was used for evaluating the integral, such that $\int_{s_0}^{s_0+L} \Delta K(s) ds = a_0 + a_1 I + a_2 I^2 + a_3 I^3$. For the purpose of reference, the values of the fitted parameters, a_j , for the three types of quadrupole magnets in the Debuncher are listed in Table 2.1.

Table 2.1: I versus K cubic fitting parameters a_j for the three types of quadrupole magnets in the Debuncher.

<i>Magnet Type</i>	<i>Length</i>	a_0	a_1	a_2	a_3
SQC	0.70104 m	3.59×10^{-4}	1.323	0.5288	-1.985
SQD	0.82800 m	-2.19×10^{-4}	1.344	0.3738	-0.848
LQE	0.87376 m	0.095	0.199	-5.7×10^{-2}	1.28×10^{-2}

A comparison between the measured transverse β functions and those calculated with the lattice code BEAMLIN⁸ [63], [64], [65], at the location of four quadrupoles are listed in Table 2.2 together with the percentage differences between the model and experimental result. In Table 2.2, $|\Delta\beta_j| = (\beta_j^m - \beta_j^e)/\beta_j^m$, for which β_j^m is the model calculated value and β_j^e is the experimental value. Within the associated errors of the measurement, the results of the β at a finite number of locations in the ring are in agreement with the model calculations. Thus, the averages are given by (i) $\langle\%|\Delta\beta_x|\rangle \sim 7.3 \pm 2.7$, and (ii) $\langle\%|\Delta\beta_y|\rangle \sim 10.8 \pm 1.3$.

⁸BEAMLIN is a collection of C++ objects for the purpose of calculating linear and nonlinear lattice parameters with results identical to MAD.

Table 2.2: Comparison between measured and predicted β function values at the location of four quadrupoles in the Debuncher.

<i>Magnet</i>	β_x^e	β_y^e	β_x^m	β_y^m	$\% \Delta\beta_x $	$\% \Delta\beta_y $
QS101(F)	15.79 ± 0.78	4.22 ± 0.21	17.95	4.72	12.0%	10.5 %
QS102(D)	4.78 ± 0.24	13.08 ± 0.65	4.72	14.30	1.2%	8.5 %
QS305(F)	18.46 ± 0.92	5.06 ± 0.25	17.73	4.61	4.1%	9.7 %
QS306(D)	5.94 ± 0.30	11.76 ± 0.58	5.30	13.81	12.0%	14.8 %

2.3.1.2 Predictions/Measurements of Chromaticity ξ

Chromaticity is defined as the variation of the transverse tunes with energy, $\xi = \Delta\nu/[\Delta p/p]$. Within the Debuncher, sextupoles are used to correct the natural chromaticity⁹ in each transverse dimension, $\xi_{xo} \approx -N/\pi \tan[\mu_x/2] \approx -10$, and $\xi_{yo} \approx -11.6$ [32], which results from magnet imperfections in the dipole and quadrupole fields. Although corrections are made with sextupole fields, there still exists a finite energy dependence of the tunes across the momentum aperture. To measure the chromaticity in each transverse dimension, the transverse tunes were measured for several values of $\Delta p/p$.

For each transverse tune measurement, protons were bunched and decelerated/accelerated using the DRF3 rf cavity¹⁰. To facilitate further discussion, the raw data for the chromaticity measurement is given in Table 2.3.

Table 2.3: Result of chromaticity measurement for $\eta = .006$

$f_{90}[\text{MHz}]$	$\Delta f/f \times 10^{-4}$	$\Delta p/p \times 10^{-2}$	ν_x	ν_y
53.10021	-0.5631	-0.9082	0.7552 ± 0.015	0.8287 ± 0.017
53.10132	-0.3540	-0.5710	0.7620 ± 0.015	0.8332 ± 0.017
53.10243	-0.1450	-0.2339	0.7674 ± 0.015	0.8359 ± 0.017
53.10286	-0.06403	-0.1033	0.7740 ± 0.015	0.8261 ± 0.017
53.10464	0.2712	0.4374	0.7841 ± 0.015	0.8398 ± 0.017
53.10565	0.4614	0.7441	0.7904 ± 0.016	0.8416 ± 0.017
53.10676	0.6704	1.081	0.7850 ± 0.016	0.8398 ± 0.017

In the first column of Table 2.3 is the readback frequency of the RF cavity (at the $h = 90$ harmonic of the revolution frequency), obtained after the beam has been either accelerated or

⁹For thin lens formulas and for a sextupole correction strength given by $m = B''$: $\xi_x = \int ds \beta_x (k - m D_x)$ and thus the natural chromaticity is found by setting $m = 0$. For the thin lens FODO cell $\xi_{xo} = -1/\pi \tan[\mu_x/2]$.

¹⁰The Debuncher DRF3 RF cavity is tuned to 1.23MHz. This cavity is used for diagnostic purposes.

decelerated to the desired point in the momentum aperture and the cavity voltage reduced. The readback frequency corresponds directly to the revolution frequency of the beam centroid.

Using a measured value of the slip factor ¹¹, $\eta = 0.0062 \pm 3. \times 10^{-4}$, the momentum spread, $(\Delta p/p) = (\Delta f/f)/\eta$, may be calculated. Figure 2.4 gives the results of the least square fits to the data in Table 2.3. The tune shifts, $\Delta\nu_j$, as a function of $\Delta p/p$ are then a direct measure of the chromaticity. The results of the measurements are $\xi_x = 1.74 \pm 0.24 \pm .015$ and $\xi_y = 0.635 \pm 0.23 \pm 0.017$. The first error quoted for $\xi_{x,y}$ are the standard deviation of the respective linear least square fit, while the second value corresponds to the error associated with the error in reading the correct value of the transverse tune (an error of $\sim 5\%$ which is incorporated in the error bars of of Figures 2.4(a) and (b)).

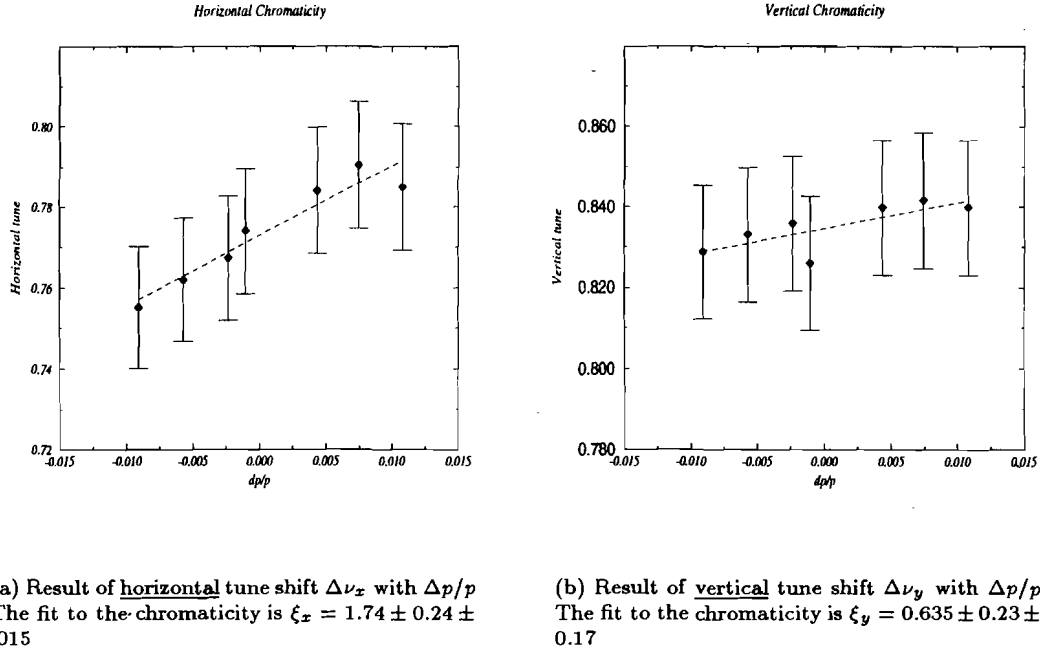
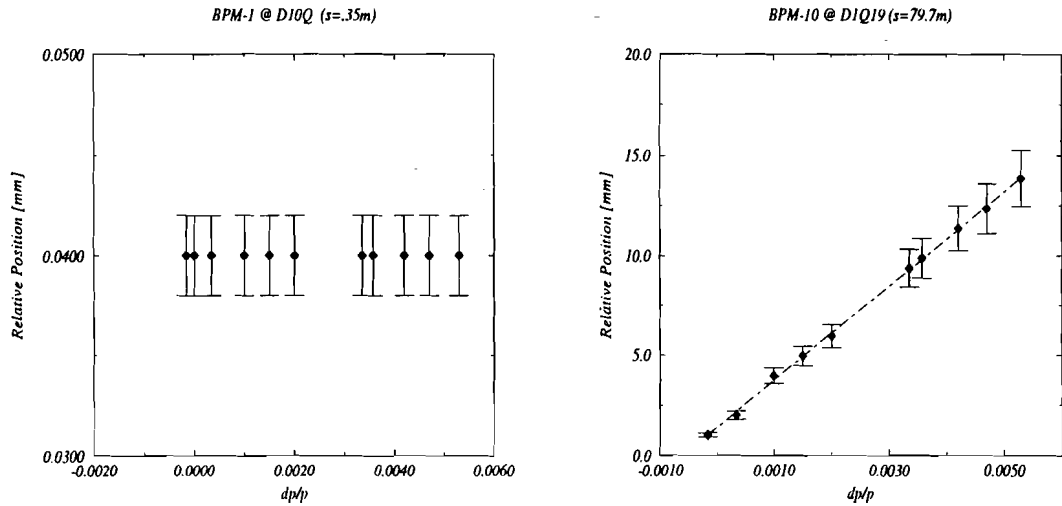


Figure 2.4: Chromaticity data with associated linear least square fit.

¹¹The details of the measurement of η is given in the following sections. The error on the slip factor measurement is $\pm 5\%$, which comes from the calibration error associated with the cavity voltage used in the measurement.

2.3.1.3 Predictions/Measurements of the dispersion, $D(s)$

The local function describing the transverse difference in the orbits between off-momentum particles and the design particle, is the dispersion function, $D(s) = \Delta x(s)/(\Delta p/p)$. Measurements of the horizontal closed orbit $\Delta x(s)$ as a function of $\Delta p/p$ were obtained with the use of beam position monitors (BPM) located throughout the ring at the location of the *focusing* quadrupoles. The dispersion $D(s_i)$, at the location s_i of each BPM, is extracted from the variation of $\Delta x(s)$ with $\Delta p/p$ from linear least square fits. Figure 2.5(a) and (b) are two representative plots of specific BPM measurements for different $\Delta p/p$ obtained from locations corresponding to (i) a quadrupole in the dispersion free straight section, and (ii) from a quadrupole in the arc section, respectively. Error bars associated with the BPM data are approximately 5%, while the resulting dispersion should also contain the standard deviation of the linear least square fit, as well as an overall (calibration) systematic error between BPMs of approximately 10%. Despite the large systematic errors, the assumption of a linear dependence between the closed orbit $\Delta x(s)$ and the energy is valid across the entire momentum aperture, and justifies the linear least square fit method for extracting the dispersion.



(a) BPM-1 at the location of the quadrupole denoted by 10Q, which corresponds to quadrupole 1 in Figure 2.2.

(b) BPM-10 at the location of the quadrupole denoted by D1Q19, which corresponds to quadrupole 19 in Figure 2.2.

Figure 2.5: Representative measurements from the BPM data as a function of $\Delta p/p$.

The results of the least square fits for obtaining a measurement of the horizontal dispersion $D(s)$ and a comparison with the theoretical prediction from BEAMLIN (represented by the dotted line) are given in Figure 2.6(a). In Figure 2.5, the error bars associated with the measured data correspond to (i) the variance of the linear least square fits, and (ii) an overall systematic error of 10%. The difference between the measured and predicted values of the dispersion, $\Delta D(s) = D_{\text{pred.}} - D_{\text{exp.}}$ shall be used as a scale factor for comparisons to lattices with $\gamma_t^{(f)}$. Large differences between the predicted and measured dispersion in sector 50/60 (arc length $s \sim 350\text{m}$ thru 500m) are believed to be attributed to poorly functioning BPMs and not a true artifact of the lattice functions¹². As such, the sector 50/60 data shall be omitted from further consideration and from comparisons with $D(s)$ from $\Delta\gamma_t^f$ lattices.

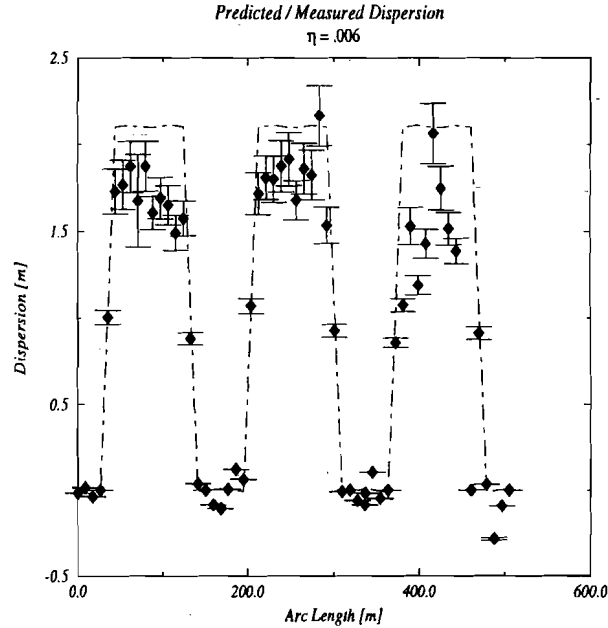


Figure 2.6: A Comparison of the predicted and measured dispersion for the $\eta = 0.006$ nominal lattice.

¹²The fact that the 50/60 sector show such large error deviations in all of the data is an indication of improper functioning of the BPMs in that sector. By contradiction, if there indeed existed a dispersion wave in sector 50/60 this would not be localized and would also degrade the measurement of γ_t . Since neither is observed, one may conclude that all evidence taken together, the BPM data in that sector should be ignored.

2.3.1.4 Predictions/Measurement of the Slip Factor, η

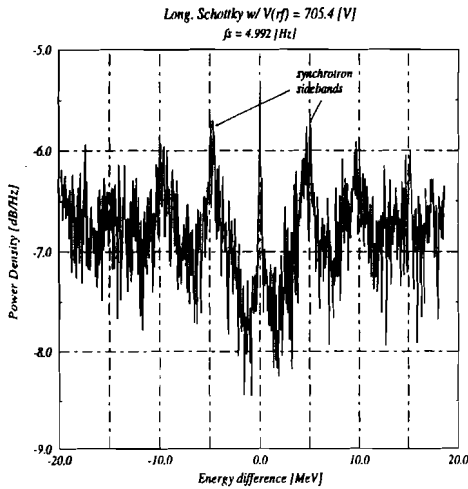
The slip factor, defined by the equation $\eta = \alpha - \frac{1}{\gamma^2}$ and the momentum compaction factor $\alpha = \frac{1}{\gamma_t^2}$, may be measured by recording the observed synchrotron sideband frequency f_s as a function applied RF- cavity voltage \tilde{V}_{rf} from the longitudinal bunched beam Schottky spectrum [27]. An expression for the slip factor, and thus γ_t , in terms of other known constants is given by Equation (2.6)

$$\eta = \frac{2\pi f_s^2 \beta^2 E}{h f_0^2 e \tilde{V}_{rf}} = \frac{2\pi L / c (p_b c) f_s^2}{F_{rf} (e \tilde{V}_{rf})} \quad (2.6)$$

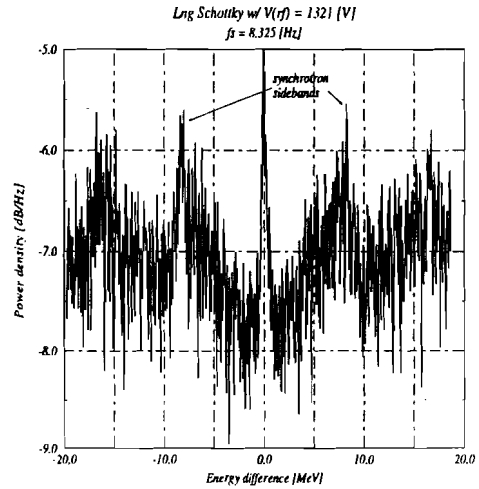
The constants which appear in the Equation (2.6) are given by: $L = 505294\text{mm}$, $p = 8.89\text{GeV}/c$, and $F_{rf} = 2.36\text{MHz}$. Upon substitution into Equation (2.6), the expression relating the synchrotron frequency to the applied RF- voltage is given by:

$$f_s^2 [\text{Hz}^2] \approx 2.51 \times 10^4 (e \tilde{V}_{rf} [\text{Volts}]) \eta \quad (2.7)$$

The longitudinal Schottky - bunched beam spectrum at the 126th harmonic for two different applied RF- voltages, $\tilde{V}_{rf} = 705.4\text{V}$ and $\tilde{V}_{rf} = 1321\text{V}$, which are given in Figures 2.7(a) and 2.7(b), respectively, depict the synchrotron sideband spectra. The superb resolution in the measurements of the synchrotron spectra was possible with the HP 8990A vector signal analyzer [7].



(a) $\tilde{V}_{rf} = 705.4\text{V}$ and $f_s = 4.992\text{ Hz}$



(b) $\tilde{V}_{rf} = 1321\text{V}$ and $f_s = 8.325\text{ Hz}$

Figure 2.7: Power density (dB/Hz) versus energy difference $x = E - E_o$ of the longitudinal Schottky signal (126th harmonic) for obtaining the synchrotron frequency f_s .

Figure 2.8 is the result of f_s^2 versus the RF- cavity voltage measurements¹³, and Equation (2.7): $f_s^2 = 2.51 \times 10^{-2} V(\text{rf})$. The error bars in Figure 2.8 correspond to 10% of the abscissa value due to the error in calibration of the RF- cavity voltage, and approximately 5% in the ordinate, which is due to the error in reading the correct value of the synchrotron frequency from Figure 2.7. The slope of the least square fit through the data gives the measured value of, $\eta = 0.0062 \pm 6 \times 10^{-4}$ which is in excellent agreement with the theoretical value of $\eta = 0.0061$.

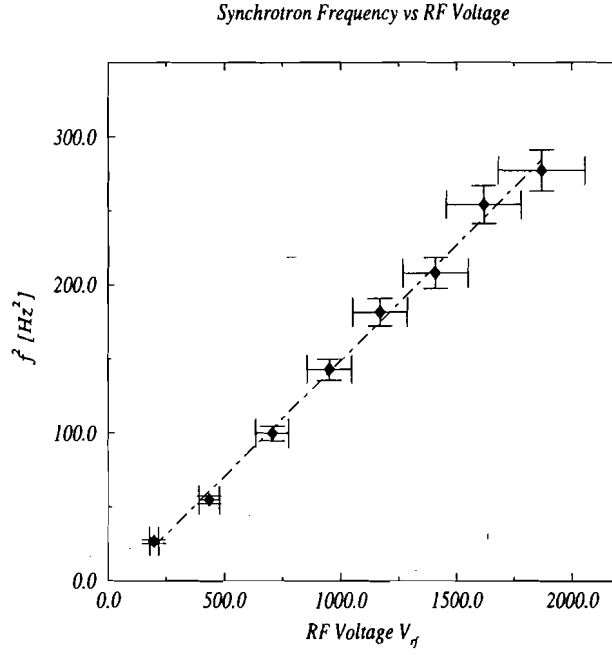


Figure 2.8: Measurements of the synchrotron frequency (f_s^2) as a function of the rf- cavity voltage on DRF3 (\tilde{V}_{rf}).

2.4 $\Delta\gamma_t$ Lattice Design

In the previous two sections, the function and optics of the nominal Debuncher lattice were described both through experiment and from the basic linear lattice model. Based upon the agreement between the measured and predicted lattice parameters, the linear lattice model was expected to be an accurate tool for the design of the dynamic $\Delta\gamma_t$ lattice. This section addresses the inherent design constraints together with the analytic methods utilized for obtaining $\gamma_t^{(f)}$.

¹³ The RF- cavity scale factor must be used: 688V/V

Since $\gamma_t^{-2} = 1/2\pi R \int ds D(s)/\rho(s)$, in order to change γ_t without moving magnets or changing the beam energy, *it was necessary to increase the dispersion in the arc sections*. The two fundamental constraints, are (i) the dispersion must be increased while maintaining zero dispersion in the straight sections, and (ii) $\Delta\gamma_t$ be accomplished with an overall zero tune shift. Tertiary constraints were also presented problematic considerations. Thus, (i) the change in the betatron phase advance per FODO cell was to be kept to a minimum, ($\delta\varphi_\beta \leq 5\%$), (ii) the betatron phase advance between the pickup and kicker must not change, ($\varphi_{PK} \approx 0$), (iii) it was necessary to keep the maximum beta function well controlled to avoid aperture restrictions, ($\delta\beta_{\max} \leq 10\%$), and (iv) also due to aperture restrictions, the maximum value of the dispersion function should not attain too large a value at one location, ($\delta D_{\max}/D_{\max} \leq 10\%$). Indeed, the average value of the dispersion should ideally increase *uniformly* throughout the arc sections.

Amongst all the constraints placed upon the resulting lattice parameters in the design of $\gamma_t^{(f)}$, were the very important hardware constraints and limitations. In particular, (i) the original lattice must be part of any dynamic $\Delta\gamma_t$ design, which means that it was not possible to change the location/size of magnets, add magnets, or add/modify the basic topography of the power supplies, and (ii) due to fast $\Delta\gamma_t/\Delta t$ ramps (current slews), it was absolutely required to minimize the *maximum* current change (ΔI_{\max}) required to produce $\gamma_t^{(f)}$.

2.4.1 Early motivations and historical review

Although there have been several investigations throughout the years which have been concerned with lattice schemes for modifying γ_t , the motivations have been quite different from that of the present thesis. Such investigations were primarily concerned with microwave instabilities caused by longitudinal space charge forces at the transition energy. The space charge forces increase dramatically at the transition energy because the bunch length tends to zero as $df/d[\Delta p/p] \rightarrow 0$ [31]. The result is a filamentation of the longitudinal emittance from (i) the change in the equilibrium bunch length, and (ii) the associated space charge tune shift.

Thus, attempts to avoid emittance growth at transition have historically motivated novel lattice cell arrangements, which have departed from the basic FODO scheme. The first lattice schemes implemented were designed to *jump* the transition energy with time scales faster than the onset of the microwave instabilities. Despite the success of the γ_t -jump methods, later generation

machines were designed with the transition energy instability problem particularly in mind. These later generation designs sought to avoid the problem altogether by pushing the lattice γ_t beyond the range of the accelerating particles, and thus, the lattice designs departed *further* from the simple FODO cell arrangements. Present generation designs have addressed the problem with even more novel basic lattice cells which render γ_t imaginary. In this section, some of this work shall be reviewed from the perspective of what could be *borrowed* in redesigning an existing lattice - the Debuncher - with only the possibility of changing the quadrupole field strengths.

2.4.1.1 Historical Perspective

Early work on the subject of γ_t *jump* schemes (then referred to as the Q -*jump* scheme) were reported by Hardt et al [45] for work on the CERN CPS as early as 1969. As mentioned in the previous paragraph, it was realized that instabilities at transition led to longitudinal emittance dilution. An obvious solution to the problem was to change γ_t very rapidly as the particles were accelerated through transition. The Q -*jump* scheme used in the CPS [46] used 6 sets of regularly spaced quadrupoles with identical field strengths and polarities to produce $\delta\gamma_t \approx 0.3$, and with a tune shift of $\delta\nu \approx .25$. In the literature by Hardt et.al., equations were developed for (i) the first order modulation $\Delta\beta$, and (ii) the first order modulation of the transition energy $\delta\gamma_t$, for small perturbations due to a set of *doublet lenses*. The equations developed by Hardt et al were specific to the CPS having a cell structure FOFDOD with a phase advance of $\pi/4$.

A brief review of γ_t *jump* methods was reported by T. Risselada [82] in a recent CERN Accelerator School Proceeding. In this paper, specific theoretical details for the earlier work at CERN were presented, and in particular, a description of π - doublets¹⁴ and the notion of producing localized dispersion waves.

Later, *high* γ_t lattice schemes were investigated and used by many groups to avoid the instabilities at transition altogether. An early paper by Gupta et al [44] describes several schemes to increase the transition energy *above the acceleration ranges* for the TRIUMF KAON factory accelerator which was being designed for 100 μ A proton beams at 30GeV. Since the transition energy from Courant and Snyder [30] is

$$\gamma_t^{-2} = -\frac{Q^3}{C} \sum_n \frac{|a_n|^2}{Q^2 - n^2}$$

¹⁴ As shall occupy much of the discussion in this chapter, π - doublets are perturbations of quadrupole lenses which are separated by π in betatron phase.

for which (i) the Fourier amplitude $a_n = \frac{1}{2\pi} \int_0^{2\pi} \beta^{3/2} / \rho e^{-in\phi} d\phi$, (ii) β is the transverse beta function, ϕ is the normalized betatron phase advance which advances by 2π for a full revolution period, and (iii) ρ is the local curvature, the principle for changing the transition energy was to produce an *extra* super-periodicity S and thus excite one of the Fourier components a_n for $n = S$ ¹⁵. From the KAON factory work, modulated drift lattices, missing magnet lattices and other novel arrangements were developed, which contrary to implementing Q-*jump* schemes with an existing machine, had no restrictions upon magnet locations in order to produce the desired modulation of the β functions, or equivalently, an extra super-periodicity at $n = S$. More recently, designs at the SSC for the low energy booster ring also considered similar lattice schemes to those investigated for the KAON factory for producing a high γ_t storage ring [101].

With a similar spirit used previously for the design of *high* γ_t lattices, which avoid the instability problem at transition altogether, *imaginary* γ_t lattices were proposed and investigated at Fermilab by D. Trbojevic, K.Y. Ng, and S.Y. Lee, for early conceptions of the Main Injector lattice [56], [57].

Recently, a project at SPEAR [96] was attempted for a variable momentum compaction electron storage ring for the purpose of controlling synchrotron tune and bunch length. Due, however, to limitations posed by the dynamic aperture, the project was abandoned.

2.4.2 Some comments on designing the dynamic γ_t lattice

Although the motivations and constraints of the dynamic $\Delta\gamma_t$ project are different from (i) γ -*jump* schemes, (ii) *high* γ lattices to avoid transition crossing, (iii) *imaginary* γ lattices, and (iv) even *dynamic* γ_t lattices as used in an electron storage ring for controlling bunch length, the basic principles affecting γ_t follow from the basic accelerator physics principles contained within the early paper by Courant and Snyder.

Within the following sections, the details for creating localized dispersion waves in the De-buncher ring with π doublets shall be presented. First, the basic equations shall be given which express the local property of the perturbations in π doublets. Next, first order expressions for the tune shift $\Delta\nu$ and $\Delta\gamma_t$ shall be derived through a standard perturbation theory of Courant and

¹⁵ There is nothing deep in this statement, since the solutions of Hill's differential equation for the dispersion function and the β functions are intimately connected. The statement of creating a non-zero spectral component at $n = S$, which people often refer to unwittingly as an *extra super-periodicity* is the same as creating localized dispersion waves as shall be seen later in the text

Snyder to probe the dependence upon the change in π doublet strength Δk . The first order expression for $\Delta\gamma_t$ is then used to make simple estimates of required field strength changes to change $\Delta\gamma_t$ by the full amount, as well as predictions for the expected tune shift. And finally, the design with a *maximum π doublet filling of the arc sections* is given together with (i) the full results of lattice parameters, (ii) the calculated tune shift $\Delta\nu$ from MAD and/or BEAMLIN, and (iii) the calculated $\Delta\gamma_t^{(f)}$ from MAD and/or BEAMLIN.

2.4.3 $\Delta\gamma_t$ with localized dispersion waves

The notion of localized dispersion waves is predicated upon the the periodicity of the inhomogeneous Hill differential equation. Thus, for a given accelerator lattice with variable *spring constant* $K(s)$, the Hill differential equation for the dispersion is

$$D'' + K(s)D - \frac{1}{\rho} \frac{p_o}{p}$$

In terms of the solution to the Hill equation for transverse betatron motion, $\beta(s)$, an integral representation of the dispersion function is given by Equation (2.8):

$$D(s) = \int \frac{\sqrt{\beta(s')\beta(s)}}{2 \sin \pi Q} K(s) \cos(\pi Q - |\mu(s') - \mu(s)|) ds \quad (2.8)$$

In Equation (2.8) Q is the fractional tune, $\beta(s')$ and $\beta(s)$ are the beta functions at the locations s' and s , respectively, and $|\mu(s') - \mu(s)|$ is the betatron phase difference between s' and s .

Perturbations to existing quadrupole strengths at locations s_i , enters Equation (2.8) from the spring constant $K(s) = \sum \Delta k(s_i) \delta(s - s_i)$, and upon integration over the full accelerator, the resulting dispersion wave $\Delta D(s)$ is given by:

$$\Delta D(s) = \sum_i \Delta k(s_i) \frac{\sqrt{\beta(s_i)\beta(s)}}{2 \sin \pi Q} \cos(\pi Q - |\mu(s_i) - \mu(s)|) \quad (2.9)$$

Because of the absolute value $|\mu(s') - \mu(s)|$ appearing in Equation (2.9), the quadrupole perturbations create cusps in the closed orbit $\Delta x(s)$ (and $D(s)$) at locations s_i . Thus, if two quadrupole strength perturbations are chosen at locations s_1 and s_2 having a betatron phase difference $\Delta\varphi = \pi$, then the resultant $\Delta D(s) = \Delta D(\Delta k_1, s_1) + \Delta D(\Delta k_2, s_2)$ may be *localized* with the proper choice of Δk_1 and Δk_2 . This arrangement, referred to as a π -*doublet*, is the basic building block in the design of the dynamic $\Delta\gamma_t$ design.

2.4.4 Introduction to π - Doublets in the Debuncher Ring

Since the $\Delta\varphi = (\pi/3)/[\text{FODO cell}]$ in the Debuncher ring, a π - doublet is formed with two quadrupoles separated by 3 basic FODO cells. Furthermore, superposition guarantees that the dispersion waves created from the focusing and defocusing quadrupoles should not interfere, since these quadrupoles are separated by a betatron phase by $\pi/6$. A more detailed discussion of overlapping π doublets, which maximally fill the arc sections, shall be given in subsequent sections.

Figure 2.9 is an illustration of a π doublet arrangement formed from two quadrupoles in one of the arc sections of the Debuncher ring. The respective magnetic field strengths of the quadrupoles which constitute the π doublet are perturbed by Δk_1 and Δk_2 , respectively. The ratio between the strengths is determined by the ratio $\sqrt{\beta(s_1)}/\sqrt{\beta(s_2)}$, which is directly the result from Equation (2.9). Thus, for $|\mu(s_1) - \mu(s_2)| = \pi$, the resultant dispersion wave is:

$$\Delta D(s) = D(s, s_1) + D(s, s_2) \quad (2.10)$$

$$= C [\Delta k(s_1) \sqrt{\beta(s_1)\beta(s)} + \Delta k(s_2) \sqrt{\beta(s_2)\beta(s)}] \quad (2.11)$$

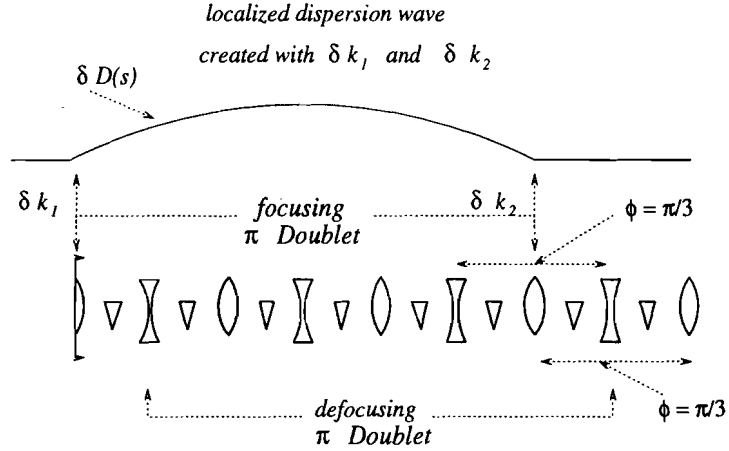


Figure 2.9: Illustration of a localized dispersion function created by a π Doublet.

Thus, the dispersion wave $D(s)$ will be local if the superposition between the two waves $\Delta D(s, s_1)$ and $\Delta D(s, s_2)$, created at s_1 and s_2 , have the same strength. Since the strength of the dispersion wave depends also upon the beta function $\beta(s_i)$, the π - doublet will produce a localized $\Delta D(s)$ given the proper ratio of $\Delta k(s_1)$ and $\Delta k(s_2)$.

An example illustrates the importance of the π doublet strength ratios upon localized dispersion waves. At the entrance of the arc sections within the Debuncher, $\beta(s_{q8}) = 16.13 \neq \beta(s_{q14}) =$

14.83, due to the fact that the regular FODO cell arrangement is broken for matching zero dispersion straight sections to the arc sections with dispersion killers. Thus, proper matching of the dispersion function, creates an extra modulation of the betatron functions and the betatron phase advance at the interface of the straight and arc sections. A π doublet strength formed from the quadrupole $q\delta$ and $q14$, must obey the relationship $k_2 = [\frac{\sqrt{\beta(s_1)}}{\sqrt{\beta(s_2)}} k_1]$, or $\delta k_{q14}/\delta k_{q8} = [\frac{\sqrt{16.13}}{\sqrt{14.83}}]$, in order to obtain a localized dispersion wave between the quadrupoles and thus a matched lattice.

2.4.4.1 Analytic expression for the $\Delta\gamma_t$ of a π doublet

In order to understand the dependence of lattice parameters upon the change in field strength, or equivalently, the currents ΔI invoked with π doublets, approximate analytic formulas provide insight into the scaling behavior of the $\Delta\gamma_t$ design.

Within the present section, an expression for the first order change $\Delta\gamma_t^{(1)}(\Delta k)$, which has been derived in many standard accelerator literature [50], shall be outlined. Furthermore, from the general equations of Courant and Snyder [30], expressions for the $\Delta\beta$ modulation and the tune shift $\Delta\nu$, due to quadrupole strength perturbations at s_i in the ring, may be derived. The derivation of $\Delta\gamma_t$ shall be compared against the results from the full lattice model calculation.

2.4.4.2 First order expression for $\Delta\gamma_t$

The well known equation for the β - functions from Courant and Snyder, in terms of the arc length in the machine is given by:

$$\frac{d^2}{ds^2} \sqrt{\beta(s)} + k(s) \sqrt{\beta(s)} - \beta^{-3/2} = 0 \quad (2.12)$$

A first order perturbation solution to Equation (2.12) for each of the relevant lattice functions has been presented by many authors. The following section briefly reviews the derivation of $\Delta[1/\gamma_t^2]$.

Given a quadrupole perturbation at a location s_i , or equivalently at a particular value of the *unperturbed* betatron phase ϕ_o , the betatron function may be expanded in terms of the *perturbed* betatron phase ϕ through $\epsilon = \phi - \phi_o$. Thus, the betatron function is given by $\beta(\phi_o) = \beta_o[1 + \delta\beta_1\epsilon + \delta\beta_2\epsilon^2 + \dots]$. With a change in coordinates:

$$\begin{aligned} \frac{d}{ds} &= \frac{d\phi}{ds} \frac{d}{d\phi} = \frac{1}{Q\beta} \frac{d}{d\phi} \\ \frac{d^2}{ds^2} &= \frac{1}{Q\beta^2} \left[\frac{d^2}{d\phi^2} - \frac{d\beta}{d\phi} \frac{d}{d\phi} \right] \end{aligned}$$

the differential equation for the β function may be re-written

$$\frac{1}{Q^2\beta^2} \left[\frac{1}{2\sqrt{\beta}} \frac{d^2\beta}{d\phi^2} - \frac{1}{4\beta^{3/2}} \frac{d\beta}{d\phi} \right] - \frac{1}{Q^2\beta^3} \left[\frac{1}{2\sqrt{\beta}} \frac{d^2\beta}{d\phi^2} \right]^2 + (k + \delta k)\beta^4 Q^2 - \frac{1}{\beta^{3/2}} = 0$$

$$\beta^2 \left[\frac{d^2\beta}{d\phi^2} - \frac{3}{2} \frac{d^2\beta}{d\phi^2} \right]^2 + (k + \delta k)\beta^4 Q^2 - 2Q^2\beta^2 = 0$$

Although an exact solution of the above equation is not possible, a perturbation analysis follows from a Taylor expansion of the the quantity $\epsilon = \phi - \phi_o$. Inserting the perturbation series in $\beta(\phi_o)$, and expanding terms $\beta(\phi_o) = \beta_o [1 + \delta\beta_1\epsilon + \delta\beta_2\epsilon^2 + \dots]^2 \approx [1 + 2\delta\beta_1]$

The first order equation is

$$\delta\ddot{\beta}_1 + 2\beta_o^2 Q^2 \delta k + 4Q^2 \delta\beta = 0$$

An expression for the first order tune shift and the first order β - wave perturbation follows from the above equation in $\delta\beta$ by taking a Fourier integral

$$\int d\phi_o e^{in\phi_o} [\delta\ddot{\beta}_1 + 4Q^2 \delta\beta] = -2Q^2 \int d\phi_o e^{in\phi_o} \beta_o^2 \delta k(\phi_o)$$

With the definition

$$J_n = \nu \int d\phi_o e^{in\phi_o} \beta_o^2(\phi_o) \delta k(\phi_o)$$

and an integration by parts, the result is

$$\int d\phi_o e^{in\phi_o} [-n^2 + 4Q^2] = -2Q^2 J_n$$

This last expression is the standard result for the first order shift in β ,

$$\frac{\delta\beta}{\beta} = -\frac{Q^2}{\pi} \sum_n \frac{J_n e^{in\phi_o}}{-n^2 + 4Q^2}$$

In a similar manner, the first order shift $\delta\gamma_t$ follows from the definition and the equation in $\delta\beta$. The definition of γ_t in a Fourier spectral representation is

$$\gamma_t^{-2} = -\frac{Q^3}{C} \sum_n \frac{|a_n|^2}{Q^2 - n^2}$$

where $a_n = \frac{1}{2\pi} \int_o^{2\pi} \beta^{3/2} / \rho e^{-in\phi} d\phi$. By writing the β function appearing in the integrand in terms of the first order shift, $\beta^{3/2}(\phi_o) = \beta_o^{3/2} [1 + \delta\beta_1\epsilon + \delta\beta_2\epsilon^2 + \dots]^2 \approx \beta_o^{3/2} [1 + \frac{3}{2}\delta\beta_1]$. Inserting this expression into that for the Fourier coefficient, $a_n = \frac{1}{2\pi} \int_o^{2\pi} \beta_o^{3/2} [1 + \frac{3}{2}\delta\beta_1] / \rho e^{-in\phi} d\phi$, and using the first order expression for $\delta\beta$

$$a_n = \frac{1}{2\pi} \int_0^{2\pi} \frac{\beta_o^{3/2}}{\rho} e^{-in\phi} d\phi \left[1 + \frac{3}{2} \frac{Q^2}{\pi} \sum_n \frac{J_n e^{in\phi_o}}{4Q^2 - n^2} \right]$$

From this last result, an expression for γ_t^{-2} follows immediately,

$$\gamma_t^{-2} = \gamma_{to}^{-2} \left[1 + \frac{9Q^4}{2\pi^2} \sum_n \frac{|J_n|^2}{(4Q^2 - n^2)^2 (Q^2 - n^2)} \right] \quad (2.13)$$

2.4.4.3 Harmonic content of π - Doublet

From the π - doublet illustrated in Figure 2.9, with a phase advance of $\phi = \pi/3$ per FODO cell, $\phi(s_1) = \phi(s_o) + 2\pi \frac{3}{N}$, and the Fourier amplitude given by $J_n = \nu \int d\phi_o e^{in\phi_o} \beta_o^2 \delta k(\phi_o)$, the expression for the phase advance of a π doublet is given by $J_n = \nu \beta(s_o) \delta k(s_o) [1 + e^{i2\pi 3n/N}] e^{-i\phi(s_1)n} = \nu \beta(s_o) \delta k(s_o) \cos[n\pi(3/N)] e^{-i\phi(s_1)n}$. Thus,

$$\delta\beta/\beta = \sum_n \frac{\nu \beta(s_o) \delta k(s_o) \cos[n\pi(3/N)] e^{-in(\phi(s) - \phi(s_1))}}{4Q^2 - n^2}$$

The effect of π doublet β modulations Fourier spectra were studied through comparison with the nominal lattice β Fourier spectra. Figure 2.10 is a simplified diagram of one sector in the Debuncher lattice indicating the location of the π doublet, formed with $Q13 \Leftrightarrow Q17$ quadrupoles.

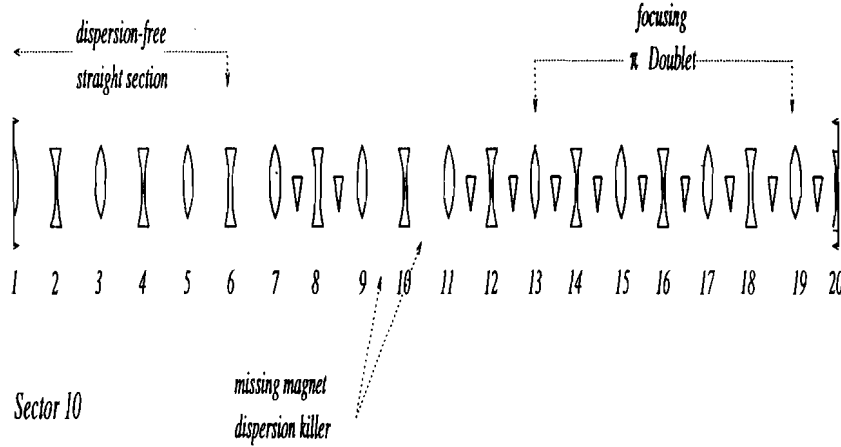


Figure 2.10: Illustration optics for one sector of the Debuncher ring indicating the location of a π doublet formed with $Q13 \Leftrightarrow Q17$ quadrupoles used in the numerical example.

A comparison between the nominal lattice ($\gamma_t^{(i)}$) $\tilde{\beta}_i(\omega)$ spectra and $\tilde{\beta}_\pi(\omega)$ with the π doublet of 2.10 is given in Figures 2.11(a). The $n = 1$ dominant line in the nominal lattice $\tilde{\beta}_i(\omega)$ Fourier spectra (top plot of Figure 2.11(a)) corresponds to the wavelength of the standard FODO lattice

spacing $\lambda = L_{fodo} \approx 1./0.1128$. Moreover, the next highest spectral line at $\lambda \approx 0.224$ corresponds the second $n = 2$ harmonic of the basic FODO cell excitation. At lower ω , the structure in the $\tilde{\beta}_i(\omega)$ Fourier structure corresponds to the longer wavelength occurrence of straight sections, or equivalently a longer wavelength periodicity in the lattice. The nominal lattice $\tilde{\beta}_i(\omega)$ spectrum is compared against the $\tilde{\beta}_\pi(\omega)$ spectrum with the π doublet excitation in the bottom plot of Figure 2.11(a). The extra periodicity produced by the π doublet corresponds to a harmonic excitation corresponding to $3 \times$ the nominal FODO spacing L_{fodo} , with a wavelength $\lambda = [3 \times L_{fodo}] \approx 1/0.038$.

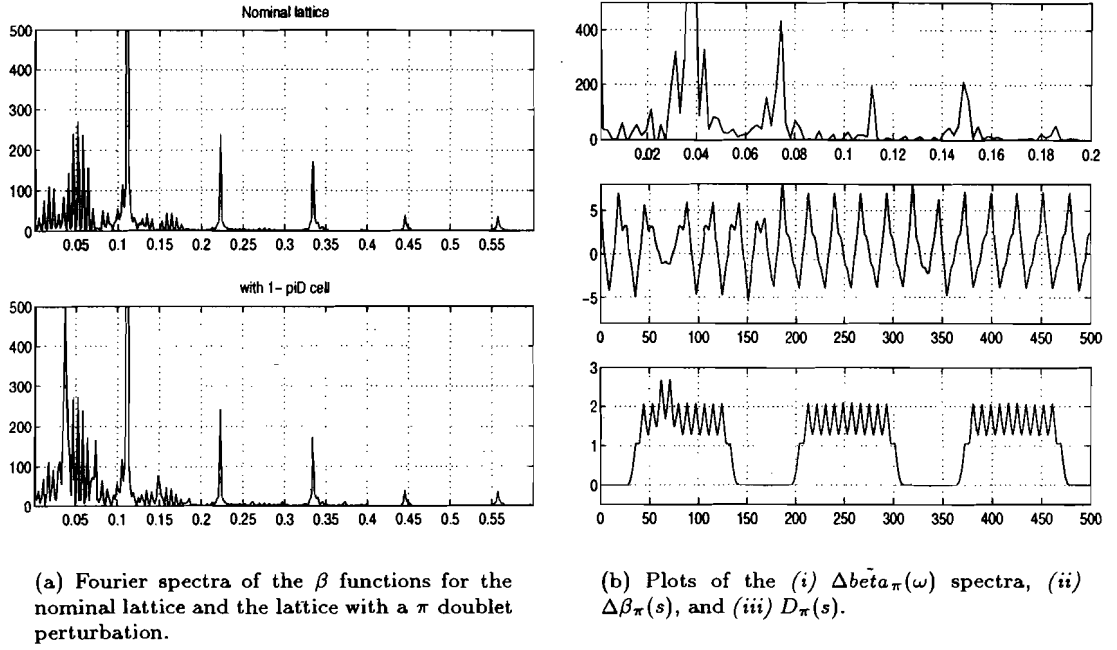


Figure 2.11: Fourier spectra, $\Delta \tilde{\beta}_\pi(\omega)$, for the single π doublet (formed with $Q13 \Leftrightarrow Q17$).

The effect of the π doublet is best illustrated in Figure 2.11(b), with the quantities: (i) $\Delta \tilde{\beta}_\pi(\omega) = \tilde{\beta}_i(\omega) - \tilde{\beta}_\pi(\omega)$ (top plot), (ii) $\Delta \tilde{\beta}_\pi(s) = \Delta \tilde{\beta}_i(s) \Delta \tilde{\beta}_\pi(s)$ (middle plot), and (iii) $D_\pi(s) = D_i(s) + \Delta D_\pi(s)$ (bottom plot).

Several features of the perturbations created with a π doublet are illustrated in the plots of 2.11(b). First, the top plot $\Delta \tilde{\beta}_\pi(\omega) = \tilde{\beta}_i(\omega) - \tilde{\beta}_\pi(\omega)$, as already pointed out, shifts the $n = 1$ dominant harmonic to a longer wavelength, such that $\lambda(n = 1) \approx [3 \times L_{fodo}]$. In the middle plot for $\Delta \tilde{\beta}_\pi(s) = \Delta \tilde{\beta}_i(s) \Delta \tilde{\beta}_\pi(s)$, the wavelength λ corresponds to the region $\Delta s = 3 \times L_{fodo}$ between the quadrupoles $Q13$ and $Q17$, while the other dominant $\Delta \beta(s)$ has a wavelength of $\lambda = 2 \times L_{fodo}$ which

follows from the well known first order perturbation formula for $\Delta\beta/\beta$ ¹⁶. An important feature of the middle plot in Figure 2.11 is the fact that $\Delta\beta = 0$ between the lenses of the π doublet.

The effect of the π doublet which is most important (but as can be seen, intimately connected with the associated $\Delta\beta$ modulations) is the resulting dispersion $D_\pi(s) = D_i(s) + \Delta D_\pi(s)$ indicated in the bottom plot of 2.11(b). The effect of $\Delta D_\pi(s)$ in Figure 2.11(b) is clear: *the π doublet produces a localized dispersion wave*, which attains a larger value inside the π doublet interval (between Q13 and Q17) and is cancelled ($\Delta D_\pi(s) = 0$) outside the π doublet interval.

2.4.4.4 Evaluation of $\Delta\gamma_t^{(1)}$

Based upon the denominator of the γ_t^{-2} in Equation (2.13) the convergence of the Fourier sum is quite rapid and with the inclusion of only the first few terms. Utilizing $\Delta\gamma_t^{(1)}$, the expression for the first order change in γ_t with equal strengths $\Delta k_1 = \Delta k_2$, and fractional tune Q :

$$\Delta\gamma_t^{-2} = \frac{9Q^4}{2\pi^2} \sum_n \frac{|J_n|^2}{(4Q^2 - n^2)^2(Q^2 - n^2)} \quad (2.14)$$

$$\begin{aligned} \Delta\gamma_t^{-2} = \frac{9Q^4}{2\pi^2} & \left[\frac{|J_1|^2}{(4Q^2 - 1^2)^2(Q^2 - 1^2)} + \frac{|J_2|^2}{(4Q^2 - 2^2)^2(Q^2 - 2^2)} \right. \\ & \left. + \frac{|J_3|^2}{(4Q^2 - 3^2)^2(Q^2 - 3^2)} \right] \end{aligned} \quad (2.15)$$

in which $|J_n|^2 = \nu^2 \beta^2(s_o) \delta k^2(s_o) \cos^2[(3\pi/N)n]$.

For the π doublet given in Figure 2.11, with a betatron function $\beta(s_{Q13}) \approx 15\text{m}$, $\nu = 9.7$, and the current $\Delta I(\delta k)$, a calculation of $\Delta\gamma_t^{-2}$ is given in Figure 2.12. The calculation of $\Delta\gamma_t^{-2}$ retains only the first 3 terms in the Fourier sum.

¹⁶For a perturbation of the lattice with Δk , $\Delta\beta/\beta(s) \sim \Delta k(s_i) \cos(2|\mu(s_i) - \mu(s)|)$ while $\Delta D(s) \sim \Delta k(s_i) \cos(|\mu(s_i) - \mu(s)|)$.

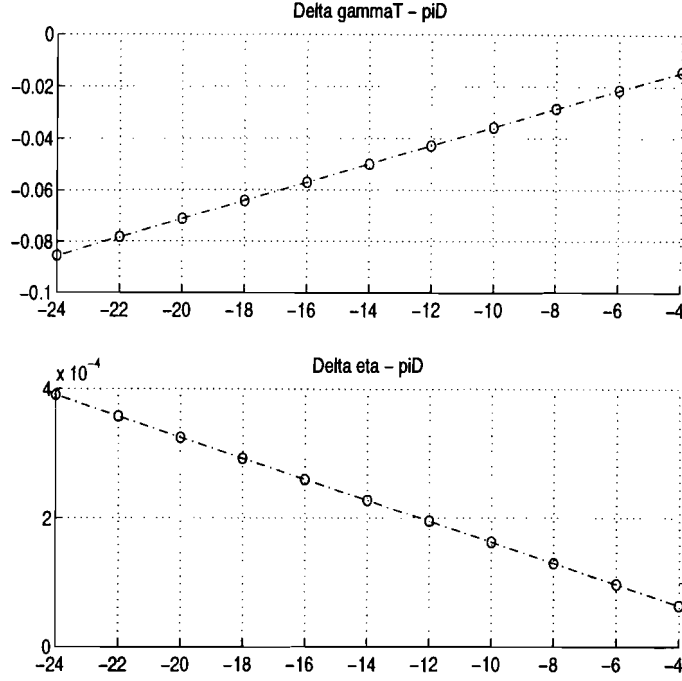


Figure 2.12: Calculation of $\Delta \gamma_t$, and η for a π doublet as a function of $\Delta I(\delta k)$ [Amps].

From the Figure 2.12, a change of $\Delta I \approx 6\text{Amps}$, produces a change in $\eta \approx 0.9 \times 10^{-4}$. It shall be shown in the next section that a maximum π doublet filling of the arc sections allows for a total of 39 π doublets. If each π doublet is allowed an average $\Delta I \approx 6\text{Amps}$, then the total $\Delta \eta \approx 0.9 \times 10^{-4} \times 39 \approx 3.5 \times 10^{-3}$. Based upon the crude estimate, this is in very good agreement with the full lattice calculation to be presented.

2.4.4.5 Maximum π - doublet filling of the arc sections

In the previous sections, the π doublet was analyzed as a candidate for producing localized dispersion waves for changing γ_t . This section presents a complete design with *interleaved* π doublets for increasing the dispersion uniformly in the arc sections of the Debuncher lattice. Thus, a complete design of $\gamma_t^{(f)}$ consists of *maximally filling the arc sections* with π doublets, for the purpose of minimizing the maximum current changes (ΔI_{\max}) required.

Previously, it was mentioned that π doublets may be formed from both a pair from the focusing quadrupole $\{\pi_f | \pi \in \text{Foc}\}$ groups and the defocusing quadrupole groups $\{\pi_d | \pi \in \text{Defoc}\}$. Furthermore, the two *types* of π doublets may be interleaved without interference between the respective localized dispersion waves since the two groups of quadrupoles (focusing and defocusing)

are separated by $\pi/6$ betatron phase. Thus, the contributions to an increased dispersion function will result if $\pi_f(\delta k_i, \delta k_j) + \pi_d(-\delta k_m, -\delta k_n)$, where the minus signs on the lens strengths of π_d indicate the opposite polarity required. The full contribution to the dispersion, and therefore γ_t , is given by:

$$\Delta\gamma_t^{(f)} = \sum_{\text{max.no. } \pi_f} \delta\gamma_t(\pi_f) + \sum_{\text{max.no. } \pi_d} \delta\gamma_t(\pi_d) \quad (2.16)$$

Figure 2.13 is an illustration of a sector in the Debuncher ring with maximum possible π doublet filling. From Figure 2.13, the maximum number of π doublets which can fill the arc sections of the entire Debuncher is $13 \times 3 = 39$ π doublets.

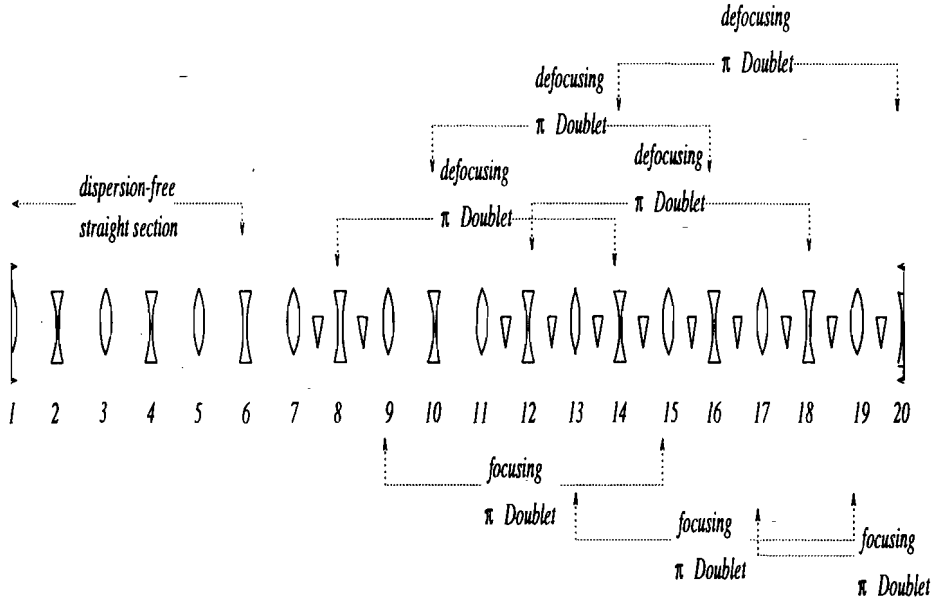


Figure 2.13: Illustration of maximum π doublet filling in the arc sections.

2.5 Specification for a complete $\Delta\gamma_t^f$ design

From the previous subsection, the concept of a maximum π doublet filling fraction in the arc section led to the notion that $\Delta\gamma_t$ is maximized by distributing $\langle \Delta I \rangle$ over many quadrupoles. For a given $\Delta\gamma_t$ produced in the arc section, however, there is an associated tune shift $\Delta\nu$ which must be removed through adjustment of quadrupole lens strengths in the *zero dispersion* straight sections. These quadrupole strength adjustments have no effect upon γ_t since the dispersion is zero

in that region of the storage ring. The *tune correction*, however must satisfy many constraints, and in general, there are 33 free parameters which may be adjusted which correspond to the total number of quadrupoles in the straight sections.

In the first part of this section, the constrained optimization problem is defined for addressing the tune shift problem. Optimization algorithms form the foundations for obtaining the straight section excitation currents throughout the $\Delta\gamma_t$ ramp. Moreover, *tune correction* must be done throughout the $\Delta\gamma_t$ ramp due to the nonlinear dependence of the tune with the π -Doublet excitation.

Throughout the remainder of this section, the full $\Delta\gamma_t$ lattice design is presented. A full description of the final lattice design includes (i) hardware requirements, (ii) excitation currents, (iii) the predicted lattice parameters, and (iv) residuals between the predicted lattice parameters in the γ_t^f lattice design and the nominal lattice. Finally, the predictions of the γ_t^f lattice are compared against experiments.

2.5.1 Introduction: The problem of minimizing tune shift

The objective of the $\Delta\gamma_t^{(f)}$ *tune shift problem* is to find the optimal zero tune shift solution through the adjustment of 33 free parameters, in general, which correspond to the set of quadrupole strengths within the straight sections, and subject to a host of lattice function constraints. By demanding the original sixfold symmetry of the Debuncher lattice, the large number of free parameters may be reduced to 6. Mathematically the optimization problem may be stated formally,

$$\begin{aligned} & \min\{\mathcal{F}(\nu)\} \quad \text{for } \nu \in \mathcal{M} \\ & \text{subject to} \quad |\Delta I_j| \leq \tau_j; \quad \Delta\varphi_{p \rightarrow k} \approx 0; \quad |\Delta\beta_i| \leq \varepsilon \end{aligned}$$

where

$$\mathcal{F}(\nu) = \sum [\Delta\nu_i]^2$$

in which \mathcal{M} is the one turn map, and ν may in general represent any of the lattice parameters, however, for the present restricted problem, it shall simply represent the transverse tunes. The restrictions upon the changes in the free parameters (the currents $|\Delta I_j|$) result from (i) trying to

equally distribute the necessary current changes so that the average change is as small as possible, (ii) staying within the practical requirements imposed by magnet current bypass shunt circuits and the fact that the straight section quadrupoles are already shunting some amount of current, which in some cases restricts the available current domain even more, and (iii) trying to maintain a highly symmetric $\Delta\gamma_t^{(f)}$ design.

While optimization of a group of parameters is a common feature of accelerator lattice design and has been incorporated into standard computer programs such as MAD or BEAMLIN, it was difficult to control the specific *constraints* inherent in the $\Delta\gamma_t$ problem with such general routines. Therefore, instead of relying upon these standard programs, specific optimization algorithms were tailored to the $\Delta\gamma_t$ in conjunction with BEAMLIN.

The following section shall present *the final result* of the $\Delta\gamma_t$ optimization problem, while the details are relegated to a thorough discussion in appendix A. Comparison of *classical* constrained optimization algorithms to the technique of *simulated annealing optimization* is reviewed in appendix A and applied to the specific $\Delta\gamma_t$ problem. The use of simulated annealing optimization is advocated as a powerful candidate for accelerator lattice designs with difficult constraints and many local extrema.

2.5.2 Details for a complete γ_t^f design

The $\gamma_t^{(f)}$ lattice design, with $\Delta\nu \approx 0$ together with other constraints, is depicted graphically in Figure 2.14, and indicates the required current changes ΔI for each quadrupole magnet. Since the final design maintains the full six-fold symmetry of the original design, only one sector is depicted in Figure 2.14. Actually, in the implementation of the $\Delta\gamma_t$, a slight break in the six-fold symmetry was allowed due to the current changes (to obtain the equivalent ΔK) required in the large quadrupoles D:QT205, D:QT405, and D:QT606. This asymmetry does not have a profound effect, so is ignored in the present discussion.

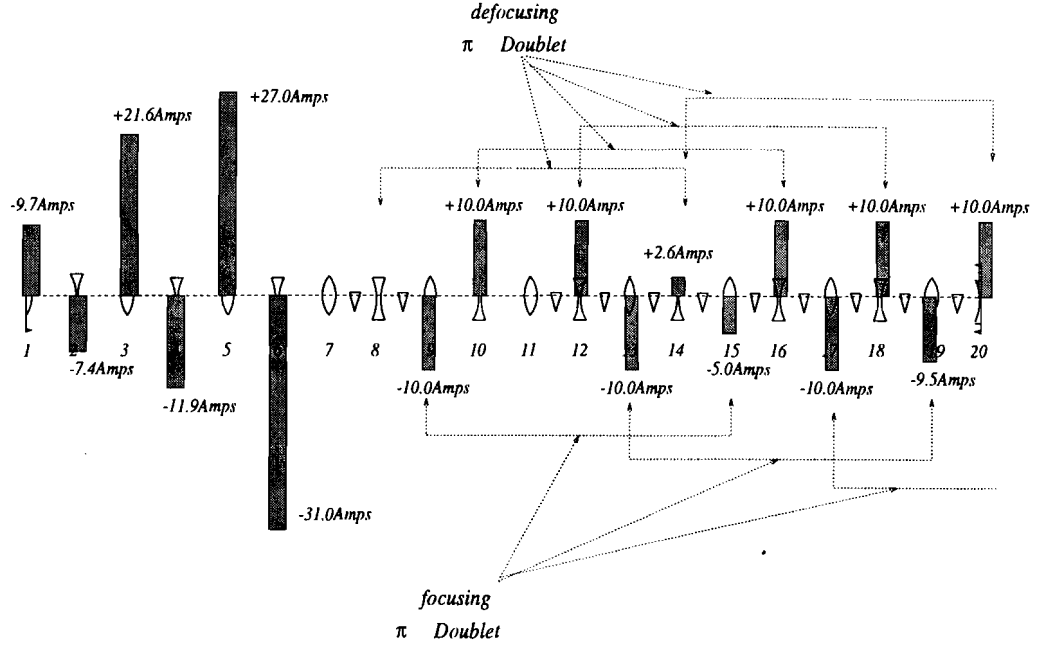


Figure 2.14: The complete $\gamma_t^{(f)}$ design for a sector of the Debuncher lattice indicating each ΔI .

A comparison of the dispersion functions for lattice designs with (i) $\gamma_t^{(f)}$ ($\eta = 0.0093$), (ii) the nominal γ_t ($\eta = 0.0062$), and (iii) γ_t^{large} ($\eta = 0.0029$), are given in Figure 2.15.

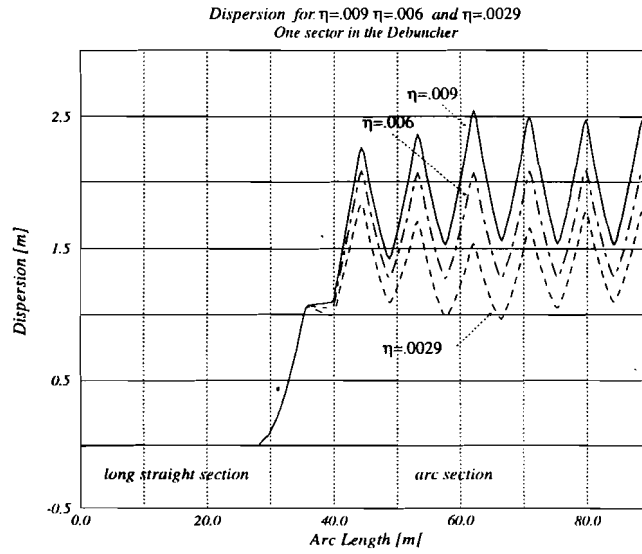


Figure 2.15: Comparison of the dispersion functions for γ_t^f ($\eta_f = 0.0094$), the nominal lattice γ_t^i , and a design for a large γ_t ($\eta = .0028$)

Another feature of the present symmetric lattice design for γ_t^f is the added benefit of produc-

ing a *bi-polar* design, i.e. the ability to *increase* $\gamma_t \longrightarrow \gamma_t^{\text{large}}$. This design may receive considerable attention, within plans of the Main Injector or the Tev33 project, in the future since an increase of $\sim 20\%$ in momentum acceptance of targeted \bar{p} may be realized. A more detailed optics study must be taken up with regard to the γ_t^{large} design, and is therefore deferred from discussion in this thesis. For early papers on the subject of small η see reference by Ando [2], and Takayama [94]. For papers related to future implications for the Tevatron project, see the *Main Injector Technical Design Handbook* [33].

In summary, the features of the design are the following:

1. the average changes of the quadrupole currents in the design are $\langle \Delta I \rangle \approx 20\text{Amps}$. This represents a 8-10% change in the quadrupole currents from the operating value of $\approx 250\text{Amps}$.
2. the tune shifts $\Delta\nu_{v,h}$ are kept less than $\sim .005$ between the initial, γ_t^i and the final γ_t^f lattice to avoid resonance crossing.
3. the change in the maximum β -function (in both transverse planes) is less than 5% of the nominal values.
4. the average of the dispersion function increases *uniformly* in the arc sections by 10%, and remains strictly zero in the straight sections.

The result of important lattice parameters for the γ_t design, which includes the full tune shift correction, is given in Table 2.4. In particular, $\Delta\phi_y(PU \rightarrow K)$ are small in both planes and thus have a negligible *heating* effect upon the stochastic cooling.

Table 2.4: Details of Lattice Parameters for the γ_t^f design

PARAM.	VAL.	PARAM.	VAL.
η	0.0093	$\Delta\beta_{PHx}$	-0.702
$\Delta\nu_x$	-0.004	$\Delta\beta_{PVy}$	-2.41
$\Delta\nu_y$	0.005	$\Delta\beta_{KHx}$	1.11
$\Delta\phi_x(PU \rightarrow K)$	$0.00683\text{rad}(0.36^\circ)$	$\Delta\beta_{KVy}$	1.19
$\Delta\phi_y(PU \rightarrow K)$	$0.023\text{rad}(1.33^\circ)$	-	-

Perhaps the most important feature of the optical lattice design is that it is completely symmetric and the changes in quadrupoles may be put into simple groupings. Table 2.5 gives the 4 types of current changes amongst the quadrupoles on the D:QF power supply and the 3 types of current changes amongst the quadrupoles on the D:QD power supply.

Table 2.5: Types of quadrupole current changes in arcs sections for the $\gamma_t^{(f)}$ design.

<i>Quad. Set</i>	<i>Specific Mag.</i>	$\Delta I(\gamma_t^{(i)})(I_{ps})$	$\Delta I(\gamma_t^{(f)})(I_{ps})$	ΔI_{ps}
<i>QF</i>	{ <i>qx07, qx11</i> }	0.(244.0)	0.0(244.0)	0.0
<i>QFA</i>	{ <i>qx09, qx13, qx17</i> }	0.(244.0)	-10.0(244.0)	0.0
<i>QFB</i>	{ <i>qx19</i> }	0.(244.0)	-9.6(244.0)	0.0
<i>QFC</i>	{ <i>qx15</i> }	0.(244.0)	-5.0(244.0)	0.0
<i>QD</i>	{ <i>qx10, qx12, qx16</i> }			
	{ <i>qx18, qx20</i> }	0.(238.8)	0.0(248.8)	10.0
<i>QDA</i>	{ <i>qx08</i> }	0.(238.8)	-10.0(248.8)	10.0
<i>QDB</i>	{ <i>qx14</i> }	0.(238.8)	-7.0(248.8)	10.0

After the tune correction to obtain $\Delta\nu \approx 0$, with optimization amongst the quadrupoles in the straight section, hardware changes were needed to accommodate the larger ΔI requirements. Table 2.6 is a list of the required currents amongst the quadrupoles in the straight section for the γ_t^f design. Also indicated (with boldface) in Table 2.6 are the magnet current shunt hardware modifications. In Figure 2.16, the result of a MAD calculation for the β functions and the horizontal dispersion function for the $\gamma_t^{(f)}$ ($\eta = 0.0093$) design is given.

Table 2.6: The straight section quadrupole current shunt settings for the nominal γ_t and $\gamma_t^{(f)}$ lattices.

<i>QuadShnt(Type)</i>	<i>I_{shunt} $\eta = 0.006$ (<i>I_{ps}</i>)</i>	<i>I_{shunt} $\eta = 0.009$ (<i>I_{ps}</i>)</i>	δI_{shunt}	δI_{ps}
Q101(20A)	-8.5(282.5)	-0.5(290.5)	8.0	8.0
Q102(50A)	-26.8(282.5)	-48.8(290.5)	-21.0	8.0
Q103(50A \rightarrow 30A)	-21.8(282.5)	-5.8(290.5)	15.8	8.0
Q104(20A \rightarrow 30A)	-0.6(282.5)	-24.6(290.5)	-26.4	8.0
Q105(50A)	-51.0(282.5)	-35.0(290.5)	15.0	8.0
Q106(20A \rightarrow 50A)	-4.2(238.)	-36.0(250.)	-30.2	12.0

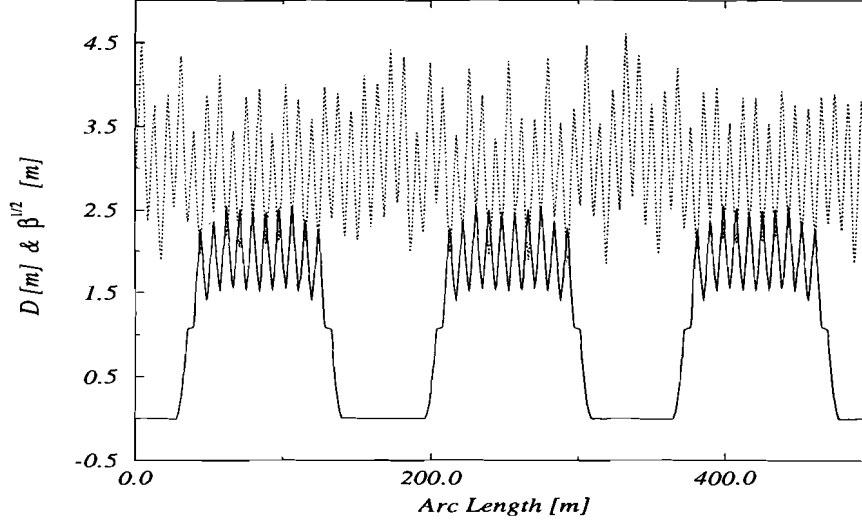


Figure 2.16: The Debuncher lattice parameters for $\gamma_t^{(f)} (\eta = 0.0093)$ from a BEAMLINE (or MAD) calculation.

2.5.2.1 Hardware for the $\Delta\gamma_t^f$ design

Amongst the many constraints within the $\Delta\gamma_t^{(f)}$ lattice design was the desire to minimize the total number of magnet current bypass shunts which would be required, and thus minimize the monetary cost. Because of the six-fold symmetry in the design *and* the fact that the majority of defocusing quadrupoles would increase in current by the *same* amount, the number of shunt circuits required was $\sim 60\%$ of the number of quadrupoles comprising the π - Doublets. Figure 2.17 indicates the location of the new magnet current shunt circuits which were installed in each of the six sectors of the Debuncher for the $\Delta\gamma_t^{(f)}$ design.

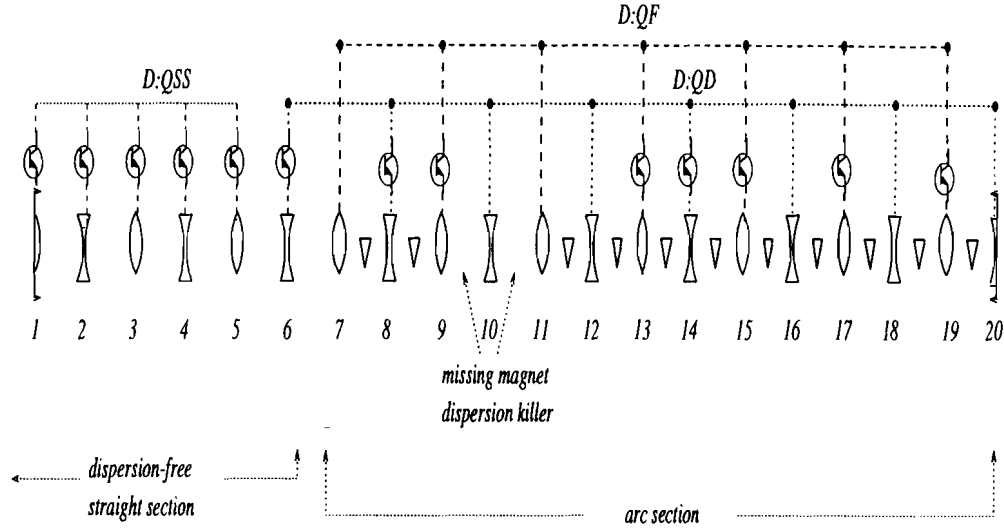


Figure 2.17: A diagram of a sector in the Debuncher indicating the location of the new magnet shunts to be used for the $\Delta\gamma_t^{(f)}$.

The nominal lattice had the following hardware: (i) 114 Quadrupoles in the Debuncher, (ii) 3 major power supplies control these quadrupoles, (iii) 3 shunt supplies, and (iv) 33 existing shunt circuits in the long straight sections for tune control. The hardware requirements for the dynamic $\Delta\gamma_t^{(f)}$ project were: (i) 42 new active power supply shunt circuits installed in the arc sections, (ii) control with CAMAC programmable ramp modules (of 465/468 type) and (iii) active feed-forward for fast slew regulation of the high voltage power supplies.

2.5.3 Experimental Results of γ_t^f

Based upon the lattices obtained in the previous section, the result of lattice parameter measurements are presented for several cases of $(\gamma_t^{(f)} \mapsto \eta = 0.007, 0.0085, 0.0093)$. In particular, before proceeding to discussions of higher order effects and issues related to a dynamic $\Delta\gamma_t^{(f)}$, confirmation must be made on two fronts: (i) experimental evaluation of the dispersion functions and (ii) measurements of $\gamma_t^{(f)}$ (through the slip factor η) for intermediate lattices.

2.5.3.1 Predictions/Measurements of the dispersion, $D(s)$

For three intermediate values of γ_t , between the nominal and the final lattice (γ_t^f), (i) $\eta = 0.0093$, (ii) $\eta = .0085$, and (iii) $\eta = .007$, measurements of the dispersion function were made and the results are given in Figures 2.18, 2.19, and 2.20, respectively. Similar to the discussion of the dispersion function measurements for the nominal lattice ($\eta = 0.006$), the dispersion function is extracted with linear least square fits to measurements of the transverse closed orbit $\Delta x(s)$ as a function of the energy $\Delta p/p$. The error bars in Figures 2.18, 2.19, and 2.20 correspond to the variance of the least square fits, yet do not include a $\approx 10\%$ systematic error resulting from absolute BPM calibration.

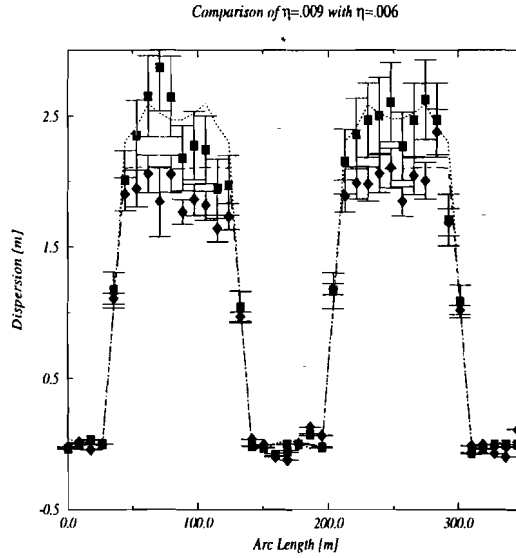


Figure 2.18: Comparison of $D(s)$ between $\eta = 0.0093$ (■) and $\eta = 0.0062$ (◆).

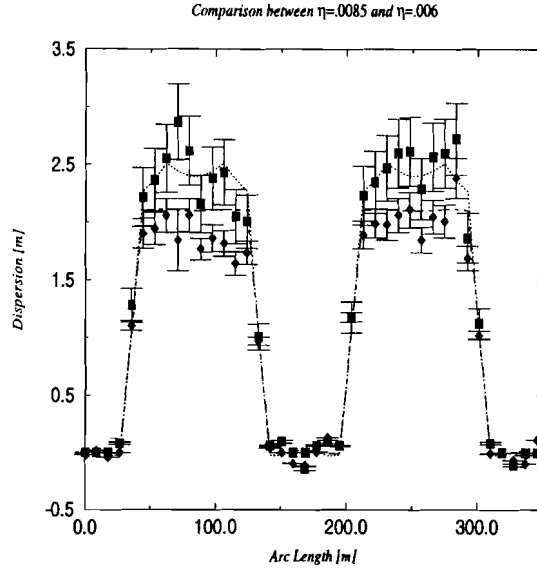


Figure 2.19: Comparison of $D(s)$ between $\eta = 0.0085$ (■) and $\eta = 0.0062$ (◆).

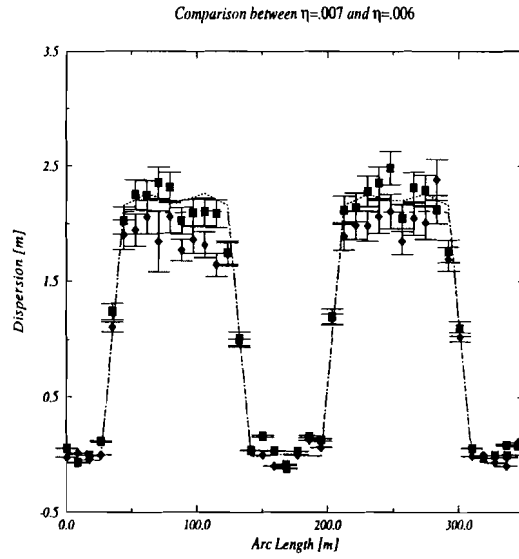


Figure 2.20: Comparison of $D(s)$ between $\eta = 0.007$ (■) and $\eta = 0.0062$ (◆).

In the Figures 2.18, 2.19, and 2.20, the comparison between the calculated and measured dispersion function is consistent in each case¹⁷.

¹⁷As indicated previously, only the first two sectors of the Debuncher lattice are plotted, since the BPM data in sector 50/60 were not functioning properly.

2.5.3.2 Predictions/Measurements of the slip factor η_f

Measurements of η , or equivalently γ_t^f , were carried out for the design case of the $\eta = 0.009$ design lattice. The experimental setup was identical to that described in the previous section for the nominal lattice with $\eta = .006$. A comparison of the longitudinal Schottky bunched beam spectra is given in Figures 2.21(a) and (b).

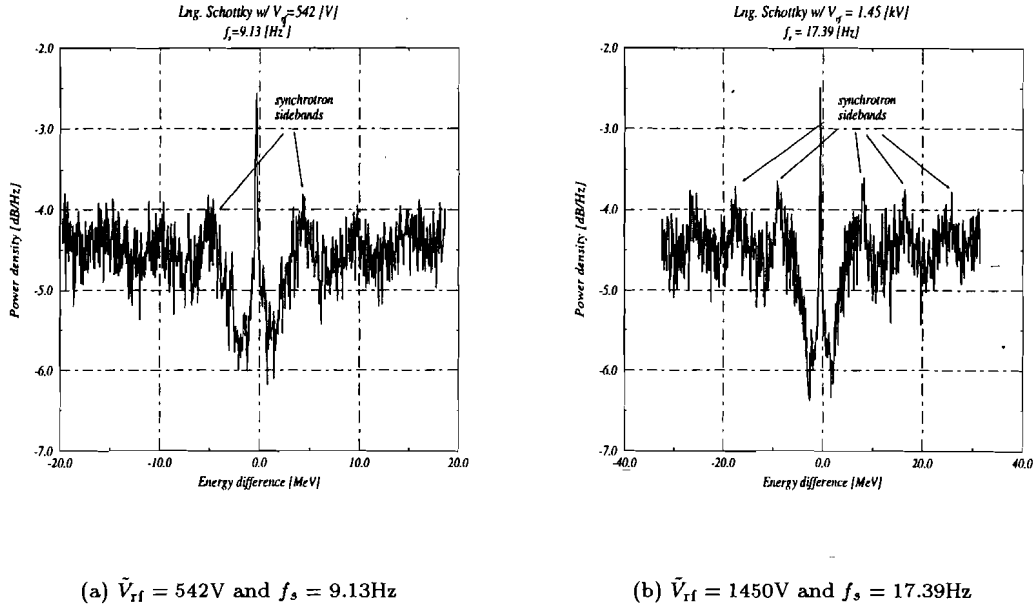


Figure 2.21: Power density (dB/Hz) versus energy difference $x = E - E_o$ of the longitudinal Schottky signal (126th harmonic) with the $\eta_f = 0.009$ lattice for obtaining the synchrotron frequency f_s .

Using measurements of the the synchrotron frequency f_s versus rf- cavity voltage \tilde{V}_{rf} , a linear least square fit was used to extract the slip factor and is given in Figure 2.22. The measured value is $\eta_{\text{meas.}} = 0.0093 \pm 2. \times 10^{-4}$, which compares to the theoretical prediction ¹⁸ of $\eta_{\text{pred.}} = 0.0095$. The error bars in Figure 2.22 and $\eta_{\text{meas.}}$ correspond to (i) the errors associated with reading the synchrotron frequency from the bunched beam spectra; $\sim 5\%$ error, and (ii) calibration error associated with the DRF3 readback (RF) voltage; $\sim 10\%$ error.

¹⁸The synchrotron frequency was obtained by choosing the frequency at the peaks of the sidebands, since it was assumed that most particles are far from the separatrix and are undergoing quasi- linear motion.

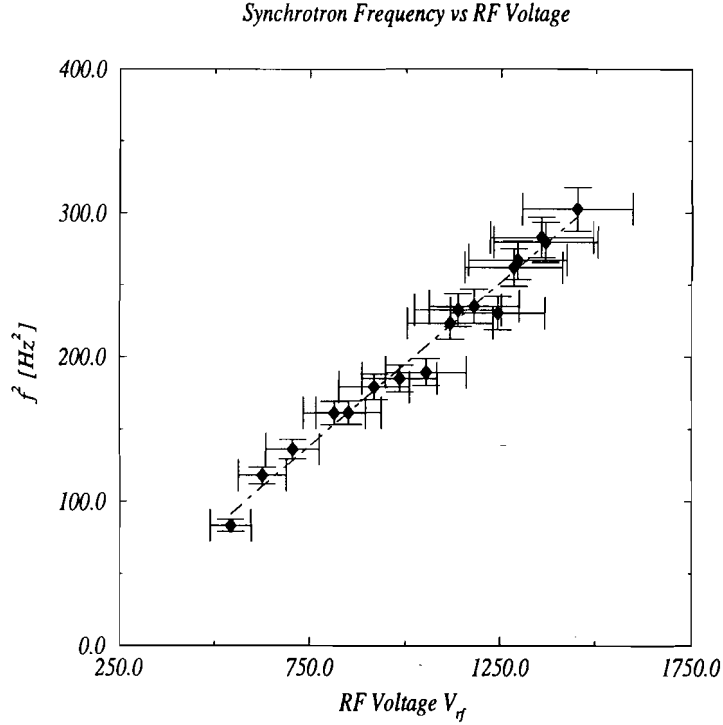


Figure 2.22: Measurements of the synchrotron frequency (f_s^2) as a function of the rf- cavity voltage on DRF3 (\tilde{V}_{rf}) for the lattice γ_t^f .

2.5.4 Measurements of Resonances for $\Delta\gamma_t$ lattice

Previous sections have dealt exclusively with linear lattice phenomena, with particular emphasis upon the $\Delta\gamma_t$ design. Issues and constraints related to nonlinear resonance crossing during $\Delta\gamma_t/\Delta t$ slews, however, played a major role. As such, experimental measurements shall be presented in this section, which address the question: what happens to the transverse resonance spectra with the implementation of the $\Delta\gamma_t$ lattice design? Should resonance structure proliferate and further enhance the strength of prominent resonances from the nominal lattice? Some theoretical guidance from Wiedemann's book is suggestive: [103]

the beneficial effect of a high super-periodicity or symmetry N in a circular accelerator becomes apparent in such a resonance diagram because the density of lines is reduced by a factor of N and the area of stability between resonances becomes proportionally larger ... Conversely, breaking a higher order of symmetry can lead to a reduction in stability if not otherwise compensated.

The above statement is a direct consequence of the resonance condition $k\nu_x + m\nu_y = iN$, with the super-periodicity given by N . Thus, if there is a high degree of symmetry, N is small and only low order resonances should be important. With the introduction of asymmetry, one may expect a proliferation of resonances, which were previously unimportant.

2.5.4.1 Resonances structure of $\gamma_t^{(i)}$ and $\gamma_t^{(f)}$

A simple experimental procedure was carried out during normal stacking of \bar{p} s to determine the relative strengths and widths of the transverse resonances for the nominal lattice ($\gamma_t^{(i)}$) and the $\gamma_t^{(f)}$ lattice. The transverse tunes were adjusted through symmetric changes in the currents of straight section quadrupoles. The relative strength of the transverse resonances were determined by monitoring the amount of beam loss as points throughout the tune plane were visited. Two parameters were used to determine beam loss (i) D:FFTTOT/M:TOR109, which is a direct measure of the amount of beam entering the Debuncher normalized by the Main Ring current¹⁹, and (ii) the stacktail power in the Accumulator, which is sensitive to small changes in the beam from the Debuncher.

Table 2.7 compares the percentage beam loss in crossing each of the major transverse resonances for the both the nominal $\gamma_t^{(i)}$ lattice and the $\gamma_t^{(f)}$ lattice. For reference to the resonance plane refer back to Figure 1.1 in the preface.

Table 2.7: A comparison between the *measured* percentage beam loss amongst the dominant transverse resonances for the nominal lattice and the $\gamma_t^{(f)}$ lattice design.

<i>resonance</i>	$(\gamma_t^{(i)} = 7.6318, \eta_i = 0.00615)$	$(\gamma_t^{(f)} (= 7.02655, \eta_f = 0.00924))$
(2/3)	80%	83%
(2/3 sum)	100%	100%
(3/4)	60%	87%
(3/4 sum)	45%	68%
(4/5)	0%	0%
(4/5 sum)	3%	36%
(diagonal)	0%	28%

¹⁹ Actually, D:FFTTOT is derived through measurements of the total integrated beam power spectral density. The signal is derived through a gap monitor (wall current monitor) and analyzed with an HP signal analyzer

2.6 Chapter Summary

Predictions and measurements of lattice parameters for the γ_t^f lattice were presented in this chapter. The discussion was limited to theoretical and experimental characterization of the static optics design for $\gamma_t^{(f)}$. Inherent within the characterization was a detailed comparison to the nominal lattice, experimental measurements and comparisons with theoretical results, and the presentation of results from a comprehensive optimization procedure.

A few of the important details contained in the chapter may be highlighted: (i) experimental determinations of the β function agree within 10% on average, (ii) the chromaticity was measured: (nominal lattice) $\xi_x = 1.74 \pm 0.24 \pm 0.15$, $\xi_y = 0.635 \pm 0.23 \pm 0.17$ ($\gamma_t^{(f)}$ lattice) $\xi_x =$, $\xi_y =$, (iii) the dispersion functions were measured for several lattices and agree with models, and (iv) the value of η (γ_t) was measured (nominal) $\eta(meas.) = 0.0062 \pm 6.0 \times 10^{-4}$, $\eta(pred.) = 0.0061$ ($\gamma_t^{(f)}$) $\eta(meas.) = 0.0093 \pm 2. \times 10^{-4}$, $\eta(pred.) = 0.0095$.

The method of producing $\gamma_t^{(f)}$ with π doublets was reviewed with specific emphasis upon the application to the Debuncher optical lattice. It was demonstrated that a closed form solution for $\Delta\gamma_t$ may be derived through first order, which predicts well the change in γ_t for a single π doublet in the Debuncher. Moreover, the first order estimate may be used to obtain a crude number for the total change in γ_t for the case with maximum π filling in the arc sections.

As a final note, the resonance structure of the Debuncher with the nominal γ_t and γ_t^f was examined briefly. The emphasis of the discussion concerned operational issues for allowable tune excursions during a fast $\Delta\gamma_t/\Delta t$ slew. In that regard, the final comments concerning the density of resonances lines in the transverse tune planes forms the precursor to the next chapter, in which the $\Delta\gamma_t/\Delta t$ is of principal concern.

CHAPTER 3

THE DYNAMIC $\Delta\gamma_t$ LATTICE

3.1 Introduction

The discussion of the first chapter considered only the constraints involved with changing an existing lattice to the final lattice $\gamma_t^{(f)}$, but without regard to the details of intermediate lattice configurations. During the $\Delta\gamma_t^{(f)}/\Delta t$ ramp between the initial and final lattice, it is implicit that each of the constraints, as outlined in the first chapter, must be upheld. While the dispersion, and thus $\Delta\gamma_t$, scales approximately linearly with the change in the π doublet strengths, the transverse tunes depend nonlinearly upon the straight section quadrupole strengths used for maintaining a zero tune shift. A discussion of this problem and the solutions are reviewed in the first section for the case of ideal hardware response.

Although it is possible to calculate/design ideal nonlinear $\Delta\nu \approx 0$ ramps, the major source of difficulties in obtaining fast slew rates are the limitations associated with the electronic hardware - power supplies and magnet current bypass shunt circuits¹. Utilizing a simple circuit model for the power supply, magnets and magnet current bypass shunt circuits, regulation errors are explained and used to motivate the necessary requirement for feedforward electronics for fast $\Delta\gamma_t^{(f)}$ slew rates.

Finally, a complete analysis of the $\Delta\gamma_t^{(f)}/\Delta t$ ramp is presented. In particular, questions related to current regulation and higher order effects are analyzed with comparisons between the measured and the calculated tunes, which are obtained through inputs of detailed parameterization of current errors as a function of time from each device. Also, chromaticity data is presented to corroborate the claim that higher order multipoles are not generated during the $\Delta\gamma_t^{(f)}$ ramping process.

3.2 Ideal $\Delta\gamma_t^{(f)}$ Ramp

The method for producing the final lattice with $\gamma_t^{(f)}$ has been discussed in the first chapter. To summarize, the design follows the two- step strategy:

1. Produce $\gamma_t^{(f)}$ with interleaved π - doublet quadrupole combinations throughout the arc sections, such that (i) the dispersion function increases *uniformly*, except in the straight sections

¹The response time of the quadrupole magnets is negligible on time scales of the $\Delta\gamma_t$ ramps $\sim 100\text{msec}$

for which the dispersion remains strictly zero, and (ii) the design maintains the full six-fold symmetry of the original $\gamma_t^{(i)}$ lattice.

2. The tune shift, $\Delta\nu$, resulting from the $\Delta\gamma_t^{(f)}$, is minimized with adjustment of field strengths amongst quadrupoles in the long straight sections. The constrained optimization problem is subject to the same constraints on lattice parameters as indicated previously in the first chapter.

Because the transverse tunes $\nu(\Delta\gamma_t, \Delta I)$ do not change linearly with $\Delta\gamma_t$ between the initial lattice with $\gamma_t^{(i)}$ and the final lattice with $\gamma_t^{(f)}$, it is necessary to perform the two step design procedure for intermediate values of $\Delta\gamma_t$ throughout the ramps. The constrained optimization problem in the second step is identical to that described in the first chapter. Thus a symmetric design is maintained by minimizing $\Delta\nu$ with respect to the six straight section quadrupole types $\{I_{q_i} | i = 1, \dots, 6\}$ and subject to the various lattice parameter constraints.

3.3 Actual $\Delta\gamma_t^f/\Delta t$ Ramp

Although within the design, the tune excursion during the $\Delta\gamma_t^{(f)}/\Delta t$ ramps was negligible small, the predominant tune excursion effects were the result of power supply and magnet current bypass shunt circuit regulation limitations for fast $\Delta\gamma_t/\Delta t$ slew rates.

To further motivate the regulation problem, Figure 3.1 depicts the measured change in current ΔI of the main power supplies during a $\frac{4}{5}\Delta\gamma_t^{(f)}/300\text{msec}$ ². In the Figure 3.1 the full values of the power supply currents are D:QSS: 282.5 \rightarrow 291.17Amps, D:QD: 239.4 \rightarrow 246.07Amps, and D:QF: 243.9 \rightarrow 243.9Amps. Although the power supply D:QF should remain constant, there is a current regulation error of $\Delta I_{QF} \sim \pm 1.32\text{Amps}$, which corresponds to a deviation of 1.1 part in 100 of the total current. Such a deviation from perfect regulation of the D:QF supply produces a tune variation on the order of $\Delta\nu \sim \pm 0.05$. Also exhibiting significant deviation from ideal regulation is the D:QSS power supply, which supports the bulk of the quadrupoles in the long straight sections. For $\frac{4}{5}\Delta\gamma_t^{(f)}/300\text{msec}$, D:QSS experiences a regulation error of $\Delta I_{QSS} \sim \pm 1.38\text{Amps}$, which may translate to a tune error $\Delta\nu \sim \pm 0.04$. This corresponds to a current regulation error in D:QSS of 9.5 parts in 1000. Although current regulation errors of D:QD do not appear to be large, i.e.

²As shall be used throughout the remaining discussions, the notation indicates the slew rate: $\Delta\gamma_t/\Delta t$. Thus, for the quadrupole power supply ramp D:QD, $\Delta I = 10\text{Amps}$ for the full $\Delta\gamma_t$.

$\Delta I_{QD} \sim \pm 0.4 \text{ Amps}$, it shall be demonstrated in the following sections that such errors in the D:QD supply would cause significant tune errors relative to the other supplies and/or trim elements $\Delta \nu \sim \pm 0.05$. Moreover, the errors in each of the elements on this scale cause large enough tune errors for complete beam loss.

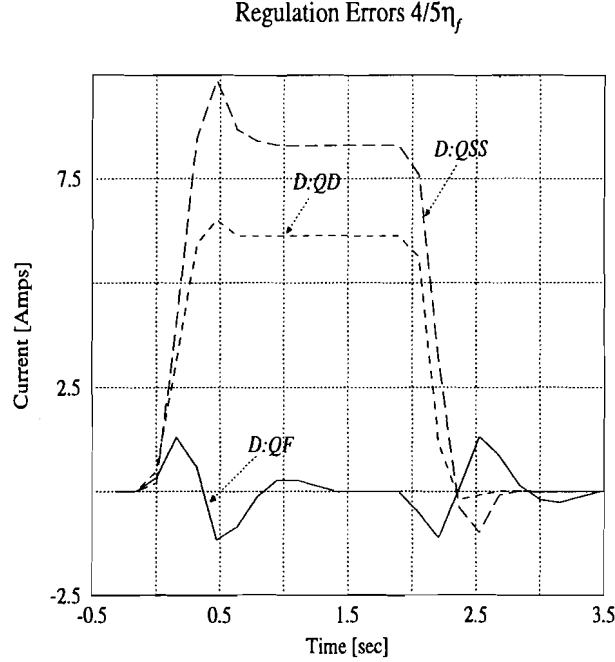


Figure 3.1: ΔI , indicating regulation errors, in each Debuncher power supply for the case of a $\frac{4}{5}\Delta\gamma_t^{(f)}/300$ msec ramp.

3.3.1 The Power Supply/Magnet/Current-Bypass Shunt Model

The power supply regulation errors depicted in Figure 3.1 of the previous subsection may be explained with the use of a simple equivalent circuit model representing the power supply, the quadrupole magnets, and the magnet current bypass shunt circuits. Figure 3.2 is a simplified equivalent circuit, in which the ideal power supply is modeled as an ideal current source with a frequency response governed solely by the low-pass Preag filter [78]. Attached in series with the power supply are the quadrupole magnets M_k and M_j , in which the sets M_j each possess a magnet current bypass shunt circuit connected in parallel for the purpose of individual control of currents, and hence, focusing strength. The frequency response of the magnet current bypass shunt circuit may be ignored,

and within the simple model may be represented as an *ideal current sink*. The current of the power supply is given by I , while the current in the bypass shunt is given in the figure by $-I_s(t)$. Each magnet may be represented by a simple resistor/inductor series combination. The resistance and inductance values for the three types of magnets present in the Debuncher ring are given by: (i) *SQC* ($R = 41.5\text{m}\Omega$, $L = 65.9\text{mH}$), (ii) *SQD* ($R = 46.3\text{m}\Omega$, $L = 77.9\text{mH}$), and (iii) *LQE* ($R = 87.8\text{m}\Omega$, $L = 34.4\text{mH}$)³.

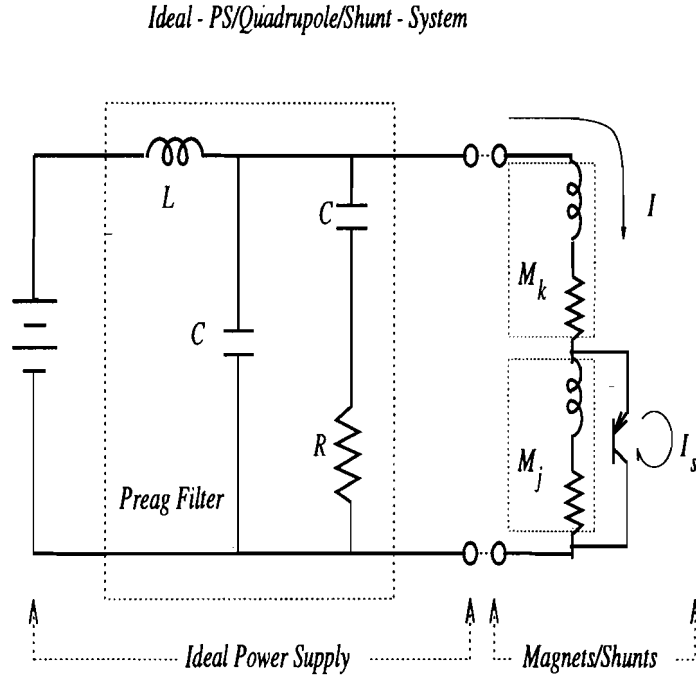


Figure 3.2: The power supply/magnet/current-bypass shunt equivalent circuit model.

From the model in Figure 3.2, an expression for the voltage $V^k(t)$ for the k -th power supply, with the given current curves for $\Delta\gamma_t/\Delta t$ is:

$$V^k(t) = \sum_{j=\text{magnets}} \left[L_j \frac{dI^k}{dt} + R_j I^k + I_s^j R_j + L_j \frac{dI_s^j}{dt} \right] \quad (3.1)$$

In this expression, the sum extends over all j magnets in the k -th power supply/magnet/current-bypass shunt system. For each k -th system, the values of the resistances and inductances for use in the model are summarized in Table 3.1. In Table 3.1, the values R_1 and L_1 are the resistance and inductive sums over magnets possessing current bypass shunt circuits, while the values R_2 and L_2 refer to sums over the remaining set of magnets. The designation *SQC* and *SQD* correspond to the

³For detailed specifications of the types of quadrupoles, consult *Tevatron I Design Report*, 1983

two major quadrupole magnet types used in the Debuncher.

Thus in each k th system, the (*internal*) feedback regulator circuit of the power supply, must respond to a rapidly changing impedance resulting from $-\Delta I_s(t)$ and $\Delta I^k(t)$ during the $\Delta\gamma_t/\Delta t$ slews. The necessary voltage required for the power supply to remain in *perfect* regulation with the reference, is given by $V^k(t)$ of Equation (3.1).

Table 3.1: Resistance and Inductance values of magnets for each power supply system used in the simple model for calculation of the required constant current power supply voltage $V(t)$ during ramps.

<i>ps</i>	<i>no. mags</i>	<i>no.w/shunts</i>	R_1	R_2	L_1	L_2	$R_{tot.}$	$L_{tot.}$
D:QF	42(SQC)	30(SQC)	1.23 Ω	0.513 Ω	1.977H	1.29H	1.74 Ω	3.267H
D:QD	5(SQD)	5(SQD)	0.73 Ω	1.079 Ω	1.180H	2.89H	1.81 Ω	4.074H
	38(SQC)	12(SQC)						
D:QSS	4(SQD)	4(SQD)	0.07 Ω	0. Ω	1.56H	0.H	0.974 Ω	1.564H
	38(SQC)	12(SQD)						

3.3.2 Feedforward Correction: Introduction

From the simple circuit model of Figure 3.2, the power supply voltage $V^k(t)$ required for a specific $\Delta\gamma_t^{(f)}/300\text{msec}$ slew rate, is completely determined. Indeed, if the power supply regulation feedback system was accorded infinite bandwidth, then the voltage would change *exactly* by $V^k(t)$, as required in order to keep a constant current. In order to maintain the required field tolerances of the initial design, the bandwidth of the power supply regulation feedback system was designed with a small value⁴. Since Equation (3.1) specifies the exact power supply voltage slew $V^k(t)$ for a given $\Delta\gamma_t/\Delta t$, this information is equivalent to a system possessing an infinite bandwidth. Thus, a method, which is easily implemented electronically, for utilizing the exact knowledge of $V^k(t)$ to improve the performance of the power supply regulation, is known as *feedforward*.

For each power supply/magnet/current-bypass shunt system, a feedforward electronic system was designed and installed for the purpose of obtaining fast $\Delta\gamma_t/\Delta t$ slew rates. The inputs to the feedforward electronics are the required changes in current of power supplies $[\Delta I^k(t)]$ and the magnet current shunt circuits $[\Delta I_s(t)]$ supplied by the reference. The output of the feedforward electronics is the voltage $V^k(t)$, which is scaled appropriately and *injected* into the power supply

⁴ It should be remembered that the Debuncher power supplies were never intended to ramp during normal operation, and so the initial designs of the regulators made no provisions for stiff current regulation during fast changes in the reference signal

regulation feedback circuit to *correct* the finite bandwidth error signal Δv_E^k . It is in this sense that *feedforward* assists the regulation feedback system, by enhancing the voltage error signal Δv_E^k . Thus, the feedforward system increases the *effective bandwidth* of the power supply's voltage regulator without the unwanted introduction of noise due to an actual increase in the bandwidth of the feedback system. *For obtaining fast $\Delta\gamma_t/\Delta t$ slew ramps, the implementation of feedforward is absolutely essential.*

Returning to the specific case given previously, Table 3.2 lists the initial and final values of each device for the $\frac{4}{5}\Delta\gamma_t^{(f)}/300\text{msec}$ case. Utilizing the simple model, the calculated voltage $V^k(t)$ from Equation (3.1) are given Figure 3.3.

Table 3.2: The currents ΔI for $\frac{4}{5}\Delta\gamma_t^{(f)}/300\text{msec}$ associated with each device.

Device	$I_{\text{start}}\text{Amps}$	$I_{\text{final}}\text{Amps}$	Device	$I_{\text{start}}\text{Amps}$	$I_{\text{final}}\text{Amps}$
QSx01	-5.99	-3.99	QSx13	-0.40	-6.80
QSx02	-26.81	-39.48	QSx14	-0.40	-5.07
QSx03	-17.77	-9.77	QSx15	-0.40	-3.47
QSx04	-0.39	-17.05	QSx17	-0.40	-6.80
QSx05	-46.00	-38.00	QSx19	-0.40	-6.47
QSx06	-4.19	-28.73	D:QSS	282.5	291.17
QSx08	-0.40	-6.80	D:QD	239.4	246.07
QSx09	-0.40	-6.80	D:QF	243.9	243.90

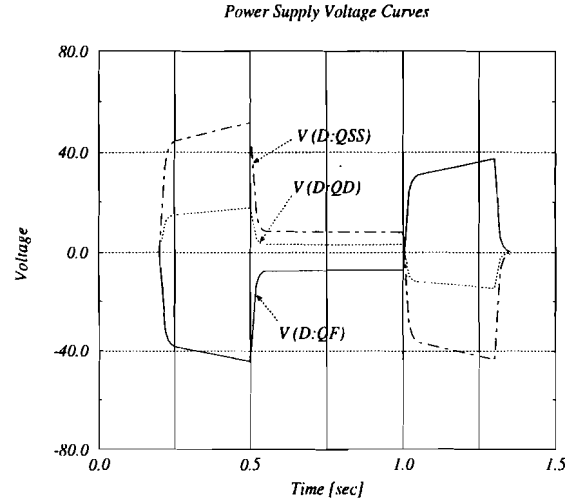


Figure 3.3: Voltage curves for each power supply with 300msec ramps and $\frac{4}{5}\Delta\gamma_t^{(f)}/300\text{ msec}$.

Prior to a detailed discussion of the feedforward system, the performance of the feedforward

method is best illustrated in Figure 3.4, which is a comparison between the measured power supply readback currents *with* and *without* the application of the feedforward systems ⁵ for the specific $\Delta\gamma_t^{(f)}/300\text{msec}$ case.

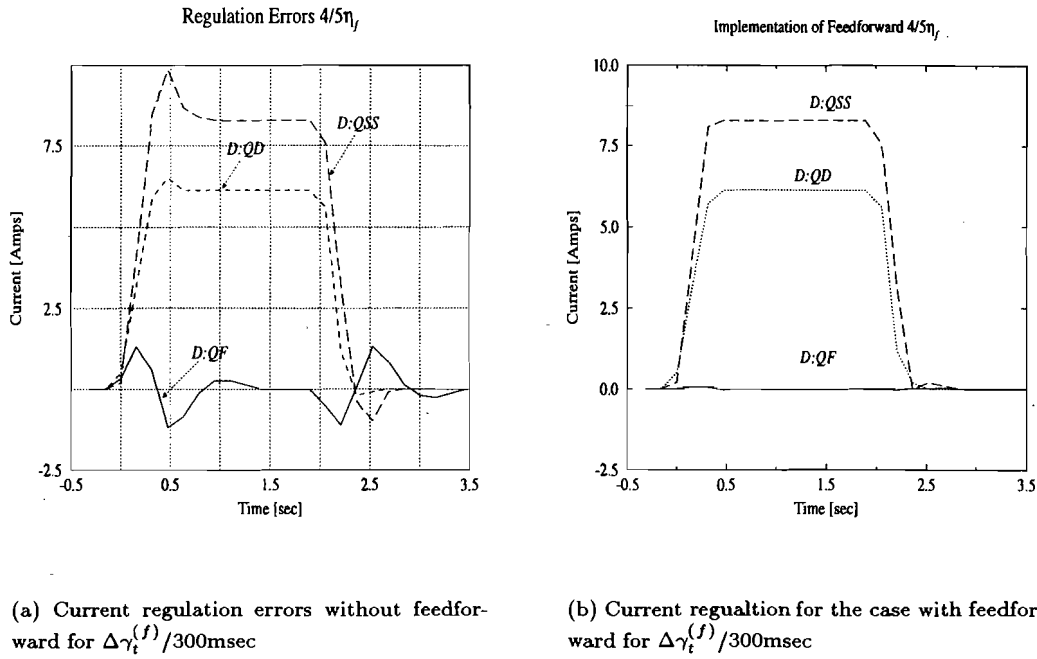


Figure 3.4: Comparison between the change in power supply currents for $\frac{4}{5}\Delta\gamma_t^{(f)}$, *with* and *without* feedforward.

3.3.3 The Feedforward Electronics System

The feedforward system for the k th power supply/magnet/current-shunt system is given in Figure 3.5. Referring to the annotations within Figure 3.5, a description is as follows

- A computer interface (1) is used to load data tables into programmable CAMAC ramp modules.
- Each 465 ramp module (2) is connected to the DAC input of a magnet current shunt circuit, while the power supplies are controlled with the 468 ramp module. Stored together with the

⁵Specifically, Figures 3.4 are taken from fast time plot measurements of D:QFI, D:QDI, and D:QSSI

$\Delta\gamma_i$ current ramp data, specific ACNET clock events are used to trigger the ramps to and from $\gamma_i^{(f)}$. From the 465 programmable ramp modules, the analog output signal is used as reference both for the magnet current shunt circuits (3) and also as input to the feedforward electronics (5). Although the power supply reference (4) requires a 16-bit word, the 468 programmable ramp module produces an equivalent analog output reference signal which may be used as an input to the feedforward electronics (5).

- The feedforward circuit (5) sums the differential analog inputs with the proper weighting and *solves* the differential equation for $V^k(t)$ Equation (3.1).
- The output signal $\tilde{V}^k(t^*)$ of the feedback circuit at time t^* is then combined with the error signal (6) $\delta v^k(t^*)$ from the power supply voltage feedback system. The resultant error signal $\Delta V^k(t^*) = \tilde{V}^k(t^*) + \delta v^k(t^*)$, is now used to fire the SCR circuit (7) and dial in the proper voltage slew, with a phase detection feedback circuit (8), to keep the error between the DAC reference and the measured current (9) zero. The superscript k on each of the quantities is a reminder that there is a feedforward system for *each* power supply/magnet/current-bypass shunt system.
- The power supply response is controlled also by a simple passive *Preag* filter (10), which is simply a low-pass device used to avoid excess noise ripple and to avoid large turn on voltage slews.

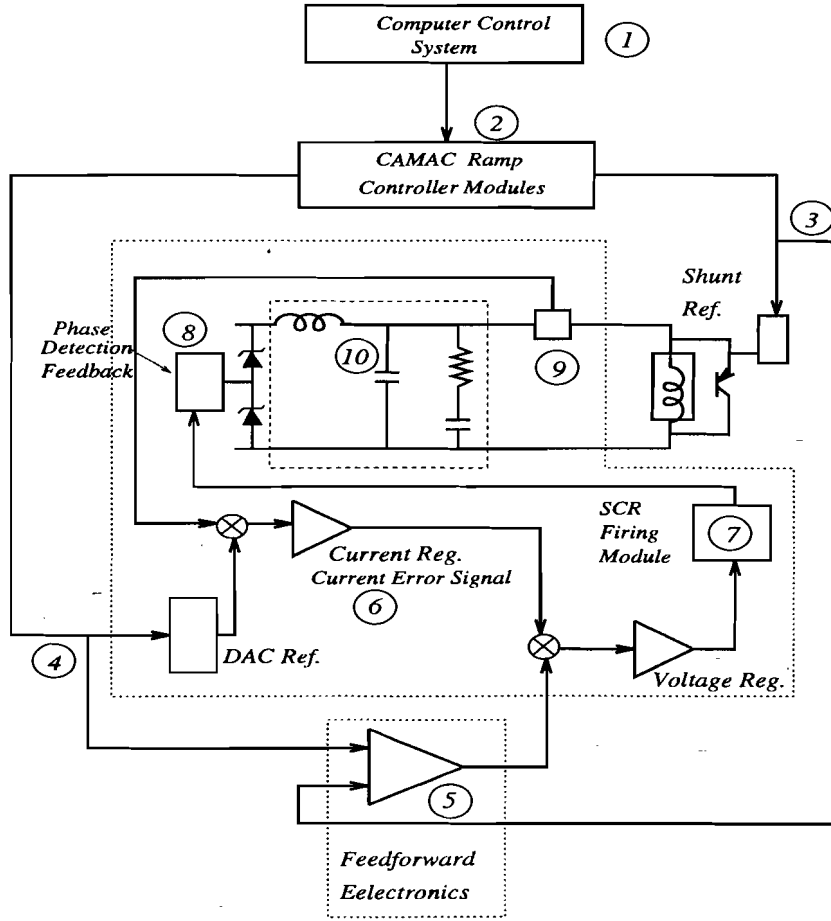


Figure 3.5: The feedforward system for the k th power supply/magnet/current-bypass shunt system.

3.3.4 Details of the Active Feedforward Circuit

As described in the previous section, the feedforward system increases the effective bandwidth of the power supply by enhancing the voltage error signal Δv_E^k produced by the finite bandwidth feedback regulator circuit. The voltage error signal is enhanced by providing the feedback loop with exact information about the required voltage slew for a given $\Delta \gamma_t / \Delta t$. The active feedback electronic circuit, which solves the differential Equation (3.1) for $V^k(t)$, is given in Figure 3.6.

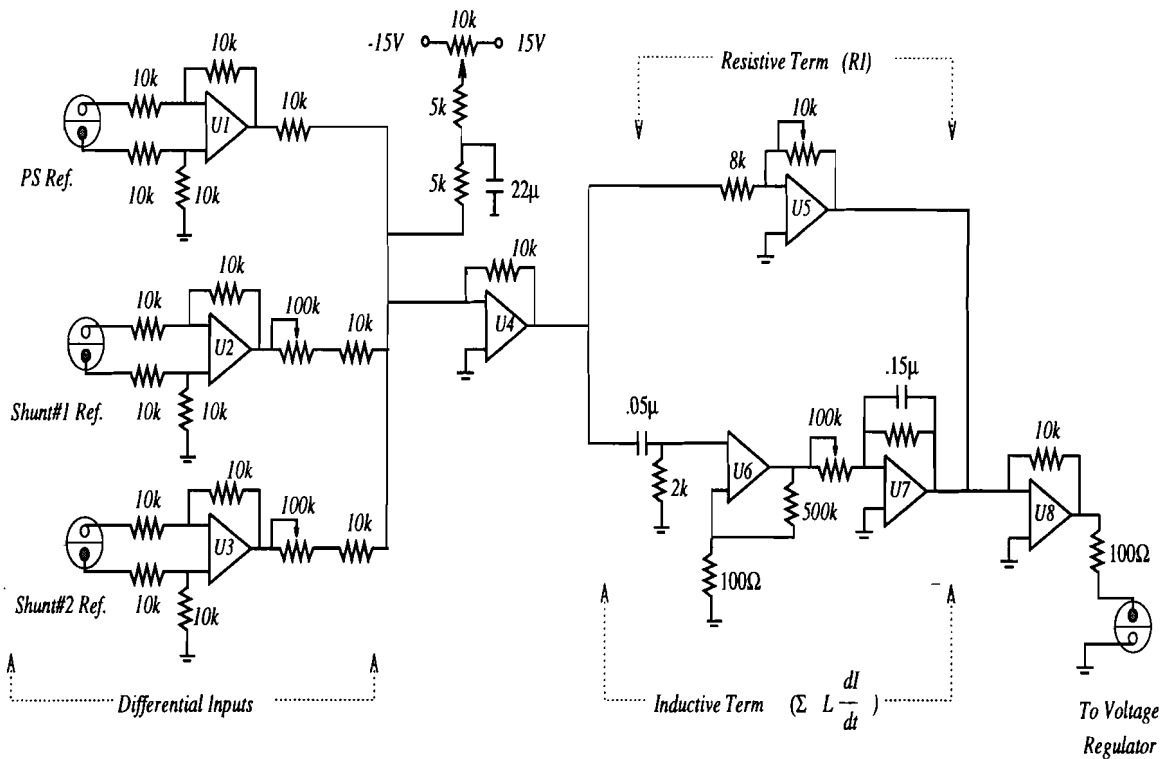


Figure 3.6: Feed-forward circuit implementation of $V^k(t) = \sum_j [L_j \frac{dI_j^k}{dt} + R_j I_j^k + I_s^j R_j + L_j \frac{dI_s^j}{dt}]$.

At the input stage of the feed-forward circuit of Figure 3.6, a set of differential amplifiers (op-amps $U1$, $U2$, and $U3$) provide high input impedance with unity gain for reference signals derived from the analog output of CAMAC 465 programmable ramp generator modules⁶. Thus, the terms in Equation (3.1) for $V^k(t)$, for the k th power supply, are directly obtained from the analog reference signals which drive each device. Resistor pots at the output of the differential amplifiers are used to provide proper weighting between each device.

The input reference signals, after appropriate weighting, are summed at the input of the inverting op-amp $U4$. The resistive terms, $\sum_j [R_j I_j^k + R_j I_s^j]$, in the equation are represented by an adjustable gain op-amp stage at $U5$, while the inductive terms, $\sum_j [L_j \frac{dI_j^k}{dt} + \frac{dI_s^j}{dt}]$, are obtained with a *pseudo* differentiator $P1$. The passive differentiator filter was chosen rather than an op-amp differentiator for stability and low noise requirements. In the filter $P1$, $C = .05\mu$ (polystyrene - for stability against temperature variations) and $R = 2k\Omega$, produce a $3dB$ roll-off to unity gain at $f_{3dB} \approx 1.6kHz$. The trade off with this particular design choice is the need for the non-inverting op-

⁶The signals have been tapped at the same point at the output of the CAMAC 465 cards. For pairs of trim elements driven by the same card, it was often the case that three twinax cables were tied together.

amp arrangement at $U6$ which must provide a gain of ≈ 5000 to account for the small differentiated signal of $P1$. For such large gain requirements, high precision (FET input) OP-27 amplifiers were used for minimizing noise.

At the output of the both the *resistive* ($U5$) and the *inductive* ($U6$ and $U7$) legs of the circuit, the signals are summed, inverted through a unity gain amplifier $U8$, and ready to be combined with the current error signal of the power supply feedback regulation circuit (refer to Figure 3.5).

3.3.5 The Magnet Current Bypass Shunt Circuit

For the purpose of implementing fast $\Delta\gamma_t/\Delta t$, it was required to improve the transient (frequency) response of the *active* magnet current bypass shunt circuits [19]. The modifications consisted of simple pole - zero compensation of the filter *transfer function* with changes to the impedance across the various op-amp feedback paths. The transient response design criteria sought to restrict overshoot $\leq 5\%$ for a slew rate of $\sim 10\text{Amp}/150\text{msec}$. A simple diagram for the magnet current bypass shunt circuit, which contains the modifications, is given in Figure 3.7.

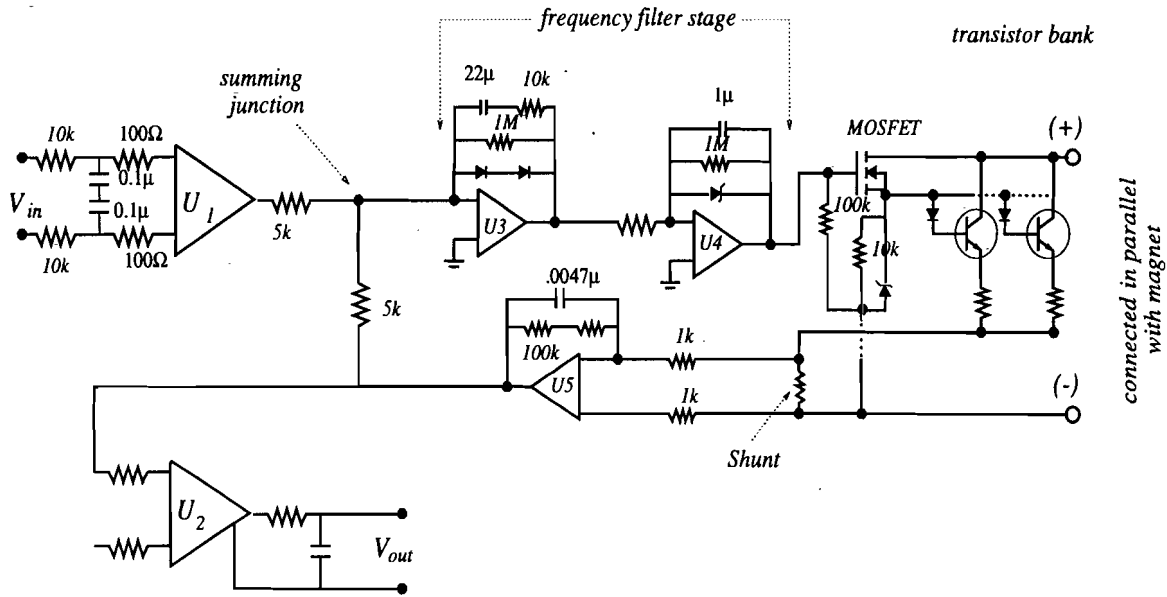


Figure 3.7: Active magnet-current bypass shunt circuit.

Since the entire trim circuit and magnet are connected in parallel and floating above ground, the isolation amplifiers $U1$ (input) and $U2$ (output) provide unity gain with very large input

impedance to avoid voltage spikes reaching the CAMAC reference electronics. The magnet current bypass shunt circuit *tracks* the input reference signal by controlling the MOSFET base current derived from the *error signal voltage* $\Delta V_E(S)$ derived at the feedback summing point S . The error signal voltage at the summing point S , $\Delta V_E = V_{\text{ref}} - V_{\text{shunt}}$, is the difference between the input reference voltage V_{ref} , and the voltage across the bypass shunt resistor V_{shunt} . If ΔV_E is nonzero, a finite MOSFET base current is produced to drive the transistors into the active region, *sink* more/less current across the bypass shunt resistor. Thus, the feedback loop constantly strives to make $\Delta V_E = 0$ at S .

3.4 Analysis of the $\Delta\gamma_t^{(f)}/300\text{msec}$ Case

For limited slew rates, it was possible to reduce the current regulation errors of each power supply, with the implementation of feedforward electronics. Slew rates greater than $\Delta\gamma_t^{(f)}/300\text{msec}$, however were not possible with the present hardware without further engineering efforts. In order to address several of the relevant issues and challenges, this section shall consider the particular case of $\Delta\gamma_t^{(f)}/300\text{msec}$.

The objectives are the following: (i) show the resulting current regulation errors for each power supply system - with feedforward, (ii) demonstrate the cause of the current errors through calculation of the voltages across each magnet, (iii) demonstrate that the current errors entirely account for the tune excursions, through comparisons between experiment and a detailed calculation which takes into account all the current regulation errors, and (iv) discuss engineering issues.

3.4.1 Current Errors in Power Supplies: $\Delta\gamma_t^{(f)}/300 \text{ msec}$ case

In Figure 3.8(a), the measured current errors for each power supply with the slew rate $\Delta\gamma_t^{(f)}/300\text{msec}$ are given. Although feedforward is used, the errors associated with D:QSS ($\pm 0.8\text{Amps}$) and D:QD ($\pm 0.6\text{Amps}$) are significant. The tune footprint throughout the $\Delta\gamma_t^{(f)}/300\text{msec}$ ramp is given in Figure 3.8(b), and are seen to cross several *fifth* order sum resonances. From the previous discussion of resonances in the Debuncher, the *fourth* order sum resonances have a measurable effect

upon beam loss. Measurements of the yield upon injection for the nominal lattice ($\eta \sim 0.006$) were $\langle \text{yield} \rangle \sim 1945.0$ compared to the measurement with γ_t^f ($\eta \sim 0.009$), $\langle \text{yield} \rangle \sim 1860.0 \pm 33..$ This represents a reduction in the yield, or equivalently, beam current in the Debuncher, of $\sim 4.3 \pm 0.5\%$.⁷

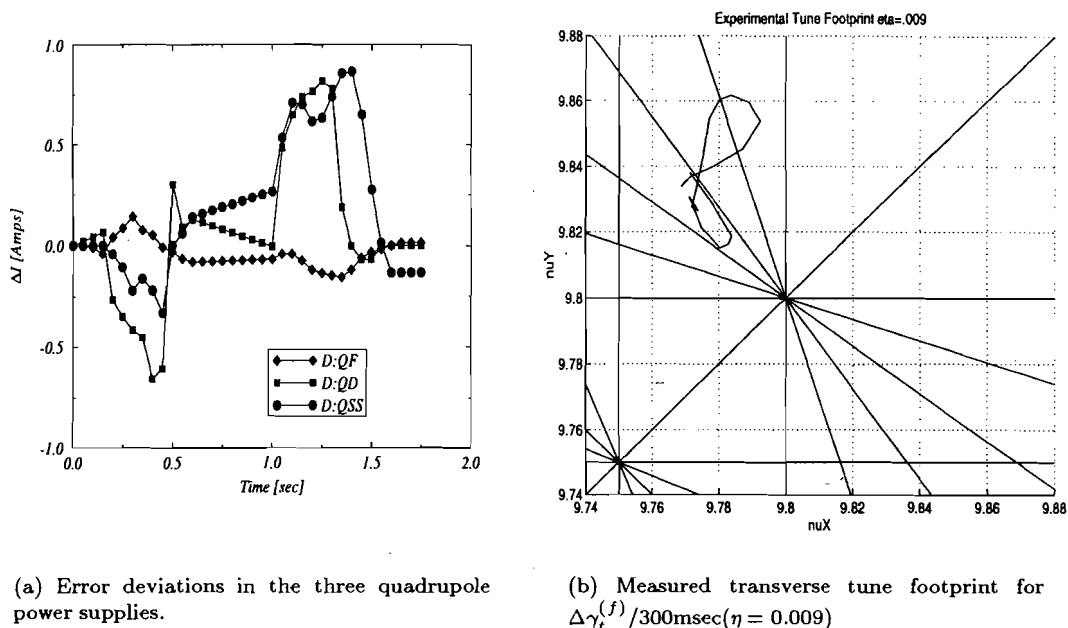


Figure 3.8: The $\Delta\gamma_t^{(f)}/300$ msec case.

The reason that D:QD and D:QSS display such large current errors is well understood on the basis of the associated current regulation errors of the magnet current bypass shunt circuits within the respective k th power supply/magnet system and may be explained through a closer examination of each of the magnet current shunt *readback*⁸ curves. The readback currents for several of the magnet current bypass shunts are given in Figure 3.9 which display regulation problems.

Since the feedforward system utilizes the analog reference signal from the 465 CAMAC module, rather than the true current through the magnet (the readback current), $V^k(t)$ does not include the errors due to current regulation problems associated with the magnet current bypass shunt circuits. Thus, with respect to the bypass shunt current errors, the power supply must rely

⁷A more detailed discussion of the nature of this measurement is given in Chapter 4. It should be briefly noted, however, that the yield measurement is obtained from a wall current monitor and frequency analyzed with an HP signal analyzer by measuring the total power in 126th harmonic. The number represented by the *yield* has been averaged for 400msec, and thus takes into account the γ_t ramp tune excursions.

⁸The MADC on board the magnet current bypass shunts is tied into ACNET, the FNAL Accelerator control system.

upon the normal feedback regulator to track the reference signals for $\Delta\gamma_t/\Delta t$. As a particular case, the current regulation errors, as given in Figure 3.9, associated with $Qx05$ and $Qx06$ contribute significantly to power supply regulation errors and a failure of the feedforward system as presently implemented.

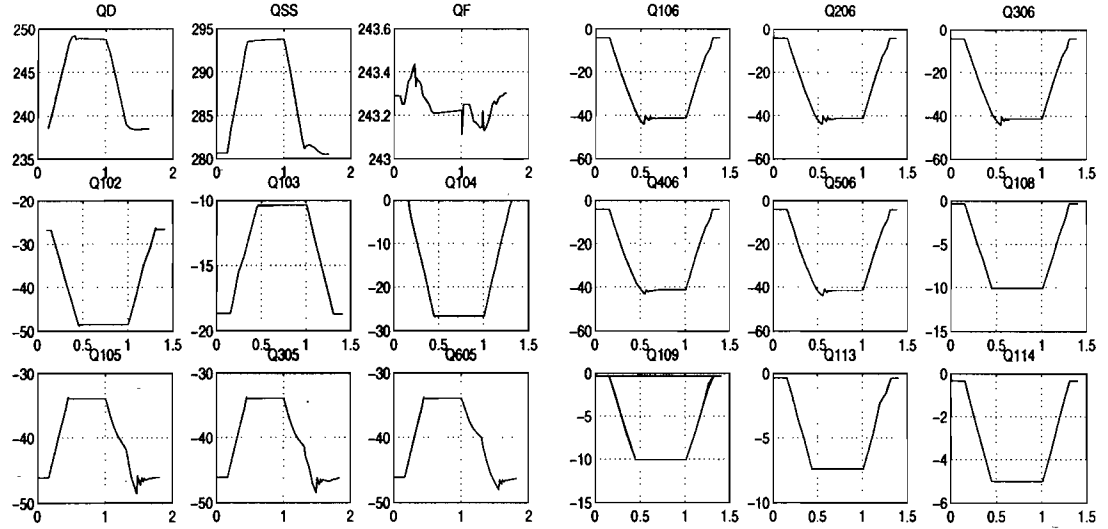


Figure 3.9: Readback currents for several magnet current bypass shunts with $\Delta\gamma_t^{(f)}/300$ msec.

The reason that the magnet current bypass shunts $Qsx05$ and $Qsx06$ do not remain in regulation is illustrated in Figure 3.10, which are plots of the voltage across several magnets for the $\Delta\gamma_t^{(f)}/300$ msec slew rate. In order for the bypass shunt circuit transistors to remain active, the voltage across each magnet must be ≥ 5 V. From 3.10, the voltage across the magnet type $Qx05$ falls below 5 V on the return ramp from $\gamma_t^{(f)}$ to $\gamma_t^{(i)}$, while the voltage across magnet type $Qx06$ falls below 5 V for the $\Delta\gamma_t^{(f)}/300$ msec case. The effect in both cases is indicated in Figure 3.9 for each of the $Qsx05$ and $Qsx06$ readback currents. Specifically, in the $Qsx05$ case, the return ramp falls out of regulation immediately and produces not only poor tracking of the reference, but also an overshoot of $\sim 5\%$ of the total swing, at the end of the ramp. The situation is similar for each of the $Qsx06$ current readbacks of 3.9, for the initiation ramp to $\gamma_t^{(f)}$.

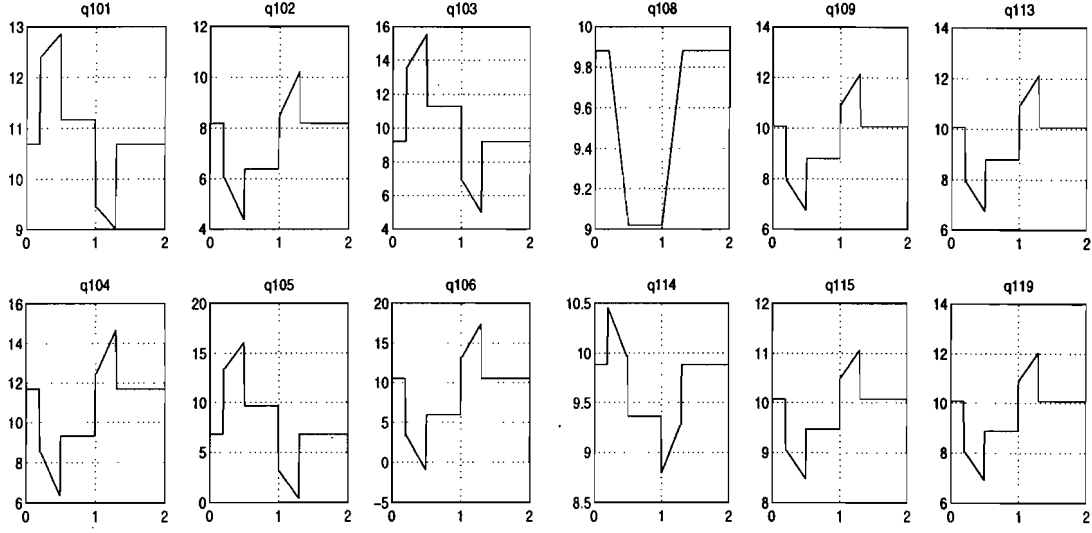


Figure 3.10: Voltages across each of the magnets possessing magnet current bypass shunts for $\Delta\gamma_t^{(f)}/300$ msec.

A few general features of the voltages across each magnet due to $\Delta\gamma_t^{(f)}/300$ msec, which are depicted in Figure 3.10, are: (i) typical voltage slews required of the arc section quadrupole circuits are $\sim \pm 2.5$ V, while those circuits in the straight section are $\sim \pm 5$ V, and (ii) the large changes in the voltages are due to the inductance (the $L_j dI_j/dt$ term).

3.4.2 Future Engineering Considerations

From the previous discussion, the present design of the magnet current bypass shunt circuits requires that the voltage across each magnet remain above 5 V in order that the bypass shunt transistors remain active. Since voltage swings dropped below the transistor (collector - emitter) voltage threshold with $\Delta\gamma_t^{(f)}/300$ msec slew rates for $Qx05$ and $Qx06$, one solution to consider is mounting constant voltage supplies across the magnet/bypass shunt. This solution guarantees that the minimum voltage swing cannot be lower than the required 5 V. The price to be paid, however, is large heat sinking requirements for the average power dissipated across the magnet current bypass shunt transistors⁹. Thus, there exists a delicate balance between voltage requirements

⁹This is a nontrivial point from an operations perspective. The issue is that the bypass shunt circuits have been designed in a manner to best heat sink the Darlington transistors. Reliability is substantially degraded with increasing power loads without proper effective heat sinking. As is well documented and realized, magnet current bypass shunt

of fast slew $\Delta\gamma_t^{(f)}/\Delta t$ lattice design and power dissipation requirements for longevity and reliability of the magnet current bypass shunt transistor elements for increased magnet/shunt voltage levels.

In Figure 3.11, summary plots of the currents ΔI_j and voltage ΔV_j across each j magnet/shunt are given¹⁰. From these plots, the average instantaneous power across the magnet current bypass shunt circuits in the arc section may be determined and is ~ 80 Watts, while the average instantaneous power across the magnet current bypass shunt circuits within the straight sections is ~ 200 Watts, thus accounting for the larger current slews required.

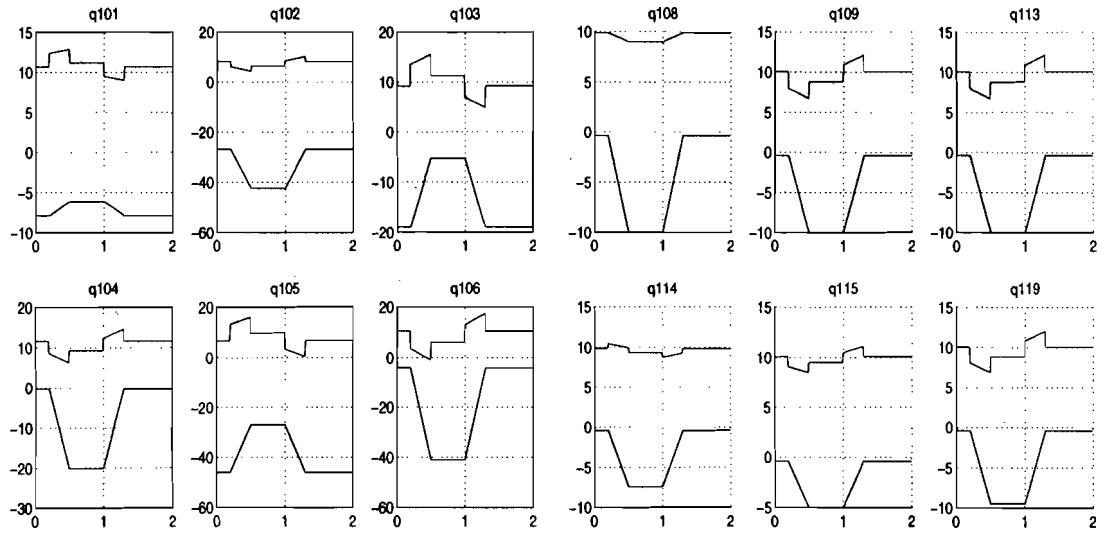


Figure 3.11: Voltage ΔV_j [Volts] (top curve) and bypass shunt current ΔI_j [Amps] (bottom curve) for $\Delta\gamma_t^{(f)}/300$ msec.

From 3.11, the total instantaneous power across several of the bypass shunt circuits may be determined. A more meaningful *engineering* number is the total instantaneous power *per* transistor, which provides an indication of whether the transistors are operating within specifications. For the 20Amps magnet current bypass shunts within the arc section, there are 4 transistors in total; for the 30Amps and 50Amps current bypass shunt circuits there are 7 transistors in total to account for the larger power requirements. This discussion should serve as a motivation for future plans for

failures can account for numerous Antiproton Source downtimes - so, power specifications must be a key component to any upgrades.

¹⁰Notice that for the case of Q108, while the shunt must change by ≈ -10 Amps, the power supply changes by $+10$ Amps, making the total voltage difference across Q108 ≈ 0 .

re-engineering the magnet current bypass shunt circuits with power requirements of fast $\Delta\gamma_t/\Delta t$ slew rates in mind.

3.4.3 Tune Excursion: $\Delta\gamma_t^{(f)}/300$ msec case

Together with the known source of tune excursion resulting from the current errors of the power supplies and magnet current bypass shunt circuits, a number of other technical questions/issues needed to be addressed. In particular, there was some concern that the $\Delta\gamma_t/\Delta t$ ramps could either generate higher order field moments, or corrupt the quadrupole field due to generation of eddy currents within the beam pipe or quadrupole windings. A deviation in the focusing fields would be detectable through a comparison of the measured transverse tunes and a calculation based upon the simple linear lattice model. Furthermore, if higher order multipoles were generated, then measurements of the chromaticity during the ramps should discern the strength of the effect.

Utilizing all the current readbacks for the $\Delta\gamma_t^{(f)}/300$ msec case as inputs to the model, the transverse tunes were calculated as a function of time throughout the entire production cycle. The calculated tunes were then compared against measured transverse tune spectrograms, obtained through the HP8990 vector signal analyzer with reverse protons. Comparisons between the measured and predicted tunes for both transverse planes are given in Figure 3.12. While the agreement is not perfect, it is consistent within 5-10% which can be attributed to two immediate sources: (i) error in reading the peak of the transverse Schottky for obtaining tune, and (ii) error associated with current errors used as inputs to the model. Nonetheless, the comparison of the transverse tune calculation to the experimental result strongly suggests that the tune excursions may be completely accounted for from current errors of the various power supplies and magnet current bypass shunts.

The top plots in Figure 3.12(a) and (b) give the comparisons between experimental (\times) and predicted (+) horizontal and vertical tunes, respectively. The bottom plots of Figure 3.12(a) and (b) are the differences $\Delta\nu_x = \nu_x^{\text{pred.}} - \nu_x^{\text{exp.}}$ and $\Delta\nu_y = \nu_y^{\text{pred.}} - \nu_y^{\text{exp.}}$, respectively.

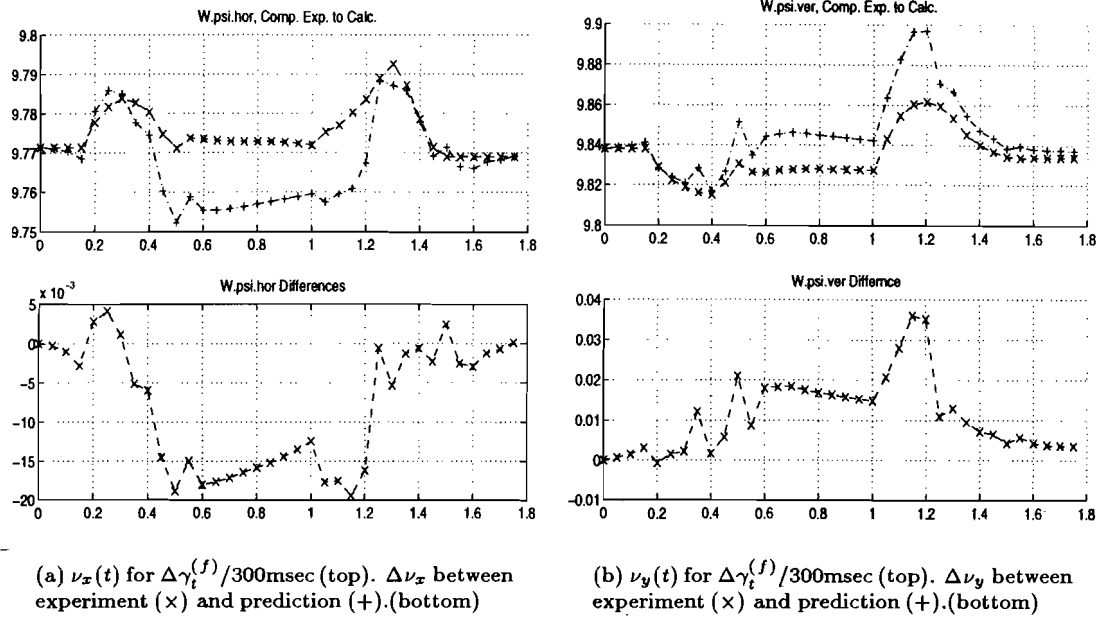


Figure 3.12: Experimental (x) and predicted (+) tunes for $\Delta\gamma_t^{(f)}/300$ msec.

3.4.4 Tune Excursion: Contribution from Each Device

From the previous section, it was found that a calculation of the transverse tunes utilizing inputs of the full current errors was in agreement with the measured tune behavior. As a result, it is possible to investigate the contribution of current regulation errors from each device, either power supply or magnet current bypass shunt circuit, to the tune excursion.

For the following discussion, it is convenient to define the tune footprint with the total current errors by $\Upsilon_{\text{total}}(t)$, and the tune footprint with all current errors *except* device j by $\Upsilon_j(t)$. Now, the contribution from the error in each device, ΔI_E^j , to the resultant tune excursion may be quantified. One manner for quantifying the effect of errors from an individual device to the tune excursion is to sum the differences between the tune footprints $\Upsilon_{\text{total}}(t)$ and $\Upsilon_j(t)$ at each time points, so that the j th residual is given by $|\mathcal{R}_j| = \sum_t |\Upsilon_j(t) - \Upsilon_{\text{total}}(t)|$. In order to determine those devices which contribute most to tune excursion, comparisons may be performed between each device in terms of the residual $|\mathcal{R}_j|$.

As an example of the calculation of $|\mathcal{R}_j|$, Figures 3.13(a) and (b) compare the horizontal

and vertical tune footprints, respectively for the two cases $\Upsilon_{\text{total}}(t)$ (denoted with (o)), the full tune footprint, and $\Upsilon_{j=QD}(t)$ (denoted with (x)), the footprint with all errors included except those for the power supply D:QD. In this particular case, errors in the D:QD power supply have the most dramatic effect upon the resulting tune excursion since the error appears on every defocusing quadrupole in the arcs together with Qx06, which has the largest effect upon tune correction.

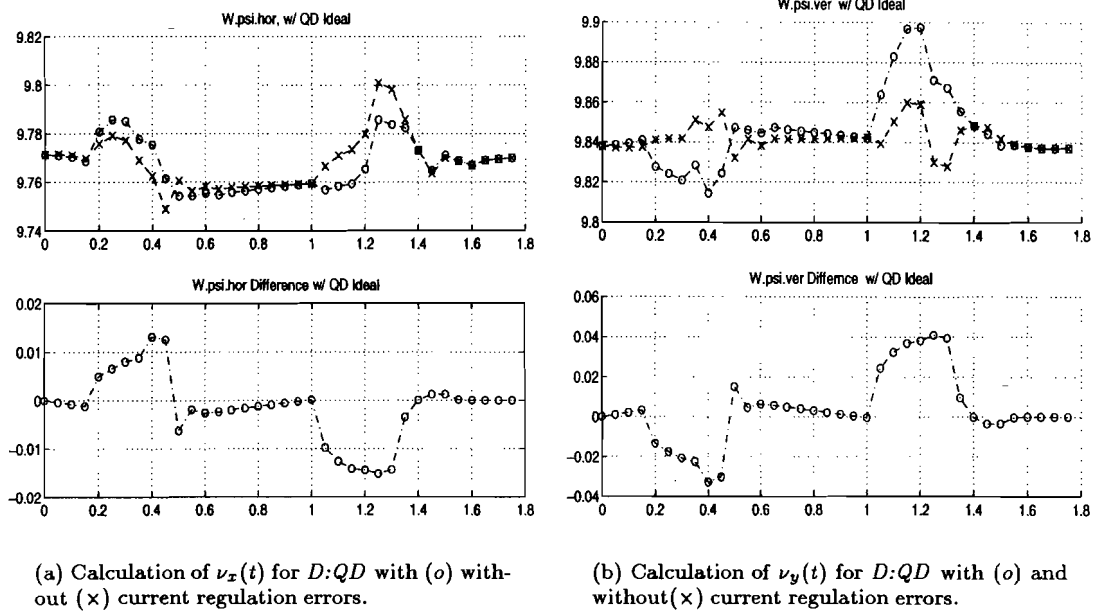


Figure 3.13: Comparison of the transverse tune spectrograms, $\Upsilon_{\text{total}}(t)$, and $\Upsilon_{j=QD}(t)$.

For the above case, the transverse footprints for the two cases $\Upsilon_{\text{total}}(t)$ and $\Upsilon_{j=QD}(t)$ are summarized in the transverse tune plane of Figure 3.14 to indicate the crossing of *fifth* order sum resonances. Crossing these *weak* resonance accounted for approximately 5% beam loss.

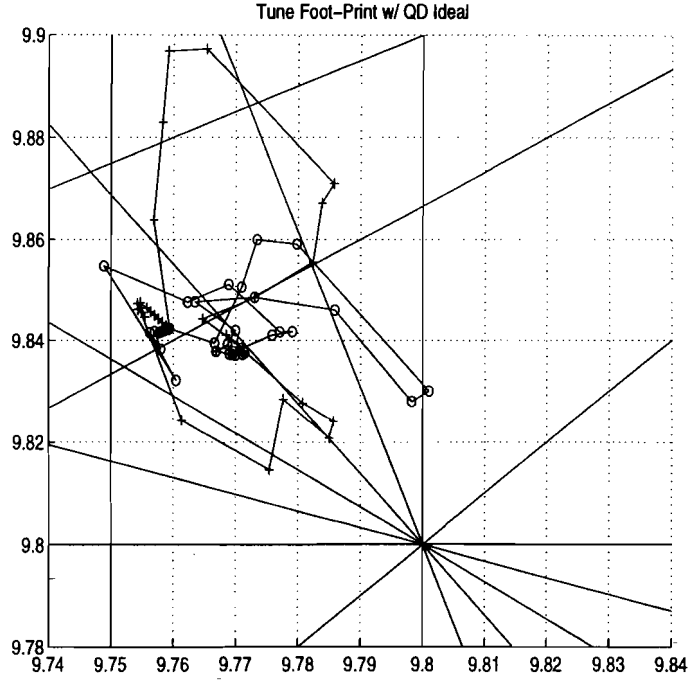


Figure 3.14: Tune footprint: $\Upsilon_{\text{total}}(t)$ (+), and $\Upsilon_{j=QD}(t)$ (o).

3.4.5 Summary: Effects of Errors to $\Delta\gamma_t^{(f)}/300\text{msec}$ Tune Excursion

The above procedure was performed for each device in the machine to determine from each the total current regulation error contribution to the full tune excursion. As defined in the previous section, the individual contribution to the tune excursion from each device may be quantified by $|\mathcal{R}_j| = \sum_t |\Upsilon_j(t) - \Upsilon_{\text{total}}(t)|$. Therefore, defining the *time averaged* normed residuals, $\langle \mathcal{R} \rangle$

$$|\langle \mathcal{R} \rangle| = \frac{1}{\Delta t} \int_{t_i}^{t_f} dt |\Upsilon_j - \Upsilon_{\text{total}}|$$

Table 3.3 list the results of the calculation \mathcal{R} for each device.

Table 3.3: Result of residuals $\langle \mathcal{R}_x \rangle \times 10^{-2}$ and $\langle \mathcal{R}_y \rangle \times 10^{-2}$ for each device.

Device	$\langle \mathcal{R}_x \rangle \times 10^{-2}$	$\langle \mathcal{R}_y \rangle \times 10^{-2}$	$\mathcal{R} \times 10^{-2}$	Device	$\langle \mathcal{R}_x \rangle \times 10^{-2}$	$\langle \mathcal{R}_y \rangle \times 10^{-2}$	$\mathcal{R} \times 10^{-2}$
QF	3.090	1.048	4.140	QX05	3.413	0.7256	4.138
QD	4.648	12.05	16.69	QX06	0.7850	0.2000	2.785
QSS	3.159	2.604	5.763	QX08	0.1784	0.5668	0.745
QX02	0.3737	1.341	1.714	QX09	0.5345	0.2005	0.735
QX03	0.3097	0.1485	0.458	QX13	0.5537	0.2160	0.769
QX04	0.1967	0.7910	0.987	QX14	0.1395	0.4128	0.552

The percentage contribution of errors from each device is found from $\langle \mathcal{R}_j \rangle / \sum_k \langle \mathcal{R}_k \rangle$. Results are given in Table 3.4.

Table 3.4: The percentage contribution of errors, $\langle \mathcal{R}_j \rangle / \sum_k \langle \mathcal{R}_k \rangle$, from each device.

<i>Device</i>	$\% \frac{\langle \mathcal{R}_x \rangle}{\sum \mathcal{R}_x^i}$	$\% \frac{\langle \mathcal{R}_y \rangle}{\sum \mathcal{R}_y^i}$	$-\% \sum \mathcal{R}$	<i>Device</i>	$\% \frac{\langle \mathcal{R}_x \rangle}{\sum \mathcal{R}_x^i}$	$\% \frac{\langle \mathcal{R}_y \rangle}{\sum \mathcal{R}_y^i}$	$-\% \sum \mathcal{R}$
QF	17.8	5.2	10.5	QX05	19.6	3.6	10.5
QD	26.7	59.3	42.3	QX06	4.5	1.0	7.1
QSS	18.2	12.8	14.6	QX08	1.0	2.8	1.9
QX02	2.2	6.6	4.3	QX09	3.1	1.0	1.9
QX03	1.8	0.7	1.2	QX13	3.2	1.1	1.9
QX04	1.1	3.9	2.5	QX14	0.8	2.0	1.4

3.4.5.1 Tolerances of each Constituent Quadrupole System

For quantitative comparison, Table 3.5 gives $\partial\nu/\partial I_E^j$ for the j th device. Each partial derivative was obtained by performing a linear least square fit through the results of 6 calculations at the current errors: $\delta I_j(\text{Amps}) = \{\pm 0.2, \pm 0.6, \pm 1.0\}$.

Table 3.5: Current tolerance, $\partial\nu/\partial I_j$, for the j th device.

<i>Device</i>	$\frac{\partial\nu_x}{\partial I_j} \times 10^{-2}$	$\frac{\partial\nu_y}{\partial I_j} \times 10^{-2}$	<i>Device</i>	$\frac{\partial\nu_x}{\partial I_j} \times 10^{-2}$	$\frac{\partial\nu_y}{\partial I_j} \times 10^{-2}$
QF	4.7557	-1.7136	QX06	-0.2428	0.6250
QD	-1.8386	5.0579	QX07	0.6907	-0.2400
QSS	1.1429	0.8678	QX08	0.2500	0.7064
QX01	0.4000	-0.1250	QX09	0.6885	-0.2564
QX02	-0.2185	0.7500	QX13	0.6592	-0.2500
QX03	0.5385	-0.2250	QX14	0.6850	-0.2400
QX04	-0.1814	0.5935	QX15	-0.2500	0.6500
QX05	0.6114	-0.1250			

To compare the relative strengths of each term in Table 3.5, Figure 3.15 is a plot of the partial derivatives as a function of the index number in the table. As expected the relative strength of tune errors due to errors in the power supplies dominate those of the error deviations in the power supply trim elements. Also, it is clear from the figure, that the resulting strengths of tune errors are equal throughout the arc sections.

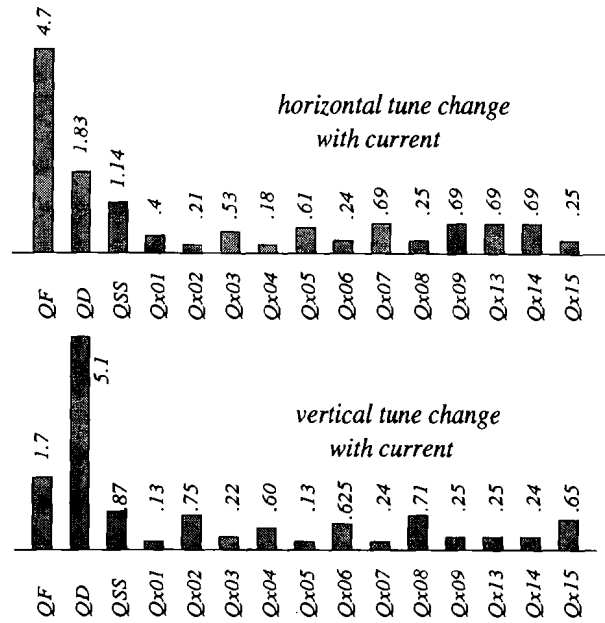


Figure 3.15: The partial derivatives $|\partial\nu_x/\partial I_j|$ and $|\partial\nu_y/\partial I_j|$ for each of the devices listed in Table 3.5.

3.4.6 Chromaticity Measurements for $\Delta\gamma_t^{(f)}/300\text{msec}$ Case

In order to investigate the possibility of generating higher order multipoles, an experimental measurement of the chromaticity for the $\Delta\gamma_t^{(f)}/300\text{msec}$ ramp was performed. The experimental method was as follows:

1. For each measurement, protons (*reverse protons*) were injected into the Debuncher in the direction counter to that normal for \bar{p} production.
2. RF was used to bunch the beam and accelerate/decelerate the bunch to the desired point in the momentum aperture.
3. The excess beam which was left behind by the RF was scraped to obtain a good measurement of the tunes.
4. Measurements of the transverse Schottky sidebands were made as a function of time (spectrograms) during the $\Delta\gamma_t^{(f)}/300\text{msec}$ ramps with the HP vector signal analyzer. These measurements were performed for each $\Delta p/p$.

5. The chromaticity $\xi(t)$ in each plane was found by a linear least square fit to the $\Delta\nu$ versus $\Delta p/p$ data.

For each value of $\Delta f/f$ the transverse tunes, $\nu_x(t)$, and $\nu_y(t)$, during the $\Delta\gamma_t^{(f)}/300\text{msec}$ ramp are given in Figure 3.16. Error bars on the measured tune *spectrograms* have been omitted in Figure 3.16 for clarity, however, each point has an error of $\leq 5\%$, which is due to the error obtaining the peak frequency of the transverse sideband and the time resolution error of the spectrograms.

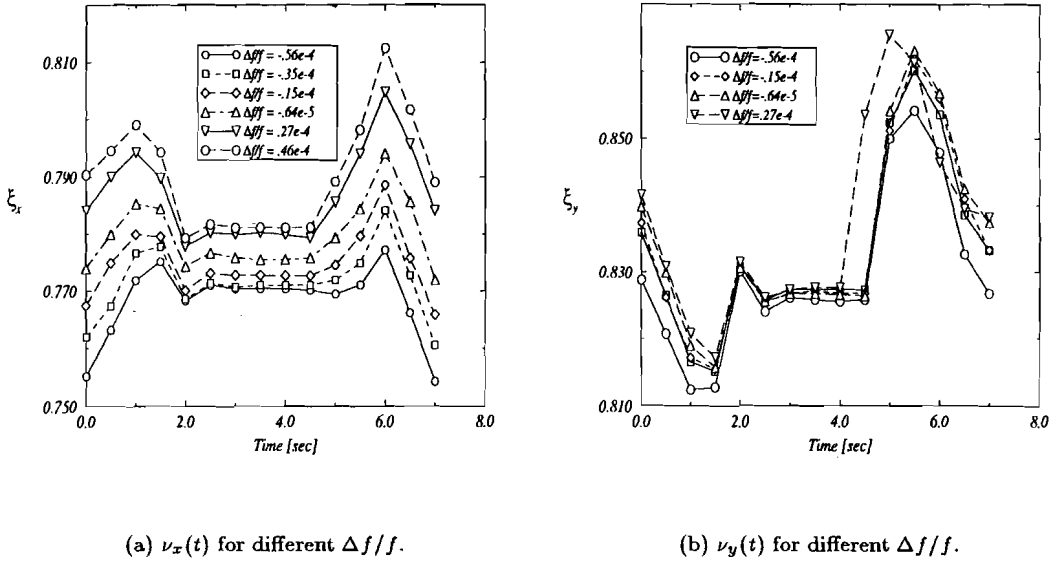


Figure 3.16: Tune spectrograms, $\nu_x(t)$ and $\nu_y(t)$, across the aperture $\Delta f/f$ for $\Delta\gamma_t^{(f)}/300\text{msec}$.

The chromaticity is defined by the relation $\xi_j = \Delta\nu_j[\eta(t)/\Delta f/f]$. For several points in time throughout the $\Delta\gamma_t^{(f)}/300\text{msec}$ ramp, a linear least square fit is performed on the $\Delta\nu_j$ from Figure 3.16 data as a function of $\Delta p/p = \eta(t)/\Delta f/f$. The result of this procedure for measuring the chromaticity ξ is given in Figure 3.17. Although there is a finite dependence of the chromaticity as a function of $\Delta\gamma_t$, it is quite small. Moreover, the tune spread in the Debuncher is small because $\Delta p/p$ rapidly decreases because of longitudinal stochastic cooling. Thus, $\Delta\xi$ can be neglected from further consideration.

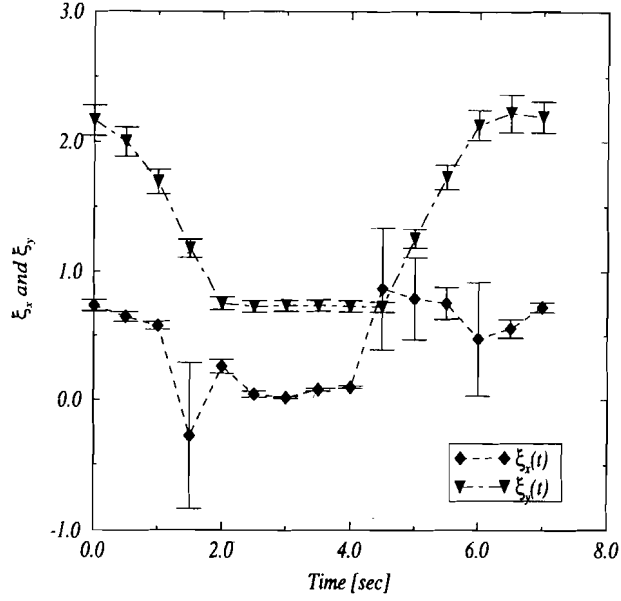


Figure 3.17: The chromaticity, $\xi_x(t)$ and $\xi_y(t)$, during $\Delta\gamma_t^{(f)}/300$ msec ramp.

3.5 Chapter Summary

In this chapter several issues related to the $\Delta\gamma_t^{(f)}/\Delta t$ ramps have been presented and analyzed. Solutions to the various problems associated with the fact that actual $\Delta\gamma_t^{(f)}$ ramps differ substantially from ideal $\Delta\gamma_t^{(f)}$ ramps, occupied the substantial part of the chapter. Notably, power supply regulation errors, which are caused by the stringent voltage slew rate requirements, result in significant beam loss due to resonance crossing. Such regulation errors must be corrected with feedforward electronics.

A simple power supply/magnet/current- bypass shunt model was used as a basis for the design of the corrective feedforward system. With the implementation of feedforward, it was found that regulation errors may be reduced by a factor of 10.

The remainder of the chapter analyzed took up the $\Delta\gamma_t^{(f)}/300$ msec design case. While the original intention was for the implementation of faster slew rates, performing the full $\Delta\gamma_t^{(f)}$ in 300msec posed considerable challenge with the present hardware. Furthermore, From a detailed investigation of the currents in each device as a function of the production cycle time, the experimental

tune spectra could be compared against calculations which accounted for the detailed current errors. The calculation was used to indicate both (i) the major devices contributing to tune excursion, and (ii) the sensitivity of current errors in each device to the associated tune.

The chromaticity was examined experimentally for the $\Delta\gamma_t^{(f)}/300$ msec ramp, in order to investigate the possibility of generating higher order multipoles. Although there is a finite dependence of the chromaticity as a function of $\Delta\gamma_t$, the tune spread of the machine, particularly due to momentum cooling, makes the effect negligible for the $\Delta\gamma_t$ project.

Having addressed the major lattice and slew rate requirement of the $\Delta\gamma_t$ project, the next chapter investigates, in depth, stochastic cooling in the Debuncher. The model developed in the next chapter is then used to study the effects of $\Delta\gamma_t/\Delta t$ and also for extrapolating cooling rate performance into eras at Fermilab with higher luminosity objectives.

CHAPTER 4

THE DEBUNCHER STOCHASTIC COOLING MODEL

4.1 Introduction

The objective of this thesis has been to investigate, both analytically and experimentally, the efficacy of a dynamic $\Delta\gamma_t$ lattice for improvements to stochastic precooling in the Antiproton Source Debuncher *through a reduction of the mixing factor*. Thus, it is necessary to be able to, both (i) predict the experimental results obtained with the present Debuncher particle flux, and (ii) extrapolate cost/benefits of a dynamic $\Delta\gamma_t$ lattice into higher particle flux regimes [33]. In order to accomplish the stated objectives, a model for the Debuncher stochastic cooling system was developed, which incorporated the measured cooling system parameters for direct comparison with (i) the cooling rates with the nominal Debuncher lattice, and later (ii) the cooling rates for a dynamic $\Delta\gamma_t$.

The main contribution of this work to the discipline of stochastic cooling is through an analysis of the specific FNAL Antiproton Debuncher systems. In particular, experimental measurements provide a strong basis for the development of a phenomenologic based computer calculation based upon the known theoretical framework. Since ample descriptions of stochastic cooling theory may be found in the references [4], [5], [22], [61], [95], [69], [70], [28], no attempt is made to enumerate *ab initio* the steps leading to the cooling equations. Rather, it is the consequences, as applied to the Debuncher, which are presented from the perspective of a *design report* intended for the *engineering* upgrade of an existing machine.

4.2 Historical Development

As early as 1968, the first concept of stochastic cooling was originated by S. van der Meer. What was needed, however, was the ability to observe individual particle orbits. With parallel efforts in two separate endeavors: (i) early work with the observation of Schottky scans [8], and (ii) feedback systems for the damping of coherent instabilities [86], stochastic cooling was elevated from the status of a good idea to a technique rich with promise for increasing the phase space density of particle beams.

A short time thereafter, the *Initial Cooling Experiment* (ICE) [16] demonstrated both longitudinal and transverse cooling with a system having an initial power of ≈ 1 kW and a bandwidth of $W \sim 100 - 180$ MHz. The ICE project was possible through the realization of momentum stack cooling by Strolin and Thorndahl, together with electronic filter developments by Carron [17]. Although the initial concept of S. van der Meer was that of transverse emittance cooling, the idea of longitudinal stochastic cooling by Thorndahl, unleashed the possibilities for collecting and storing large amount of antiprotons for high luminosity $p\bar{p}$ collision experiments.

Progress in stochastic cooling technology was subsequently advanced with the CERN SPS and the Fermilab Tevatron I project and through the newly available technology in high-powered, wide-bandwidth TWT¹ amplifiers. Although the notion of sensing individual particle fluctuation was still not entirely realized², large steps forward have been accomplished with amplifiers possessing high power with suitable linearity over octave bandwidths in the GHz regime.

In parallel with the rapid strides in the hardware technology of stochastic cooling, theoretical efforts by groups at CERN and LBL/FNAL were quickly providing a formal understanding of the stochastic cooling principles. What had emerged was a rich scientific subfield. Amongst the physical phenomenology having particular connection and impact upon the developments of stochastic cooling were collective beam phenomena [24], [21], theory of fluctuations [23], within the broader context of Markov processes [20], [80], and elements from controls theory [48].

4.3 Stochastic Cooling: Definitions

Two definitive texts, which had formed the foundation for a complete treatment of coasting beam stochastic cooling theory, were that of J. Bisognano [4], [5], and later for bunched beams by S. Chattopadhyay [22], [25]. The efforts from both investigators presented a theoretical formulation of stochastic cooling of particle beams in a storage ring as a unified whole based upon both the kinetic theory in phase space and the fluctuation theory in frequency space.

Figure 4.1 is a conceptual drawing of a stochastic cooling system used in a circular storage

¹ The power amplifier stages for cooling systems are TWT - Traveling Wave Tube amplifiers, which have octave frequency bandwidths 1-2GHz, 2-4GHz, and 4-8GHz, with typical saturated output power ranges of up to 200Watts

² For the Debuncher with $W \sim 2$ GHz, $L_{pu} \sim 2.5$ cm, and $I_p \sim 5 \times 10^7$ there are ~ 500 ps under a single pickup (pu) at any one time.

ring. A lucid definition of stochastic cooling has been so concisely stated in Chattopadhyay's thesis [22], that it is worthwhile repeating verbatim:

Stochastic cooling is the damping of transverse betatron oscillations and longitudinal momentum spread or synchrotron oscillations of a particle beam by a feedback system. In its simplest form, a pick-up electrode (sensor) detects the transverse positions or momenta and longitudinal momentum deviation of particles in a storage ring and the signal produced is amplified and applied downstream to a kicker electrode, which produces electromagnetic fields that deflect the particles, in general, in all three directions. The time delay of the cable and electronics is designed to match the transit time of particles along the arc of the storage ring between the pick-up and kicker so that an individual particle receives the amplified version of the signal it produced at the pick-up. If there were only a single particle in the ring, it is obvious that betatron oscillation and momentum off-set could be damped. However, in addition to its own signal, a particle receives signals from other beam particles (Schottky noise), since more than one particle will be in the pickup at any time. In the limit of an infinite number of particles, no damping could be achieved; we have Liouville's theorem with constant density of the phase-space fluid. For a finite, albeit large number of particles, there remains a residue of the single particle damping which is of practical use in accumulating low phase-space density beams of particles such as antiprotons.

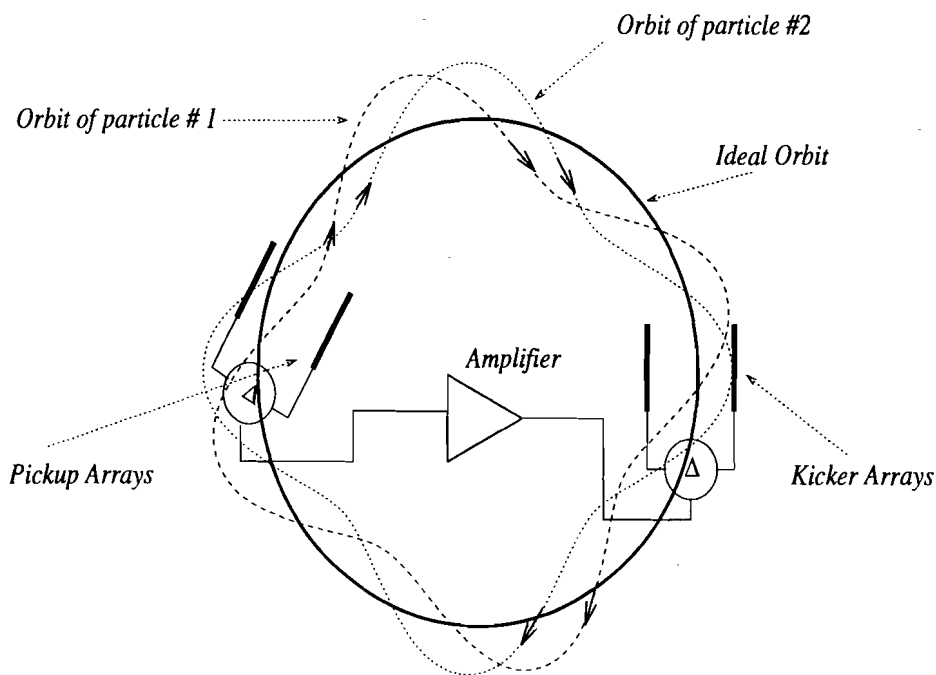


Figure 4.1: Conceptual illustration of a stochastic cooling system within a particle storage ring.

4.3.1 Basic Physical Processes

In Hamiltonian mechanics, the *dynamical* evolution of a system is described with a convenient set of canonical variables, which define the coordinates of the system in phase space [39], [34], [92]. If the system is an ensemble of particles acting under *conservative* interactions, the system is said to be Hamiltonian and Liouville's theorem states that the phase volume may be deformed without change to the phase density. Non-conservative forces, as resulting from self- interactions in a feedback system which are *velocity dependent* [51], are non-Hamiltonian, and thus, *Liouville's theorem does not apply*. Therefore, stochastic cooling is merely a method of introducing an interaction which is a dissipative, velocity dependent force in order to decrease the phase space density. In particular, the non- Hamiltonian interaction of a stochastic cooling system in a storage ring is the *self- interaction* of a particle *scattering* with itself through an electronic system of amplifiers and/or filters. Thus it is the coherent, velocity dependent self interaction which leads to a reduction of the phase space volume. In addition to the ideal coherent interaction, however, there is also the *two particle scattering* through the feedback loop. Thus, the effect of particle j 's signal upon particle i at the kicker leads to diffusion, which is in direct competition with the cooling self- interaction.

The kinetic theory of stochastic cooling of Bisignano and Chattopadhyay is predicated upon the two fundamental interactions just described: (*i*) the coherent self- interaction through the feedback loop, and (*i*) the incoherent *two particle* interaction representing the presence of other particles in the beam. Chattopadhyay has distilled these fundamental processes of stochastic cooling into two diagrams reminiscent of Feynman scattering diagrams [35] as depicted in Figure 4.2. In his theoretical *treatise*, Chattopadhyay takes these diagrams quite literally in developing interaction Lagrangians with transit time matched Green functions.

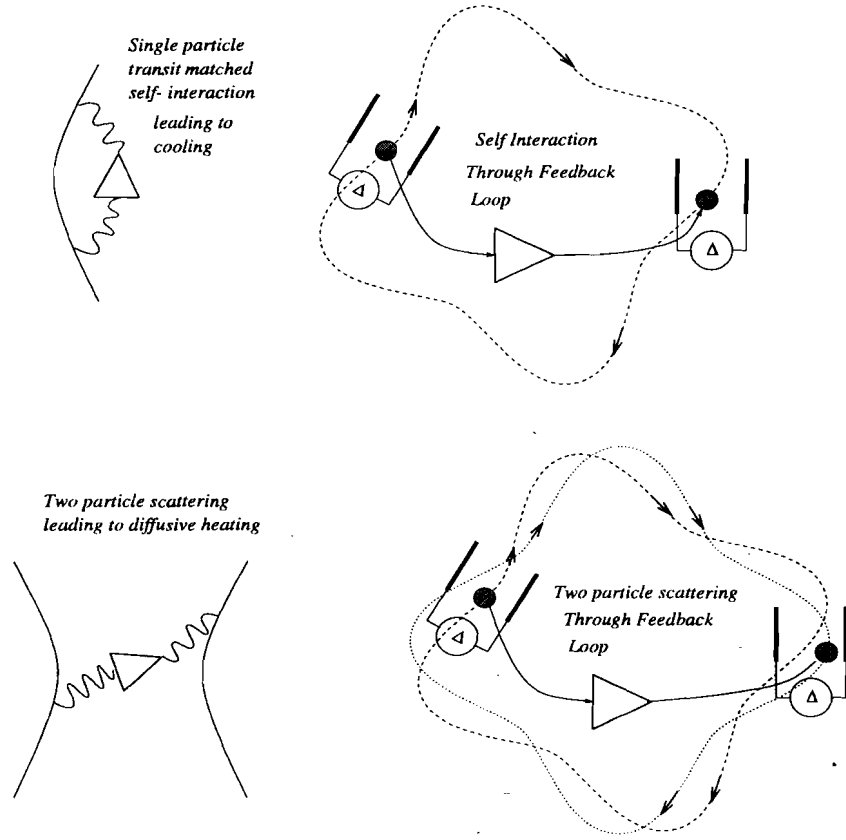


Figure 4.2: Scattering interpretation of the the two stochastic cooling interactions[22].

4.3.2 Macroscopic Quantities and Simple Systems

Having briefly described the basic *microscopic* processes involved with stochastic cooling, the *macro-* behavior of the stochastic cooling *system* shall now be addressed. The emphasis in this brief section shall be to underscore (i) the relevant measurable quantities involved with a stochastic cooling system, and (ii) the scaling behavior as a function of the cooling time. For convenience, the longitudinal and transverse systems are segregated into separate descriptions, however, a few words shall be said about the unifying physical features of each.

4.3.2.1 Longitudinal system

The simplest longitudinal stochastic cooling system would operate in the following manner: (i) the *voltage* signal of a distribution of particles, which is derived from the *sum mode* of a pair of

pickup plates [38], is amplified, (ii) the amplified signal is differentiated, thus producing a voltage signal with a zero crossing at the central frequency, and (iii) the differentiated signal voltage is applied to the kicker plates, such that higher/lower momentum particles are decelerated/accelerated towards the central frequency. Dramatic improvements to the simple system just described are possible with the use of recursive notch filters which produce an energy dependent gain designed to reduce the noise signal from particles already cooled to the central momentum. The simplest realization of a notch filter is with the half wave shorted transmission line, having a transfer function (impedance) $Z \sim \tan[2\pi\omega/\omega_o]$, which to first order, varies linearly as the frequency difference, or equivalently, the energy difference. If the filter is lossy, however, $|Z|^2$ of the notch filter will not fall to zero in the notches at the revolution harmonics, thus diffusion will be enhanced compared with a lossless filter. Moreover, as the beam cools, the Schottky power spectra $\Sigma(\omega)$ will increase if Z is lossless, thus, $|Z|^2 \sim \Delta E$ means diffusion increases as the beam is cooled [28].

The response of a simplified recursive notch filter is $N(\Omega) = 1 - Ae^{-i\Omega L/c} = 1 - Ae^{-i\Omega\tau_o}$. Thus, Figure 4.3 is a plot of the magnitude $|N(l\omega)|$ which together with the phase is given by

$$|N(l\omega)| = [1 + A^2 - 2A \cos 2\pi l f / f_o] \quad (4.1)$$

$$\arg(N) = \tan^{-1} \frac{A \sin 2\pi l f / f_o}{1 - A \cos 2\pi l f / f_o} \quad (4.2)$$

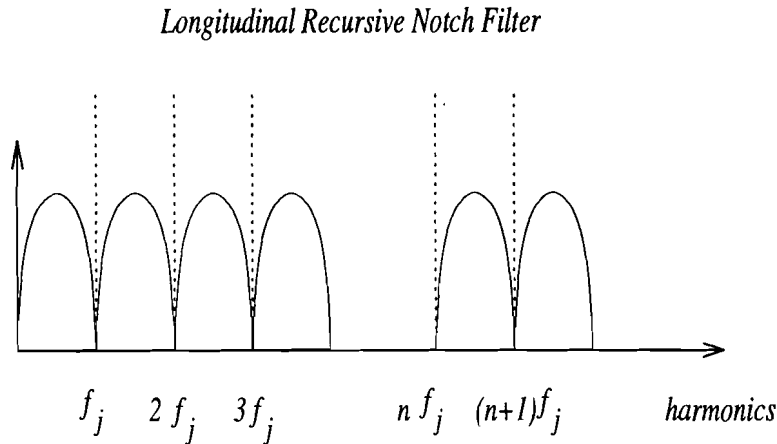


Figure 4.3: A simplified diagram of the ideal recursive notch filter in frequency space.

Since the cooling gain is dominated by the response of the recursive notch filter, the full electronic transfer function of the stochastic cooling system, shall take the simple form, as a function of ΔE ,

$$G(\Delta E) = -g [\sin[\tau \Delta E] + i(1/A - \cos[\tau \Delta E])] \quad (4.3)$$

Thus, Equation (4.3) represents the transfer function of (i) the pickup $P_{\parallel}(\Delta E)$, (ii) the kicker $K_{\parallel}(\Delta E)$, (iii) the amplifiers and notch $g_e N(\Delta E)$, and (iv) an overall phase factor $\exp[i\varphi]$:

$$G_{\parallel}(\Delta E) = e f_o^2 P_{\parallel}(\Delta E) \otimes K_{\parallel}(\Delta E) \otimes g_e N(\Delta E) \exp[i\varphi] \quad (4.4)$$

The full gain $G_{\parallel}(\Delta E)$ of Equation (4.4) is dominated by the notch filter, $N(\Delta E)$, since over the energy (frequency) range of the beam, both P_{\parallel} and K_{\parallel} are constant.

A more detailed description of the longitudinal cooling system shall be developed in subsequent sections. In particular, the time evolution of the beam width σ may be obtained from the second moment of a Fokker Planck transport equation, which makes use of the simple model of $G(\Delta E)$ in Equation (4.3) for the system response.

4.3.2.2 The transverse cooling system:

A description of the transverse stochastic cooling system is similar in many respects to the longitudinal system. Physically, the voltage signal at the pickup electrode pair is derived from the *difference mode*, thus sensitive to the transverse electromagnetic modes. Moreover, the system acts to *reduce* the transverse (betatron) oscillations of the beam, which corresponds to a reduction in the transverse (dipole) sideband power. The gain of the cooling system may be considered constant across the sidebands, and in the Debuncher, a recursive notch filter is used to reduce the noise from coupling to the longitudinal mode. A simplified illustration of the transverse notch filter, which has zeros at (i) the revolution harmonics and (i) between the sidebands, is given in Figure 4.4.

Transverse Recursive Notch Filter

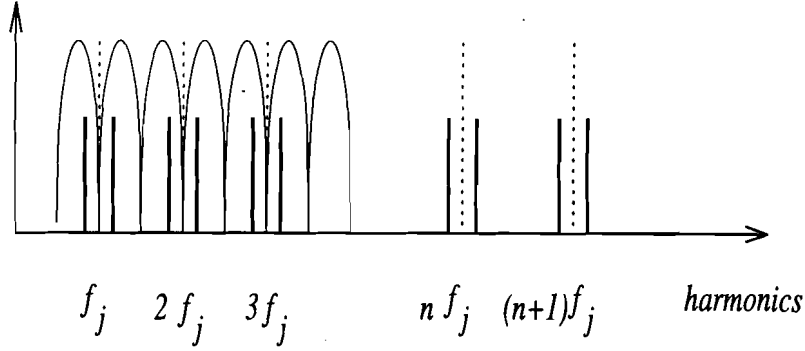


Figure 4.4: A simplified diagram of the ideal transverse recursive notch filter in frequency space.

The equation for transverse cooling, or equivalently, an expression for the change in the transverse emittance, consists of (i) the total electronic gain of the cooling system, g , (ii) the quantity $f_o/[\Delta f_n]$ proportional to the mixing factor, and (iii) the electronic noise, ρ .

$$\frac{1}{\tau} = \frac{W}{2N} \left[2g - g^2 \left(\frac{1}{n_l} \sum_n \frac{f_o}{\Delta f_n} + \rho \right) \right] \quad (4.5)$$

Equation (4.5) expresses the following physical relationships: (i) the cooling rate is proportional to the system bandwidth W , thus obviating the desire for large bandwidth systems, (ii) the cooling rate is *inversely* proportional to the number of particles N , thus expressing the fact that the larger the number of particles the slower the cooling rate, and (iii) there should exist an optimal cooling gain g_{opt} given by the extremum of the parabolic functional $\tau^{-1}(g)$.

4.3.3 Brief Description of Stochastic Cooling Hardware

In the Debuncher, there are three distinct stochastic cooling systems: the vertical, horizontal, and the longitudinal systems each with a 2-4GHz bandwidth. Each of the Debuncher stochastic cooling systems are operated below the optimal gain with the output power from the TWT amplifiers driven at saturation ($\sim 75\text{Watts/TWT}$). The *total* operating power of the systems is typically $\sim 1000\text{Watts}$, although during Run1B levels of $\sim 1300\text{Watts}$ had been achieved. Such power levels correspond to system gains between $\sim 90 - 100\text{dB}$. Presently, the transverse system reduces an

initial beam emittance of $17\pi\text{mm-mrad}$ to $4\pi\text{mm-mrad}$ over a production cycle time of $\approx 2.4\text{sec}$ ³, while the longitudinal system reduces $\Delta p/p \approx 0.3\%$ to $\Delta p/p \approx 0.17\%$.

Although possessing its own set of amplifiers and ancillary electronics, the longitudinal system derives signals from both the horizontal and vertical pickup arrays. Unlike the transverse systems, however, the longitudinal system is sensitive to particle momenta by summing the signals from the top and bottom loop coupler pairs. Subsequently, the signal is filtered and acts back upon the beam with both sets of transverse kickers, which are applied in sum mode. There are 128 loop coupler pickup pairs, which constitutes the particle signal detection system for the transverse stochastic cooling systems (and hence 256 pickup pairs used for the longitudinal system). The 128 pickup pairs are equally distributed between 6 *tanks* and are located in the D10-D20 straight sections. An exactly similar arrangement is used for the kicker arrays located in the D30-D40 straight sections.

Figure 4.5 is a simplified schematic of a transverse stochastic cooling system in the Debuncher. As indicated in Figure 4.5, signals from a particular pickup pair are *added* π out of phase. The microwave hybrid device is able to output either the Δ (difference) signal or the Σ (sum) signal. The signals from the 4 separate tanks are pre-amplified and phase adjusted before finally being combined. Phase adjustment between the combined stochastic cooling tanks is accomplished with a variable path length microwave device (trombone).

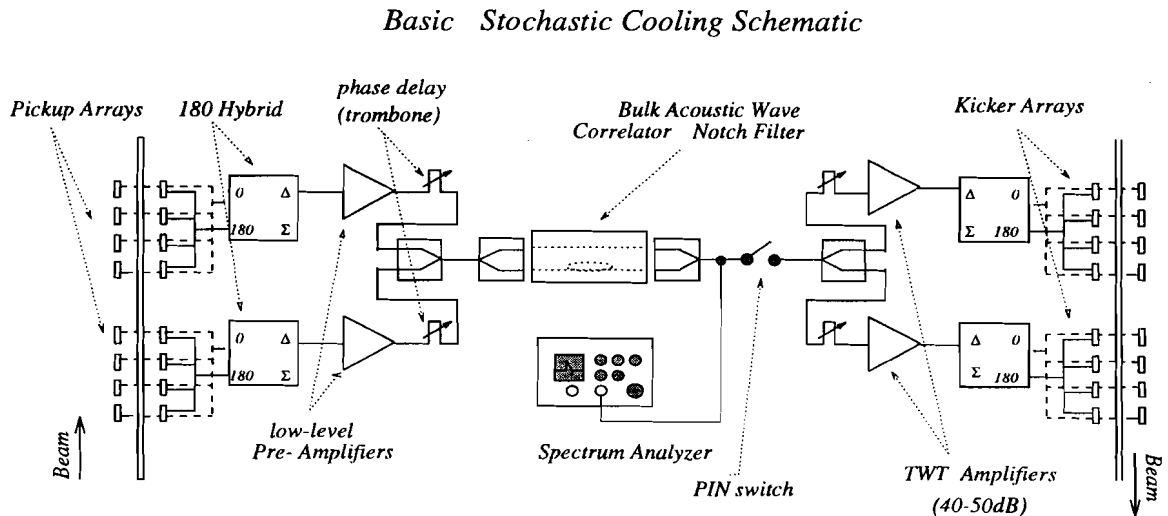


Figure 4.5: A basic schematic of a (transverse) stochastic cooling system in the Debuncher.

³This number does change depending upon the stack size, since it has been found that stack rate degradation must be compensated by longer cycle times

Once the pickup signals are combined, a correlator notch filter provides the proper gain shaping for stochastic cooling. In the case of the transverse system, the notch eliminates the revolution harmonic frequencies and also noise between the transverse sidebands, while in the longitudinal system the filter produces a notch in the center of the longitudinal distribution which has the proper gain and phase slope. A correlator notch filter, or equivalently, a recursive filter, works with the same principle of an interferometer, by splitting and recombining a signal between a short path length and a long path length. In the Debuncher, the long path length, or delay, is controlled by the use of a bulk acoustic crystal, which historically had their origin from the stringent requirements of radar systems. At the output of the notch filter is a point at which spectrum analyzer measurements may be made. The PIN switch is used for opening the cooling loop and may be triggered open/closed on any accelerator timing event.

4.4 Longitudinal Stochastic Cooling in the Debuncher

The momentum stochastic cooling system is designed to *increase the number density* of a particle beam in a storage ring about the central beam energy E_o . In the Debuncher, a correlator notch filter is used to *increase* the energy dependence of the gain $G(x)$, in order to reduce the Schottky noise at the kicker electrodes from particles at E_o . Thus the ideal momentum/filter stochastic cooling system should (i) have an electronic filter which has finite, *complex* gain $G(x)$ *except* at the center of the beam distribution $\Psi(x)$, corresponding to infinitesimally narrow notches at all revolution harmonics and with a zero crossing phase shift of π , and (ii) not introduce noise through intermodulation distortion. An idealization of the closed loop gain, assuming a flat phase response for the pickup and kickers, has been given in Equation (4.3) as $G(x) = -g[\sin[\tau x] + i(1/A - \cos[\tau x])]$.

4.4.1 The Fokker Planck Description

The *number density* of particles per energy shall be represented by $\Psi = dN/dE$. Moreover, it shall be useful to define the distribution function $\psi(x)$, which is defined through the energy difference $x = \Delta E = E - E_o$, and which is *independent of particle number*,

$$\Psi(x, t) = N\psi(x, t)$$

Under the action of a stochastic cooling system, the evolution of the longitudinal distribution function $\psi(x, t)$, is accurately described by the Fokker Planck equation⁴ and forms the basis for a computer model for the Debuncher systems, The longitudinal Fokker- Planck equation follows from Bisognano:

$$\frac{\partial \psi(x, t)}{\partial t} = - \frac{\partial \phi(x, t)}{\partial x} \quad (4.6)$$

$$\begin{aligned} \phi(x, t) = \sum_{m_1 \leq m \leq m_2} \left[\psi(x, t) \text{Real} \left[\frac{G_m(x)}{\epsilon_m(x, t)} \right] \right. \\ \left. - \psi(x, t) \frac{\partial \psi(x, t)}{\partial x} \frac{N \pi \beta^2 E}{2 \eta f_0} \frac{|G_m(x)|^2}{m |\epsilon_m(x, t)|^2} \left\{ 1 + \mathcal{U}_m(x, t) \right\} \right] \end{aligned} \quad (4.7)$$

The quantities appearing in Equations (4.6) and (4.7) are the following: (i) $\phi(x, t)$ is the conserved flux of particles, undergoing collisional interactions through the feedback loop, (ii) the sum is over all revolution harmonics, however the gain $G_m(x)$ is only finite within the cooling bandwidth W from $f = 2 - 4\text{GHz}$, (iii) $G_m(x)$ is the energy dependent gain function of the cooling loop at each m -th harmonic in units of GeV/sec, (iv) $\mathcal{U}_m(x, t)$ is the energy dependent noise/signal ratio at each m th harmonic during the cooling cycle, and which may be defined through the Schottky power $\Sigma(x, t)$, such that $\mathcal{U}_m(x, t) = \Sigma_{\text{noise}}/\Sigma_{\text{signal}}$ and may be written as $\mathcal{U}_m(x, t) \sim \Sigma_{\text{noise}}/\psi(x, t)$ (v) $\epsilon_m(x, t)$, is the signal suppression factor, or equivalently, the closed loop response function, at each m -th harmonic as a function of time, and (vi) the relationship between the energy and frequency is given by $x = \beta^2 E \Delta f_m / [\eta m f_0]$ for which $\Delta f_m = f - m f_0$. The constants of the machine are $f_0 = 0.590035 \times 10^6 \text{Hz}$, $\eta = .006$, $E_0 = 8.938 \text{GeV}$, $\gamma = 9.5287$, and $\beta = 0.989$, such that the energy variable $x = 2.469 \text{MeV-sec} \Delta f_m / m$. An expression for the signal suppression factor $\epsilon_m(x, t)$, is given

⁴In general, the character of a Fokker-Planck equation is results from an *approximation* of the Master equation (the Boltzmann equation with the full collision term): thus, given, $f(\mathbf{w}, t)$, full distribution function in the pair of canonical variables \mathbf{w} , and a collision operator $\Gamma[f]$:

$$\frac{df}{dt} = \frac{\partial f}{\partial t} + \mathbf{v} \cdot \nabla f - \nabla \Phi \cdot \frac{\partial f}{\partial \mathbf{v}} = \Gamma[f]$$

The Fokker Planck approximation is a truncation of $\Gamma[f]$ with a Taylor expansion:

$$\Gamma[f] \sim \frac{\partial}{\partial w_i} [f D] + \frac{\partial^2}{\partial w_i \partial w_j} [f D]$$

For complete discussions, the development appears in a wide array of contexts: Reichl - *Modern Statistical Mechanics* [80], Binney and Tremaine - *Galactic Dynamics* (p.506) [3], Ichamaru - *Statistical Plasma Physics* [49], Stix - *Nonlinear Waves in Plasma* [91].

by the dispersion relation:

$$\epsilon_m(x, t) = 1 + \frac{N\pi \beta^2 E}{m 2\eta f_o} G_m(x) \int \frac{\partial \psi(x', t)}{\partial x'} \frac{dx'}{(x - x') + i\eta} \quad (4.8)$$

The first term in Equation (4.7) represents the cooling - self interaction through the feedback loop, and involves the effect of the closed feedback loop through the signal suppression, $\epsilon_m(x, t)$. The second term of Equation (4.7) represents the diffusive - two particle interaction term. In Equation (4.7) and (4.8), the gain $G_m(x)$ passes through zero at $x = 0$, and has a phase shift of π , which is a feature of the recursive filter. The effect is to increase the density by reducing the large energy deviation of particles at the tails of the distribution function. Therefore, one expects for an initial distribution ψ_o at $t = 0$, $G(x) \approx -x$, and $\lambda(t) > t$ for $t > 0$, then $\psi(x, t) \sim \lambda(t)\psi_o[\lambda(t)x]$, which is the statement that density increases and thus the beam width decreases.

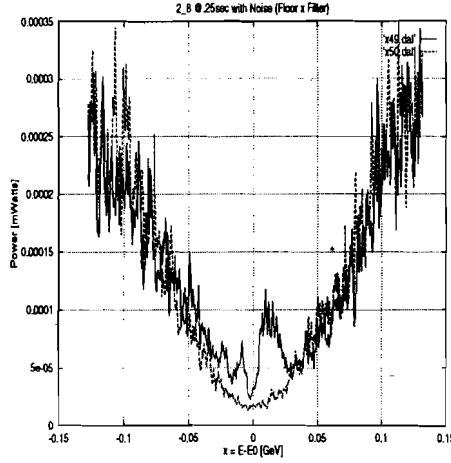
Competing with the cooling process is a nonlinear diffusion effect resulting from the scattering from other particles in the beam through the feedback loop. The general character of the *nonlinear* diffusion equation is $\frac{\partial}{\partial x} \left[\gamma(x) \psi(x) \frac{\partial \psi}{\partial x} \right]$, in which the sum over the gain and the suppression factor have been grouped in a function $\gamma(x)$. A comparison of *non-linear* diffusion, to *linear* diffusion, $\frac{\partial}{\partial x} \left[\gamma(x) \frac{\partial \psi}{\partial x} \right]$ shows that the product $\psi(x) \frac{\partial \psi}{\partial x}$, constituting the Schottky heating, has the effect of diffusing particles closer to the beam centroid and acting less upon particles further in the tails of the distribution. In the present Debuncher cooling systems, the thermal noise $\mathcal{U}_m(x, t)$ is quite large and dominates the diffusion effects. Furthermore, in the aforementioned formulation, external diffusion arising from intrabeam scattering are negligible and therefore omitted.

4.4.2 Schottky Signals at Microwave Frequencies

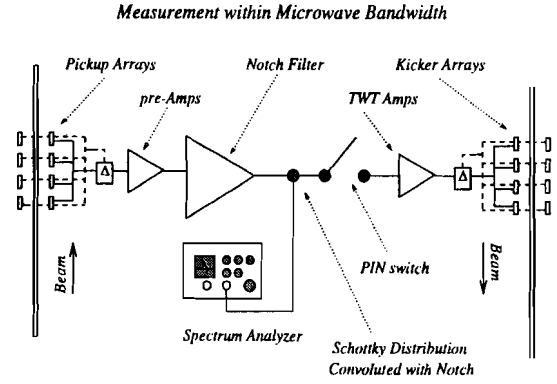
Inputs to the Fokker Planck transport Equations (4.6) and (4.7), may be provided from a number of measurements, which occupy the remainder of this section. Specifically, observation of Schottky signals within the microwave bandwidth of the cooling systems may be used to provide information about (i) the beam properties, (ii) a direct measure of the noise/signal ratio, (iii) the signal suppression, which in turn may be used to extract $G_{\parallel}^m(x)$, and (iv) open loop network analyzer measurements, which are also used to extract $G_{\parallel}^m(x)$. More specifically, a detailed time integration of the longitudinal Fokker Planck equation for momentum stochastic cooling requires knowledge of: (i) the full system gain in G_{\parallel}^m in [MeV/sec] at each harmonic m , (ii) a characterization of the filter

function in terms of gain slope τ in $[1/\text{MeV}]$, (iii) the beam width σ in $[\text{MeV}]$ and strength in Watts, (iv) the notch center at each harmonic in $[\text{MeV}]$.

Figure 4.6(a) is a typical spectrum analyzer Schottky signal measurement taken at the point depicted in Figure 4.6(b). The measured spectra was taken at 2.8GHz with and without beam. Thus, the noise baseline, may be used to obtain the convexity τ , or equivalently, the gain slope, of the notch filter from Equation (4.3).



(a) Longitudinal measurement with/without beam at 2.8GHz.



(b) Simplified diagram of stochastic cooling system indicating the point at which the spectrum is measured.

Figure 4.6: Configuration for the longitudinal spectrum analyzer measurement.

The spectrum analyzer measurement of Figure 4.6(a) is the power at the output of the notch filter, P_{out} . For an input Schottky beam power density $[\text{Watt/Hz}]$ $\mathcal{P}_{\text{in}}^{\text{beam}} = \Sigma(x)\Sigma^*(x)$ and an input noise power $\mathcal{P}_{\text{in}}^{\text{noise}} = I(x)I^*(x)$,

$$\mathcal{P}_{\text{out}} = |G(x)|^2 \otimes \left[\mathcal{P}_{\text{in}}^{\text{beam}} + \mathcal{P}_{\text{in}}^{\text{noise}} \right] \quad (4.9)$$

$$= \mathcal{P}^{\text{signal+noise}} \quad (4.10)$$

Equation (4.9) expresses the fact that the observed power is just the convolution of the gain (squared) transfer function with the input beam power, consisting of both $(\mathcal{P}_{\text{in}}^{\text{beam}})$ and the noise floor power $(\mathcal{P}_{\text{in}}^{\text{noise}})$. Using Equation (4.9), the specific model used for fitting the observed longitudinal Schottky spectra follows from two choices: (i) the Schottky beam voltage signal is taken as a simple Gaussian $\Sigma(x) = \exp\left[-\frac{(x-x_0)^2}{2\sigma^2}\right]$, and (ii) a voltage gain function $G(x) = -g\left[\sin[\tau x] + i(1/A - \cos[\tau x])\right]$, which

is the simple model for a recursive notch filter. The observed power and the noise power may be used for obtaining fundamental quantities of the system. Thus, Equation (4.11) is the *output signal + the noise power*

$$\begin{aligned} \mathcal{P}_{\text{out}} = & \beta_s \exp\left[-\frac{(x - x_s)^2}{2\sigma^2}\right] \left[\sin^2\{\tau x\} + \left(\frac{1}{A} - \cos\{\tau x\}\right)^2 \right] \\ & + \beta'_s \left[\sin^2\{\tau x\} + \left(\frac{1}{A} - \cos\{\tau x\}\right) \right] + \lambda \end{aligned} \quad (4.11)$$

while the *output noise power* is given in Equation (4.12).

$$\mathcal{P}_{\text{noise}} = \beta_n \left[\sin\{\tau x\} \right]^2 + \left[\frac{1}{A} - \cos\{\tau x\} \right]^2 + \lambda \quad (4.12)$$

The free parameters appearing within the simple models of (4.11) and (4.12) for \mathcal{P}_{out} and $\mathcal{P}_{\text{noise}}$, respectively, are (i) x_s is the beam center at the m th harmonic, (ii) x_N is the center of the recursive notch at the m th harmonic, (iii) σ is the beam width, (iv) τ is the curvature and thus the depth of the notch, (v) λ is a simple offset. In fixing a few of the parameters, especially those associated with the notch center and the notch width, fits to the the noise spectrum were made without beam, and (vi) although written separately for the model, the linear parameters $\beta'_s = \beta_n$, and thus, fits for β_s and β_n provide information about the *noise to signal ratio*. With a standard nonlinear least square fitting routine [40], free parameters may be extracted from the Schottky measurements.

4.4.3 Longitudinal thermal noise: $\mathcal{U}_{\text{therm}}^{\parallel}$

From the Schottky power measurements and the models of section 4.4.2 for $\mathcal{P}_{\text{signal} + \text{noise}}$ and $\mathcal{P}_{\text{noise}}$, a parameterization can be used in the computer code. The longitudinal thermal noise/signal ratio is given by $\mathcal{U}_{\text{therm}}^{\parallel} = \mathcal{P}_{\text{noise}}/\mathcal{P}_{\text{signal}}$. In particular from the simple model of section 4.4.2, the expression for $\mathcal{U}_{\text{therm}}^{\parallel}$ may be written in terms of the fitted parameters. Thus, the two quantities which are directly measurable have been given by Equations (4.11) and (4.12),

$$\begin{aligned} \mathcal{P}_{\text{signal} + \text{noise}} = & \left[\beta_s \exp[-x^2/\sigma^2] + \beta'_s \right] |G(x)|^2 + \lambda_s \\ \mathcal{P}_{\text{noise}} = & \beta_n |G(x)|^2 + \lambda_n \end{aligned}$$

in which λ_s and λ_n are offsets, and $\beta'_s \approx \beta_n$. From these expressions the signal power $\mathcal{P}_{\text{signal}}$ is

$$\mathcal{P}_{\text{signal}} = \left[\beta_s \exp[-x^2/2\sigma^2] + \right] |G(x)|^2 \lambda_s - \lambda_n \quad (4.13)$$

The thermal *noise/signal* $\mathcal{U}_{\text{therm}}^{\parallel}$ is obtained from Equation (4.13), thus,

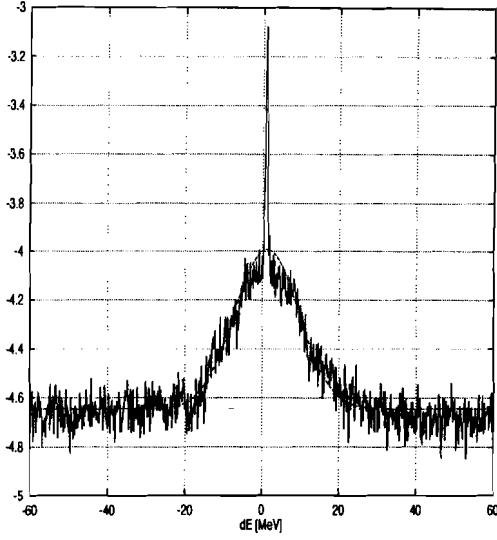
$$\mathcal{U}_{\text{therm}}^{\parallel}(x, t) \approx \left[\frac{\beta_n + \lambda_n}{\beta_s \sqrt{2\pi}\sigma(t)\psi(x, t) + (\lambda_s - \lambda_n)} \right] \quad (4.14)$$

In Equation (4.14), $\mathcal{U}_{\text{therm}}^{\parallel}(x, t)$ has been written directly in terms of the dimensionless quantity $\sqrt{2\pi}\sigma(t)\psi(x, t)$, which is obtained at each time step within the Fokker Planck calculation. Furthermore, from the expression for the thermal noise, outside the distribution, $\lim_{x \rightarrow \pm\infty} \mathcal{U}_{\text{therm}}^{\parallel} \rightarrow \infty$ expressing the fact that without coherence through the feedback loop, the dominant effect is diffusive heating of the distribution.

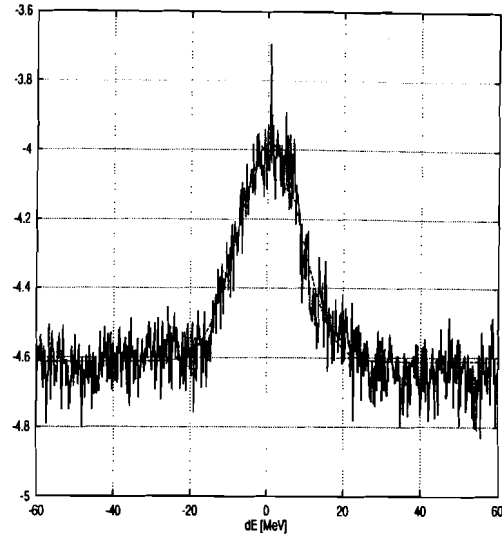
4.4.3.1 The Fits

For obtaining the linear parameters, β_s and β_n for $\mathcal{U}_{\text{therm}}^{\parallel}(x, t = 0)$ in Equation (4.14), fits are made in the following manner: (i) utilize simple Gaussian fits to the longitudinal Schottky at the 127th harmonic (from the 79MHz Schottky detector *outside* the cooling loop), for extracting the beam width σ , (ii) constrain the gain function $G(x)$, by fitting for the noise spectra $\mathcal{P}^{\text{noise}} = G(x, \tau) \otimes \mathcal{I}(x)$. for the convexity τ , and (iii) using the specific models given in Equations (4.11) and (4.12), for $\mathcal{P}_{\text{signal+noise}}$ and $\mathcal{P}_{\text{noise}}$, respectively, determine parameterization required of $\mathcal{U}_{\text{therm}}^{\parallel}$.

A fit to the beam width σ is obtained from the measurements of the 127th longitudinal Schottky signal. Figure 4.7(a) and (b), are fits to the longitudinal Schottky spectra at the beginning of the cycle (at $\Delta t = 0.2\text{sec}$ with beam width $\sigma = 8.315\text{MeV}$) and for $\Delta t = 1.0\text{sec}$ (with beam width $\sigma = 8.13\text{MeV}$), respectively. The spike in Figure 4.7(a) is the result of the slow de-coherence associated with bunch rotation.



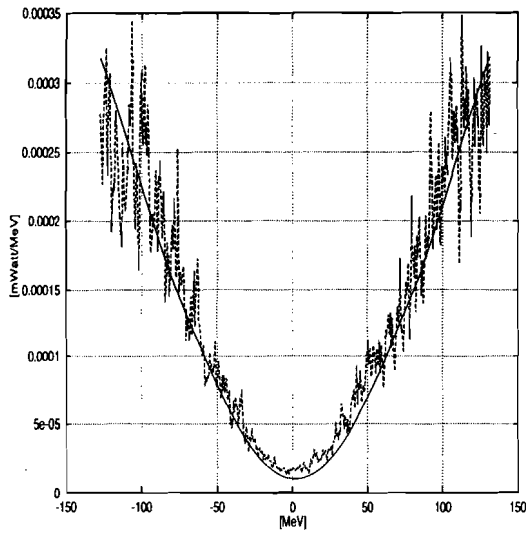
(a) Beam spectra at 127th harmonic in dBm,
 $\Delta t = 0.1\text{sec}$, $\sigma = 8.32\text{MeV}$



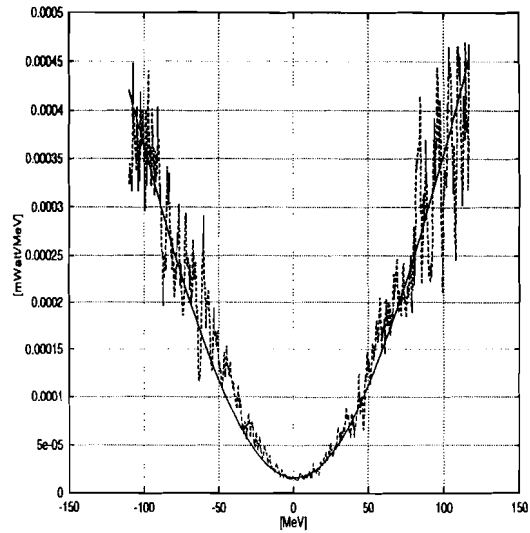
(b) Beam spectra at 127th harmonic in dBm,
 $\Delta t = 1.0\text{sec}$, $\sigma = 8.13\text{MeV}$

Figure 4.7: Fits to the longitudinal beam Schottky spectra at the 127th revolution harmonic.

The fits to the noise spectra $\mathcal{P}_{\text{noise}}$ (no beam) at 2.8GHz and 3.2GHz are given in Figures 4.8(a) and (b), respectively. From the fits the value of the convexity is given by $\langle \tau \rangle = 2.58 \times 10^{-2}\text{MeV}^{-1}$.



(a) Noise spectra at 2.8GHz



(b) Noise spectra at 3.2GHz

Figure 4.8: Fits to the longitudinal noise spectra downstream from the notch filter.

Utilizing the fixed parameters τ , and σ , fits to $\mathcal{P}_{\text{signal}+\text{noise}}$ were made at several harmonics within the microwave bandwidth. Figures 4.9(a) and (b) are representative fits to the data at 2.8GHz and 3.2GHz, respectively.

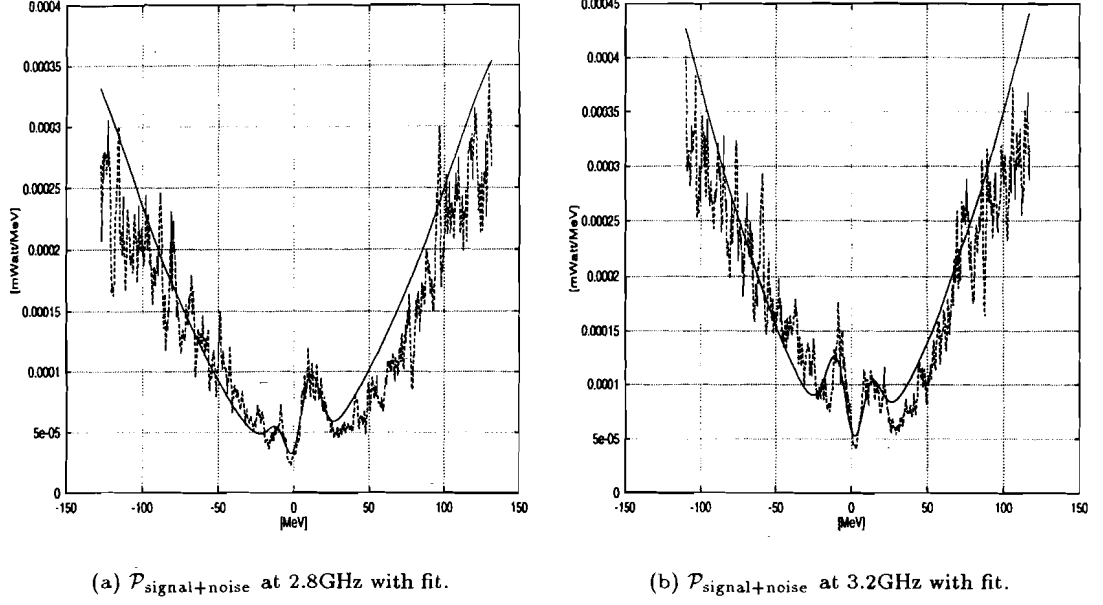


Figure 4.9: Fits to the longitudinal beam spectra $\mathcal{P}_{\text{signal}+\text{noise}}$ in the microwave bandwidth.

A summary of the results for the linear parameter fits β_s and β_n (Equations (4.11) and (4.12)) at two frequencies in the cooling bandwidth, with $\tau = 0.0198\text{MeV}^{-1}$ and $\sigma = 8.645\text{MeV}$, is given in Table 4.1.

$$\mathcal{U}_{\text{therm}}^{\parallel}(x, t) \approx \left[\frac{\beta_n + \lambda_n}{\beta_s \sqrt{2\pi}\sigma(t)\psi(x, t) + (\lambda_s - \lambda_n)} \right]$$

Table 4.1: Summary of fitted parameters for $\mathcal{U}_{\text{therm}}^{\parallel}(x, t)$.

Frequency[GHz]	$\beta_s[\text{mWatt/Hz}]$	$\beta_n[\text{mwatt/Hz}]$	$\lambda_s[\text{mWatt/Hz}]$	$\lambda_n[\text{mWatt/Hz}]$
2.8	0.18×10^{-2}	0.70×10^{-4}	0.33×10^{-4}	0.10×10^{-4}
3.2	0.26×10^{-2}	0.19×10^{-3}	0.53×10^{-4}	0.16×10^{-4}

The parameterization resulting from the fits to $\mathcal{P}_{\text{signal}}$ and $\mathcal{P}_{\text{noise}}$ allow a determination of $\mathcal{U}_{\text{therm}}^{\parallel}$ as given previously in Equation (4.14). Figure 4.10 is a plot of the experimentally determined

parameterization, which has been subsequently employed within the Fokker Planck model calculation for predicting the evolution of the particle distribution function.

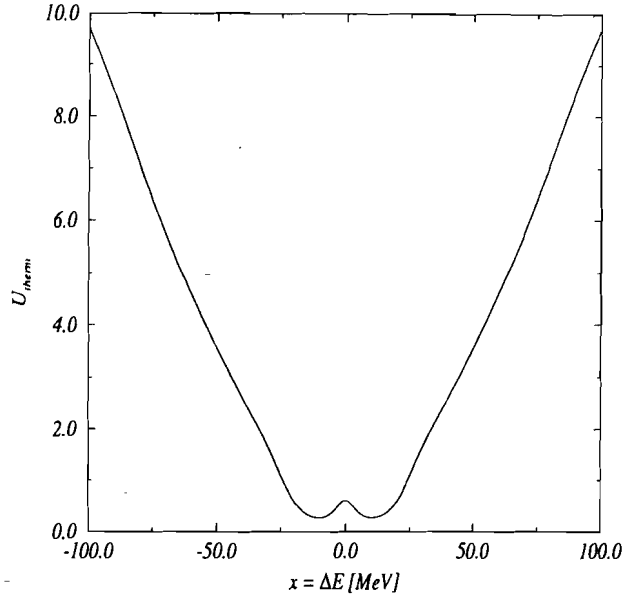


Figure 4.10: The parameterization of $U_{\text{therm}}^{\parallel}$ which is used in the Fokker Planck calculation.

4.4.4 Signal Suppression $\epsilon_{\parallel}(x)$ & $\langle G_{\parallel} \rangle$

Signal suppression measurements provide a means for extracting the stochastic cooling system gain $G(x)$ using nonlinear fitting models. A description of signal suppression, or equivalently, the closed loop gain factor, follows from standard treatments of controls theory for feedback systems. Figure 4.11 is a simplified diagram of the stochastic cooling feedback system, together with the beam which *closes the loop*. The quantities appearing in the illustration are (i) $B(\omega)$, which is the frequency (energy) dependent *beam response function*, (ii) ψ_p , which is the beam signal at the pickup including the modulations of the feedback signal, (iii) V_d and V_k , the voltages at the Schottky detector and kicker respectively, and (iv) $G(\omega)$, which is the frequency (energy) dependent gain function.

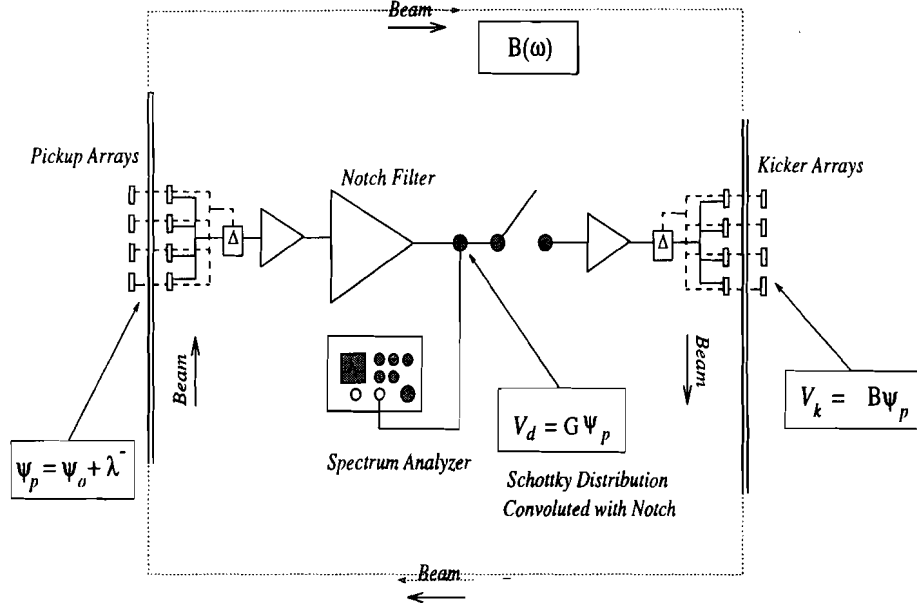


Figure 4.11: A simplified diagram of the stochastic cooling feedback system used for defining signal suppression.

The simplified *derivation* of signal suppression ϵ was first performed by Sacherer [87] and follows from a controls theory analysis. Referring to the quantities in Figure 4.11, the beam signal at the pickup ψ_{pu} is modified by modulations induced on the beam by the kicker $\lambda = BV_k$. Since $V_k = G\psi_{pu} = G\psi_o + BG V_k$, the following expression may be found for λ :

$$\lambda = \left[\frac{BG}{1 - BG} \right] \psi_o$$

Therefore, the expression for the signal at the detection point is

$$V_d = \frac{\psi_o G}{1 - BG}$$

for which the denominator is identified as the signal suppression factor:

$$\epsilon = 1 - BG = \frac{V_{\text{open}}}{V_{\text{closed}}}$$

The equation for ϵ is an operator expression for the dispersion relation written previously

$$\epsilon_m = 1 + \frac{N\pi}{m} \frac{\beta^2 E}{\eta f_o} G_m(x) \int \frac{\partial \psi(x')}{\partial x'} \frac{dx'}{(x - x') + i\eta}$$

As indicated, the signal suppression is obtained directly from the open and closed loop Schottky power such that $\mathcal{P}_{\text{open}}/\mathcal{P}_{\text{closed}} = |\epsilon|^2$. The expression for $|\epsilon|^2$ follows from the observation

that the open loop Schottky signal mirrors the beam distribution in frequency (energy) space $\mathcal{P}_{\text{open}} = \psi_o(x)$, whereas the closed loop Schottky signal necessarily contains the effect of the feedback system, such that $\mathcal{P}_{\text{closed}} = \psi_o(x)/|\epsilon|^2$.

4.4.4.1 Experimental Extraction of G_{\parallel}

The procedure for extracting the gain is as follows: (i) make open and closed loop Schottky measurements at several revolution harmonics within the cooling bandwidth; (ii) construct the quantity $|\epsilon_m(x)|^2$ directly from the measured Schottky signals Σ_{open} and Σ_{closed} , respectively; and (iii) perform a nonlinear least square fit to $|\epsilon_m(x)|^2$ based upon the definition written in terms of the *unknown* gain constant (G_{\parallel}) and other *known* machine constants.

As depicted in Figure 4.11, the detection of the Schottky signals is at the output of the notch filter, but before the PIN switch. After the PIN switch there is an additional $\sim 40 - 50\text{dB}$ of gain provided by TWT amplifiers. Both open and closed loop Schottky signals, just after the notch filter, may be made by gating the PIN switch for times long enough for a single sweep of the spectrum analyzer (typically $\sim 100 - 200\text{msec}$).

With the complex gain $G_m = G_{\Re}^{(m)} + iG_{\Im}^{(m)}$, the expression for ϵ at the m th revolution harmonic in the cooling bandwidth is written in terms of the *real* part, ϵ_{\Re} , and *imaginary* part, ϵ_{\Im} .

$$\epsilon_{\Re}^{(m)} = 1 + \frac{N\pi\beta^2 E}{m\eta f_0} \left[\pi G_{\Re}^{(m)} \frac{\partial\psi}{\partial x} + G_{\Im}^{(m)} PV \int \frac{\partial\psi}{\partial x'} \frac{dx'}{x-x'} \right] \quad (4.15)$$

$$\epsilon_{\Im}^{(m)} = \frac{N\pi\beta^2 E}{m\eta f_0} \left[\pi G_{\Im}^{(m)} \frac{\partial\psi}{\partial x} - G_{\Re}^{(m)} PV \int \frac{\partial\psi}{\partial x'} \frac{dx'}{x-x'} \right] \quad (4.16)$$

In particular, the gain function at each harmonic $G_m(x; \tau_m)$ in terms of the gain slope τ_m , and the beam distribution $\psi(x; \sigma)$, in terms of the beam width σ are given by

$$G_m(x; \tau) = -g_m \left[\sin[\tau_m x] + i(1 - \cos[\tau_m x]) \right] \quad (4.17)$$

$$\psi(x; \sigma) = A \exp[-(x - x_o)^2 / 2\sigma^2] \quad (4.18)$$

Fits to the beam distribution parameters were obtained from the longitudinal spectra at the 127th harmonic. The results of the beam distribution fits to Equation (4.18) may be summarized as follows, (i) the beam distribution center $x_o = 1.19 \pm .08\text{MeV}$ and (ii) the beam width $\sigma = 8.635 \pm .103\text{MeV}$. Spectrum analyzer measurements of the baseline noise, obtained without beam,

at a point in the feedback circuit downstream of the notch filter, provide a determination of the gain slope in the equation with fits to $G_m(x; \tau_m)$. Results of fitting τ_m with Equation (4.17) were given in the previous section and found to be $\tau_m \sim \tau = 2.503 \times 10^{-2} \text{MeV}^{-1}$ across the cooling system bandwidth.

Since the free parameters σ , x_o , and τ may be found from independent measurements of the distribution function and the noise spectra, respectively, only one free parameter is required for extracting $\langle G_{\parallel}^m \rangle$ from $|\epsilon(x)|^2$. From Equations (4.15) and (4.16) for ϵ_{\Re} and ϵ_{\Im} , respectively,

$$|\epsilon_m(x; \alpha, \tau, \sigma)|^2 = \left\{ 1 + \alpha \left[\pi g_{\Re} \frac{d\psi}{dx} + g_{\Im} PV \int \frac{\partial \psi}{\partial x'} \right] \right\}^2 + \left\{ \alpha \left[\pi g_{\Im} \frac{d\psi}{dx} - g_{\Re} PV \int \frac{\partial \psi}{\partial x'} \right] \right\}^2 \quad (4.19)$$

Specifically, the gain at each revolution harmonic m is found through the relationship

$$\alpha = \frac{N\pi\beta^2 E}{m\eta f_0} \langle G_{\parallel}^m \rangle$$

4.4.4.2 Fits and Results

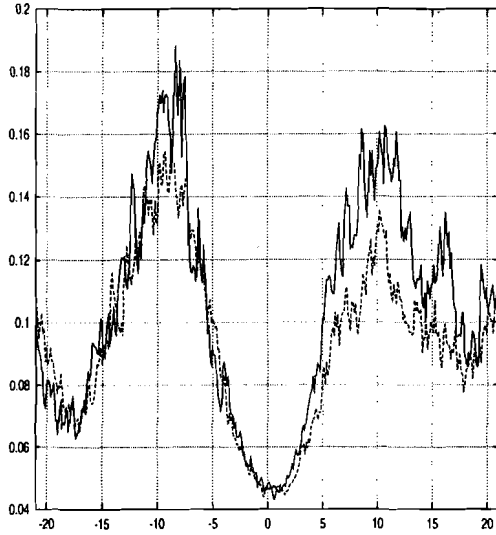
Extracting the gain, $\langle G_{\parallel}^m \rangle$, from fits to $|\epsilon_m(x; \alpha, \tau, \sigma)|^2$ is summarized as follows: (i) at a sideband in the cooling frequency band, measure the signal suppression $\epsilon(x, t)$ measuring the open and closed loop Schottky signals; (ii) measure the beam distribution at the 127th harmonic and perform simple Gaussian fits for the beam width σ from $\mathcal{P} = A_{\text{norm}} \exp[-(x - x_o)^2/\sigma^2]$; (iii) obtain the gain slope τ of the cooling system by fitting the noise power spectrum at each harmonic in the cooling system bandwidth to $G_m(x) = -g_m \left[\sin[\tau_m x] + i(1 - \cos[\tau_m x]) \right]$ and (iv) using Equations (4.15), and (4.16), for ϵ_{\Re} , ϵ_{\Im} , respectively, the magnitude $|\epsilon|^2$ is fit for α defined through Equation (4.19).

The result of three sets of signal suppression data at 3.2GHz ($m = 5423$) are given in Figures 4.12, with trigger times 0.15sec, 0.25sec, and 0.35sec, respectively for determining $\langle G_{\parallel} \rangle$. For each measurement, it is expected that α , and therefore $(G_{\parallel})_m = \alpha \times \left[m\eta f_0 / [\pi N \beta^2 E] \right]$, be constant, as the value of σ and A_{norm} change due to longitudinal cooling. Thus, these measurements provide consistency checks between the fitting procedure for $|\epsilon(x; \alpha)|^2$ and independent measurements of the beam parameters from the longitudinal Schottky measurements outside the cooling band.

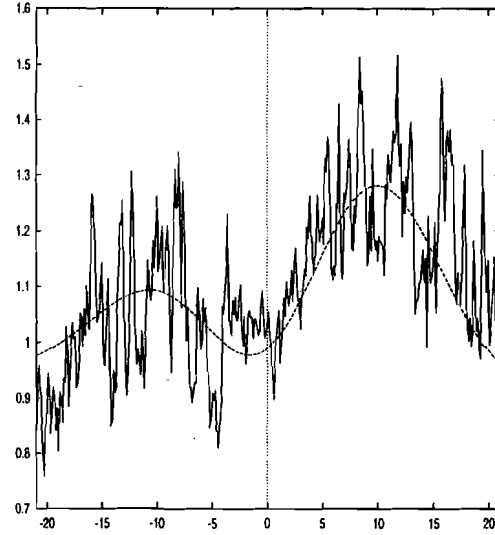
Figure 4.12(a) is a plot of the the open and closed loop Schottky signal measurements obtained at 3.2GHz and triggered at 0.15sec after beam is injected into the Debuncher. As previously described, the open loop measurement is made by gating the PIN switch open for ~ 200 msec corresponding to the sweep time of the spectrum analyzer measurement. The resulting signal suppression $|\epsilon(x; \alpha)|^2$ and the associated model fit for α given by Equation (4.19) is given in Figure 4.12(b). The value of the free fitting parameter in this expression is $\alpha = 8.89 \pm .026$, and therefore the gain is given by

$$(G_{\parallel})_m = \frac{m}{N\pi} \frac{\alpha}{k} = \frac{5423}{4.5 \times 10^7 \pi} \frac{1}{2.25 \text{MeV}^{-1}} \alpha \text{sec}^{-1} \quad (4.20)$$

which corresponds to $(G_{\parallel})_m = 8.73 \times 10^{-4} \text{MeV/sec}$.



(a) Open and closed loop Schottky spectra (mWatts/MeV) versus energy (MeV).



(b) Ratio $|\epsilon(x; \alpha)|^2$ with $(G_{\parallel})_m = 8.73 \times 10^{-4} \text{MeV/sec}$.

Figure 4.12: (a) Comparison of the open and closed loop measurements, and (b) the resulting signal suppression $|\epsilon|^2$ at 3.2GHz at 0.1sec.

Similar to the above plots, Figure 4.13(a) is a plot of the the open and closed loop Schottky signal measurements obtained at 3.2GHz but triggered at 0.25sec after beam has been injected into

the Debuncher. The resulting signal suppression $|\epsilon(x; \alpha)|^2$ and the associated model fit for α are given in Figure 4.13(b). The value of the fitting parameter in this expression is $\alpha = 8.79 \pm .047$, which corresponds to $(G_{\parallel})_m = 8.64 \times 10^{-4} \text{MeV/sec}$.

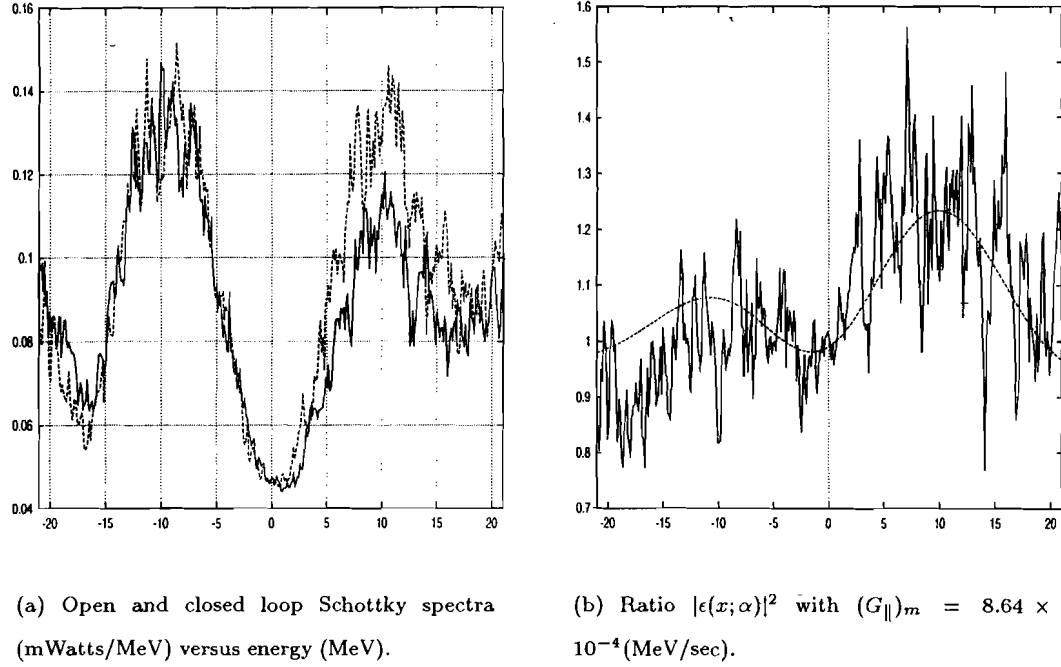


Figure 4.13: (a) Comparison of the open and closed loop measurements, and (b) the resulting signal suppression $|\epsilon|^2$ at 3.2GHz at 0.25sec.

With a trigger time of 0.35sec after injection, Figure 4.14(a) is a plot of the the open and closed loop Schottky signal measurements obtained at 3.2GHz. The resulting $|\epsilon|^2$ and the associated model fit for $\alpha = 8.57 \pm 0.042$ is given in Figure 4.14(b). The fit corresponds to $(G_{\parallel})_m = 8.54 \times 10^{-4} \text{MeV/sec}$.

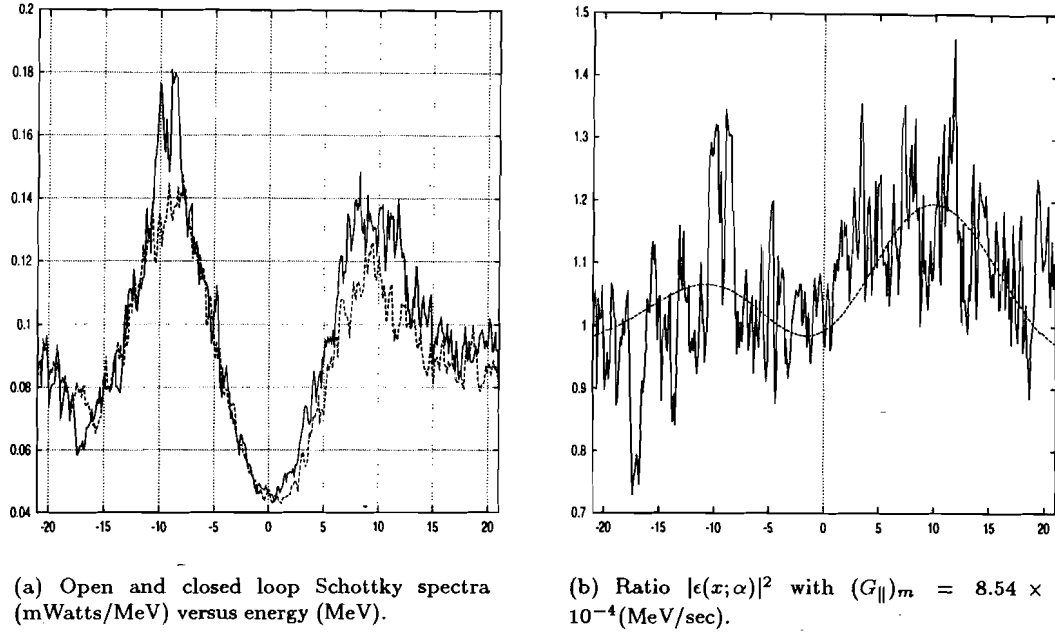


Figure 4.14: (a) Comparison of the open and closed loop measurements, and (b) the resulting signal suppression $|\epsilon|^2$ at 3.2GHz at 0.3sec.

A summary of the results for extracting $(G_{||})_m$ given in Figures 4.12 through 4.14 is given in Table 4.2.

Table 4.2: Experimental Fits to $\langle G_{||} \rangle$.

Δt	α	$\langle G_{ } \rangle N = 4.0 \times 10^7$
0.15 sec	9.89 ± 0.02	$8.73 \times 10^{-4} \text{MeV/sec}$
0.25 sec	8.79 ± 0.03	$8.64 \times 10^{-4} \text{MeV/sec}$
0.35 sec	8.57 ± 0.03	$8.54 \times 10^{-4} \text{MeV/sec}$

Measurements of signal suppression were difficult to extract at other frequencies across the microwave cooling bandwidth. Therefore, independent measurement at other frequencies shall be provided through network analyzer measurements, which is taken up in the next section.

4.4.5 Longitudinal Open-loop transfer function measurements

Signal suppression measurements provide an experimental procedure for extracting the magnitude of the system gain $\langle G_{||} \rangle$. Another technique for extracting the gain is through direct excitation of the beam through the stochastic cooling system with open loop network analyzer measurements.

Open loop transfer function measurements are the most direct means for obtaining the system gain and phase. Figure 4.15 is a simplified diagram indicating the experimental setup for Debuncher stochastic cooling *open loop network analyzer measurements* for obtaining the S_{21} transfer matrix element, defined as the signal input power to the output signal power, as a function of frequency

$$S_{21}(\Delta f) = \left[\frac{\mathcal{P}_{\text{in}}(\Delta f)}{\mathcal{P}_{\text{out}}(\Delta f)} \right] \quad (4.21)$$

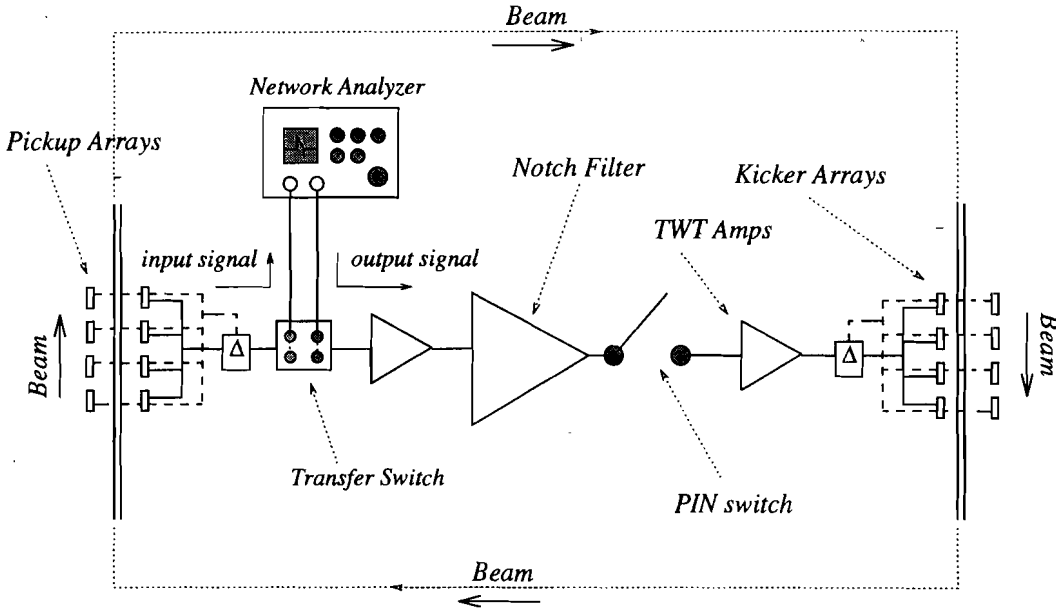


Figure 4.15: Experimental Arrangement for the network analyzer beam transfer function measurements.

The S -parameter matrix element S_{21} consists of (i) the notch filter transfer function, $N(\omega)$, (ii) the beam transfer function [21], [10], $B(\omega)$, and (iii) the pickup and kicker transfer function $P(\omega)$ which is constant across the operating frequency bandwidth. Thus, the expression for S_{21}

$$S_{21}(\omega) = N(\omega) \otimes B(\omega) \otimes P(\omega) \quad (4.22)$$

In terms of (i) the energy difference $x = \beta^2 E / m\eta(df/f_0)$, (ii) an explicit integral expression for the *longitudinal beam response function* $B(x)$, and (iii) the total transfer function of the cooling system $G(x) = N(x)P(x)$, the longitudinal S_{21} parameter is given by:

$$(S_{\parallel}^m)_{21}(x) = \bar{\kappa} G_m(x) \left[iPV \int \frac{\partial \psi(x')}{\partial x'} \frac{dx'}{x - x'} + \pi \frac{\partial \psi(x')}{\partial x'} \right] \quad (4.23)$$

Specifically, Equation (4.23) consists of the quantities $G_m(x)$ which is the gain at the m th revolution harmonic, ψ , which is the beam (energy) distribution and normalized to the total number of particles, and the constant $\bar{\kappa} = N\pi\beta^2 E/\eta f_0$.

For extracting the gain, fits are performed to the magnitude of S_{21} given from (4.23) by

$$|(S_{21}^m)(x)| = \bar{\kappa}G \left\{ \left[\pi g_r(x, \tau) \frac{\partial \psi(x, \sigma)}{\partial x'} + g_i(x, \tau) PV \int \frac{\partial \psi}{\partial x'} \frac{dx'}{x - x'} \right]^2 + \left[g_r(x, \tau) PV \int \frac{\partial \psi(x, \sigma)}{\partial x'} \frac{dx'}{x - x'} + \pi g_i(x, \tau) \frac{\partial \psi}{\partial x'} \right]^2 \right\}^{1/2} \quad (4.24)$$

As before the gain $G(x; \tau)$ and the beam distribution $\psi(x; \sigma)$ take on a simple form,

$$G(x, \tau) = g_r(x, \tau) + i g_i(x, \tau) = \sin(\tau x) + i(1 - \cos(\tau x)) \quad (4.25)$$

$$\psi(x; \sigma) = 1/[\sqrt{2\pi}\sigma] \exp[-x^2/\sigma^2] \quad (4.26)$$

in which ψ has been normalized to the total number of particles and the free parameters τ and σ

may be fit independently of Equation (4.23) for S_{21} . Therefore, the only free parameter in Equation (4.24) is the gain G .

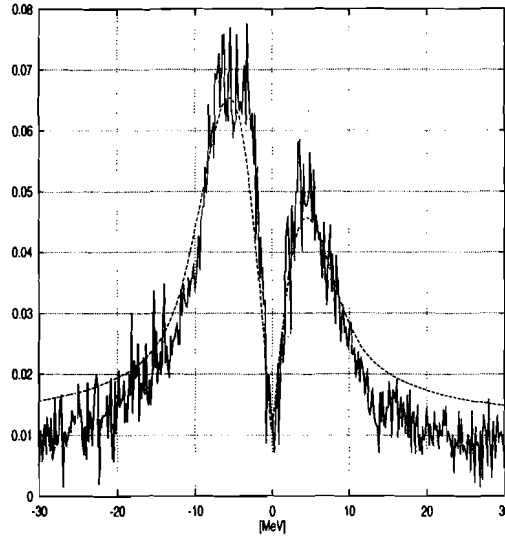
4.4.5.1 Experimental Results

The open loop network analyzer measurements through the stochastic cooling feedback system were performed by allowing the unbunched, $I \sim 2 \mu\text{Amp}$ antiproton beam to circulate for several minutes. Narrow frequency measurements, $\Delta f \sim 100\text{kHz}$, were made at three revolution harmonic frequencies across the cooling system bandwidth, corresponding to 2.1GHz, 3.0GHz, and 3.8GHz. From independent measurements of the notch filter with no beam, it was found that across the cooling system bandwidth the gain slope $\tau = 2.503 \times 10^{-2} \text{MeV}^{-1}$. For each measurement, a new pulse of antiprotons were injected into the Debuncher, and thus the beam distribution for each S_{21} measurement was saved, fit for σ , and used in the fits of $|S_{21}|$ for extracting the gain.

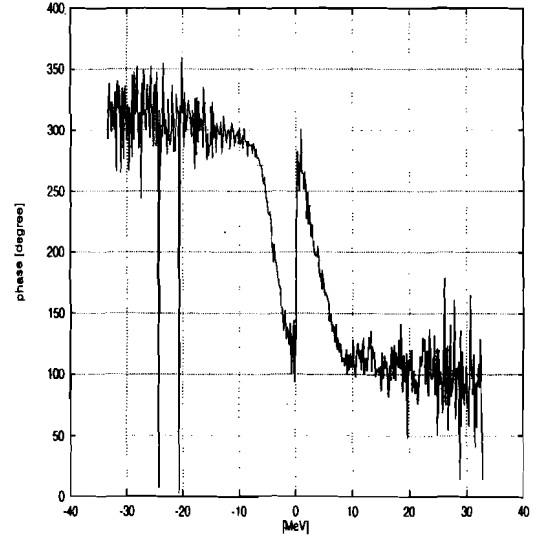
Fits to the magnitude $|(S_{\parallel}^m)_{21}|$ at 2.1GHz is given in Figure 4.16(a). The corresponding $(S_{\parallel}^m)_{21}$ phase response is given in Figure 4.16(b). For performing the fits to $|(S_{\parallel}^m)_{21}|$ in 4.16(a) the corresponding longitudinal Schottky beam distribution is given in Figure 4.17, with a $\sigma = 3.377\text{MeV}$. The free parameter of equation $|(S_{\parallel}^m)_{21}|$ is given by

$$\alpha = \frac{\kappa G_m}{m\sqrt{2\pi}\sigma} = 1.0363$$

With $N \sim 1.8 \times 10^7$, $\kappa = N \pi 2.46\text{MeV}\cdot\text{sec}$, $m = 3728$, and $\sigma = 3.77\text{MeV}$, $G_m = 7.35 \times 10^{-4}\text{MeV}/\text{sec}$, which is in agreement with the value of the gain obtained through signal suppression.



(a) $|(S_{\parallel}^m)_{21}|$ Magnitude. Fit corresponds to $G_m = 7.35 \times 10^{-4}\text{MeV}/\text{sec}$



(b) $(S_{\parallel}^m)_{21}$ Phase (degrees).

Figure 4.16: $(S_{\parallel}^m)_{21}$ measurements at $f = 2.1\text{GHz}$, corresponding to the $m = 3728$ revolution harmonic.

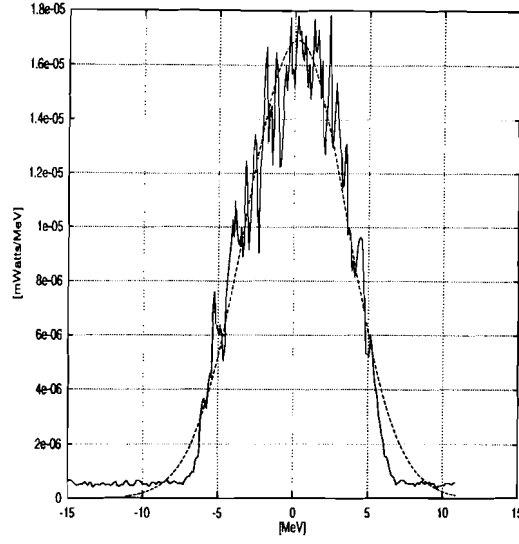


Figure 4.17: Longitudinal beam distribution for $(S_{||}^m)_{21}$ measurements at $f = 2.1\text{GHz}$

If the output power of the network analyzer is too strong, the beam will absorb energy through the resistive term. Thus the magnitude of the $S_{21} = S_{21}^{\text{real}} + iS_{21}^{\text{im}}$ response will be mostly from S_{21}^{im} . In Figure 4.18, the magnitude and phase of $|(S_{||}^m)_{21}|$ at 3.0GHz are given together with the corresponding measured longitudinal Schottky beam distribution in Figure 4.19. The fit was obtained with (i) $S_{21} = 0.1 \times S_{21}^{\text{real}} + iS_{21}^{\text{im}}$ indicating the strong reduction in the real S_{21} response, (ii) $x_o = 2.0\text{MeV}$ indicating that the notch is not centered exactly at the revolution harmonic, and (iii) the beam width $\sigma = 3.7\text{MeV}$. Fitting $|S_{21}|$,

$$\alpha = \frac{\kappa G_m}{m\sqrt{2\pi}\sigma} = .902$$

With $N \sim 1.8 \times 10^7$, $\kappa = N\pi 2.46\text{MeV-sec}$, $m = 5084$, and $\sigma = 3.7\text{MeV}$, $G_m = 6.88 \times 10^{-4}\text{MeV/sec}$.

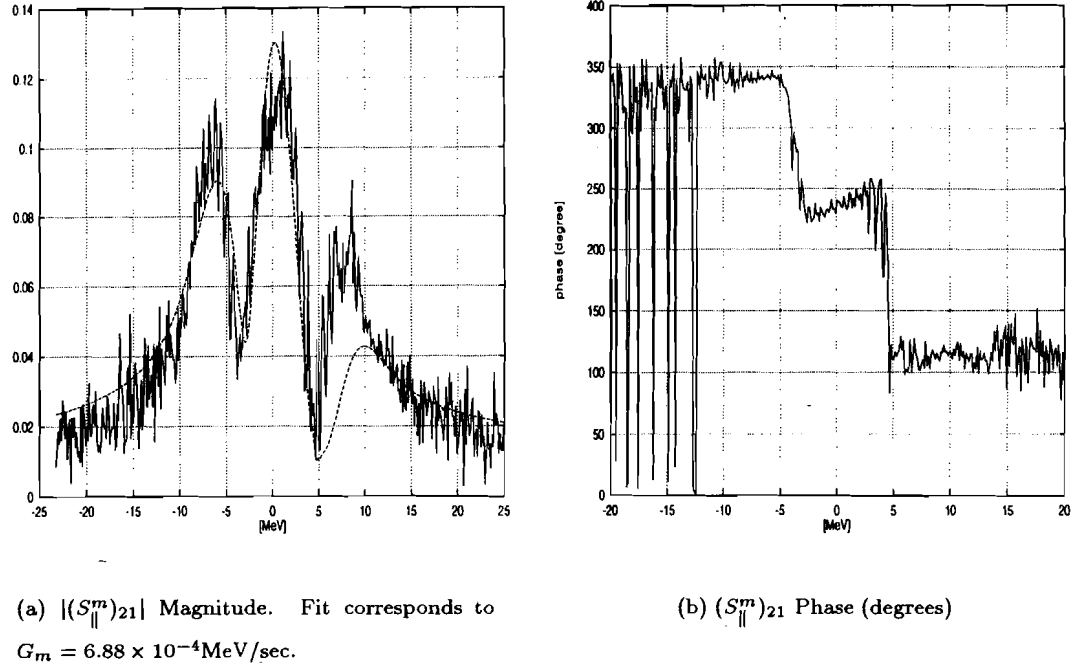


Figure 4.18: $(S_{\parallel}^m)_{21}$ measurements at $f = 3.0\text{GHz}$, corresponding to the $m = 5084$ revolution harmonic.

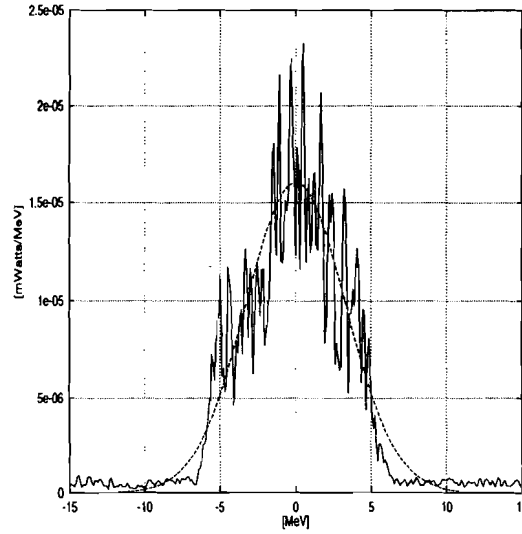


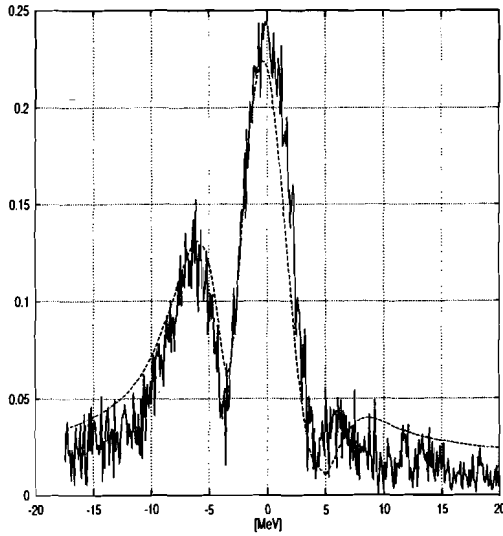
Figure 4.19: Longitudinal beam distribution for $(S_{\parallel}^m)_{21}$ measurements at $f = 3.0\text{GHz}$

The magnitude and phase of $(S_{\parallel}^m)_{21}$ at 3.8GHz are given in Figure 4.20 together with the corresponding measured longitudinal Schottky beam distribution in Figure 4.21. As with the

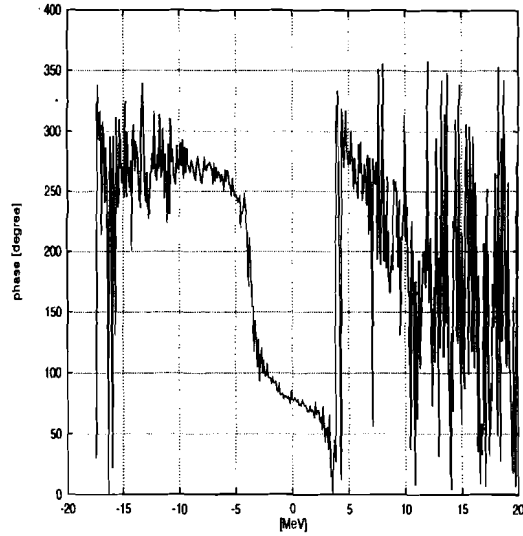
previous case at 3.0GHz, the beam absorbed a fraction of the output power of the network analyzer, and therefore the S_{21} response is dominated by the reactive part. The parameters involved in the fit were (i) $S_{21} = 0.1 \times S_{21}^{\text{real}} + iS_{21}^{\text{im}}$, (ii) $x_o = 2.0\text{MeV}$ indicating that the notch is not centered exactly at the revolution harmonic, (iii) the gain slope of the notch $\tau = 2.03 \times 10^{-2}\text{MeV}^{-1}$, and (iii) the beam width $\sigma = 3.5\text{MeV}$. The fitted parameter

$$\alpha = \times \frac{\kappa G_m}{m\sqrt{2\pi}\sigma} = 0.843$$

With $N \sim 1.8 \times 10^7$, $\kappa = N\pi 2.46\text{MeV}\cdot\text{sec}$, $m = 6440$, and $\sigma = 3.5\text{MeV}$, $G_m = 7.82 \times 10^{-4}\text{MeV}/\text{sec}$.



(a) $|(S_{\parallel}^m)_{21}|$ Magnitude. Fit corresponds to $G_m = 7.82 \times 10^{-4}\text{MeV}/\text{sec}$.



(b) $(S_{\parallel}^m)_{21}$ Phase (degrees)

Figure 4.20: $(S_{\parallel}^m)_{21}$ measurements at $f = 3.8\text{GHz}$, corresponding to the $m = 6440$ revolution harmonic.

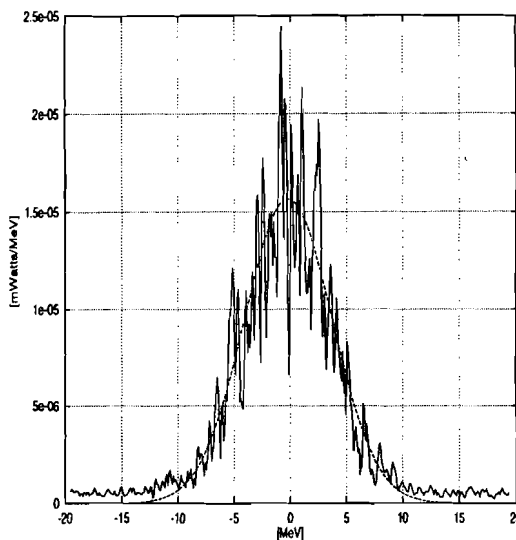


Figure 4.21: Longitudinal beam distribution for $(S_{||}^m)_{21}$ measurements at $f = 3.8\text{GHz}$

A summary of the results of extracting $\langle G_{||} \rangle$ across the cooling system bandwidth are given in Table 4.3. The most accurate fit was that for 2.1GHz given in Figures 4.16. For the measurements at 3.0GHz and 3.8GHz, the error in the fit is large because (i) the model is quite crude in fitting the spectra in which much of the microwave power is absorbed by the beam, and (ii) the beam distributions are not Gaussian, in particular, the edges of the distribution fall rather abruptly to zero.

Table 4.3: Summary of the open loop network analyzer fits to $\langle G_{||} \rangle$.

Frequency	$\langle G_{ } \rangle \ N = 1.8 \times 10^7$
2.1GHz	$7.35 \times 10^{-4} \text{MeV/sec}$
3.0GHz	$6.88 \times 10^{-4} \text{MeV/sec}$
3.8GHz	$7.82 \times 10^{-4} \text{MeV/sec}$

In conclusion, the experimental determination of the longitudinal cooling system gain $\langle G_{||} \rangle$ obtained with the open loop network analyzer measurements independently confirm the values obtained from the signal suppression measurement. Agreement between the results is within the $\sim 5 - 10\%$ error margin resulting from the error in the number of particles and also from assumptions of the model fits.

4.5 Transverse Stochastic Cooling

From a mathematical perspective, the description of transverse stochastic cooling is simplified, compared with the longitudinal counterpart, for two reasons: (i) the gain of the system is constant across the transverse tune lines, and (ii) to first order, there is no need to calculate the beam distribution; all that is required is the evolution of the beam emittance, thereby reducing a nonlinear partial differential equation to a first order differential equation. Thus, the transverse cooling equation [61] for the transverse beam size, ε_\perp , is given by:

$$-\frac{1}{\varepsilon_\perp} \frac{d\varepsilon_\perp}{dt} = \frac{f_o}{N} \sum_{m_1 \leq m \leq m_2} \left[\text{Real} \left\{ \frac{g_m(q_m\omega)}{\epsilon_m(q_m\omega)} \right\} + \frac{1}{2} \frac{|g_m(q_m\omega)|^2}{|\epsilon_m(q_m\omega)|^2} \{ M_m(q_m\omega, \sigma_p) + \mathcal{U}_m^\perp(q_m\omega) \} \right] \quad (4.27)$$

In Equation (4.27) (i) the sum is over sidebands at the revolution harmonic m within the microwave frequency band $\Delta f = (m_2 - m_1)f_o$ (ii) $q_m = (m \pm Q)\omega$, for which Q is the fractional tune, (iii) $g_m(q_m\omega)$ is the electronic gain at the m th harmonic given in terms of the transfer function as $g_m(q_m\omega) =$, (iv) $\epsilon_\perp(q_m\omega)$ is the *transverse* signal suppression factor, which is proportional to the transverse beam response function only, since the gain is flat across the sideband, (v) $M_m(q_m\omega, \sigma_p)$ is the mixing factor, and (vi) $\mathcal{U}_\perp(q_m\omega)$ is the noise/signal ratio. As discussed in previous sections, the right hand side of Equation (4.27) consist of two terms (i) the cooling interaction, and (ii) the heating, or diffusion term.

The *mixing* factor, $M_m(q_m\omega, \sigma_p)$ appearing in Equation (4.27) is defined as *the ratio of the dipole Schottky signal spectral density at the sideband associated with the m th revolution harmonic to the average dipole transverse Schottky signal spectral density*, $M_m(q_m\omega) = \Sigma_{\text{dipole}}(q_m\omega) / \langle \Sigma_{\text{dipole}} \rangle$ in which $\langle \Sigma_{\text{dipole}} \rangle = \left[\frac{\beta_p (ef_o \langle A \rangle)^2}{2\omega_o} \right]$ is the average signal spectral density for an observed beta function β_p at and beam size $\langle A \rangle$ at the pickup. For a Schottky signal having parabolic frequency distribution⁵,

$$\Sigma_{\text{dipole}}(\omega) \sim \psi\left(\frac{\omega}{m \pm Q}\right) \sim N/(\eta\omega_o\sigma_p/p)$$

and an expression for the peak transverse Schottky signal to the average transverse Schottky signal is $M(\omega) = f\beta^2 E\psi(\Delta E)/[2W\eta N]$. With a distribution function $\psi(\Delta E) = N/[\sqrt{2\pi}\sigma] \exp[-(\Delta E)^2/\sigma^2]$, then

$$M(\omega) = \frac{1}{2m\sqrt{2\pi}\eta(\sigma_p/p)} \quad (4.28)$$

⁵D. Möhl. *Physics and Techniques of Stochastic Cooling*, Physics Reports 58, No.2 (1980) 73-119

This definition of Equation (4.28), which is explicit in the longitudinal beam width σ_p/p , obviates the connection between the longitudinal cooling and transverse cooling equations.

The thermal noise associated with the transverse system, as represented by $\mathcal{U}_m^\perp(q\omega)$ in Equation (4.27), is defined as *the ratio of the transverse noise spectral density to the average dipole Schottky signal spectral density*,

$$U_m^\perp(q\omega) = \left[\frac{2\omega_o \Sigma_n(\omega)}{\beta(qf_o A)^2 N} \right] \quad (4.29)$$

The fact that the gain acts equally across the transverse sideband simplifies both the calculation and the experimental determination of the system parameters. In the simplest manifestation of Equation (4.27), the time constant τ specifies the cooling rate by:

$$\frac{1}{\tau} = -\frac{1}{\epsilon_\perp} \frac{d\epsilon_\perp}{dt} = \frac{2W}{N} [2g - g^2 \{M + U\}] \quad (4.30)$$

Another form of Equation (4.27) given in the literature, which makes includes the bad mixing between the kicker and the pickup, represented by $\tilde{M}(q_m\omega)$, is given by

$$\begin{aligned} \frac{1}{\epsilon_\perp} \frac{d\epsilon_\perp}{dt} = - \sum_{m_1 \leq m \leq m_2} \left[\text{Real} \left\{ \frac{g_m(q_m\omega)}{\epsilon_m(q_m\omega)} \right\} (1 - \tilde{M}(q_m\omega)) \right. \\ \left. + \frac{|g_m(q_m\omega)|^2}{|\epsilon_m(q_m\omega)|^2} \{ M_m(q_m\omega, \sigma_p) + U_m^\perp(q_m\omega) \} \right] \end{aligned} \quad (4.31)$$

4.5.1 Schottky signals & $\mathcal{U}_\perp(q_m\omega)$

By comparison with the longitudinal analysis, extracting the relevant phenomenologic quantities, which appear in the transverse stochastic cooling Equation (4.27), from measurements are greatly simplified by the flat gain slope across each transverse sideband. Referring once again to Figure 4.5, which depicts a simplified diagram of the stochastic cooling system and the location of the measurement point after the correlator notch filter, transverse Schottky signals may be used to extract the noise/signal ratio for the determination of $\mathcal{U}^\perp(q_m\omega)$.

Closed loop measurements *with* and *without* beam were made at three frequencies within the bandwidth of the vertical stochastic cooling system (i) 2.2GHz, (ii) 3.0GHz, and (iii) 3.8GHz. The measurements were performed by measuring the average Schottky power *at the peak* of the corresponding transverse sideband and triggered at the beginning of the cooling cycle ($\sim \Delta t \approx 200\text{msec}$). Results of the measurements at the selected frequencies across the cooling band are given in Table 4.4.

Table 4.4: $\mathcal{U}^\perp(q_m\omega)$ Result of measurements across the microwave band at the beginning of cycle ($\Delta t = 0.1\text{sec}$ after injection).

<i>Frequency</i>	$\mathcal{P}_{\text{signal+noise}}$	$\mathcal{P}_{\text{noise}}$	$\mathcal{U}^\perp(q_m\omega)$
2.2GHz	-74.9dB	-75.7dB	4.98
	3.23×10^{-8}	2.69×10^{-8}	
3.0GHz	-78.2dB	-79.0dB	5.04
	1.51×10^{-8}	1.26×10^{-8}	
3.2GHz	-75.8dB	-76.6dB	4.84
	2.63×10^{-8}	2.18×10^{-8}	

Transverse noise/signal ($\mathcal{U}^\perp(q_m\omega)$) measurements were also measured as a function of time throughout the cooling cycle. Figures 4.22 and 4.23 are the results of measurements at 2.2GHz obtained with the spectrum analyzer frequency span $FS = 0\text{Hz}$, and resolution bandwidth $RB = 300\text{Hz}$, for the two cases: (i) at the peak of the dipole tune line, which is the *signal + noise* power ($\mathcal{P}_{\text{signal+noise}}$), and (ii) for the case with no beam, which is given by the *noise* power ($\mathcal{P}_{\text{noise}}$). The thermal noise to signal ratio at the peak of the dipole Schottky line $q_m\omega$ from these measurements is given by

$$\mathcal{U}^\perp(q_m\omega) = \frac{\mathcal{P}_{\text{noise}}}{\mathcal{P}_{\text{signal}}} = \frac{\mathcal{P}_{\text{noise}}}{\mathcal{P}_{\text{signal+noise}} - \mathcal{P}_{\text{noise}}}$$

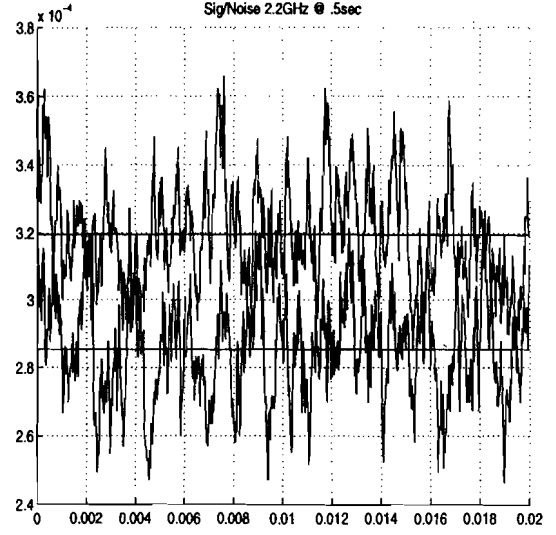
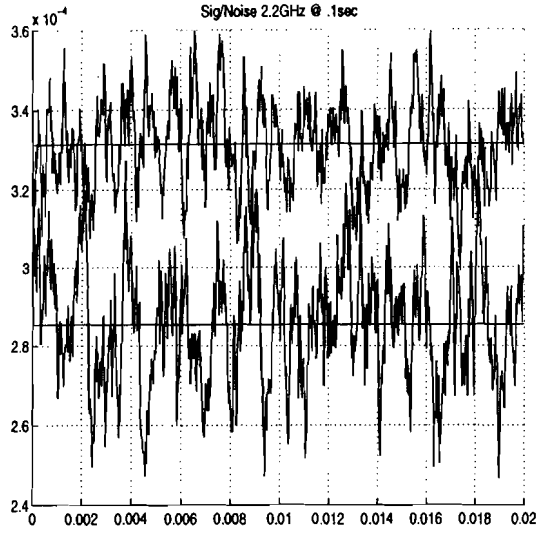


Figure 4.22: Measurements of the transverse signal/noise at (a) 0.1sec, and (b) 0.5sec, into the cooling cycle.

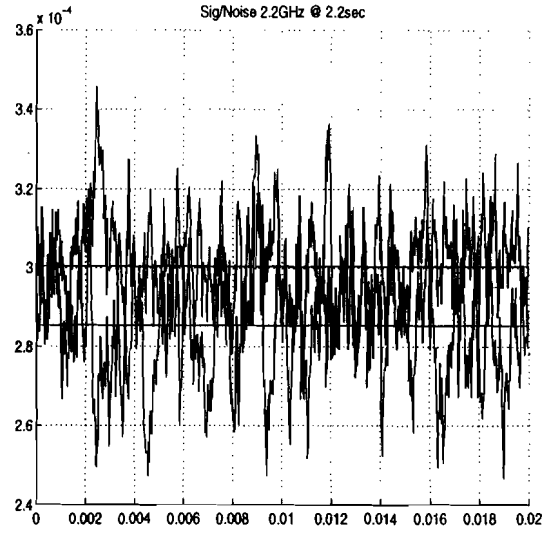
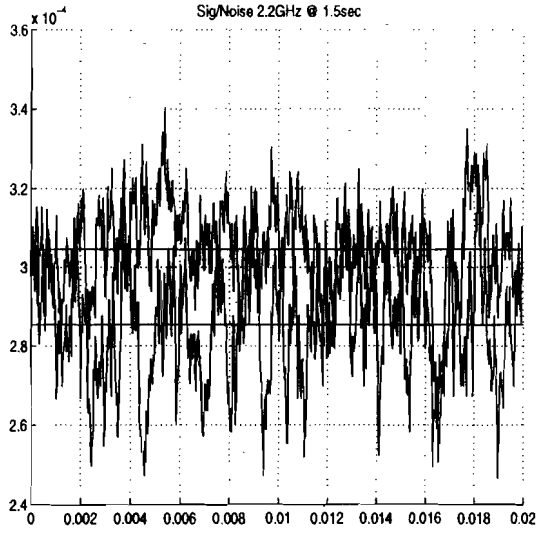


Figure 4.23: Measurements of the transverse signal/noise at (a) 1.5sec, and (b) 2.2sec, into the cooling cycle.

The results of the measurements and the value of $U^\perp(q_m\omega)$ as a function of time at 2.2GHz are given in Table 4.5.

Table 4.5: $\mathcal{U}^\perp(q_m\omega)$ for 2.2GHz as a function of time.

$time\Delta t$	$\mathcal{P}_{\text{signal+noise}}$	$\mathcal{P}_{\text{noise}}$	$\mathcal{U}^\perp(q_m\omega)$
(1) 0.1 sec	3.320×10^{-4}	2.862×10^{-4}	6.25
(2) 0.5 sec	3.232×10^{-4}	2.862×10^{-4}	8.33
(3) 1.0 sec	3.053×10^{-4}	2.862×10^{-4}	14.9
(3) 2.2 sec	3.008×10^{-4}	2.862×10^{-4}	20.0

4.5.2 Signal Suppression $\epsilon_\perp(\omega)$ & $\langle g_\perp \rangle$

For the case of transverse stochastic cooling, the signal suppression factor $\epsilon_\perp(\omega)$, is proportional to a term giving the transverse beam response.

$$\epsilon_m^\perp = 1 + \frac{N}{m} G_m(\omega) \int \frac{\psi(\omega') d\omega'}{(\omega - \omega') + i\eta} \quad (4.32)$$

Since the entire dipole Schottky line is *suppressed* by the feedback loop, due to the flat gain across the line, the useful quantity is the *peak* signal suppression obtained at the center of the distribution. Such a simplification makes the extraction of the gain a trivial matter [69] since

$$\epsilon_m(q\omega) \approx 1 + g_m(q_m\omega) M_m(q_m\omega)/2 \quad (4.33)$$

From the definition of the mixing factor at the m th band, given in Equation (4.28), the open loop transverse Schottky power is $\psi_o = \mathcal{P}_{\text{open}}$. Thus, with $\epsilon = [\mathcal{P}_{\text{open}}/\mathcal{P}_{\text{closed}}]$, the approximation by Möhl, for the signal suppression at the center of a Gaussian beam distribution, Equation (4.33) becomes

$$\left[\frac{\mathcal{P}_{\text{open}}}{\mathcal{P}_{\text{closed}}} \right]_m = \left[1 + g_m M_m/2 \right]^2 \quad (4.34)$$

The result of simple least square fits to the *peak* transverse power spectra measurements for the open and closed loop data, $\mathcal{P}_{\text{open}}$ and $\mathcal{P}_{\text{closed}}$, respectively, are given in Table 4.6 for (i) 2.2GHz, (ii) 3.0GHz, and (iii) 3.8GHz. Together with the values of the measured power, the gain $\langle g_\perp \rangle$ is calculated for each m th harmonic from Equation (4.34) with $M = \sqrt{2}/[m\eta\sqrt{\pi}(\Delta p/p)]$.

Table 4.6: Experimental fits to transverse signal suppression, ϵ_m^\perp across the microwave bandwidth, at the beginning of the cycle $\Delta t = .1\text{sec}$.

<i>Frequency</i>	$\mathcal{P}_{\text{open}}$	$\mathcal{P}_{\text{closed}}$	$ \epsilon ^2$	M_l at peak	$\langle g_\perp^m(q_m\omega) \rangle$
2.2GHz	-82.0dB	-82.6dB		11.9	0.008
	$6.31 \times 10^{-9}\text{W}$	$5.49 \times 10^{-9}\text{W}$	1.072		
3.0GHz	-83.9dB	-84.8dB		8.7	0.017
	$4.07 \times 10^{-9}\text{W}$	$3.31 \times 10^{-9}\text{W}$	1.108		
3.8GHz	-81.75dB	-82.4dB		8.17	0.013
	$6.68 \times 10^{-9}\text{W}$	$5.75 \times 10^{-9}\text{W}$	1.077		

Transverse signal suppression measurements as a function of time within the production cycle were made at 2.2GHz. Figures 4.24(a) and (b) indicate the result of linear least square fits to the total integrated power at the peak of the transverse tunes, at 0.5sec and 1.0sec, respectively. The measurements were performed in a similar manner to those described in the previous section for the longitudinal signal suppression. In particular, open loop measurements were made by gating the PIN switch on for $\sim 200\text{msec}$ and measuring the total power at the peak of the dipole Schottky line with zero frequency span and a resolution bandwidth 10kHz.

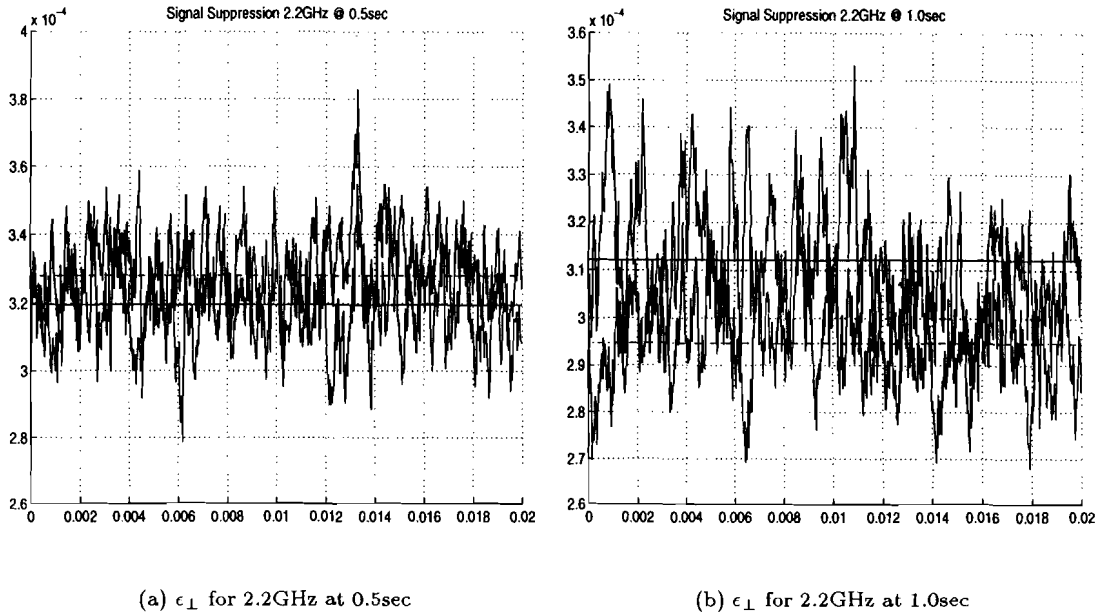


Figure 4.24: Transverse signal suppression measurements at $f = 2.2\text{GHz}$ for (a) 0.5sec and (b) 1.0sec into the cooling cycle.

The result of the fits to $\mathcal{P}_{\text{open}}$ and $\mathcal{P}_{\text{closed}}$ in Figures 4.24(a), (b), and (c), are listed in Table 4.7, together with an average electronic gain $\langle g_{\perp}(q_m\omega) \rangle \approx 0.01$ calculated from Equation (4.33) with M at 2.2GHz, as a function of time.

Table 4.7: Experimental fits to transverse signal suppression, ϵ_m^{\perp} at 2.2GHz as a function of time. Values for $\mathcal{P}_{\text{open}}$ and $\mathcal{P}_{\text{closed}}$ are obtained from fits to data in Figure 4.24.

Time Δt	$\mathcal{P}_{\text{open}}$	$\mathcal{P}_{\text{closed}}$	$ \epsilon ^2$
0.1sec	$3.36 \times 10^{-4} \text{mW}$	$3.35 \times 10^{-4} \text{mW}$	1.003
0.5sec	$3.28 \times 10^{-4} \text{mW}$	$3.19 \times 10^{-4} \text{mW}$	1.028
1.0sec	$3.12 \times 10^{-4} \text{mW}$	$2.95 \times 10^{-4} \text{mW}$	1.057

4.5.3 Open-loop Transfer Function & $\langle \tilde{g}_{\perp} \rangle$

Transverse open loop network analyzer measurements through the stochastic cooling feedback system, as given previously in Figure 4.15, are similar to those described for the longitudinal case. Despite the similarity, the analysis for extracting $\langle \tilde{g}_{\perp} \rangle$ are greatly simplified for the transverse case because the gain is constant across the measured sideband frequency. Thus, for the transverse case, the S_{21} response is given by

$$S_{21}(\Delta f) = \left[\frac{\mathcal{P}_{\text{in}}(\Delta f)}{\mathcal{P}_{\text{out}}(\Delta f)} \right] \quad (4.35)$$

$$S_{21}(\omega) = N(\omega) \otimes Y(\omega) \otimes P(\omega) \quad (4.36)$$

for which $Y(\omega)$ is now the transverse (dipole) beam transfer function [10]. Therefore, the expression for the transverse open loop measurement at the m th harmonic, is

$$(S_{\perp}^m)_{21} = \bar{k} g_m(\omega) \left[PV \int \frac{\psi(\omega') d\omega'}{\omega - \omega'} + i\pi\psi(\omega') \right] \quad (4.37)$$

Measurements of $(S_{\perp}^m)_{21}$ were made at several transverse sideband frequencies across the microwave cooling bandwidth. A representative $(S_{\perp}^m)_{21}$ measurement at 3.0GHz over a 100kHz frequency span is given in Figures 4.25. The magnitude $|(S_{\perp}^m)_{21}| = V_{\text{in}}/V_{\text{out}}$ in Figure 4.25(a) mirrors the frequency distribution. Figure 4.25(b) illustrates the proper phase change of π through the center of the sideband from the beam transfer function.

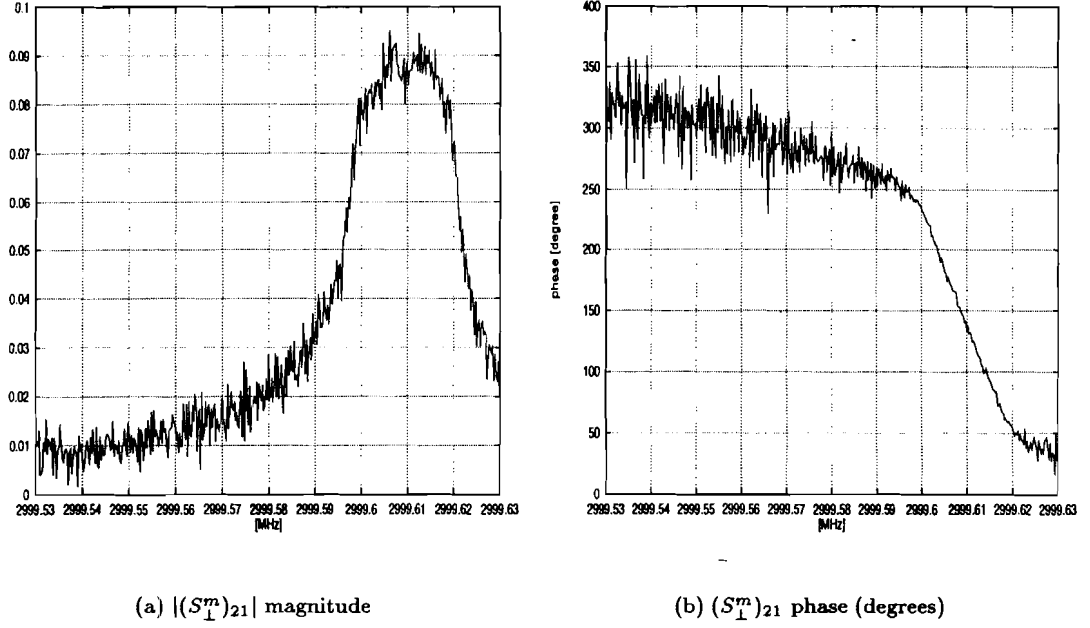


Figure 4.25: Transverse open loop measurements at the 3.1GHz sideband.

For extracting $\langle \tilde{g}_{\perp} \rangle$, a simple expression for $(S^m_{\perp})_{21}$ results from taking only the center of the distribution. From S. van der Meer [98], the value of $(S^m_{\perp})_{21}$ at the center of the distribution may be written

$$V_{in}/V_{out} = \frac{N e^2 Z_{pu} G_E \sqrt{\beta_p \beta_k} \sqrt{N_p N_k}}{m \eta [\Delta p/p]_{95\%} \sqrt{2\pi}} \quad (4.38)$$

$$g_m = N Z_{pu} G_E \frac{e f_o}{\beta^2 E} \sqrt{\beta_p \beta_k} \sqrt{N_p N_k} \quad (4.39)$$

Thus,

$$|(S^m_{\perp})_{21}|(\text{at peak}) = V_{in}/V_{out}(\text{at peak}) = \frac{g_m}{m \eta [\Delta p/p]_{95\%} \sqrt{2\pi}} \quad (4.40)$$

Utilizing Figure 4.25, at the peak of the distribution $|(S^m_{\perp})_{21}| \approx .089$, $\sigma = 3.9\text{MeV}$, so that approximately 95% of the beam is given by $\pm 2 \times \sigma$ and

$$[\Delta p/p]_{95\%} = [\Delta E/E]_{95\%} \approx 4\sigma/E_o \approx .0011\text{MeV} \quad (4.41)$$

Therefore with $m = 5048$, $\eta = 0.006$,

$$g_m = m \eta [\Delta E/E]_{95\%} \sqrt{2\pi} |(S^m_{\perp})_{21}|(\text{at peak}) = .0075 \quad (4.42)$$

which is in agreement with that obtained with the transverse signal suppression measurements.

Figures 4.26(a) and (b) are the results of network analyzer measurements at the edges of the frequency cooling band, i.e. 2.1GHz and 3.8GHz respectively.

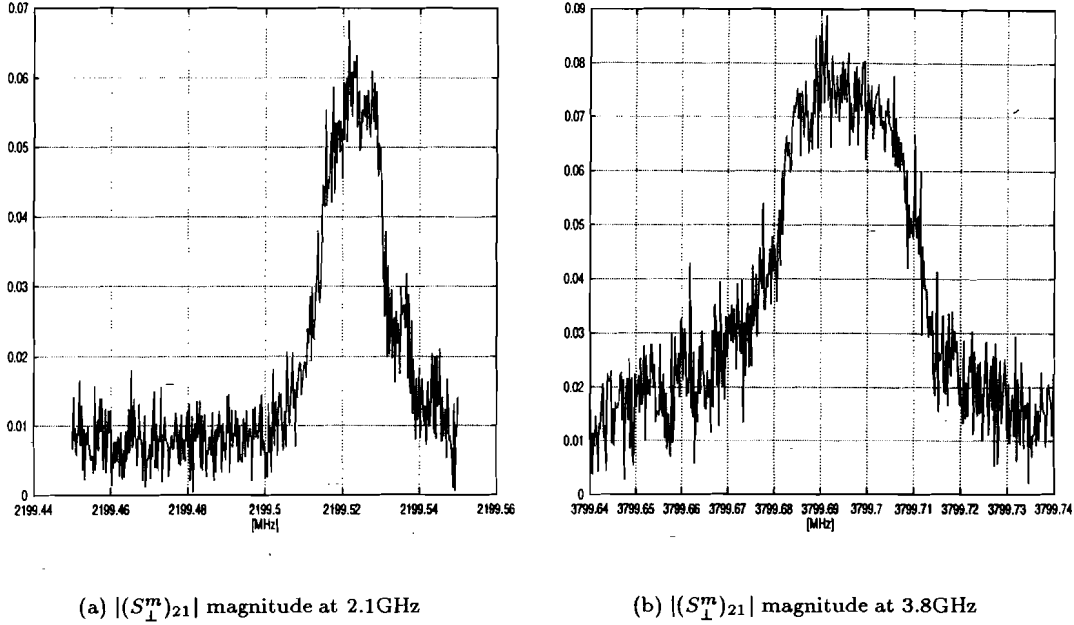


Figure 4.26: Transverse $|(S_L^m)_{21}|$ measurements at 2.1GHz and 3.8GHz.

A summary of the transverse open loop network analyzer measurements for the extraction of the gain across the cooling bandwidth is given in Table 4.8.

Table 4.8: Summary of the open loop network analyzer fits to $\langle g_{\perp} \rangle$.

Frequency	$\langle g_{\perp} \rangle N = 1.8 \times 10^7$
2.1GHz	7.5×10^{-3}
3.0GHz	5.0×10^{-3}
3.8GHz	7.7×10^{-3}

4.6 Computational Results

In the previous sections, the necessary physical quantities for calculating stochastic cooling rates have been experimentally determined. Specifically, the following quantities have been obtained at several frequencies across the cooling frequency band: (i) the cooling system gain: G_{\parallel}^m (longitu-

dinal) and g_{\perp}^m (transverse), (ii) the thermal signal/noise: $\mathcal{U}_{\parallel}^m$ (longitudinal) and \mathcal{U}_{\perp}^m (transverse), and (iii) determination of the signal suppression as a function of time: ϵ_{\parallel}^m (longitudinal) and ϵ_{\perp}^m .

In this section, the experimental quantities shall be used to numerically characterize the cooling performance through integration of the stochastic cooling equations. To complete the analysis, comparisons between the relative strength of the cooling and heating effects shall be given and discussed.

4.6.1 Longitudinal system: cooling, diffusion, optimal gain and comparisons

As given previously in the text, a nonlinear Fokker-Planck transport equation describes the evolution of the particle beam's momentum distribution throughout the cooling process. In terms of the energy difference, $x = E - E_0$, the transport equation for the number of particles per unit energy $\Psi = N\psi(x, t) = dN/dx$, is given by the expression

$$\frac{\partial \psi(x, t)}{\partial t} = -\frac{\partial \phi(x, t)}{\partial x} \quad (4.43)$$

$$\begin{aligned} \phi(x, t) = & \sum_{m_1 \leq m \leq m_2} \left[\psi(x, t) \mathcal{R}eal \left[\frac{G_m(x)}{\epsilon_m(x, t)} \right] \right. \\ & \left. - \psi(x, t) \frac{\partial \psi(x, t)}{\partial x} \frac{N\pi\beta^2 E}{2\eta f_0} \frac{1}{m} \frac{|G_m(x)|^2}{|\epsilon_m(x, t)|^2} \left\{ 1 + \mathcal{U}_m(x, t) \right\} \right] \end{aligned} \quad (4.44)$$

Once again the quantities appearing in the above equation are as follows: (i) $\phi(x, t)$ is the conserved flux of particles, undergoing collisional interactions through the feedback loop, (ii) the sum is over all revolution harmonics, however the gain $G_m(x)$ is only finite within the cooling bandwidth W from $f = 2 - 4\text{GHz}$, (iii) $G_m(x)$ is the energy dependent gain function of the cooling loop at each m -th harmonic in units of GeV/sec, (iv) $\mathcal{U}_m(x, t)$ is the energy dependent noise/signal ratio at each m th harmonic during the cooling cycle, and which may be defined through the Schottky power $\Sigma(x, t)$, such that $\mathcal{U}_m(x, t) = \Sigma_{\text{noise}}/\Sigma_{\text{signal}}$. (v) $\epsilon_m(x, t)$, is the signal suppression factor, or equivalently, the closed loop response function, at each m -th harmonic as a function of time, and (vi) the constants of the machine are $f_0 = 0.590035 \times 10^6 \text{Hz}$, $\eta = .006$, $E_0 = 8.938 \text{GeV}$, $\gamma = 9.5287$, and $\beta = 0.989$, such that the energy variable $x = 2.469 \text{MeV-sec} \Delta f_m / m$.

The cooling and diffusion sums of the longitudinal stochastic cooling Equation (4.44), $S_1(x, t)$

and $S_2(x, t)$, respectively, such that,

$$\frac{\partial \psi(x, t)}{\partial t} = -\frac{\partial}{\partial x} \left[S_1(x, t) - S_2(x, t) \right] \quad (4.45)$$

may be evaluated explicitly through digamma functions [42], $\tilde{\psi}(z)$. Moreover, given the experimental values of the phenomenologic models, the relative strengths between $S_1(x, t)$ and $S_2(x, t)$ may be determined to evaluate the system with relation to optimal gain. Finally, the full model is utilized for a comparison of the calculated cooling rate to the measured beam width as a function of the production cycle.

From the experimental measurements of signal suppression for both the longitudinal and transverse systems, $\epsilon_{\parallel} \approx 1$ and $\epsilon_{\perp} \approx 1$ respectively. Thus, it is because the stochastic cooling systems in the Debuncher are *gain limited*, i.e. the thermal noise is so large that the systems can not operate at higher power levels without damage to the hardware, that signal suppression is not expected to have a pronounced effect upon the cooling equations. Nevertheless, with higher gain, the effect of signal suppression shall become important, and it is for this reason that a careful evaluation of $S_1(x, t)$ and $S_2(x, t)$ is worthwhile. Moreover, for investigation of the optimal gain, inclusion of the signal suppression effects is absolutely essential.

4.6.1.1 Longitudinal cooling term: $S_1(x, t)$

An analytic expression for $S_1(x, t)$ shall be derived in this section. For a complex gain $G_m(x) = \langle G \rangle [g_{m, \Re} + i g_{m, \Im}]$, and complex signal suppression factor $\epsilon_m(x, t) = [\epsilon_{m, \Re} + i \epsilon_{m, \Im}]$, the cooling term $S_1(x, t)$ of Equation (4.45) (which represents the first term in Equation (4.7)) is given by

$$S_1(x, t) = \psi(x, t) \sum_{m_1 \leq m \leq m_2} \text{Real} \left[\frac{G_m(x)}{\epsilon_m(x, t)} \right] = \frac{G_{\Re, m} \epsilon_{\Re, m} + G_{\Im, m} \epsilon_{\Im, m}}{\epsilon_{\Re, m}^2 + \epsilon_{\Im, m}^2} \quad (4.46)$$

The real and imaginary part of $\epsilon_m(x, t)$ may be written explicitly

$$\epsilon_{m, \Re} = \left[1 + \frac{N \pi \bar{k}}{m} \langle G \rangle (g_{\Re} \pi \mathcal{R} + g_{\Im} \mathcal{P} \mathcal{V}) \right] \quad (4.47)$$

$$\epsilon_{m, \Im} = \left[\frac{N \pi \bar{k}}{m} \langle G \rangle (g_{\Im} \pi \mathcal{R} - g_{\Re} \mathcal{P} \mathcal{V}) \right] \quad (4.48)$$

in which (i) the residue is $\mathcal{R} = \partial\psi/\partial x$, (ii) the principle value is $\mathcal{PV} = P \int dx' \partial\psi/\partial x' / [x - x']$, and (iii) the constant \bar{k} is evaluated in terms of the known machine constants:

$$\bar{k} = \frac{\beta^2 E}{\eta f_o} = \frac{8939 \text{ MeV}}{2(.006)(.590035 \text{ MHz})} = 2.465 \text{ MeV -sec}$$

Thus, expanding the expression $S_1(x, t)$ in (4.46),

$$S_1(x, t) = \psi(x, t) \times \sum_{m_1 \leq m \leq m_2} \langle G \rangle g_{\Re} \frac{1 + \frac{N\pi\bar{k}}{m} \langle G \rangle (g_{\Re, m}^2 + g_{\Im, m}^2) / g_{\Re}}{\left[1 + \frac{N\pi\bar{k}}{m} \langle G \rangle (g_{\Re} \pi \mathcal{R} + g_{\Im} \mathcal{PV})\right]^2 + \left[\frac{N\pi\bar{k}}{m} \langle G \rangle (g_{\Im} \pi \mathcal{R} - g_{\Re} \mathcal{PV})\right]^2} \quad (4.49)$$

Define the following quantities,

$$a(x) = N\pi\bar{k} \langle G \rangle (g_{\Re, m}^2 + g_{\Im, m}^2) / g_{\Re} \quad (4.50)$$

$$b(x) = N\pi\bar{k} \langle G \rangle (g_{\Re} \pi \mathcal{R} + g_{\Im} \mathcal{PV}) \quad (4.51)$$

$$c(x) = N\pi\bar{k} \langle G \rangle (g_{\Im} \pi \mathcal{R} - g_{\Re} \mathcal{PV}) \quad (4.52)$$

then the sum $S_1(x, t)$ is

$$S_1(x, t) = \psi(x, t) \sum_{m_1 \leq m \leq m_2} \langle G \rangle g_{\Re} \frac{1 + \frac{a(x)}{m}}{\left[1 + \frac{b(x)}{m}\right]^2 + \left[\frac{c(x)}{m}\right]^2} \quad (4.53)$$

$$= \psi(x, t) \sum_{m_1 \leq m \leq m_2} \langle G \rangle g_{\Re} \frac{m[m + a(x)]}{[m^2 + 2mb(x) + (b^2 + c^2(x))]} \quad (4.54)$$

The sum $S_1(x)$ may be evaluated analytically in terms of the integral representation of the *digamma function* $\bar{\zeta}(z) = d \ln \Gamma / dz$,

$$\bar{\zeta}(z) = \int_0^\infty \left\{ \frac{e^{-t}}{t} - \frac{e^{-zt}}{1 - e^{-t}} \right\} dt$$

Thus, with the following definitions,

$$\xi(x) = \sqrt{-c^2(x)} = ic(x) \quad (4.55)$$

$$\tau_{\pm}(x) = \frac{1}{2} [\pm a(x) \mp 2b(x)] + i \frac{1}{2c(x)} [b^2(x) - b(x)a(x) - c^2(x)] \quad (4.56)$$

$$\alpha_{\pm}(x) = (m_2 + 1) + b(x) \pm \xi(x) \quad (4.57)$$

$$\beta_{\pm}(x) = m_1 + b(x) \pm \xi(x) \quad (4.58)$$

the exact result for the sum between m_1 and m_2 is

$$S_1(x, t) = \psi(x, t) \left\{ (1 + m_2 - m_1) + \tau_+(x) [\bar{\zeta}(\alpha_+) - \bar{\zeta}(\beta_+)] \right. \\ \left. - \tau_-(x) [\bar{\zeta}(\alpha_-) - \bar{\zeta}(\beta_-)] \right\} \quad (4.59)$$

The expressions for the digamma function are computationally advantageous compared to brute force evaluation of the recursive sums, since quadrature method for evaluating $\bar{\zeta}$ requires trivial CPU expenditure.

4.6.1.2 Longitudinal heating term

The second term in the Fokker Planck equation contains the following sum

$$S_2(x, t) = \psi(x, t) \frac{\partial \psi}{\partial x} N \pi \bar{k} \sum_m \frac{1}{m} \frac{|G_m(x)|^2}{|\epsilon_m(x, t)|^2} \left\{ 1 + \mathcal{U}_m(x) \right\} \quad (4.60)$$

As described in the previous discussion of the cooling term, consider the average value of the measured gain to be taken across the bandwidth of the system, so that $\langle G \rangle$ may be factored from the above equation. Based upon measurements, the term $\{1 + \mathcal{U}_m(x)\}$ is well represented by the average value $\langle 1 + \mathcal{U}(x, t) \rangle$. Thus, the sum $S_2(x, t)$ may be written

$$S_2(x, t) = \psi(x, t) \frac{\partial \psi}{\partial x} N \pi \bar{k} \langle G \rangle^2 \{1 + \mathcal{U}(x, t)\} s' \quad (4.61)$$

in which the sum s' is given by

$$s' = \sum_{m_1 \leq m \leq m_2} \frac{1}{m} \frac{|g(x)|^2}{|\epsilon_m(x, t)|^2} = \sum_{m_1 \leq m \leq m_2} \frac{1}{m} \frac{g_{\Re, m}^2(x) + g_{\Im, m}^2(x)}{\epsilon_{\Re, m}(x) + \epsilon_{\Im, m}(x)} \\ \sum_{m_1 \leq m \leq m_2} \frac{[g_{\Re, m}^2 + g_{\Im, m}^2]/m}{\left[1 + \frac{N \pi \bar{k}}{m} \langle G \rangle (g_{\Re} \pi \mathcal{R} + g_{\Im} \mathcal{P} \mathcal{V})\right]^2 + \left[\frac{N \pi \bar{k}}{m} \langle G \rangle (g_{\Im} \pi \mathcal{R} - g_{\Re} \mathcal{P} \mathcal{V})\right]^2} \quad (4.62)$$

Just as before, the following definitions are made:

$$a'(x) = (g_{\Re, m}^2 + g_{\Im, m}^2) \quad (4.63)$$

$$b(x) = N \pi \bar{k} \langle G \rangle (g_{\Re} \pi \mathcal{R} + g_{\Im} \mathcal{P} \mathcal{V}) \quad (4.64)$$

$$c(x) = N \pi \bar{k} \langle G \rangle (g_{\Im} \pi \mathcal{R} - g_{\Re} \mathcal{P} \mathcal{V}) \quad (4.65)$$

such that,

$$S_2(x, t) = \psi(x, t) \frac{\partial \psi}{\partial x} N \pi \bar{k} \langle G \rangle^2 \{ \langle 1 + \mathcal{U}(x, t) \rangle \} \sum_{m_1 \leq m \leq m_2} \frac{\frac{a'(x)}{m}}{\left[1 + \frac{b(x)}{m} \right]^2 + \left[\frac{c(x)}{m} \right]^2} \quad (4.66)$$

$$= N \pi \bar{k} \langle G \rangle^2 \{ \langle 1 + \mathcal{U}(x) \rangle \} \sum_{m_1 \leq m \leq m_2} \frac{m a'(x)}{[m^2 + 2mb(x) + (b^2(x) + c^2(x))]} \quad (4.67)$$

Now the sum $S_2(x, t)$ may be evaluated analytically in terms of *digamma functions* with the aid of the following definitions

$$\xi(x) = \sqrt{-c^2(x)} = ic(x) \quad (4.68)$$

$$\alpha_{\pm} = (m_2 + 1) + b(x) \pm \xi(x), \quad \beta_{\pm} = m_1 + b(x) \pm \xi(x), \quad \tau_{\pm} = \frac{a[b \pm \xi(x)]}{2\xi(x)} \quad (4.69)$$

$$(4.70)$$

Finally, the full equation for the diffusion term is

$$S_2(x, t) = \psi(x, t) \frac{\partial \psi}{\partial x} N \pi \bar{k} \langle G \rangle^2 [\langle 1 + \mathcal{U}(x) \rangle] \left\{ \tau_+ [\tilde{\zeta}(\alpha_+) - \tilde{\zeta}(\beta_+)] - \tau_- [\tilde{\zeta}(\alpha_-) - \tilde{\zeta}(\beta_-)] \right\} \quad (4.71)$$

4.6.1.3 Comparison of $S_1(x, t)$ and $S_2(x, t)$

A comparison between the cooling and diffusion terms, $S_1(x, t)$ and $S_2(x, t)$ respectively, are given in Figure 4.27 at the beginning of the cooling cycle, t_o . The value of the gain, which were used in computing the terms $S_1(x, t)$ and $S_2(x, t)$ in Figure 4.27 $\langle G \rangle = 8.0 \times 10^{-4}$ Mev/sec, and gain slope (convexity) $\tau = 2.5 \times 10^{-2}$ 1/MeV, are those obtained experimentally. Also compared in the Figure 4.27 are the values of $S_1(x, t)$ and $S_2(x, t)$ *with* and *without* signal suppression $\epsilon(x)$ for $N = 4.5 \times 10^7$ particles and $\eta = 0.006$.

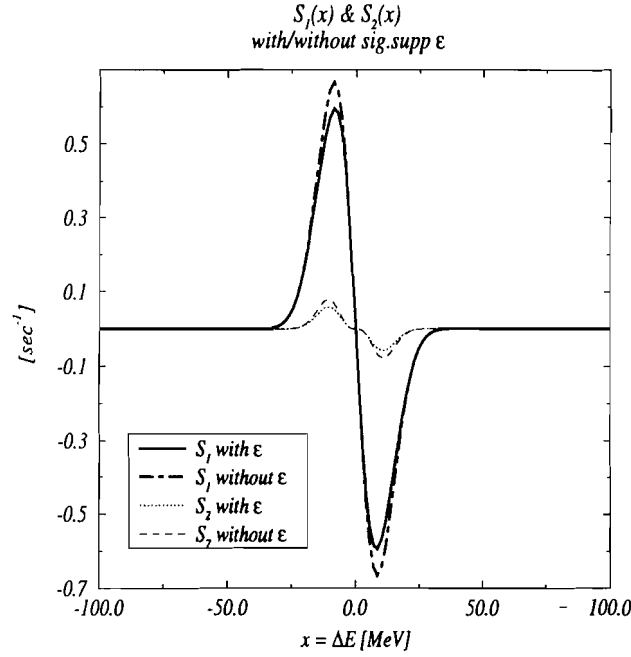


Figure 4.27: Comparison of $S_1(x, t = 0)$ and $S_2(x, t = 0)$ with and without signal suppression and with $\langle G \rangle = 8.0 \times 10^{-4}$ Mev/sec, $\tau = 2.5 \times 10^{-2}$ MeV $^{-1}$.

4.6.1.4 Model comparison to longitudinal cooling measurements

Measurements of the longitudinal Schottky spectra at the 127th harmonic were obtained for trigger times throughout the \bar{p} production cycle for comparison with model calculations. For each time point, the spectra were fit with the nonlinear least square model $\phi(x) = \beta_1 \exp\left[\frac{-(x-x_o)^2}{2\sigma^2}\right]$. Figure 4.28 is the experimental values for the beam width σ as a function of time in the \bar{p} production cycle, obtained from nonlinear fits to the beam spectra. Superposed over the longitudinal data in Figure 4.28 is the *model calculation*. The comparison between the longitudinal Fokker Planck model calculation, with inputs obtained from *independent* experimental measurements described in previous sections, and the experimental data for the widths σ is striking. The gain and gain slope, which were the average values obtained from signal suppression and from the open loop transfer function measurements, used in the calculation were $\langle G \rangle = 7.5 \times 10^{-4}$ Mev/sec, and $\tau = 2.5 \times 10^{-2}$ MeV $^{-1}$, respectively.

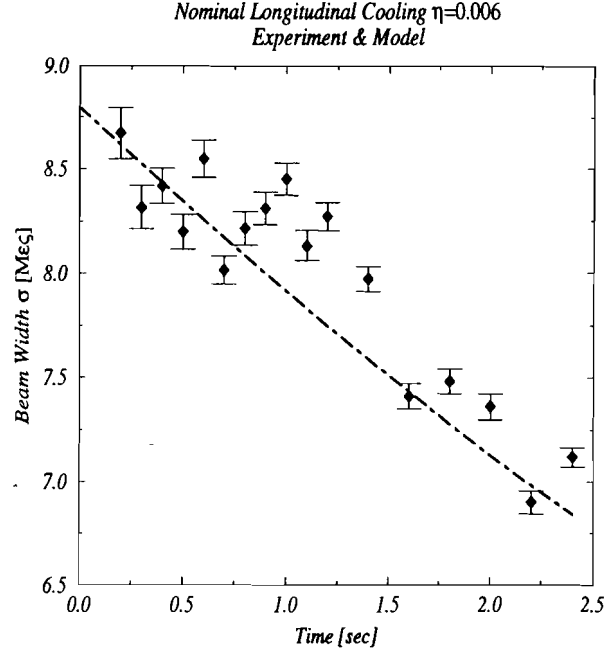


Figure 4.28: Comparison of beam width to model prediction with $\langle G \rangle = 7.5 \times 10^{-4}$ Mev/sec, $\tau_c = 2.5 \times 10^{-2} \text{MeV}^{-1}$.

From the calculated beam width σ , the mixing factor $M = 1./[\sqrt{\pi}\eta\sigma_p/p]$ may be obtained as an input to the transverse cooling model calculation. In the next section, comparisons between the experimental transverse cooling rates and the model calculations are presented.

4.6.1.5 Transverse model comparison with cooling rate measurement

The transverse cooling equation with experimental input parameters, now take the simpler form given by

$$\frac{d\epsilon_{\perp}}{dt} = -\epsilon_{\perp} \left[\frac{\langle g_{\perp} \rangle}{\langle \epsilon_{\perp}(t) \rangle} \right] + [\langle M(t) \rangle + \langle U_{\perp}(t) \rangle] \frac{|g_m(q_m\omega)|^2}{\langle |\epsilon_{\perp}(t)|^2 \rangle} \quad (4.72)$$

The quantities in Equation (4.72), have been obtained experimentally, and in particular, (i) $U_{\perp}(t)$ has been obtained throughout the cooling cycle, (ii) $\epsilon_{\perp}(t)$ is measured at the beginning of the cycle, (iii) the mixing factor $M(t)$ is obtained throughout the cycle from the longitudinal calculation for $\sigma_p(t)/p$, and (iv) the system gain g_{\perp} has been obtained through signal suppression and open loop network analyzer measurements.

Figure 4.29 is a plot of the measured peak power of the 127th harmonic vertical dipole Schottky line as a function of the production cycle. The measurement was made with zero frequency

span ($FS = 0\text{Hz}$), and a resolution bandwidth of 1.0kHz . As given in the previous discussions, the measured power in the transverse sideband is proportional to the transverse emittance. Superposed on the transverse spectra in Figure 4.29 is the result of the full calculation with the transverse calculation for ε_{\perp} with $\langle g_{\perp} \rangle = .007$, together with the calculated $\sigma_p/p(t)$, which enters through the mixing factor $\langle M(t) \rangle$. From the previous section, $\sigma_p/p(t)$ was obtained from the longitudinal Fokker-Planck equation with $\langle G_{\parallel} \rangle = 7.5 \times 10^{-4}\text{MeV/sec}$, $\sigma(t_o) = 8.64\text{MeV}$, and $\tau = 2.503 \times 10^{-2}\text{MeV}^{-1}$.

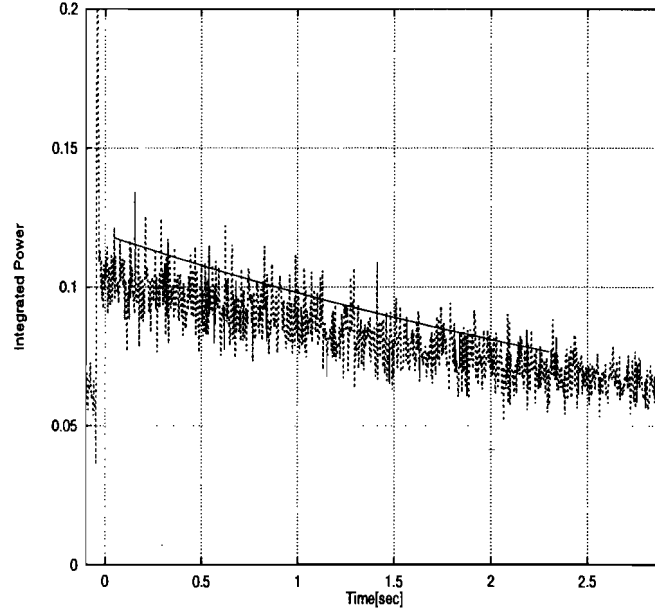


Figure 4.29: A comparison of the *measured integrated power* within the 127th harmonic vertical Schottky sideband as a function of time against the transverse cooling calculation. $\langle g_{\perp} \rangle = 7.0 \times 10^{-3}$

As another independent check, Figure 4.30 is a comparison between the full stochastic cooling model calculation and the experimental measurements of the integrated Schottky power in a transverse sideband at discrete times throughout the cooling cycle. The measurements of the Schottky sidebands were obtained with the vector signal analyzer and were subsequently fit to a Gaussian distribution. An integration of the the resulting curve is the total power contained in the sideband. From Figure 4.30, the model calculation predicts the cooling rates exceedingly well.

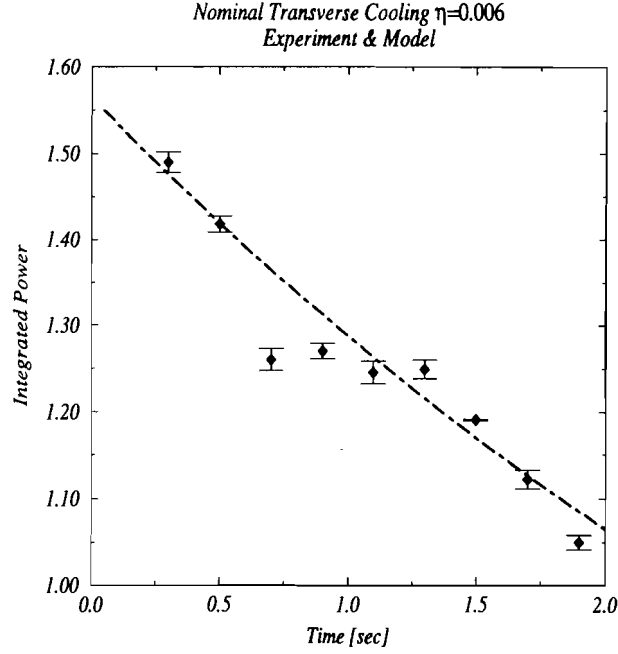


Figure 4.30: A comparison of the measured integrated vertical Schottky power obtained with Gaussian fits and the cooling model with $\langle g_{\perp} \rangle = 7.0 \times 10^{-3}$.

4.7 Chapter summary

The discussion of this chapter has been restricted to that of the present Debuncher stochastic cooling system, both through experimental measurements and through the description of a computer model based upon the well known stochastic cooling equations. Most striking is the success of the computer model in predicting the cooling rates for both the transverse and longitudinal systems. Furthermore, it has been demonstrated that the independent experimental determinations of fundamental system quantities are self-consistent with the computational results. Thus, the validity of stochastic cooling model, as described in this chapter, shall form the basis for further predictions of the model. Specifically, a summary of the experimental measurements for fundamental parameters of the cooling is given.

The *longitudinal noise/signal ratio* is defined by the parameterization $\mathcal{U}_{\text{therm}}^{\parallel}(x, t) \approx \left[\beta_n + \lambda_n / [\beta_s \sqrt{2\pi} \sigma(t) \psi(x, t) + (\lambda_s - \lambda_n)] \right]$, Averages obtained from the spectra fits are $\beta_s \approx .22 \times 10^{-2} \text{mWatt/Hz}$, $\beta_n \approx .13 \times 10^{-3} \text{mWatt/Hz}$, $\lambda_s \approx .43 \times 10^{-4} \text{mWatt/Hz}$, and $\lambda_n \approx .13 \times 10^{-4} \text{mWatt/Hz}$.

The *transverse noise/signal ratio*, \mathcal{U}_\perp were measured across the stochastic cooling band and throughout the production cycle; measurements at the beginning of the cycle ($\Delta t = .1sec$) are (a) 2.2GHz $\mathcal{U}^\perp(q_m\omega) = 4.98$, (b) 3.0GHz $\mathcal{U}^\perp(q_m\omega) = 5.04$, and (c) 3.8GHz $\mathcal{U}^\perp(q_m\omega) = 4.84$, (iii) throughout the cooling cycle $\mathcal{U}^\perp(q_m\omega)$ is given by (a) $\mathcal{U}^\perp(t = 0.1sec) = 6.25$, (b) $\mathcal{U}^\perp(t = 0.5sec) = 8.33$, (c) $\mathcal{U}^\perp(t = 1.0sec) = 14.9$, and (d) $\mathcal{U}^\perp(t = 2.2sec) = 20.0$.

The *longitudinal system gain*, G_\parallel were found from signal suppression measurements From the signal suppression measurements at 3.2GHz and with $N = 4.0 \times 10^7$ as a function of time, (a) $\langle G_\parallel(0.15sec) \rangle 8.73 \times 10^{-4} \text{MeV/sec}$, (b) $\langle G_\parallel(0.25sec) \rangle 8.64 \times 10^{-4} \text{MeV/sec}$, and (c) $\langle G_\parallel(0.35sec) \rangle 8.54 \times 10^{-4} \text{MeV/sec}$. Open loop network analyzer measurements were also used for obtaining the system gain as an independent check. At three frequencies across the microwave band, the results are: (a) 2.1GHz $G_\parallel = 7.35 \times 10^{-4} \text{MeV/sec}$, (b) 3.0GHz $G_\parallel = 6.88 \times 10^{-4} \text{MeV/sec}$, and (c) 3.8GHz $G_\parallel = 7.82 \times 10^{-4} \text{MeV/sec}$.

The *longitudinal gain slope*, τ was obtained across the cooling bandwidth through measurements of the noise signal through the notch filter. Results of the measurement is: $\langle \tau \rangle = 2.58 \times 10^{-2} \text{MeV}^{-1}$.

The *transverse system gain* was obtained through transverse signal suppression measurements and the results are given by: (a) $\langle g_\perp^m(2.2GHz) \rangle = 0.008$, (b) $\langle g_\perp^m(3.0GHz) \rangle = 0.017$, and (c) $\langle g_\perp^m(3.2GHz) \rangle = 0.013$. Open loop network analyzer measurements have also been used to confirm the values obtained from the signal suppression results. The transverse system gain extracted from the $(S_\perp)_{21}$ measurements are: (a) $\langle g_\perp^m(2.1GHz) \rangle = 0.0075$, (b) $\langle g_\perp^m(3.0GHz) \rangle = 0.005$, and (c) $\langle g_\perp^m(3.8GHz) \rangle = 0.0077$.

The *computational model* utilizes the measured phenomenologic results in order to calculate the evolution of the longitudinal distribution function. Thus, given the equation,

$$\frac{\partial \psi(x, t)}{\partial t} = -\frac{\partial}{\partial x} \left[S_1(x, t) - S_2(x, t) \right]$$

the two terms have been evaluated in terms of digamma functions and are given by:

$$S_1(x, t) = \psi(x, t) \sum_{m_1 \leq m \leq m_2} \text{Real} \left[\frac{G_m(x)}{\epsilon_m(x, t)} \right] = \frac{G_{\Re, m} \epsilon_{\Re, m} + G_{\Im, m} \epsilon_{\Im, m}}{\epsilon_{\Re, m}^2 + \epsilon_{\Im, m}^2}$$

$$S_2(x, t) = \psi(x, t) \frac{\partial \psi}{\partial x} N \pi \bar{k} \sum_m \frac{1}{m} \frac{|G_m(x)|^2}{|\epsilon_m(x, t)|^2} \left\{ 1 + \mathcal{U}_m(x) \right\}$$

Evaluation of $S_1(x, t)$ and $S_2(x, t)$ form the basis of a *calculation for the beam distribution* $\psi(x, t)$ from the full Fokker Planck equation. From the second moment of the distribution the beam width is obtained

$$\langle \sigma(t)^2 \rangle = \int x^2 \psi(x, t) dx$$

A comparison between the model calculation of $\sigma(t)$ and the experimental measurement were in excellent agreement.

The *transverse emittance* calculation is performed by using the calculated longitudinal beam width $\sigma(t)$ for the mixing factor. Comparison between the experimental integrated transverse side-band power agrees well with the calculation, which utilizes the independent phenomenologic inputs.

CHAPTER 5

THE STOCHASTIC COOLING RESULTS WITH A DYNAMIC $\Delta\gamma_t$

5.1 Introduction

The first two chapters have addressed several technical issues for obtaining a dynamic $\Delta\gamma_t$ lattice. Experimental measurements of the fundamental lattice parameters have also been presented and compared with predictions. In the previous chapter, stochastic cooling phenomenology in the Antiproton Debuncher has been discussed through measurements and through a model based upon a Fokker Planck equation. Within this chapter, the major experimental results of the dynamic $\Delta\gamma_t$ project are presented, which demonstrate improvements to stochastic cooling rates based upon a reduction in the mixing factor.

5.1.1 Beam Loss Normalization: T_γ

To normalize out the beam loss effects due to transverse resonance (stop-band) crossing during the $\Delta\gamma_t/\Delta t$ ramps, both indirect and direct measurements of cooling parameters were made as a function of T_γ , which is defined as the total time duration in which the $\gamma_t^{(f)}$ lattice configuration is maintained, and is indicated in the \bar{p} production time-line of Figure 5.1. Therefore, if resonance crossing occurs only during the $\Delta\gamma_t/\Delta t$ slew due to associated current regulation errors, then each set of measurements *as a function of T_γ* will incur the same amount of beam loss. In counterpoint, if the final low $\gamma_t^{(f)}$ lattice configuration is on or near a stop-band resonance, then longer T_γ will incur more beam loss, and give the appearance of cooling, at least through a reduction in transverse Schottky power. In order to absolutely guarantee that the latter scenario is not a factor, and any beam loss occurs *only* during the $\Delta\gamma_t/\Delta t$ slew process, a fundamental and necessary check is through a measurement of the total integrated longitudinal Schottky power, triggered at the beginning and end of the cycle. These measurements correspond to measuring the total number of particles as a function of T_γ . Therefore, as long as a stopband resonance is not encountered with $\gamma_t^{(f)}$, the number of particles will be independent of T_γ for both the beginning and end of the cycle.

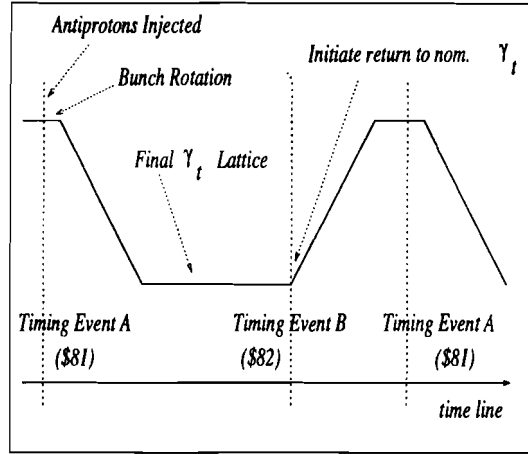


Figure 5.1: Time line and trigger events for defining T_γ during \bar{p} production cycle.

In Figure 5.1, (i) the relevant trigger events for the $\Delta\gamma_t/\Delta t$ ramps are indicated, and (ii) as mentioned previously, the quantity $T_\gamma = |T_A(\$81) - T_B(\$82)|$ is defined specifically for the trigger events. The sequence of events indicated in the time line of Figure 5.1 for the dynamic $\Delta\gamma_t$ ramps are as follows: (1) instructions to programmable CAMAC modules are sent out on a timing event A (a TCLK \$81 Tevatron clock event in FNAL parlance), (2) the 465/468 programmable CAMAC ramp modules initiate the $\Delta\gamma_t/\Delta t$ ramp $\gamma_t^{(i)} \rightarrow \gamma_t^{(f)}$ by sending analog reference signals to the magnet current shunt circuits (and power supplies¹); (3) the low $\gamma_t^{(f)}$ lattice is maintained until the event B occurs, which triggers the return $\Delta\gamma_t/\Delta t$ ramp $\gamma_t^{(f)} \rightarrow \gamma_t^{(i)}$. For each change of the timing delay between the \$82 and \$81 TCLK events², which is by definition T_γ , the performance parameters and Schottky signals (both transverse and longitudinal and triggered at the beginning and end of the cycle), were measured by averaging over several production *super-cycles* ($\sim 10 - 15$ minutes).

5.1.2 The Measurements

There are two types of data which were used to investigate the cooling effects of the dynamic $\Delta\gamma_t$ lattice, (a) direct measurement of the transverse and longitudinal Schottky signals, and (b) indirect measurements through several standard Antiproton Source *performance parameters*, which include (i) Debuncher \bar{p} yield (YIELD), (ii) the Debuncher to Accumulator transfer efficiency (DAE),

¹Digital reference current values are sent to the power supplies, whereas an analog reference signal is sent to each of the magnet current shunt circuits

²Actually, the trigger event \$82 is variable and is referenced to $\$81 + \tau$, for which τ is the adjustable time delay.

(iii) the Accumulator stacking efficiency (ASE), and perhaps most important, (iv) the average stack rate (SR)³. In either case, measurements were made as a function of the time duration, T_γ , which has been defined as the *total time within the production cycle for which the lattice has the final value* $\gamma_t^{(f)} (\eta = 0.0093)$

Direct measurements of the transverse and longitudinal cooling through Schottky spectra provide the best determination of the effect due to the increase in the momentum compaction factor (small $\gamma_t^{(f)}$). Moreover, the results of fits to the Schottky spectra are directly amenable to comparisons with the predictions obtained from the stochastic cooling model. The agreement between the stochastic cooling model predictions and the observed longitudinal widths and transverse emittance, as a function of T_γ , shall be presented for the two cases: (i) $\frac{4}{5}\Delta\gamma_t^{(f)}/300\text{msec}$ and (ii) $\Delta\gamma_t^{(f)}/300\text{msec}$.

With regard to the indirect measurement effects of the dynamic $\Delta\gamma_t$ lattice, i.e. the *performance parameters*, a theoretical prediction is not readily apparent due to the large number of competing effects. Instead, empirical data shall be given to corroborate (i) the direct Schottky measurements of improved precooling as a function of T_γ , and (ii) the claim that improved precooling improves the overall performance of the Antiproton Source.

5.2 Indirect Experimental Results: The performance parameters

Within this section, three sets of data shall be presented for the indirect performance parameter results: (i) $\frac{1}{3}\Delta\gamma_t^f/300\text{msec}$, (ii) $\frac{4}{5}\Delta\gamma_t^f/300\text{msec}$, and (iii) $\Delta\gamma_t^f/300\text{msec}$. For the first data set, only the performance parameters were recorded, however, for the last two data sets, the direct measurements of the Schottky spectra were measured at injection into the Debuncher and just before extraction. A full summary of the results shall be given in the last section of the chapter.

³A more detailed description is as follows: (i) the *yield* is obtained by measuring the total Schottky power obtained from the longitudinal monitor in the Debuncher, divided by the amount of beam current targeted from a measure of the injection line toroid (M:TOR109). (ii) *Debuncher/Accumulator efficiency*, is the ratio of the amount of beam which is transferred into the Accumulator from the total integrated Schottky power (A:FFTTOT), divided by the total Schottky power (D:FFTTOT) in the Debuncher, (iii) the *Accumulator efficiency* is the total beam power on the Accumulator injection orbit, which is averaged over a super-cycle, divided by the average number of antiprotons stacked, i.e. accumulator efficiency $\sim \text{A:FFTTOT}/\text{A:STCKRT}$, (iv) the *stack rate* is the total antiproton beam current, averaged over one *super-cycle* ($200\text{sec}/2.4\text{sec} = 83$ production cycles)

5.2.1 The early data: $\frac{1}{3}\Delta\gamma_t^f$

During the initial commissioning of the γ_t project, it was realized rather quickly that power supply regulation was a non-trivial problem which threatened even modest $\Delta\gamma_t/\Delta t$ slew rates. Indeed the second chapter demonstrated that a feedforward system is an essential feature for a dynamic $\Delta\gamma_t$.

While testing and *working out the details* of the feedforward system early in the commissioning of the dynamic $\Delta\gamma_t/\Delta t$ project, preliminary measurements of performance parameters provided the first indications of cooling as a function of T_γ , i.e. first indication that the cooling rate did increase because of a reduction in the mixing factor. Figures 5.2 and 5.3 are the results of (a) the Debuncher yield, (b) the Debuncher to Accumulator efficiency, (c) the Accumulator stacking efficiency, and (iv) the averaged stack rate, as a function of T_γ for these initial measurements for $\frac{1}{3}\gamma_t^{(f)}/300\text{msec}$ (flat top of $\eta^{(f)} = .007$).

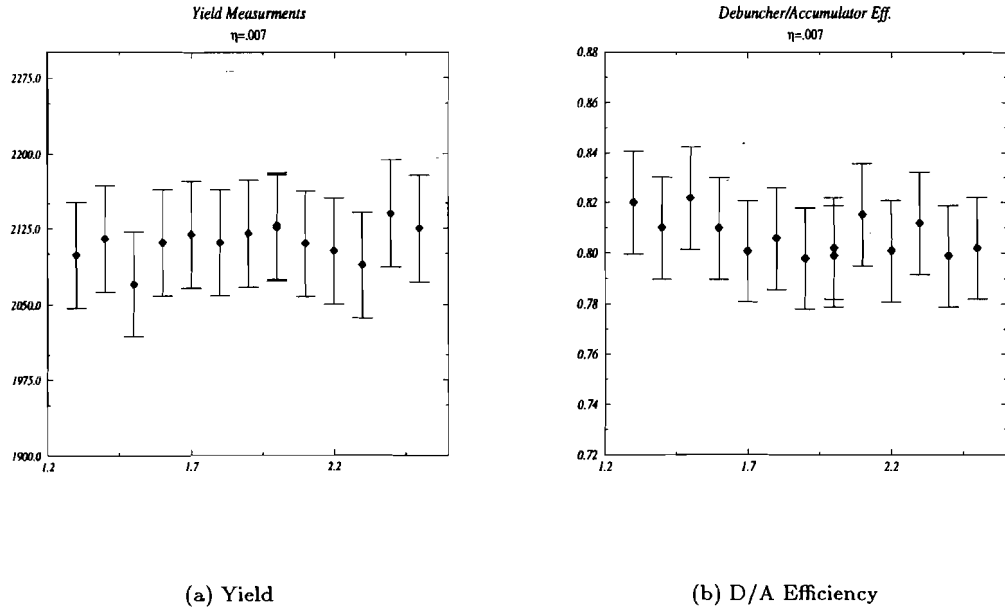


Figure 5.2: The performance parameters (a) yield, and (b) D/A Efficiency, as a function of T_γ for $\frac{1}{3}\Delta\gamma_t/300\text{msec}(\eta = .007)$.

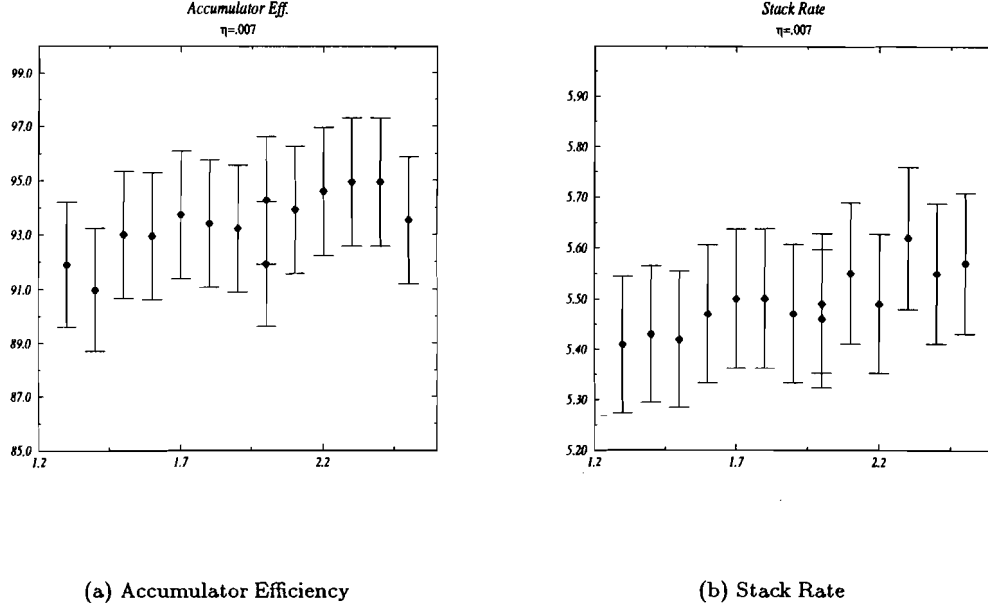


Figure 5.3: The performance parameters (a) Accumulator efficiency and (b) stack rate, as a function of T_γ for $\frac{1}{3}\Delta\gamma_t/300\text{msec}(\eta = .007)$.

Within each of the plots of 5.2 and 5.3, the error bars correspond to the standard deviation of measurements taken with approximately 250 production pulses per point. Furthermore, in order to avoid systematic effects in the measurements given in Figures 5.2 and 5.3, each subsequent T_γ measurement was preceded with a return to the nominal *static* lattice configuration with $\gamma_t^{(i)}$, for a period corresponding to several super-cycles. A new value of T_γ was chosen, which was out of sequence from the previous value, alternating between large and small time delay values.

From Figure 5.2(a), the *yield* into the Debuncher is constant as a function of T_γ , which indicates that any trend in the data cannot be accounted by variations of particle flux. Figure 5.3(a) and 5.3(b), give the first *suggestion* of improved cooling through the small increase in Accumulator efficiency and the stack rate. Utilizing linear least square fits to the data of Figure 5.2, and 5.3 the *time rate of change* in each of the parameters is given by the slopes: (i) $AE/\text{time} \sim 2.92 \pm 0.6$, which corresponds to a fractional change $\sim 4.8\%$, and (ii) $SR/\text{time} \sim 0.14 \pm 0.03$ which corresponds to a fractional change $\sim 3.8\%$.

5.2.2 $\frac{4}{5}\Delta\gamma_t^{(f)}/300\text{msec}$ and $\Delta\gamma_t^{(f)}/300\text{msec}$: Performance Parameters

Figures 5.4 and 5.5 are plots of performance parameter data for $\frac{4}{5}\Delta\gamma_t^{(f)}$ (corresponding to $\eta^{(f)} = .0085$). The procedure for obtaining the performance data was identical to that described in the previous section for the $\frac{1}{3}\Delta\gamma_t$ for the T_γ data. In particular, the error bars are obtained by taking the standard deviation of the distribution in performance parameter values taken over several production *super-cycles*. Systematics were eliminated by returning the lattice to the nominal value prior to the measurement of a new T_γ value. Also the values of T_γ were chosen with an alternating sequence to avoid any correlations between measurements.

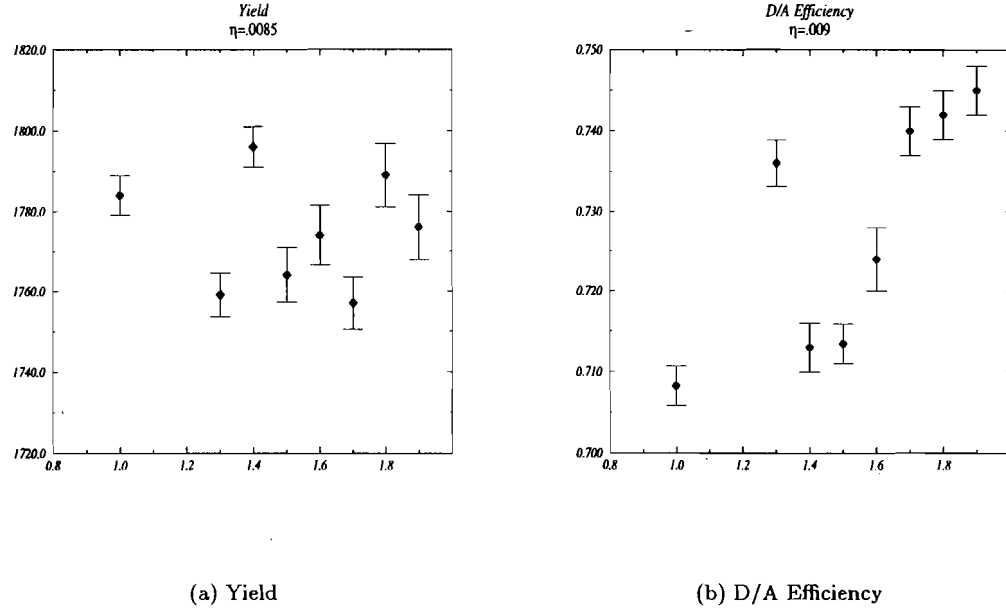


Figure 5.4: The performance parameters for $\frac{4}{5}\Delta\gamma_t^{(f)}/300\text{msec}$ ($\eta = 0.0085$).

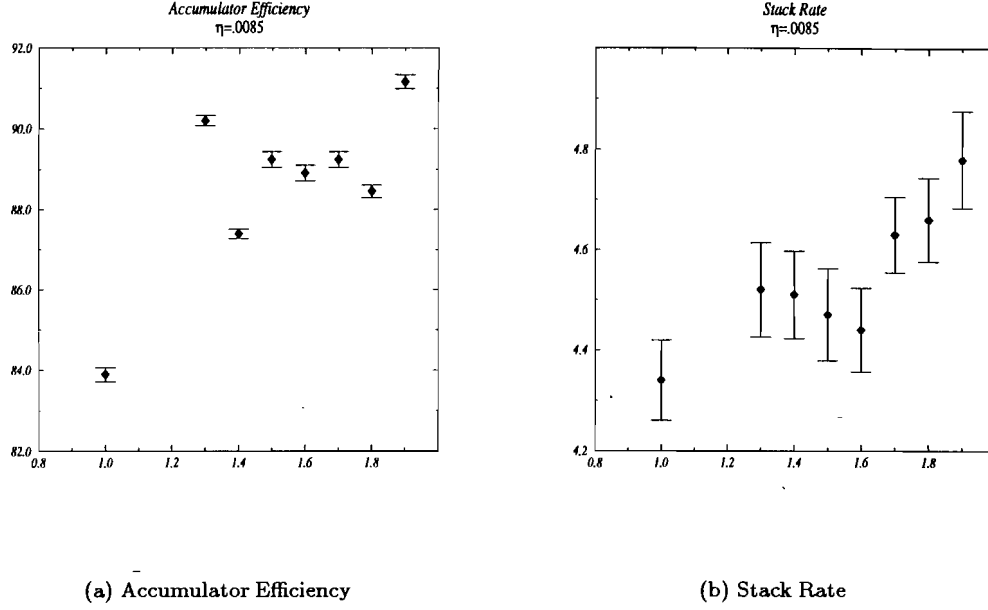
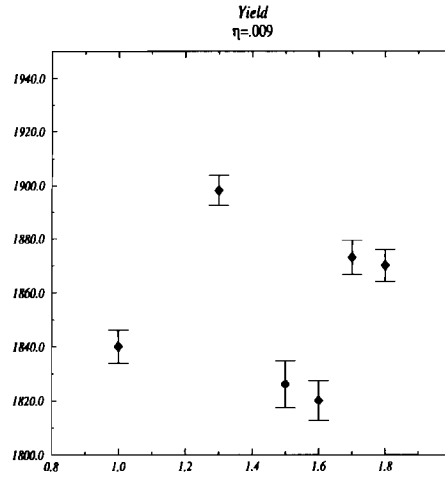


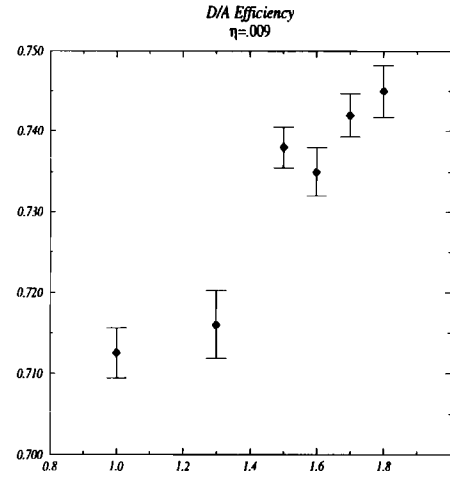
Figure 5.5: The performance parameters for $\frac{4}{5}\Delta\gamma_t^{(f)}/300\text{msec}(\eta = 0.0085)$.

Least square fits for obtaining the fractional change of the performance parameters of Figure 5.4 and 5.5 for the $\frac{4}{5}\Delta\gamma_t^{(f)}/300\text{msec}$ versus T_γ data are given by: (i) D/A versus time $\sim 0.38 \pm .01$, corresponding to a fractional change in the D/A efficiency of $\sim 7.3\%$, (ii) AE/time $\sim 5.5 \pm 1.1$ corresponding to a fractional change in AE of $\sim 10.3\%$, and (iii) SR/time 0.41 ± 0.1 , which corresponds to a fractional change in SR of $\sim 14.7\%$.

The *performance parameter* data for $\Delta\gamma_t^{(f)}$ is given in Figures 5.6 and 5.7. Again, to eliminate systematics, the time delay T_γ was always chosen concurrently between small and large values, not monotonically increasing or decreasing. Furthermore, each T_γ measurement point is separated by approximately 15 minutes, and between each point the performance parameters were measured with the nominal lattice.

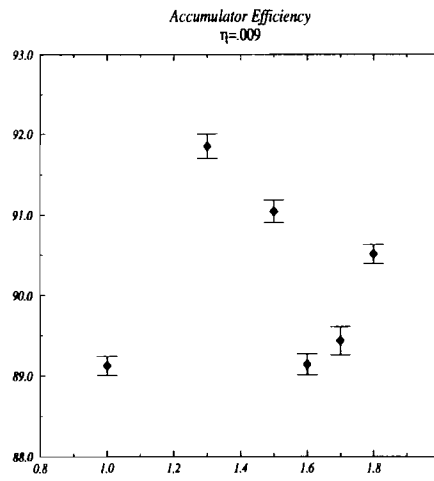


(a) Yield

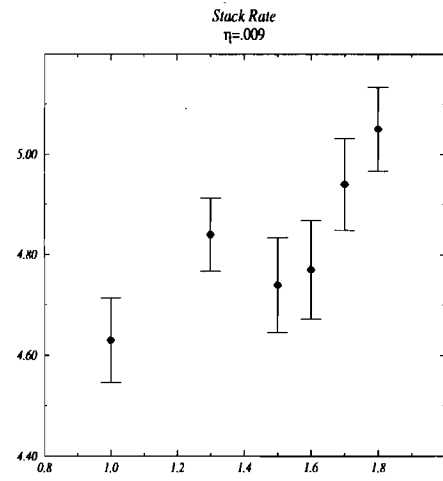


(b) D/A Efficiency

Figure 5.6: The performance parameters for $\Delta\gamma_t^{(f)}/300\text{msec}(\eta \approx 0.0093)$.



(a) Accumulator Efficiency



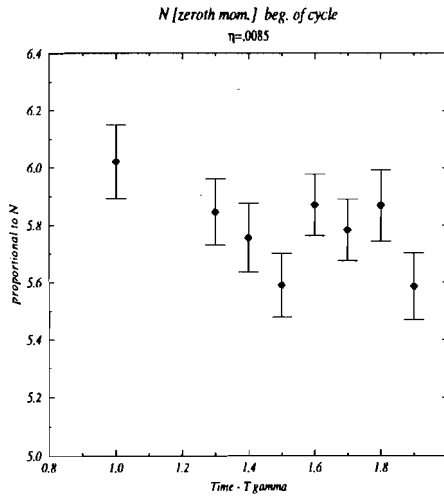
(b) Stack Rate

Figure 5.7: The performance parameters for $\Delta\gamma_t^{(f)}/300\text{msec}(\eta \approx 0.0093)$.

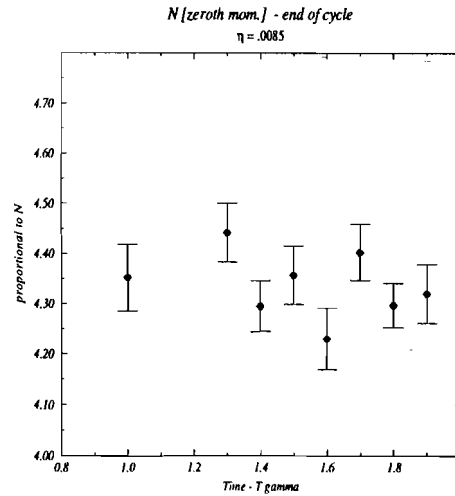
The fractional change in each parameter in Figures 5.6 and 5.7 for $\Delta\gamma_t^{(f)}$ versus T_γ are obtained with least square fits. The results of the fits are: (i) D/A *versus* time $\sim 0.04 \pm .007$, corresponding to a fractional change in the D/A efficiency of $\sim 9.0\%$, (ii) AE/time was inconclusive, and (iii) SR/time 0.42 ± 0.1 , which corresponds to a fractional change in SR of $\sim 13.4\%$.

5.2.2.1 Particle Number as a function of T_γ

In order to justify the validity of the performance parameter data obtained for the $\frac{4}{5}\Delta\gamma_t^{(f)}/300\text{msec}$ and $\Delta\gamma_t/300\text{msec}$ cases, Figures 5.8 and 5.9 are plots of the total integrated longitudinal Schottky power as a function of T_γ , respectively, at the beginning and the end of the cycle. Since, the integrated power $\mathcal{P} = \beta_1 \exp\left\{\frac{-(x-\alpha_1)^2}{2\alpha_2^2}\right\} + \alpha_3$ is proportional to the number of particles in the beam $\mathcal{N}(T_\gamma) = \int_{-\infty}^{\infty} dx' \psi(x', t) \sim \beta_1 \alpha_2$, the results underscore the fact that particle loss has been factored out of the data as a function of T_γ .

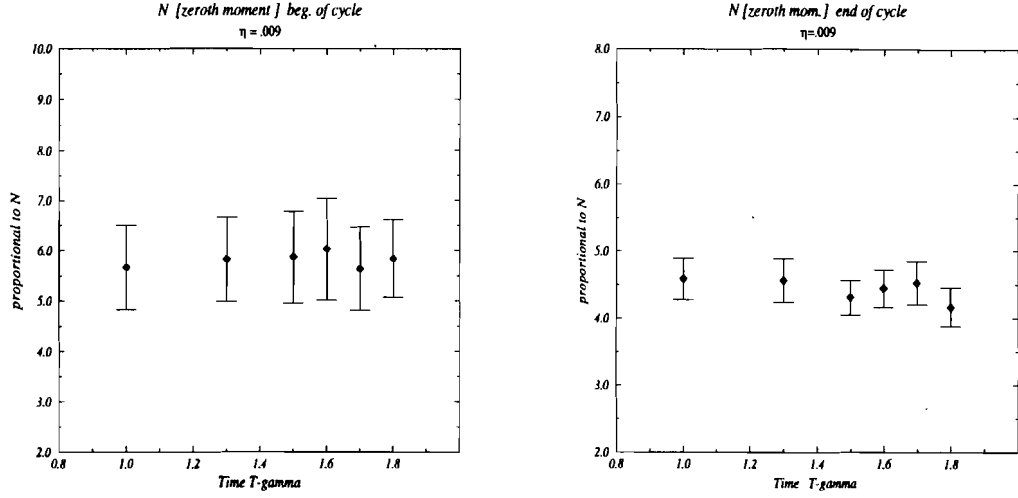


(a) $\mathcal{N}(T_\gamma)$ beginning of \bar{p} production cycle.



(b) $\mathcal{N}(T_\gamma)$ end of \bar{p} production cycle.

Figure 5.8: The measured zeroth moment of the longitudinal distribution *versus* T_γ for $\frac{4}{5}\Delta\gamma_t^{(f)}$ ($\eta = 0.0085$).



(a) $N(T_\gamma)$ beginning of \bar{p} production cycle.

(b) $N(T_\gamma)$ beginning of \bar{p} production cycle.

Figure 5.9: The measured zeroth moment of the longitudinal distribution *versus* T_γ for γ_t^f ($\eta = 0.009$).

5.3 Direct Cooling Measurements and Debuncher Cooling Model

Similar to the procedure outlined in chapter 3, and from the discussion of the previous section pertaining to the number of particles as function of T_γ , gaussian fits with $\mathcal{P} = \beta_1 \exp\left\{\frac{-(x-\alpha_1)^2}{2\alpha_2^2}\right\} + \alpha_3$ to the longitudinal and transverse Schottky spectra provide a direct measure of stochastic cooling performance and comparison with model calculation. The results of the fits to the longitudinal and transverse spectra as a function of T_γ shall be presented in this section. First, a discussion of the Debuncher stochastic cooling model predictions as a function of T_γ shall be given, both to motivate the experimental data and to explain the model calculation. Next, the longitudinal widths and peak transverse power (proportional to the transverse emittance) shall be presented for the two cases $\frac{4}{5}\Delta\gamma_t^{(f)}/300\text{msec}$ and $\Delta\gamma_t/300\text{msec}$, together with the result of the model predictions. Finally, the next section presents a summary of all the results, direct and indirect.

5.3.1 Theory: The Debuncher Stochastic Cooling Model

The Debuncher stochastic cooling model, described in the previous chapter, has been used to predict the final longitudinal beam width and the transverse emittances as a function of T_γ . As input to the model calculations, both longitudinal and transverse signal suppression data are used to extract $\langle G_\parallel \rangle$ and g_\perp respectively.

With the input parameters for both the longitudinal and transverse calculation, numerical integration is used to calculate the longitudinal width $\sigma_f(t; T_\gamma)$ and the final transverse emittance, $\varepsilon_f(T_\gamma)$, for a comparison with the experimental data for the dynamic γ_i^f lattice. The details of the calculation are given in the following two steps: (i) the longitudinal calculation is performed first, obtaining $M(t; T_\gamma)$ through σ_p/p from the integrating the partial differential equation with a flux

$$\frac{\partial \psi}{\partial t} = \frac{\partial}{\partial x} \begin{cases} \psi(x) \sum_m \Re \left[\frac{G_m(x)}{\epsilon_m(x; \gamma_i^f)} \right] - \psi(x) \frac{\partial \psi}{\partial x} \frac{\beta^2 E}{2\eta_f f_0} \sum_m \frac{1}{m} \frac{|G_m(x)|^2}{|\epsilon_m(x; \gamma_i^f)|^2} \left\{ 1 + \mathcal{U}_m(x) \right\} & t_i < t < T_\gamma \\ \psi(x) \sum_m \Re \left[\frac{G_m(x)}{\epsilon_m(x; \gamma_i^i)} \right] - \psi(x) \frac{\partial \psi}{\partial x} \frac{\beta^2 E}{2\eta_i f_0} \sum_m \frac{1}{m} \frac{|G_m(x)|^2}{|\epsilon_m(x; \gamma_i^i)|^2} \left\{ 1 + \mathcal{U}_m(x) \right\} & \text{otherwise} \end{cases} \quad (5.1)$$

where $\eta_f = 1/\gamma_{if}^2 - 1/\gamma_o^2$; (ii) a calculation of the final emittance, $\varepsilon_\perp^f(T_\gamma)$, is found by integrating

$$\frac{1}{\varepsilon_\perp} \frac{d\varepsilon_\perp(t)}{dt} = \begin{cases} F(\sigma, \gamma_i^f) = -\langle g_\perp \rangle \frac{W}{N} + \langle |g_\perp|^2 \rangle \frac{W}{N} [M(\gamma_i^f) + U] & t_i < t < T_\gamma \\ F(\sigma, \gamma_i^i) = -\langle g_\perp \rangle \frac{W}{N} + \langle |g_\perp|^2 \rangle \frac{W}{N} [M(\gamma_i^i) + U] & \text{otherwise} \end{cases} \quad (5.2)$$

An expression for the final emittance as a function of the time T_γ is $\varepsilon_f(T_\gamma) = \int_0^{t_f} \Theta_\perp(t) dt$. Since the mixing factor is reduced for $t_i < t < T_\gamma$, the rate of cooling should increase and thus the final transverse emittance should decrease.

5.3.2 The full results as function of T_γ

The full results of the direct stochastic cooling measurements from the longitudinal and transverse Schottky signals, recorded at the beginning and end of production/cooling cycle, are given for both the $\frac{4}{5} \Delta \gamma_i^f / 300 \text{msec}$ and $\Delta \gamma_i^f / 300 \text{msec}$ case.

From the fitting parameters defined in the introduction of this section, the power in a transverse Schottky sideband is given by $P \sim \alpha_2 \beta_1$. Since the power density of the transverse (dipole) Schottky spectrum is given by $\langle P_d \rangle \sim q^2 N f_n^2 \langle A^2 \rangle \psi(f_n)$ [23] the power from the fits, $P = \alpha_2 \beta_1$ is proportional to the beam emittance. At the beginning of the \bar{p} production cycle the plot of $\alpha_2 \beta_1$

as a function of T_γ should be flat, indicating the same pulse intensity at the start of the cycle. For those measurements at the end of the cycle β_1 should be a monotonically decreasing function of T_γ .

5.3.2.1 The $\frac{4}{5}\gamma_i/300\text{msec}$ Results

The result of the beam widths from fits to the longitudinal Schottky spectra at the beginning of the cycle (triggered 0.2sec from an S81 event) and at the end of the cycle (triggered at 2.2sec from an S81 event) are given in Figures 5.10(a) and (b), respectively, for the $\frac{4}{5}\gamma_i^f/300\text{msec}$ case. Superposed upon the data in Figure 5.10(b) is the result of the longitudinal stochastic cooling calculation. The model predicts a change in the final width σ_f with T_γ for $\frac{4}{5}\gamma_i^f/300\text{msec}$ of $\Delta\sigma_f/T_\gamma \sim .25\text{MeV/sec}$, which corresponds to a fractional change of σ_f of $\approx 3.9\%$.

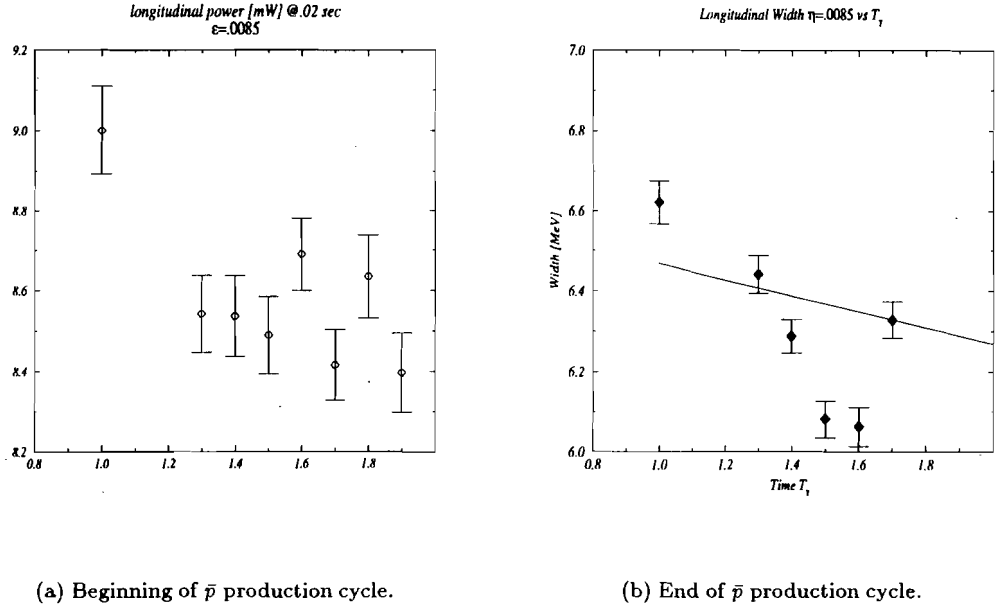


Figure 5.10: The measured longitudinal widths *versus* T_γ for $\frac{4}{5}\gamma_i^f/300$ msec ($\eta = 0.0085$) together with results of the longitudinal stochastic cooling model, with inputs to the cooling model, $\langle G \rangle = 2.5 \times 10^{-4}\text{MeV/sec}$ and $\tau_c = .02051/\text{MeV}$.

The results of the integrated transverse dipole (sideband) power (in mWatts) is given in Figures 5.11 for the beginning and the end of the cycle, respectively. As mentioned in the previous paragraph, the integrated transverse sideband power density is proportional to the beam emittance. Therefore, Figure 5.11 indicates that the initial beam emittance as a function of T_γ is a constant

~ 0.16 mWatts. At the end of the cycle, the emittance is a monotonically decreasing function of T_γ , indicating an increased cooling as a function of a reduced mixing factor.

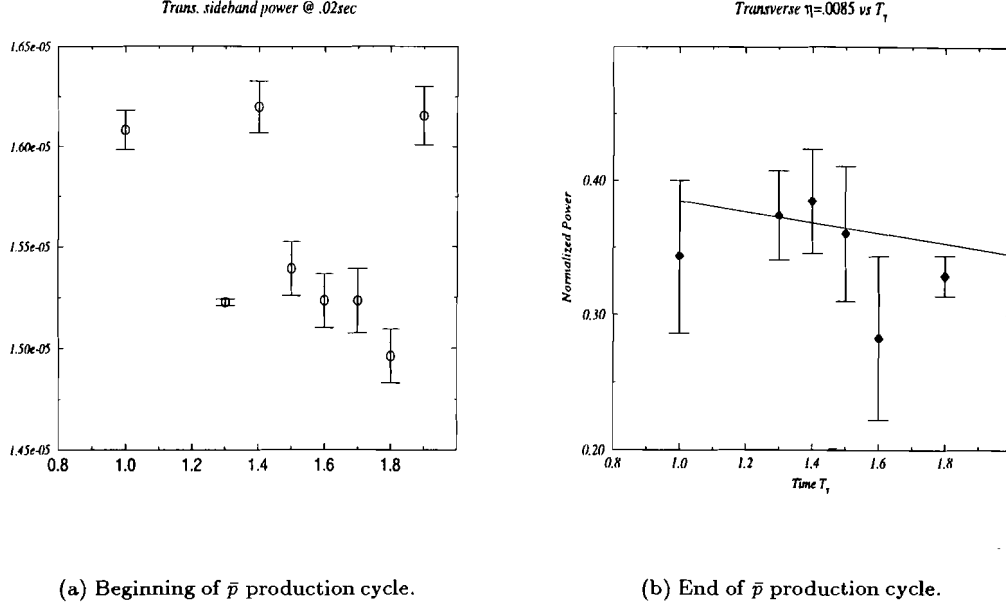
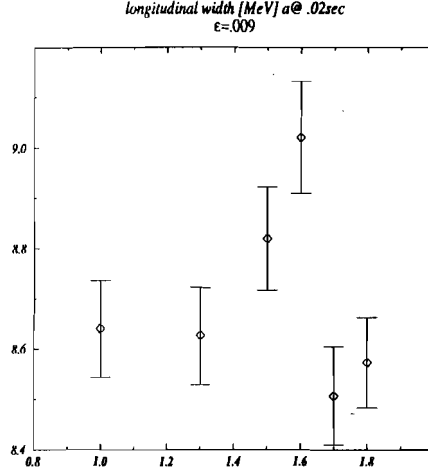


Figure 5.11: Transverse Schottky sideband power *versus* T_γ for $\frac{4}{5}\gamma_t^f/300$ msec ($\eta = .0085$) at the beginning and the end of the cycle.

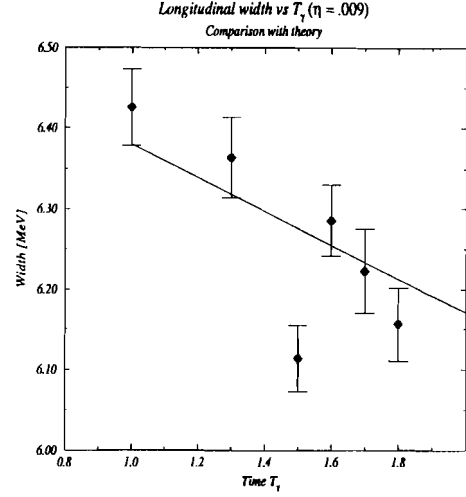
The model calculation, which is compared with the data in Figure 5.11, predicts a change of the integrated transverse power ($\sim \epsilon$) with T_γ of $\Delta\epsilon/\Delta T_\gamma \approx .032$ mWatts/sec, which corresponds to a fractional change in ϵ of $\approx 7.0\%$.

5.3.2.2 The $\Delta\gamma_t^{(f)}/300$ msec Results

Results of the measured widths to the longitudinal Schottky spectra triggered at the beginning and end of cycle are given in Figure 5.12 for the case of $\Delta\gamma_t^{(f)}/300$ msec. The model calculation for the final widths σ_f , predicts a change of σ_f with T_γ of $\Delta\sigma_f/\Delta T_\gamma \approx .25$ MeV/sec which corresponds to a fractional change in σ_f of $\approx 4.1\%$.



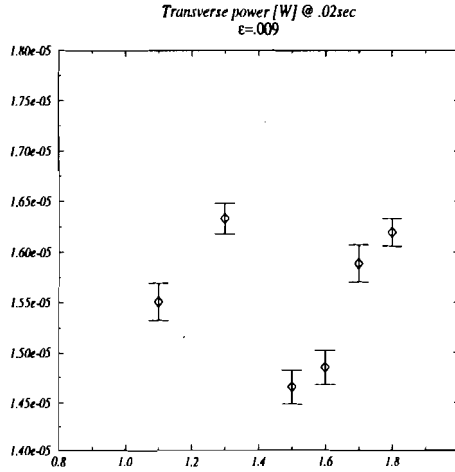
(a) Beginning of \bar{p} production cycle.



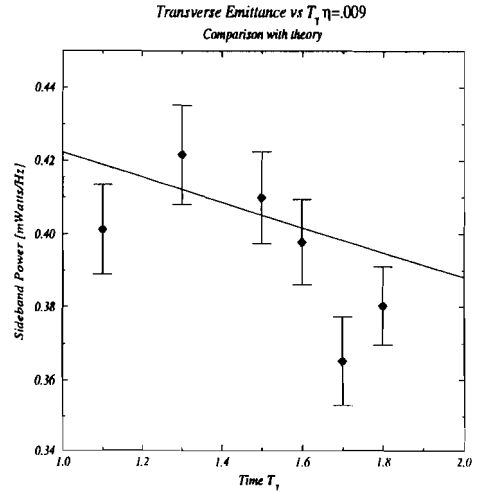
(b) End of \bar{p} production cycle.

Figure 5.12: The measured longitudinal widths *versus* T_γ for $\Delta\gamma_i^{(f)}/300$ msec ($\eta = 0.0094$) together with cooling model results for inputs: $\langle G \rangle = 2.5 \times 10^{-4}$ and $\tau_c = .0205$.

The results of the transverse dipole power density (in mWatts) is given in Figures 5.13 for the beginning and the end of the cycle, respectively.



(a) Beginning of \bar{p} production cycle.



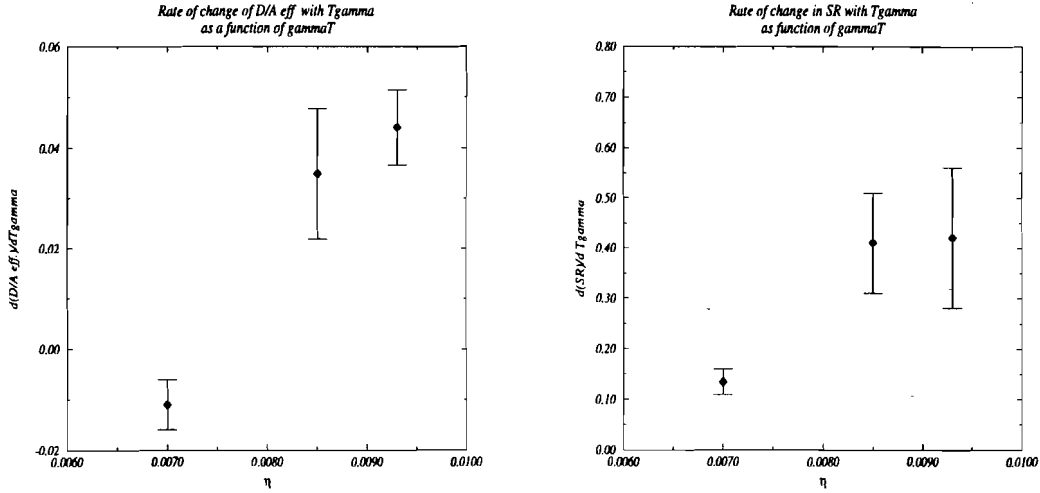
(b) End of \bar{p} production cycle.

Figure 5.13: Transverse Schottky sideband power *versus* T_γ for $\Delta\gamma_i^{(f)}/300$ msec ($\eta = .0094$) at the beginning and the end of the cycle.

Figure 5.13 indicates that the rate of change in a quantity proportional to the emittance ϵ with T_γ is $\Delta\epsilon/\Delta T_\gamma \approx 0.032$, which corresponds to a fractional change in ϵ of $\sim 7.6\%$.

5.4 Summary $\Delta\gamma_i^f$ versus T_γ : Indirect and Direct

As a comparison between the different sets of data, Figures 5.14 (a) and (b) are summary plots of the rate of change of (i) the D/A efficiency with T_γ , $\mathcal{R}_{DA} = \partial DAE/\partial T_\gamma(\eta)$, and (iii) the stack rate with T_γ , $\mathcal{R}_{SR} = \partial SR/\partial T_\gamma(\eta)$, respectively. Despite the low statistics with η , Figures 5.14(a) and (b), represent the predominant motivation for a dynamic $\Delta\gamma_i$ lattice.



(a) Debuncher to Accumulator transfer efficiency as a function of η .

(b) Stack Rate efficiency as a function of η .

Figure 5.14: Experimentally determined dependence of T_γ upon the the Debuncher/Accumulator efficiency and the stack rate for three values of η .

In particular, Figure 5.14(a) indicates that $\Delta\mathcal{R}_{DA}/\Delta\eta \approx 28.0$ for values of $\eta \leq 0.008$, while the rate drops off to $\Delta\mathcal{R}_{DA}/\Delta\eta \approx 16.3$ between $\eta = 0.008$ and $\eta = 0.0095$. Therefore, although there is still an improvement for larger η , the effect does begin to saturate.

Since the \bar{p} stacking rate is intimately related to the Debuncher/Accumulator efficiency, the rapid fall off of $\mathcal{R}_{SR} = \partial SR/\partial T_\gamma(\eta)$ with larger η witnessed in the data of Figure 5.14(b) is not surprising. Indeed, at smaller values of η ($\eta \leq 0.008$), $\Delta\mathcal{R}_{SR}/\Delta\eta \approx 18.$, while in the range $0.008 \leq \eta \leq 0.0095$, $\Delta\mathcal{R}_{SR}/\Delta\eta \approx 10.$

Collectively, these statements, summarized by Figures 5.14(a) and (b), suggest the rate of stack rate improvement diminishes for increasing η . In the next chapter, calculations with the full Fokker Planck model shall investigate the η dependence of the cooling rates further, with the present stochastic cooling parameters and extrapolation into a regime of higher particle flux and higher system gain.

5.5 Chapter Summary

The experimental results of the dynamic $\Delta\gamma_i$ have been reviewed and found to be consistent with the theoretical predictions. In particular, improvements to the performance parameters as a function of η confirm the notion that Antiproton Source performance is directly effected by improved Debuncher stochastic precooling. While theoretical predictions of the performance parameters have not been attempted, the experimental results of fractional improvements to the parameters are consistent with earlier measurements as discussed in Chapter 1 (see Figure 1.2 and the accompanying discussion). Thus, it was found that under the present conditions, a fractional improvement of $\sim 4\%$ in the stacking rate *per* $\Delta\eta = 0.001$ has been obtained. The corresponding fractional improvement in the Debuncher to Accumulator (D/A) transfer efficiency is approximately $\sim 3-4\%$ *per* $\Delta\eta = 0.001$. The nearly one-to-one improvement in D/A efficiency and stacking rate observed with the $\Delta\gamma_i$ *versus* T_γ experiments is consistent with that obtained from the previous measurements cited above.

Longitudinal and transverse Schottky Measurements *versus* T_γ have provided the most direct evidence of increased cooling as a function of η . Moreover, comparisons with the stochastic cooling model are in good agreement. In summary, it was found that for each $\Delta\eta \approx 0.001$ (i) the fractional change in ε is $\sim 2.5\%$, and (ii) the fractional change in σ_f is $\sim 1.4\%$.

CHAPTER 6

STOCHASTIC COOLING EXTRAPOLATIONS AND GENERAL CONCLUSIONS

6.1 Introduction

The purpose of the dynamic $\Delta\gamma_i$ project was to investigate the feasibility of utilizing optics modifications to improve the stochastic cooling rates under the auspice of a marked increase in particle flux. In any variety of the proposed scenarios for future operation of the Fermilab Tevatron, an increased particle flux to the Antiproton Source is an inherent design feature and assumption. Thus, the performance of the Debuncher *precooling* system with the increased particle flux stands amongst the numerous technical challenges, which are presently being addressed in earnest.

The Main Injector Project represents the first stage of the future *luminosity upgrades* at Fermilab within the immediate future. With respect to the operation of the Antiproton Source Debuncher, the predominant parameters represented by the Main Injector project are: (i) a faster repetition rate for producing \bar{p} s and a larger intensity (3.2×10^{12} protons/pulse $\rightarrow 5 \times 10^{12}$), and (ii) a modification of the Debuncher yield of $6.7 \times 10^7 \bar{p}$ /pulse $\rightarrow 8.9 \times 10^7 [\bar{p}$ /pulse], thus a factor of 1.32 above the present number of particles. With the incorporation of beam sweeping and a Li lens upgrades, the increase of antiprotons into the Debuncher shall be expected to increase from $6.7 \times 10^7 [\bar{p}$ /pulse] $\rightarrow 18.5 \times 10^7 [\bar{p}$ /pulse], yielding a factor of 2.7 more particles than with present scenarios.

In response to the need for improved precooling in the Debuncher within the Main Injector Era and beyond, the pickup arrays shall be cooled to 4°K, in order to dramatically reduce the noise to signal ratio, which presently limits the ability to operate at optimum gain. This upgrade decreases the effective noise temperature by a factor of 4 from 125°K to 30°K. Together with ancillary improvements to power handling capability of the kicker tanks, such a reduction of the noise figure shall allow an increase of the power in each system by ≈ 1.6 above the present power levels. Thus, a crude estimate would suggest a direct improvement of the overall gain in each system, $G_{||}$ and g_{\perp} respectively, to increase by a factor of ≈ 1.8 .

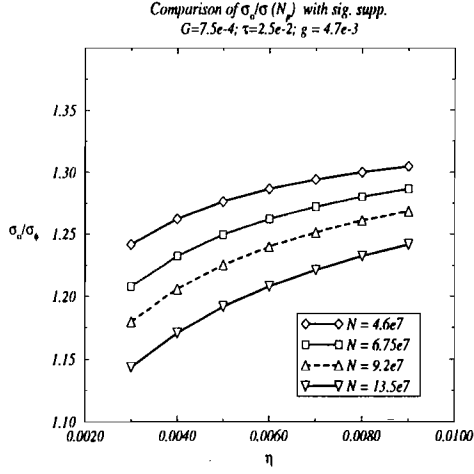
6.2 Projections of the Debuncher stochastic cooling model

Based upon the stated scenarios and upgrades, the stochastic cooling model, which has been discussed in chapter 4 for the nominal lattice and Debuncher parameters, may be used to extrapolate cooling rates in terms of three parameters: (i) the number of particles ($N_{\bar{p}}$), which shall most certainly increase, (ii) the system gain (G_{\parallel} and g_{\perp}), which shall increase by a factor of $\approx 1.3 - 1.5$, and (iii) several values of the lattice parameter η (or equivalently γ_t). This section shall present extrapolations of the full Fokker Planck calculation for the longitudinal width $\sigma(t)$, which is then used as input for the transverse calculation for the emittance $\varepsilon(t)$, through the mixing factor $M \sim 1/\sigma(t)$.

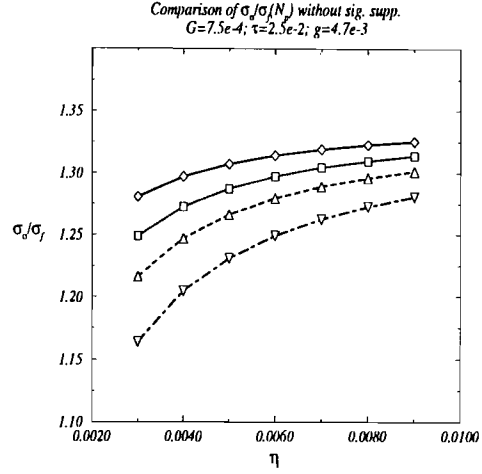
6.2.1 Longitudinal Rates with present system gain

Utilizing the longitudinal Fokker Planck Equation (4.7), the beam width as a function of time in the cooling cycle was calculated as a function of η (or equivalently γ_t), several values of N , and the system gain G_{\parallel} . The resulting $\sigma(t; \eta)$ is then utilized to calculate the emittance $\varepsilon(t; \eta)$ in terms of an increase in g_{\perp} . In Figure 6.1(a), comparisons of the ratio σ_o/σ_f (initial σ_o to the final σ_f) are made between several values of N as a function of η for the present values of system gain, $G_{\parallel} = 7.5 \times 10^{-4} \text{MeV}$ and $\tau = 2.5 \times 10^{-2} \text{MeV}^{-1}$. For comparison, Figure 6.1(b) are comparisons of σ_o/σ_f as a function of η for different values of N *without* signal suppression included in the calculation. While at $N = 4.6 \times 10^7$, the effect of signal suppression upon the σ_f is negligible, this is not the case for an increase in particle number, and a decrease in η .

If the thermal noise is neglected from the calculation a dramatic improvement of the cooling rate for σ would not result with the present value of G_{\parallel} . This is the statement that the system is gain limited, and that the present value of the gain is small enough to render the diffusion force negligible as compared with the cooling force, as has been plotted for comparison of the two terms $S_1(x)$ and $S_2(x)$ in Figure 4.27 of the chapter 4. Figure 6.2(a) and (b) compare σ_o/σ_f for several N and η for the case with the thermal noise/signal ratio $\mathcal{U} = 0$ and $G_{\parallel} = 7.5 \times 10^{-4} \text{MeV}$, with and without signal suppression, respectively. With signal suppression, the omission of the thermal term \mathcal{U} does not have a profound effect for the value of the present system gain.

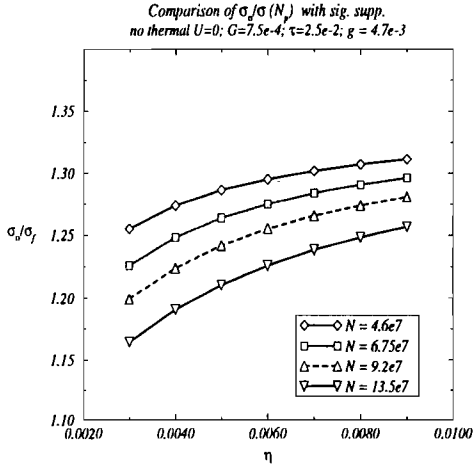


(a) σ_o/σ_f with signal suppression as a function of η

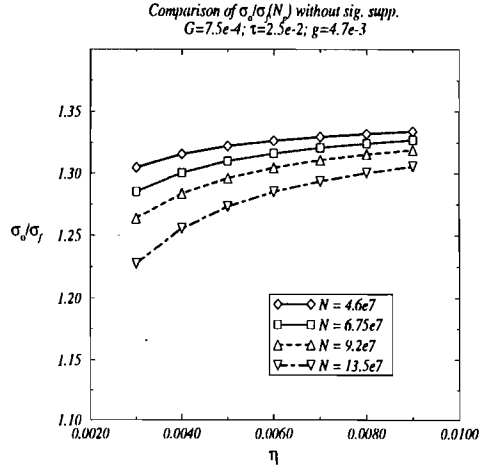


(b) σ_o/σ_f without signal suppression as a function of η

Figure 6.1: Comparisons of σ_o/σ_f as a function of N and η for the present values $G_{\parallel} = 7.5 \times 10^{-4} \text{MeV}$ and $\tau = 2.5 \times 10^{-2} \text{MeV}^{-1}$.



(a) σ_o/σ_f ($U=0$) with signal suppression as a function of η



(b) σ_o/σ_f ($U=0$) without signal suppression as a function of η

Figure 6.2: Comparisons of σ_o/σ_f as a function of N and η for the present values but without thermal noise $U=0$, $G_{\parallel} = 7.5 \times 10^{-4} \text{MeV}$, and $\tau = 2.5 \times 10^{-2} \text{MeV}^{-1}$.

At the present gain, $G = 7.5 \times 10^{-4} \text{MeV}$, the fractional change, Δ_σ of σ_o/σ_f with η , is $\Delta_\sigma \approx 3.5\%$ between $\eta = 0.006$ and $\eta = 0.009$. The calculation is consistent with the result obtained experimentally in the previous chapter as a function of T_γ (see Figure 5.12), in which a $\approx 3\%$ change in the beam width was observed for $\sigma(T_\gamma)$.

6.2.2 Longitudinal rates with increased gain

For the case in which the system gain is increased by a factor of 1.5, such that $G_{\parallel} = 11.25 \times 10^{-4} \text{MeV}$, marked improvements in the cooling rates are possible. Figures 6.3(a) and (b) compare σ_o/σ_f calculations, with and without signal suppression respectively, for several values of incident particle flux N into the Debuncher. With the increased value of the system gain, signal suppression is no longer negligible and must be included in calculations in order to accurately calculate the time evolution of the longitudinal beam widths $\sigma(t)$, and also the transverse emittance $\varepsilon(t)$

Comparisons of σ_o/σ_f with and without the inclusion of thermal noise \mathcal{U} in the calculations are provided in 6.4(a) and (b) to underscore the relative importance of the diffusion term at larger values of the gain.

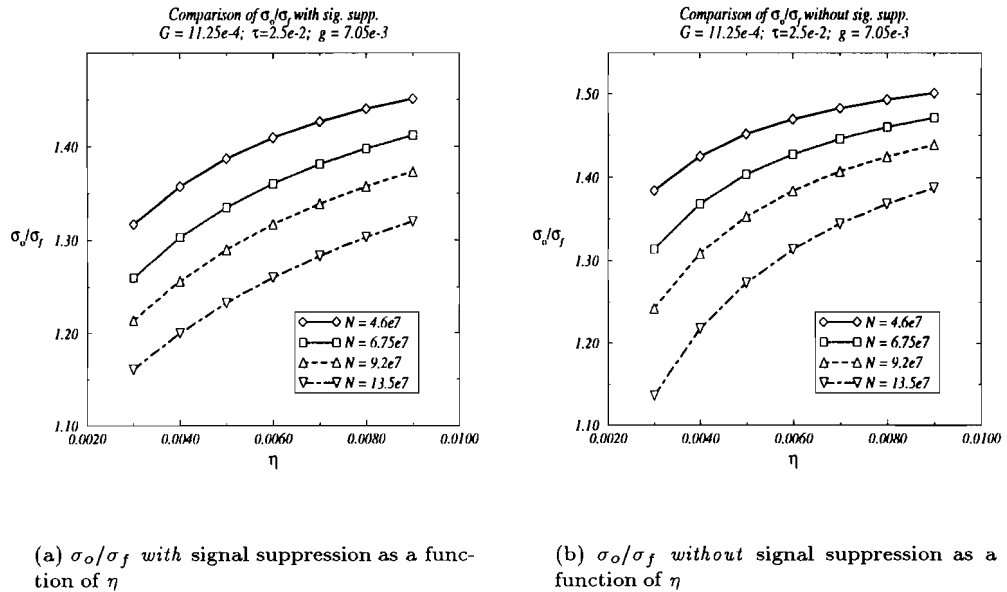
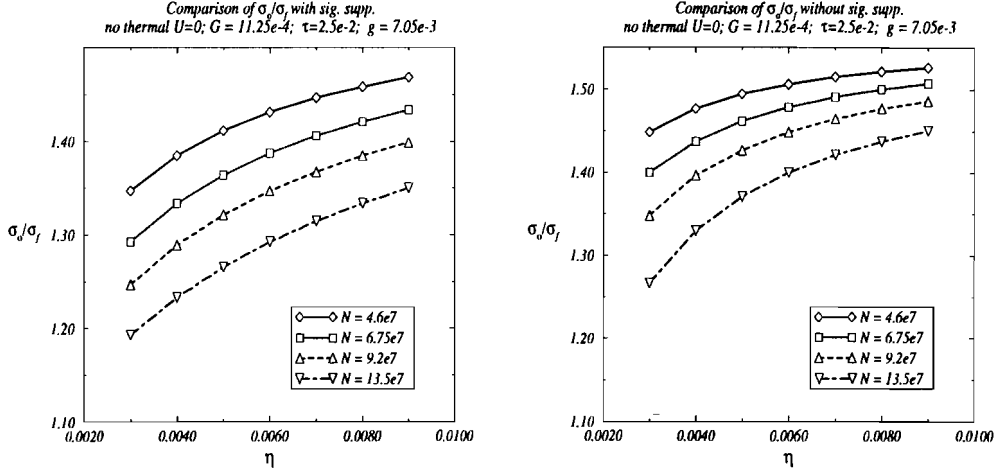


Figure 6.3: Comparisons of σ_o/σ_f as a function of N and η for $G_{\parallel} = 11.25 \times 10^{-4} \text{MeV}$ and $\tau = 2.5 \times 10^{-2} \text{MeV}^{-1}$.



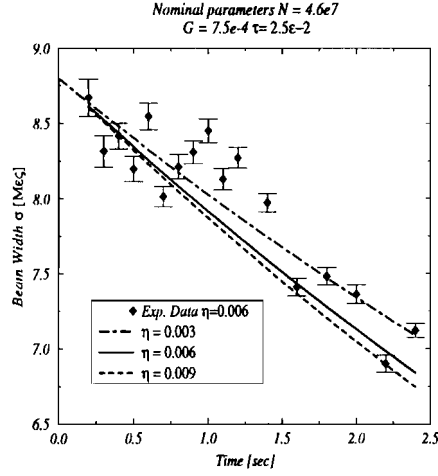
(a) σ_o/σ_f ($U = 0$) with signal suppression as a function of η

(b) σ_o/σ_f ($U = 0$) without signal suppression as a function of η

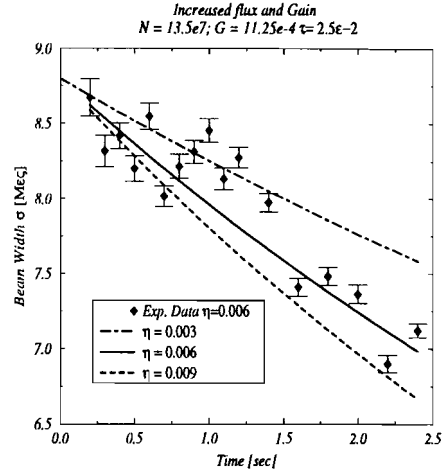
Figure 6.4: Comparisons of σ_o/σ_f as a function of N and η for the present values but without thermal noise $U = 0$, $G_{\parallel} = 7.5 \times 10^{-4} \text{ MeV}$, and $\tau = 2.5 \times 10^{-2} \text{ MeV}^{-1}$.

A few observations from Figure 6.3 are apparent, (i) with $N = 4.6 \times 10^7$ and $\eta = 0.006$ fixed, the final beam width σ_f decreases by a factor of ≈ 1.11 for an increase in the system gain of ≈ 1.5 . The fractional change in σ_o/σ_f for the increased gain, from $\eta = 0.006$ to $\eta = 0.009$, is $\Delta_{\sigma} \approx 6\%$. Thus, although operating *closer* to optimal gain with $1.5 \times G_{\text{nominal}}$, the dependence of the final width σ_f , and hence the longitudinal cooling rate is larger, but not dramatically so.

As a further comparison of the dependence of longitudinal cooling rate as function of η , Figures 6.5(a) and (b) compare calculated rates at several values of η for: (i) the present case with $G = 7.5 \times 10^{-4}$, $N = 4.6 \times 10^7$, and (ii) a case with an increased gain and particle flux $G = 11.25 \times 10^{-4}$ and $N = 13.5 \times 10^7$, respectively. Despite the increase in particle number by 50%, the final width σ_f in Figure 6.5(b) with a lattice $\eta = 0.009$, shall still be reduced by $\sim 8\%$ compared with the case for which $\eta = 0.006$.



(a)

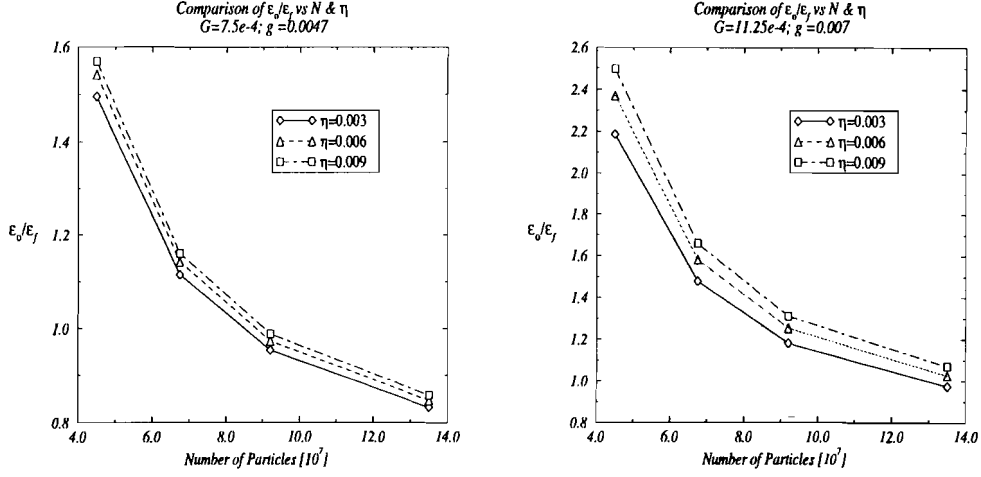


(b)

Figure 6.5: Comparison of longitudinal cooling rates for several values of η and compared against the present experimental rate.

6.2.3 Dependence of the transverse rates with η

With the values of $\sigma(t; \eta, N, \varepsilon)$ obtained from the longitudinal Fokker Planck calculation described in the previous subsection, the transverse cooling rates for $\varepsilon(t; \eta, N)$ have been calculated. Figures 6.6(a) and (b) compare the ratio of the initial emittance to the final emittance, $\varepsilon(t = 0; N, \eta)/\varepsilon(t = t_f; N, \eta)$, as a function of N for different values of η . In particular, Figure 6.6(a) utilizes the present gain in each cooling system ($G_{\parallel} = 7.5 \times 10^{-4}$ and $g_{\perp} = 4.7 \times 10^{-3}$) for calculating $\sigma(t)$ and $\varepsilon(t)$. Figure 6.6(b), however, compares $\varepsilon(t = 0; N, \eta)/\varepsilon(t = t_f; N, \eta)$ for different η as function of N with the gain increased in *each* system by a factor of 1.5 from the present values, thus, $G_{\parallel} = 11.25 \times 10^{-4}$ and $g_{\perp} = 7.05 \times 10^{-3}$. The effects of signal suppression have been included in the calculations for both the longitudinal beam width $\sigma(t)$ and $\varepsilon(t)$.



(a) ϵ_o/ϵ_f for $g_{\perp} = 4.7 \times 10^{-3}$, $G_{\parallel} = 7.5 \times 10^{-4}$ MeV, and $\tau = 2.5 \times 10^{-2}$ 1/MeV

(b) ϵ_o/ϵ_f for $g_{\perp} = 7. \times 10^{-3}$, $G_{\parallel} = 11.25 \times 10^{-4}$ MeV, and $\tau = 2.5 \times 10^{-2}$ 1/MeV

Figure 6.6: Comparisons of ϵ_o/ϵ_f as a function of N and η .

The dependence of the transverse stochastic cooling rate upon η is further elucidated in Figure 6.7(a), in which the ratio $\epsilon(t=0; N, \eta)/\epsilon(t=t_f; N, \eta)$ is plotted directly as a function of η for different values of gain and number of particles N .

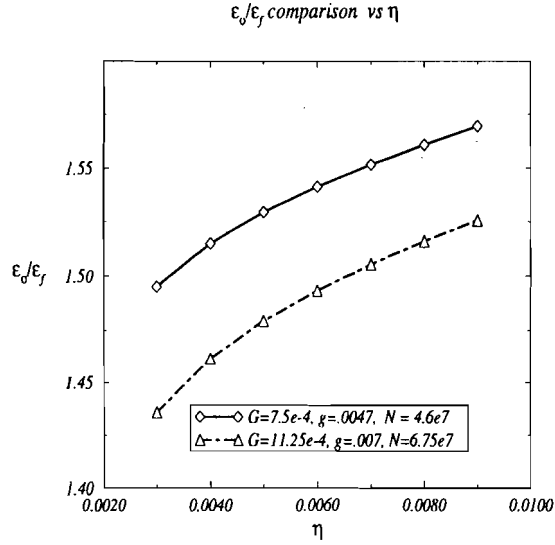


Figure 6.7: Plots of $\epsilon(t=0; N, \eta)/\epsilon(t=t_f; N, \eta)$ as a function of η for different values of gain and number of particles N .

Specifically, two calculations are compared in Figure 6.7(a): (i) the present parameters, thus, $G_{\parallel} = 7.5 \times 10^{-4}$, $g_{\perp} = 4.7 \times 10^{-3}$, and $N = 4.6 \times 10^7$, and (ii) an increased particle flux by a factor ≈ 1.5 , and an increased gain in each system of ≈ 1.5 , thus, $G_{\parallel} = 11.25 \times 10^{-4}$, $g_{\perp} = 7.05 \times 10^{-3}$, and $N = 6.75 \times 10^7$.

From 6.7 two observations may be made, (i) the fractional change in between $\eta = 0.006$ and $\eta = 0.009$ is $\approx 3\%$, in either case, and (ii) although the increase in transverse cooling is not profoundly effected by η , approximately the same cooling rates can be obtained with $\sim 50\%$ more beam and $\sim 50\%$ more gain.

6.2.4 Summary of the cooling rate extrapolations

Within the short discussion of this chapter, extrapolations of cooling rates were made in terms of the particle flux N , the system gain G_{\parallel} and g_{\perp} , and η (γ_t), utilizing the Debuncher stochastic cooling model. While the variety of future scenarios must be investigated more thoroughly and for more specific cases, general trends may be discerned from the results of this chapter, and previous chapters, concerning the benefits of a dynamic γ_t lattice. According to the the calculations of this chapter, with the stochastic cooling model, and considering the source of errors, the conclusions are the following: (i) the longitudinal beam width may be reduced by $\sim 3 - 4\%$ *per* $\Delta\eta \sim 0.001$ and an increase of the gain $\Delta G \sim 1.5G_{\text{nominal}}$, and (ii) the transverse emittance may be reduced by $\sim 2 - 3\%$ *per* $\Delta\eta \sim 0.001$ and increase in gain of $\Delta g \approx 1.5g_{\text{nominal}}$. The first of the conclusions suggests that $\eta \approx 0.0095$ should reduce the final width σ_f of $\sim 10.5 - 14\%$ compared with the nominal lattice of $\eta = 0.006$, assuming the gain may be increased by $\sim 50\%$. The second observation suggests a reduction of the beam emittance ε_f by $\sim 7 - 10\%$ with the implementation of $\eta \approx 0.0095$ and an increase in the transverse system gain of $\sim 50\%$.

6.3 Final Comments regarding a dynamic $\Delta\gamma_t$

Many results related to a dynamic $\Delta\gamma_t$ lattice have been presented in this thesis. *First*, the feasibility of constructing the necessary lattices has been demonstrated with the use of π doublet filling of the arc sections. A robust $\Delta\gamma_t$ design has been constructed, for which (i) initial commissioning requirements were amply satisfied, (ii) it is possible to produce *larger* $\Delta\gamma_t$ than obtained in the commissioning described in this thesis from the perspective of beam stability, with the provision

of power supply engineering efforts for obtaining reasonable slew rates, (iii) the result of lattice calculations for the $\Delta\gamma_t$ design are in excellent agreement with the experimentally measured results, and (iv) a bi-polar design which obtains a *small* value of η for increasing the momentum acceptance $\sim 20\%$ is feasible with the $\Delta\gamma_t$ lattice design.

The *second* observation concerns resonance crossing. It was shown that power supply errors produce tune excursions which can be detrimental to the beam by crossing significant resonances through 5th order. Solutions to the tune excursion problem during the $\Delta\gamma_t/\Delta t$ represent *the most obdurate challenge* to the successful implementation of a dynamic $\Delta\gamma_t$ lattice as a permanent *operational* feature of the Antiproton Source.

As had been well known before the commissioning of the dynamic $\Delta\gamma_t$ project, the present Debuncher stochastic cooling systems are gain limited due to the large thermal noise at the input to the amplifiers. As a result, the systems are far from the optimal gain, and thus, the diffusion term is small in comparison to the cooling term. The *third* observation concerning the present feasibility project is that under the *present* conditions, a reduction in the diffusion term, *through a reduction of the mixing factor* does not have a profound effect. It has been found that during a cooling cycle of $\Delta t \approx 2.4\text{sec}$, the stacking rate can be increased by $\sim 5\%$. Thus, a more positive cost/benefits analysis would result with the system operating closer to optimal. Such shall be the case under the proposed upgrades scheduled for Antiproton operation in the Main Injector era.

The *final* observations to be made concern (i) the ability to predict stochastic cooling rates with the numerical computer model developed and described in the third chapter, and (ii) the accuracy of the related experimentally measured input parameters. In the previous two chapters, comparisons of the longitudinal and transverse stochastic cooling models to experimental measurements of the beam width and emittance (actually, the power in the transverse Schottky sideband), respectively. Agreement between the model and measurements was, in general, quite good despite the fact that (i) variations of input parameters across the microwave band were averaged for simplicity, (ii) details of improper phasing were not measured carefully, thus only crude estimates were used in the models, and (iii) extraction of the gain, G_{\parallel} and g_{\perp} from signal suppression and open loop measurements were in good agreement, however, introduce an error at a level of 20%.

APPENDIX A

SOME NOTES RELEVANT TO THE $\Delta\gamma_t/\Delta t$ OPTIMIZATION PROBLEM

A.1 Introduction

The $\Delta\gamma_t/\Delta t$ optimization problem was stated formally in chapter 1 in the following manner:

$$\begin{aligned} & \min\{\mathcal{F}(\nu)\} \quad \text{for } \nu \in \mathcal{M} \\ & \text{subject to} \quad |\Delta I_j| \leq \tau_j; \quad \Delta\varphi_{p \rightarrow k} \approx 0; \quad |\Delta\beta_i| \leq \varepsilon \\ & \text{where} \\ & \mathcal{F}(\nu) = \sum [\Delta\nu_i]^2 \end{aligned}$$

for which \mathcal{M} is the one turn map, and ν may in general represent any of the lattice parameters, however, for the present restricted problem shall simply represent the transverse tunes. The restrictions upon the changes in the free parameters, the currents $|\Delta I_j|$, results from (i) trying to equally distribute the necessary current changes so that the average change is as small as possible, (ii) staying within the practical requirements imposed by shunts and the fact that the straight section quadrupoles are already shunting some amount of current, which in some cases restricts the available current domain even more, and (iii) trying to maintain a highly symmetric $\Delta\gamma_t^{(f)}$ design.

A.2 General Comments

The following sections shall discuss some of the possible solution methods of the $\Delta\gamma_t/\Delta t$ optimization problem with (i) *classical optimization*, notably quadratic models for which conjugate gradient/set methods are a subset, and (ii) *simulated annealing optimization*, for which the object function is sampled through a Monte Carlo algorithm. General discussions of some selected methods are included together with details of an object function for the tune space of the Debuncher.

A.2.1 Classical Methods Optimization methods

As posed, the constrained $\Delta\gamma_t$ optimization problem is represented well by a number of classic gradient search algorithms. In particular, if the constraints are not very complicated to implement, it is possible to accurately utilize a quadratic function obtained with the first rank (Jacobian) and second rank (Hessian) tensors, such that the object function is given by

$$\Delta\nu \approx \mathbf{J} \cdot \delta\mathbf{I} + \delta\mathbf{I} \cdot \{\tilde{\mathbf{H}}\} \cdot \delta\mathbf{I} \quad (\text{A.1})$$

Quadratic models, based upon the the form of Equation (A.1), are particularly well suited for any of the following minimization algorithms¹: (i) Newton method, (ii) restricted step methods, (iii) quasi-Newton methods, and (iv) conjugate direction methods², including the most popular method of conjugate gradient as a subset. In the case of the conjugate direction methods, the algorithms rely upon a line search, which has the steps: (i) determine a direction of search $\mathbf{s}^{(k)}$, (ii) find some $\alpha^{(k)}$ to minimize $f(\mathbf{x}^{(k)} + \alpha^{(k)}\mathbf{s}^{(k)})$ with respect to $\alpha^{(k)}$, and (iii) set $\mathbf{x}^{(k+1)} = \mathbf{x}^{(k)} + \alpha^{(k)}\mathbf{s}^{(k)}$. From this, $\nabla f^{(k+1)T}\mathbf{s} = 0$ and conjugacy can be found with the Hessian tensor, $\mathbf{s}^{(i)T} \cdot \{\tilde{\mathbf{H}}\} \cdot \mathbf{s}^{(j)} = 0$ and may be formally satisfied with a Gram- Schmidt procedure.

The problem of treating optimization problems composed of several competing objectives, ie. $\min \tilde{\mathcal{F}}(\vec{x}) = \min(f_1(\vec{x}), f_2(\vec{x}), \dots, f_k(\vec{x}))$ with associated constraints $g_i \leq 0, h_i = 0$, was treated first in economics by V. Pareto [73]. For an informative and interesting application to the design of the LHC superconducting magnets using the Pareto- optimality criteria, see Russenschuck, [84], [85]. The Pareto- optimal solution \vec{x}^* produces a set of solutions when there is no \vec{x} such that $f_k \leq f_k(\vec{x}^*)$ and $f_k < f_k(\vec{x}^*)$ for at least one k . Therefore the Pareto - optimal solution set describes a situation for which an improvement of one object function compromises *at least one* other objective.

A.2.2 Simulated Annealing Optimization

For object functions possessing many local minima, the gradient algorithms are plagued with strong dependencies upon the start values. In the past 15 years, large scale optimization problems in econometrics and in VLSI [54] design have benefited from a Monte Carlo technique called simulated annealing. A more recent article by Martin and Ott [62], suggests that combination with other local search heuristics greatly improves the most complex of problems such as the traveling salesman and the graph partition problem.

¹ The treatment of constrained optimization requires construction of the *Lagrangian* function $\mathcal{L} = \mathcal{F}(x) - \sum \lambda_i c_i(x)$, then $\nabla \mathcal{L}(\mathbf{x}^*, \lambda^*) = 0$ is the minimizer within the feasible region.

² Conjugacy, $\mathbf{s}^{(i)T} \mathbf{G} \mathbf{s}^{(j)} = 0$, is a direct way of invoking *quadratic termination*, ie. the notion that a method will locate a minimizing point \mathbf{x}^* of a quadratic function after a finite number of iterations. An intuitive way of realizing this is given by the following: let $\mathbf{x}^* = \mathbf{x}^{(1)} + \sum \alpha_i^* \mathbf{s}^{(i)}$ and some point $\mathbf{x} = \mathbf{x}^{(1)} + \sum \alpha_i \mathbf{s}^{(i)}$, then a quadratic $q(\alpha) = (\alpha - \alpha^*)^T \mathbf{G} (\alpha - \alpha^*)$. Minimization is achieved by choosing $\{\mathbf{S}\}$ conjugate so that $\alpha_i = \alpha_i^*$, then the conjugacy is simply a transformation of \mathbf{G} to a system α which are decoupled.

The notion of simulated annealing is quite simple and intuitive both for large combinatoric and smooth problems. Given an object function, and a fundamental parameter, such as *temperature*, which is a measure of the energy of the system, relative to the ground state minimum, the global features of the object function may be probed at the beginning of the search since the system may search large areas of the object function without encountering barriers due to local minima. The temperature parameter plays the key role in deciding in a probabilistic manner, whether to accept movement to some point in the configuration space which does not decrease the object function. Thus, unlike the descent methods, there is a natural mechanism to escape a local minimum and probe nearby features of the function. The *radius* by which the function may be probed is controlled by a separate step size parameter.

As the number of function evaluation increase, what is required is a schedule, or *order parameter* to both decrease the temperature and decrease the step size. As the system anneals, the sampled configuration space should reside close to the minima.

A.3 Optimization with a second order model

For the transverse tunes, calculated through the linear lattice model of the Debuncher, it is sufficient to consider an expansion in of the perturbed excitation currents through the Hessian tensor. Table A.1 and Table A.2 compare the components of the aforementioned tensors for the nominal lattice and for the case in which the $\Delta\gamma_t$ has been created *without* tune correction. For each comparison the difference between the elements between the two cases. Although the change is small between the first rank Jacobian elements, significant deviation does enter in the second rank Hessian.

Table A.1: Jacobian matrix elements for the tune optimization problem free parameters - the quadrupoles in the straight sections quadrupoles.

J_{ij}	$\eta_1 = 0.009$		$\eta_2 = 0.006$		<i>Difference</i>	
	$\partial\nu_x/\partial dI_j$ $\times 10^{-3}$	$\partial\nu_y/\partial dI_j$ $\times 10^{-3}$	$\partial\nu_x/\partial dI_j$ $\times 10^{-3}$	$\partial\nu_y/\partial dI_j$ $\times 10^{-3}$	$\Delta\partial\nu_x/\partial dI_j$ $\times 10^{-3}$	$\Delta\partial\nu_y/\partial dI_j$ $\times 10^{-3}$
(1)	3.729	-1.458	3.833	-1.252	-0.104	-0.206
(2)	5.605	-2.089	5.488	-2.207	0.118	0.118
(3)	6.338	-1.255	6.263	-1.257	0.075	0.002
(4)	-2.118	8.152	-2.149	7.405	0.031	0.747
(5)	-1.957	5.152	-1.904	5.963	-0.053	-0.811
(6)	-2.412	7.335	-2.446	6.232	0.034	1.103

Table A.2: Hessian matrix elements for the tune optimization problem free parameters - the quadrupoles in the straight sections quadrupoles.

H_{ij}^k	$\eta = 0.009$		$\eta = 0.006$		<i>Difference</i>	
	$\partial^2 \nu_x$	$\partial^2 \nu_y$	$\partial^2 \nu_x$	$\partial^2 \nu_y$	$\Delta(\partial^2 \nu_x)$	$\Delta(\partial^2 \nu_y)$
	$\times 10^{-5}$	$\times 10^{-5}$	$\times 10^{-5}$	$\times 10^{-5}$	$\times 10^{-5}$	$\times 10^{-5}$
(1,2)	0.944	-0.933	-3.150	-0.562	4.093	-0.371
(1,3)	4.858	0.421	4.867	0.324	-0.009	0.098
(1,4)	2.607	-1.086	1.524	1.411	1.084	-2.498
(1,5)	-2.607	2.658	-0.787	0.212	-1.820	2.446
(1,6)	1.053	-4.572	-1.057	-0.693	2.110	-3.880
(2,3)	-5.755	-0.167	-5.050	-0.235	-0.706	0.068
(2,4)	-0.269	3.453	0.904	1.888	-1.173	1.565
(2,5)	2.689	-1.214	0.751	-0.164	1.938	-1.050
(2,6)	-1.032	1.722	0.912	0.534	-1.944	1.188
(3,4)	-1.273	-1.651	-1.340	-1.094	0.067	-0.557
(3,5)	2.561	1.417	2.312	1.507	0.249	-0.090
(3,6)	0.659	-0.453	0.085	0.057	0.574	-0.510
(4,5)	0.723	-9.798	0.224	-0.723	0.499	-9.075
(4,6)	-0.288	18.178	0.312	2.301	-0.599	15.878
(5,6)	0.477	-15.237	-0.431	-3.340	0.908	-11.896

In the introductory comments, it was postulated that one could utilize a quadratic expansion of the tunes for small perturbations of the excitation currents, $\Delta \bar{\nu} \approx \mathbf{J} \cdot \delta \mathbf{I} + \delta \mathbf{I} \cdot \{\tilde{\mathbf{H}}\} \cdot \delta \mathbf{I}$. For convenience, the tensors are given below for the configuration space defined by the free parameter set of excitation currents (the quadrupoles in the straight sections of the Debuncher lattice): $\{\delta I_{qf1}, \delta I_{qf2}, \delta I_{qf3}, \delta I_{qd1}, \delta I_{qd2}, \delta I_{qd3}\}$.

$$\mathbf{J}_{ij} = \begin{pmatrix} \partial \nu_1 / \partial I_1 & \partial \nu_1 / \partial I_2 & \dots & \partial \nu_1 / \partial I_6 \\ \partial \nu_2 / \partial I_1 & \partial \nu_2 / \partial I_2 & \dots & \partial \nu_2 / \partial I_6 \end{pmatrix}$$

$$\mathbf{J}_{ij}(\eta = .006) = \begin{pmatrix} 3.832 & 5.487 & 6.262 & -2.148 & -1.903 & -2.446 \\ -1.251 & -2.207 & -1.256 & 7.405 & 5.962 & 6.231 \end{pmatrix} \times 10^{-3}$$

$$\mathbf{J}_{ij}(\eta = .009) = \begin{pmatrix} 3.729 & 5.605 & 6.338 & -2.118 & -1.957 & -2.412 \\ -1.458 & -2.089 & -1.255 & 8.152 & 5.152 & 7.335 \end{pmatrix} \times 10^{-3}$$

$$\{\mathbf{H}\}_{ij}^k = \begin{pmatrix} 0. & \partial^2 \nu_k / \partial I_1 \partial I_2 & \partial^2 \nu_k / \partial I_1 \partial I_3 & \dots & \partial^2 \nu_k / \partial I_1 \partial I_6 \\ \partial^2 \nu_k / \partial I_2 \partial I_1 & 0. & \partial^2 \nu_k / \partial I_2 \partial I_3 & \dots & \partial^2 \nu_k / \partial I_2 \partial I_6 \\ \dots & \dots & \dots & \dots & \dots \\ \partial^2 \nu_k / \partial I_6 \partial I_1 & \partial^2 \nu_k / \partial I_6 \partial I_2 & \dots & \dots & 0. \end{pmatrix}$$

$$\{\mathbf{H}\}_{ij}^x(\eta = .009) = \begin{pmatrix} 0. & 0.944 & 4.858 & 2.607 & -2.607 & 1.053 \\ 0.944 & 0. & -5.755 & -0.269 & 2.689 & -1.032 \\ 4.858 & -5.755 & 0. & -1.273 & 2.561 & 0.659 \\ 2.607 & -0.269 & -1.273 & 0. & 0.723 & -0.288 \\ -2.607 & 2.689 & 2.561 & 0.723 & 0. & 0.477 \\ 1.053 & -1.032 & 0.659 & -0.288 & 0.477 & 0. \end{pmatrix} \times 10^{-5}$$

$$\{\mathbf{H}\}_{ij}^y(\eta = .009) = \begin{pmatrix} 0. & -0.933 & 0.421 & -1.086 & 2.658 & -4.572 \\ -0.933 & 0. & -0.167 & 3.453 & -1.214 & 1.722 \\ 0.421 & -0.167 & 0. & -1.651 & 1.417 & -0.453 \\ -1.086 & 3.453 & -1.651 & 0. & -9.798 & 18.178 \\ 2.658 & -1.214 & 1.417 & -9.798 & 0. & -15.237 \\ -4.572 & 1.722 & -0.453 & 18.178 & -15.237 & 0. \end{pmatrix} \times 10^{-5}$$

$$\{\mathbf{H}\}_{ij}^x(\eta = .006) = \begin{pmatrix} 0. & -3.149 & 4.866 & 1.523 & -0.786 & -1.056 \\ -3.149 & 0. & -5.049 & 0.904 & 0.751 & 0.912 \\ 4.866 & -5.049 & 0. & -1.340 & 2.311 & 0.085 \\ 1.523 & 0.904 & -1.340 & 0. & 0.223 & 0.311 \\ -0.786 & 0.751 & 2.311 & 0.223 & 0. & -0.430 \\ -1.056 & 0.912 & 0.085 & 0.311 & -0.430 & 0. \end{pmatrix} \times 10^{-5}$$

$$\{\mathbf{H}\}_{ij}^y(\eta = .006) = \begin{pmatrix} 0. & -0.561 & 0.323 & 1.411 & 0.212 & -0.692 \\ -0.561 & 0. & -0.235 & 1.887 & -0.163 & 0.534 \\ 0.323 & -0.235 & 0. & -1.094 & 1.506 & 0.057 \\ 1.411 & 1.887 & -1.094 & 0. & -0.723 & 2.300 \\ 0.212 & -0.163 & 1.506 & -0.723 & 0. & -3.340 \\ -0.692 & 0.534 & 0.057 & 2.300 & -3.340 & 0. \end{pmatrix} \times 10^{-5}$$

A comparison of the quadratic model for predicting tune shifts³ is given in Table A.3 for several cases.

$$\mathcal{S} = \{\delta I_{qf1}, \delta I_{qf2}, \delta I_{qf3}, \delta I_{qd1}, \delta I_{qd2}, \delta I_{qd3}\}$$

³The more general problem of predicting shifts in other parameters, in particular the value of β functions at selected points, requires a calculation of $\partial^2 \beta_k / \partial I_i^2$, which in the case of tune shifts were considered negligible. These must be done if one is to rigorously include restrictions of the feasible domain through constraint equations on these variables.

Table A.3: Test of the quadratic model with Jacobian and Hessian given in Tables A.1 and A.2, respectively, against the actual lattice calculation. The comparison is used to quantify the accuracy of the quadratic model for calculating the tune shifts $\Delta\nu$.

S	$\Delta\tilde{\nu}$		Δ	$\% \psi$
	<i>latt. model</i>	<i>quadratic</i>		
$\{1, 1, 1, -1, -1, -1\}$	(.0220, -.0252)	(.0221, -.0254)	$(6.3 \times 10^{-5}, 3.7 \times 10^{-3})$	(.31, .61)
$\{2, 2, 2, -2, -2, -2\}$	(.0439, -.0504)	(.0440, -.0515)	$(1.4 \times 10^{-4}, 1.1 \times 10^{-3})$	(.62, 1.2)
$\{3, 3, 3, -3, -3, -3\}$	(.0656, -.0756)	(.0659, -.0777)	$(2.3 \times 10^{-4}, 2.1 \times 10^{-3})$	(.93, 1.8)
$\{4, 4, 4, -4, -4, -4\}$	(.0872, -.1009)	(.0875, -.1043)	$(3.0 \times 10^{-4}, 3.3 \times 10^{-3})$	(1.3, 2.4)
$\{5, 5, 5, -5, -5, -5\}$	(.1087, -.1262)	(.1091, -.1311)	$(3.4 \times 10^{-4}, 4.8 \times 10^{-3})$	(1.6, 3.0)
$\{6, 6, 6, -6, -6, -6\}$	(.1302, -.1517)	(.1305, -.1583)	$(3.4 \times 10^{-4}, 6.5 \times 10^{-3})$	(1.9, 3.6)
$\{7, 7, 7, -7, -7, -7\}$	(.1515, -.1775)	(.1518, -.1781)	$(2.0 \times 10^{-4}, 8.0 \times 10^{-3})$	(2.2, 4.1)
$\{8, 8, 8, -8, -8, -8\}$	(.1729, -.2037)	(.1729, -.2135)	$(2.5 \times 10^{-5}, 9.8 \times 10^{-3})$	(2.5, 4.6)

Two main avenues of optimization inquiry were studied for the simple quadratic model: (i) the direction set methods, and (ii) the simulated annealing method. The motivation for comparing the two methods in the quadratic model is predicated on the belief that the annealing methods are easier to implement for the more complex case, especially for the inclusion of inequality constraints. Although in the restricted problem of demanding a high degree of symmetry, the direction set methods may be fine, the reliability in finding the proper minimum with the annealing method is greater. This statement shall be qualified in this section.

A variation of the simulated annealing method by Goffe et. al. [37] and Corana [29], have been used to study the quadratic model with 6 free parameters. The specific *annealing schedule* used is based upon the Metropolis algorithm, in which points visited in the domain are accepted randomly based upon a *Boltzmann* criteria $p = \exp[(f_p - f)/T]$, for the function value f_p , the function value at the present point f , and the order parameter T . The schedule is as follows: (i) n_s , *number of steps*, or function evaluations, are performed with the a step size, (ii) n_t iterations of the n_s evalauations are performed before the step size is reduced, thus limiting the domain as the system anneals; the step size v_i changes according to the equation

$$v_i = \begin{cases} v_i [1 + c_i (\frac{n_a/n_s - 6}{.4})] & n_a/n_s > .6 \\ \frac{v_i}{[1 + c_i (\frac{.4 - n_a/n_s}{.4})]} & \text{otherwise} \end{cases} \quad (\text{A.2})$$

in which n_a is the number of events accepted from the Metropolis criteria, and (iii) after n_t iterations, the *temperture* T parameter in the Metropolis criteria is changed by a simple scaling relation $T \rightarrow rT$, where $r < 1$. The smaller r , the more rapid the solution anneals to an extremum.

The plots Figure A.1 are the graphical representation of a particular simulated annealing result for the 6 parameter quadratic model. The schedule chosen has the reduction factor $r = .2$, an initial temperature of $T = 2.$, $n_s = 20$, and $n_t = 5$.

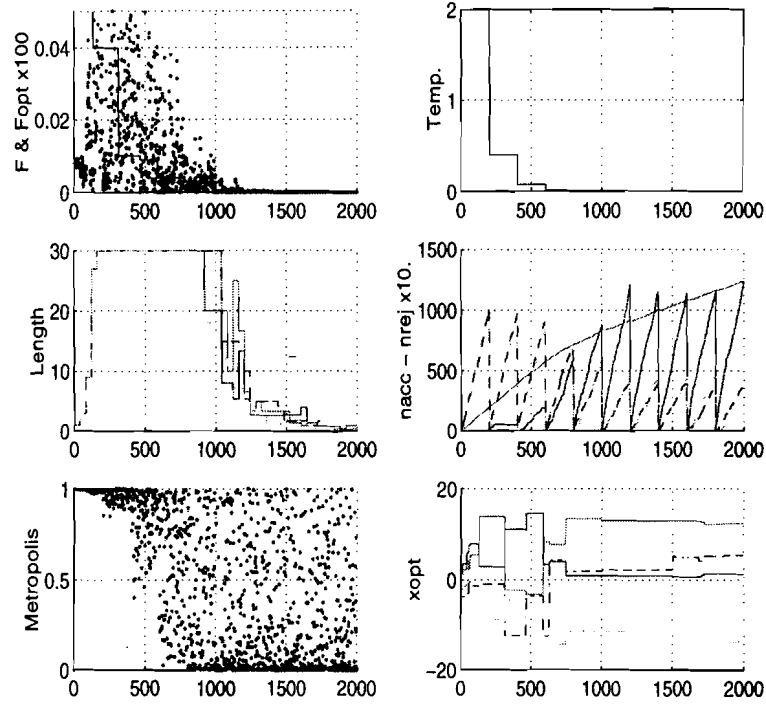


Figure A.1: A simulated annealing results for the 6 parameter quadratic model.

The top left plot in Figure A.1 illustrates the values of the function f sampled (represented as points) together with the optimal function f_p as a function of the number of evaluations N . As can be seen in the bottom right plot for the optimal points x_{opt} , a solution for an extremum becomes stable after 500 evaluations, which is highly dependent upon the step size (middle left plot) and the temperature T , (the top right plot).

A.4 Conclusion: Optimization within Lattice Calculation

The real power of the simulated annealing optimization algorithm is not restricted to quadratic models, in fact, the ease of the method is more manifest through the direct implementation of the algorithm into the lattice calculations. Thus, because obtaining each point in tune space through

a lattice calculation, i.e. calculating the *one turn map* to determine the lattice functions, is computationally expensive, and also difficult with complicated constraints, an appropriate annealing schedule may be used to reduce the total number of evaluations *while* maintaining the ability to search a large domain of local minima.

APPENDIX B

NUMERICAL INTEGRATION FOR THE LONGITUDINAL COOLING MODEL

B.1 Introduction

Numerical analysis and methods for solving partial differential equations have long constituted an exciting area of applied mathematics. For their part, physicists have contributed profoundly to the field of numerical analysis, particularly with the need to solve nonlinear hydrodynamic (fluid) or magneto-hydrodynamic problems (nonlinear plasma in tokamaks) problems involving the Navier Stokes equations, Burgers equations, and transport equations. This brief appendix reviews a few of the methods which have been employed for the solution of the longitudinal Fokker Planck equation for the stochastic cooling model in the Debuncher.

B.2 Analytic Methods

In utilizing numerical methods for obtaining the solution to partial differential equations, it is essential to check the approximations with those equations for which an exact solution is possible. This section considers the two terms in the longitudinal Fokker Planck equation, separately, with appropriate approximations to yield exact solutions, which may then be used for tests against the computer model.

B.2.1 Method of Characteristics for Cooling

From the longitudinal cooling equation for the distribution function $\psi(\mathbf{x}, t)$, and the simple model for the gain $\text{Real}[G(x)] \sim -g \sin[\tau x]$, the effect of the cooling interaction may be studied in the absence of diffusion. Indeed, with the simplified gain an exact solution is obtained with the *method of characteristics*. The following derivation is given by Zwillinger [105].

Given a quasi-linear partial differential equation

$$a_1(\mathbf{x}, u)u_{x_1} + \cdots + a_n(\mathbf{x}, u)u_{x_n} = b(\mathbf{x}, u)$$

define

$$\frac{\partial x_k}{\partial s} = a_k(\mathbf{x}, u)$$

Using these expressions, the following *differential* equation results

$$\frac{du}{ds} = b(\mathbf{x}, u)$$

Integration of this equation requires the knowledge of the trajectory along some curve in s in x_k and u determined by some initial conditions, $g(\mathbf{x}, u) = 0$. Solution to the above differential equations in x and u determine an implicit solution in a set of variables $S = \{s, t_1, t_2, \dots, t_N - 1\}$. If these equations can be inverted in the set of variables S then an explicit solution is obtained.

For the cooling term $\Re\{G\} \sim -g \sin(\tau x)$ so that

$$\psi_t = [g \sin(\tau x) \psi]_x$$

with $\psi(t = 0) = \psi_o$

$$\psi_t - g \sin(\tau x) \psi_x = g \tau \cos(\tau x) \psi \quad (\text{B.1})$$

$$\frac{du}{ds} = \frac{\partial x_1}{\partial s} \psi_t + \frac{\partial x_2}{\partial s} \psi_x \quad (\text{B.2})$$

$$(\text{B.3})$$

$$\frac{\partial x_1}{\partial s} = 1, \quad \frac{\partial x_2}{\partial s} = -g \sin(\tau x) \approx -g \tau x, \quad \frac{du}{ds} = g \tau \cos(\tau x) \psi \approx g \tau \psi$$

where the approximations are accurate since that portion sampled by the distribution function is essentially linear. Initially,

$$t(s = 0) = 0 \quad x(s = 0) = t_1 \quad \psi(s = 0) = \psi_o(t_1)$$

Using the approximation:

$$\frac{dt}{ds} = 1, \quad \frac{dx}{ds} = -g \tau x, \quad \frac{d\psi}{ds} = g \tau \psi$$

Upon integrating these equations

$$x(s) = x(s = 0) \exp[-g \tau s] = t_1 [-g \tau s] \quad (\text{B.4})$$

$$\psi(s, t_1) = \psi_o(t_1) [g \tau s] \quad (\text{B.5})$$

The solution:

$$\psi(x, t) = \exp[g \tau t] \psi_o(x \exp[g \tau t])$$

Solution to the full problem without the approximations

$$\psi_t - g \sin(\tau x) \psi_x = g \tau \cos(\tau x) \psi \quad (\text{B.6})$$

$$\frac{du}{ds} = \frac{\partial x_1}{\partial s} \psi_t + \frac{\partial x_2}{\partial s} \psi_x \quad (\text{B.7})$$

$$(\text{B.8})$$

$$\frac{\partial x_1}{\partial s} = 1, \quad \frac{\partial x_2}{\partial s} = -g \sin(\tau x), \quad \frac{du}{ds} = g \tau \cos(\tau x) \psi$$

then,

$$\frac{dt}{ds} = 1, \quad \frac{dx}{ds} = -g \sin(\tau x) \quad \frac{d\psi}{ds} = g \tau \cos(\tau x) \psi$$

Upon integrating these equations

$$x(s) = \frac{t_1}{\tau} \arctan \left[\exp[-g\tau s] \right]$$

$$\frac{d\psi}{ds} = g \tau \cos\left(\tau \frac{t_1}{\tau} \arctan \left[\exp[-g\tau s] \right]\right) \psi$$

The above equation illustrates that although formal implicit expressions may be obtained with the method of characteristics, it is often difficult to obtain explicit expressions for the exact solution. Nonetheless, a numerical solution may be used to test against the convergence of the finite difference formulas derived for the solution to the various terms. for which the exact solution is

$$\psi(x, t) = \exp[g\tau t] \psi_o(x \exp[g\tau t])$$

B.2.1.1 Linear Diffusion Green Function

For the case in which the cooling interaction is entirely dominated by diffusion, the relevant PDE is $\psi_t = [\gamma(x)\psi\psi_x]_x$, for which $\gamma(x) = |G|^2\{1 + \mathcal{U}\}$. For the test cases, $\gamma(x) = 4g^2 \sin^2(\tau x/2)$.

To obtain an exact solution of linear diffusion with $\gamma(x) = g$ is straight forward. A Green function for linear diffusion a solution to the equation $\psi_t = g^2 \psi_{xx}$ is

$$\psi(x, t) = \int_{-\infty}^{\infty} dx' G(x|x', t) \psi(x', 0)$$

with the Green function $G(x|x', t) = 1/\sqrt{4g\pi t} \exp[-(x - x')^2/4gt]$. For an initial Gaussian distribution $\psi_o(x, 0) = 1/\sqrt{2\pi\sigma^2} \exp[-(x')^2/2\sigma^2]$ the second moment is given by $\langle x^2 \rangle = \sqrt{4\sigma^2 + gt}$

Although it is a straight forward exercise to derive the linear diffusion Green function, the Green function for the nonlinear (Schottky) diffusion is not readily obtainable. Thus, it is necessary to resort to numerical techniques.

B.3 Numerical Finite Difference Methods

B.3.1 Explicit Methods

Several variants of *explicit* methods exist for finite differencing [1]. In this approach, a simple finite difference scheme was implemented for which an initial distribution is pushed forward in time on a two dimensional grid. The easiest variant of the Euler method is the leapfrog scheme, or *Lax - Wendroff* method, which gives better stability by using overlapping meshes.

B.3.1.1 Euler Method

In the classic finite difference Euler method, the partial differential equation $u_t = -\nabla F(u)$ for $u(x, t)$ is solved on a discretized grid $(x, t) \rightarrow (j, n)$, with the first order accuracy in time and second order accuracy in the *spatial* variable. Hence,

$$\begin{aligned} u_t &= \frac{u_j^{n+1} - u_j^n}{\Delta t} \\ u_x &= \frac{u_{j+1}^n - u_{j-1}^n}{2\Delta x} \end{aligned}$$

The Euler method is conditionally stable if the fundamental scale of the problem $\lambda = \Delta t / [2\Delta x] \leq 1$. For nonlinear problems, in which $F = u^k$ for example, the stability condition takes the approximate form $\lambda_F = k\Delta t / [2\Delta x] \leq 1$. Therefore, for nonlinear problems, the simple Euler method is particularly unsuitable because of the requirements placed upon the grid spacing in order to maintain numerical stability.

B.3.1.2 General Two Step Lax-Wendroff

Amongst the many explicit finite difference algorithms which exist to improve the conditional stability beyond that of the Euler method, such as the flux corrected transport of Boris and Book [9], the *two step Lax-Wendroff* method [79] makes use of intermediate mesh points by performing a centered average. Given the advective partial differential equation

$$u_t = -\nabla F$$

the differencing scheme is given by the following steps: (i) find the half points

$$\begin{aligned} u_{j+1/2}^{n+1} &= \frac{1}{2} [u_{j+1}^n + u_j^n] - \frac{\Delta t}{2\Delta x} [F_{j+1}^n - F_j^n] \\ u_{j-1/2}^{n+1} &= \frac{1}{2} [u_j^n + u_{j-1}^n] - \frac{\Delta t}{2\Delta x} [F_j^n - F_{j-1}^n] \end{aligned}$$

(ii) use the half points $u_{j\pm 1/2}^{n+1}$ to calculate the fluxes at th half points $F_{j\pm 1/2}^{n+1/2}$, and finally (iii) calculate the $n + 1$ grid points for u

$$u_j^{n+1} = u_j^n - \frac{\Delta t}{\Delta x} [F_{j+1/2}^{n+1/2} - F_{j-1/2}^{n+1/2}]$$

The two-step Lax Wendroff method for Fokker Planck equation follows immediately with the appropriate substitution of the flux F .

B.3.2 Implicit Methods: Linear Diffusion

Implicit methods offer two advantages over Euler methods; (i) coarse and long time behavior with no restriction on grid spacing, and (ii) *unconditional* numerical stability. If an implicit finite difference method is to be used, however, the partial differential equation to be solved must be linear.

For a linear diffusion problem $\psi_t = \nabla^2 F(\psi)$ the difference scheme is obtained with centered derivatives defined on half grid points:

$$\frac{\psi_j^{n+1} - \psi_j^n}{\Delta t} = -\rho \left[\frac{F_{j+1/2}^{n+1} - F_{j-1/2}^{n+1}}{2\Delta x} - (1 - \rho) \left[\frac{F_{j+1/2}^n - F_{j-1/2}^n}{2\Delta x} \right] \right]$$

for which the flux points are given by:

$$\begin{aligned} F_{j+1/2} &= \frac{1}{4}(\psi_{j+1} + \psi_j)(\tau_{j+1} + \tau_j) - \frac{D}{4} \frac{\psi_{j+1} - \psi_j}{\Delta x} (\gamma_{j+1} + \gamma_j) \\ F_{j-1/2} &= \frac{1}{4}(\psi_j + \psi_{j-1})(\tau_j + \tau_{j-1}) - \frac{D}{4} \frac{\psi_j - \psi_{j-1}}{\Delta x} (\gamma_j + \gamma_{j-1}) \end{aligned}$$

Given the definitions,

$$\begin{aligned} \lambda_{\pm} &= \frac{1}{4}[(\tau_{j+1} + \tau_j) \pm D(\gamma_{j+1} + \gamma_j)] \\ \beta_{\pm} &= \frac{1}{4}[(\tau_j + \tau_{j-1}) \pm D(\gamma_j + \gamma_{j-1})] \end{aligned}$$

the system of equations results:

$$a\psi_j^{n+1} + b\psi_{j-1}^{n+1} + c\psi_{j+1}^{n+1} = a'\psi_j^n + b'\psi_{j-1}^n + c'\psi_{j+1}^n$$

which defines a tridiagonal system of equations:

$$\mathbf{A}\psi^{n+1} = \mathbf{B}\psi^n$$

A formal solution follows with the inversion of \mathbf{A} ,

$$\psi^{n+1} = \mathbf{A}^{-1} \mathbf{B} \psi^n$$

Despite the simplicity of implicit methods for *linear* diffusion equations, nonlinear diffusion equations are not directly solvable with this technique. Instead, two different techniques may be used in conjunction with implicit finite differencing for nonlinear equations, (i) approximate linearization, and (ii) predictor- corrector methods. While unconditional stability is a guarantee, some estimate of the errors introduced with the linearization or the successive approximations must be performed. Such error estimates are nontrivial and represent the major obstacle with the use of implicit methods for nonlinear equations.

B.4 Tests of the Finite Difference Equations

A number of tests are used to ensure that the numerical finite difference equations are converging to the exact solution of the partial differential equation. First, the individual terms of the equation are isolated and solved for the simple cases: (a) linear convection, and (b) linear and nonlinear diffusion. In each case, m -th moments of the distribution are calculated (the zeroth through third moment) which is defined over the grid space \mathcal{X}

$$\langle x^m(t) \rangle = \int_{\mathcal{X}} dx' x'^m(t) \psi(x', t)$$

Physically, the zeroth moment $\langle x^0(t) \rangle$ represents the conservation of particle number as a function of time, the first moment $\langle x^1(t) \rangle$ represents development of asymmetry about the origin, or a net convection (net beam velocity from the central energy of the entire distribution), and the $\langle x^2(t) \rangle$ moment represents the change of the beam width σ .

BIBLIOGRAPHY

- [1] W.F. Ames, *Numerical Methods for Partial Differential Equations*, New York, 2nd ed. Academic Press, 1977
- [2] A. Ando, K. Takayama, *Synchrotron Oscillations with Very Small η* , IEEE Trans. on Nucl. Sci. **NS-30**, No. 4. p.2604, 1983
- [3] J. Binney, S. Tremaine, *Galactic Dynamics*, Princeton NJ., Princeton University Press, 1987
- [4] J. Bisognano, C. Leemann *Stochastic Cooling*, AIP Conf. Proc. **87**, Physics of High Energy Accelerators, New York, R.A. Carrigan ed., p.583, 1982
- [5] J. Bisognano, *Stochastic cooling: recent theoretical directions* IEEE Trans. Nucl. Sci., **NS-30** No.4, p.2393, 1983
- [6] J. Bisognano, *Vertical Transverse Stochastic Cooling*, BECON-10, LBID-119, 1979
- [7] *Blue Vector Signal Analyzers for Difficult Measurements on Time-Varying and Complex Modulated Signals* HP Journal, Dec. 1993
- [8] J. Borer, *Non-destructive Diagnostics of Coasting Beams with Schottky Noise* Proc. 9th Int. Conf. of High Energy Phys. pp 53-65 SLAC, 1974
- [9] J.P. Boris, D.L. Book, *Solution of Continuity Equations by the Method of Flux-Corrected Transport*, J. Comp. Phys. **20**, 397, 1976
- [10] D. Boussard, *Schottky Noise and Beam Transfer Function Diagnostics*, CERN Accelerator School Proceedings 1987 CERN **87-03**, Vol. II, p.416, 1987
- [11] R. Brinkmann, *Insertion* CERN Accelerator School, **87-03**, Vol. II, 1987
- [12] K.L. Brown, R.V. Servanckx, *First- and Second-Order Charged Particle Optics*, AIP Conf. Proc. **127**, Physics of High Energy Particle Accelerators, New York, p.62, 1985
- [13] P.J. Bryant, *Design of a Ring Lattice*, CERN Accelerator School Proceedings, CERN **91-04**, 1991
- [14] D.S. Burnett, *Finite Element Analysis*, Reading, Addison-Wesley Publishing Co., 1994

- [15] F.W. Byron, R.W. Fuller, *Mathematics of Classical and Quantum Physics*, Reading, Addison-Wesley, 1970
- [16] G. Carron *Stochastic Cooling tests in ICE* Phys. Lett. 77B, p. 353, 1978
- [17] G. Carron, L. Thorndahl, *Stochastic Cooling of Momentum Spread by Filter techniques* CERN/ISR-RF/78-12, 1978
- [18] J.R. Cary, *Lie Transform Perturbation Theory for Hamiltonian Systems*, Phys. Rep. **79**, No.2, p.129, 1981
- [19] F.Cilyo, J. McCarthy, B. Wisner, *Magnet Current Bypass Shunt*, IEEE Trans. on Nucl. Sci. **NS-30**, No. 4, 1983
- [20] S. Chandrasekhar, *Stochastic Problems in Physics and Astronomy*, Rev. Mod. Phys. **15**, No. 1, 1943
- [21] A. Chao, *Physics of Collective Beam Instabilities in High Energy Accelerators*, New York, John Wiley & Sons Inc., 1993
- [22] S. Chattopadhyay, *On Stochastic Cooling of Bunched Beams from Fluctuation and Kinetic Theory*, Ph.D thesis, LBL-14826, 1982
- [23] S. Chattopadhyay, *Some Fundamental Aspects of Fluctuations and Coherence in Charged- Particle Beams in Storage Rings*, CERN **84-11**, 1984
- [24] S. Chattopadhyay, *Vlasov Theory of Signal Suppression for Bunched Beams interacting with a Stochastic Cooling Feedback Loop*, IEEE Trans. on Nucl. Sci. **NS-30**, No. 4. p.2646, 1983
- [25] S. Chattopadhyay, *A Formulation of Transversely Coupled Betatron Stochastic Cooling of Coasting Beams* IEEE Trans. on Nucl. Sci. Vol **NS-30**, No. 4., p.2652, 1983
- [26] M. Church, J.P. Marriner *The Antiproton Sources: Design and Operation*, Ann. Rev. Nucl. Part. Sci. **43**, pp.253-95, 1993
- [27] Mike Church, *Measurements of η in the Accumulator*, Fermilab Pbar Note 523
- [28] F.T. Cole, F.E. Mills, *Increasing the Phase Space Density of High Energy Particle Beams*, Ann. Rev. Nucl. Part. Sci., **30**, pp.295-335, 1981
- [29] Corana *Minimizing Multi-modal Functions of Continuous Variables with Simulated Annealing*, ACM Transactions on Mathematical Software, vol. 13, no. 3, 1987, (262-280)

- [30] E.D. Courant, H.S. Snyder *Theory of the Alternating-Gradient Synchrotron*, Annals of Physics **3**, pp.1-48, 1958
- [31] D. Edwards, M.J. Syphers, *An Introduction to the Physics of Particle Accelerators*, New York, John Wiley and Sons, Inc., 1993
- [32] Fermi National Accelerator Laboratory, *Tevatron 1 Design Report*, Batavia, 1984
- [33] Fermi National Accelerator Laboratory Main Injector Dept. *Main Injector Technical Design Handbook*, 1994
- [34] A. Fetter, J.D. Walecka, *Theoretical Mechanics of Particles and Continua*, New York, McGraw-Hill, Inc., 1980
- [35] R.P Feynman, *The Theory of Fundamental Processes*, New York, W.A. Benjamin, 1961
- [36] H. Frauenfelder, E. Henley, *Subatomic Physics*, New York, Prentice Hall, Inc., 1980.
- [37] Goffe, Ferrier, and Rogers, *Global Optimization of Statistical Functions with Simulated Annealing*, Journal of Econometrics, vol 60., no. 1/2, Jan./Feb., 1994, (65-100)
- [38] D.A. Goldberg, G.R. Lambertson, *Dynamic Devices: A Primer on Pickups and Kickers*, New York AIP Conf. Proc. **249**, The Physics of Particle Accelerators, 1992
- [39] H. Goldstein, *Classical Mechanics*, Reading, Addison-Wesley Publishing Co., 1980
- [40] G. Golub, V. Pereyra, *The differentiation of pseudo- inverses and nonlinear least squares problems whose variables separate*, SIAM J. Numer. Anal. **10**, 413-432, 1973
- [41] M. Goossens, F. Mittelbach, A. Samarin, *The Latex Companion*, Reading, Addison Wesley Company Inc., 1994
- [42] I.S. Gradshteyn, I.M. Ryzhik, *Table of Integrals, series, and products*, Orlandao, Academic Press, Inc. 1980
- [43] Hans Grote and F.Christoph Iselin *The MAD Program (Methodical Accelerator Design). User's Reference Manual*. European Organization for Nuclear Research, Geneva, Switzerland. CERN/SL/90-13
- [44] R.C. Gupta, J.I.M. Botman, M.K. Craddock; *High Transition Energy Magnet Lattices*, IEEE Transactions of Nuclear Science. **NS-32**, No. 5, p.2308, 1985

- [45] W. Hardt, H. Schönauer, A. Sorensen; *Passing Transition in the future CPS*, Proc. of the 8th Int. Conf. on High Energy Acc., 323, CERN, 1971
- [46] W. Hardt, *Gamma- transition jump Scheme of the CPS*, IEEE Trans. on Nucl. Sci. Vol NS-30, No. 4., p.434, 1983
- [47] E. Harmes, *The Antiproton Source Rookie Book*, Fermilab Operations Dept.
- [48] P. Horowitz, W. Hill, *The Art of Electronics*, Cambridge; New York, Cambridge University Press, 1980
- [49] S. Ichimaru, *Basic Principles of Plasma Physics: A Statistical Approach*, Reading, W.A. Benjamin, Inc., 1973
- [50] A.I. Iliev, *Analytic Approach to design of High Transition Energy Lattices with Modulated β -Functions*, IEEE Particle Accelerator Conference, p.1907, 1991
- [51] J.D. Jackson, *Classical Electrodynamics*, New York, John Wiley and Sons, Inc., 1975
- [52] J. Killeen, K.D. Marx, *The Solution of the Fokker-Planck Equation for a Mirror-Confined Plasma*,
- [53] J. Killeen, *Computational Methods for Kinetic Models of Magnetically Confined Plasmas* Springer Series in computational physics, New York, Springer-Verlag, 1986
- [54] S. Kirkpatrick, C.D. Gelatt, Jr., M.P. Vecchi, *Optimization by Simulated Annealing*, Science, **220** No. 4598, p.671, 1983
- [55] P.F. Kunz, *Object Oriented Programming*, SLAC-PUB-5629, 1991
- [56] S.Y. Lee, K.Y. Ng, D. Trbojevic, *Design and Study of Accelerator Lattices without Transition*, FERMILAB-FN-595, 1992
- [57] S.Y. Lee, K.Y. Ng, D. Trbojevic, *Minimizing dispersion in flexible momentum compaction lattices*, Physical Review E, **48**, No. 4, p.3040, (1993)
- [58] J. MacLachlan, *User's Guide to ESME v. 8.0*, FERMILAB-TM-1835, 1993
- [59] J. Marion, M. Heald, *Classical Electrodynamical Radiation*, New York, Academic Press, Inc. 1980
- [60] J. Marriner, *Debuncher Momentum Cooling System*, FERMILAB- \bar{p} Note 473

- [61] J. Marriner, D. McGinnis, *An Introduction to Stochastic Cooling*, AIP Conf. Proc. **249**, The Physics of Particle Accelerators, New York, p.693, 1992
- [62] O. Martin, S. Otto, *Combining Simulated Annealing with Local Search Heuristics*, preprint IPNO-TH-93-53, 1993
- [63] L. Michelotti, *WXYZPTLK: A practical, user-friendly C++ implementation of differential algebra: User's guide*. FERMILAB-FN-535, 1990
- [64] L. Michelotti, *C++ Object for Beam Physics* FERMILAB-CONF-91-159, 1991
- [65] L. Michelotti *WXYZPTLK and BEAMLIN: C++ objects for beam physics*, Fermi Note, Fermilab
- [66] L. Michelotti *Resonance Topology*, FERMILAB-Conf-87/50, 1987
- [67] L. Michelotti, *Phase Space Concepts*, AIP Conference Proceeding **184**, Physics of Particle Accelerators, New York, p.891, 1989
- [68] L. Michelotti, *Intermediate Classical Mechanics with Applications to Beam Physics*, New York, John Wiley & Sons, Inc., 1993
- [69] D. Möhl, *Stochastic Cooling*, from CERN Accelerator School Proceedings, CERN 87-03, Vol. II, p.453, 1987
- [70] D. Möhl, G. Petrucci, L. Thorndahl, S. van der Meer, *Physics and Techniques of Stochastic Cooling*, Physics Reports **58**, pp.73-119, 1980
- [71] J. Morgan, *Measuring Debuncher Tunes*, Fermilab Operations Dept.
- [72] A. Natarajan, N. Mohankumar, *A Comparison of Some Quadrature Methods for Approximate Cauchy Principal Value Integrals*, Journal of Computational Physics, **116**, pp.365-368, 1995
- [73] V. Pareto, *Cours d'Economie Politique*, Pouge 1896; translation by Schwier, *A.S Manual of Political Economy*, The Macmillan Press, 1971.
- [74] R.J. Pasquinelli, *Bulk Acoustic Wave (BAW) Devices for Stochastic Cooling Notch Filters*, IEEE Particle Accelerator Conference, p.1395, 1991
- [75] R.K Pathria *Statistical Mechanics*, Toronto, Pergamon Press, 1972

- [76] S.G. Peggs, R.M. Talman, *Nonlinear Problems in Accelerator Physics*, Ann. Rev. Nucl. Part. Sci. **36**, pp. 287-325, 1986
- [77] J. Peoples, *Antiproton Source*, AIP Conference Proceeding **184**, Physics of Particle Accelerators, New York, p.1846, 1989
- [78] W.F. Preag, *A High Current Low-Pass Filter for Magnet Power Supplies*, IEEE Trans. Ind. Elec. and Contr Inst., IECE-17, No. 1, 16-22, 1970
- [79] W.H. Press, B.P. Flannery, S.A. Teukolsky, W.T. Vetterling, *Numerical Recipes in C: The Art of Scientific Computing*, Cambridge; New York, Cambridge University Press, 1992
- [80] L.E. Reichl, *A Modern Course in Statistical Mechanics*, Austin, University of Texas Press, 1980
- [81] F. Riggiero, *Kinetic Theory of Charged Particle Beams*, from CERN Accelerator School Proceedings, CERN **90-04**, p.52, 1990
- [82] T. Risselada, *Gamma Transition Jump Scheme*, from CERN Accelerator School Proceedings, CERN **91-10**, 1991
- [83] A.G. Ruggiero, *Signal Suppression Analysis for the Momentum Stochastic Cooling with a Multiple System*, IEEE Trans. on Nucl. Sci. **NS-30**, No. 4. p.2596, 1983
- [84] S. Russenchuck, *Pareto-Optimization in Computational Electromagnetics*, CERN AT/92-27, 1992
- [85] S. Russenschuck, T. Tortschanoff, *Mathematical Optimization for Superconducting Accelerator Magnets*, CERN AT/93-37, 1993
- [86] Sacherer F. (1974) *Transverse Bunched beam Instabilities Theory* Proc. 1st Course Int. Sch. Part. Acc., Erice, CERN 77-13, 1974
- [87] F. Sacherer, *Stochastic Cooling Theory*, CERN-ISR-TH/78-11, 1982
- [88] D. Sagan, *On the physics of Landau damping*, Am. J. Phys. **62** (5), p.450, 1994
- [89] R.V. Servranckx, K.L. Brown *Circular Machine Design Techniques and Tools*, AIP Conference Proceedings **153**, Physics of Particle Accelerators, New York, 1987
- [90] P. Schmüser, *Basic Course on Accelerator Optics*, from CERN Accelerator School Proceedings, CERN **87-10**, 1987

- [91] T.H. Stix, *The Theory of Plasma Waves*, New York, McGraw- Hill, 1962
- [92] K. Symon, *Applied Hamiltonian Dynamics*, AIP Conference Proceedings **249**, The Physics of Particle Accelerators, p.277, New York, 1989
- [93] M. Syphers, T. Sen, *Notes on Amplitude Function Mismatch*, SSCL-604, 1992
- [94] K. Takayama, *How can we Reduce the Momentum Spread of 4% in the Debuncher*, FERMILAB \bar{p} Note 136
- [95] A.V. Tollestrup, G. Dugan *Elementary Stochastic Cooling* FERMILAB-TM-1277, 1983
- [96] P. Tran, *Status of the variable momentum compaction storage ring experiment in SPEAR*, 1993 PAC, p.173
- [97] N.G. van Kampen, *Stochastic Differential Equations*, Physics Reports, **24** No. 3, p.171-228, 1976
- [98] S. van der Meer, *A Different Formulation of the Longitudinal and Transverse Beam Response*, CERN/PS/AA/80-4, 1980
- [99] S. Werkema, *Measurements of Accumulator Beta Function Values*, FERMILAB- \bar{p} Note
- [100] S. Werkema, *Performance of the Antiproton Source During Run 1B*, FERMILAB- \bar{p} Note - 559
- [101] U. Wienands, R.V. Servranckx, *A Racetrack Lattice for the TRIUMF KAON Factory Booster*, IEEE Particle Accelerator Conference, 1991
- [102] F. Willeke, G. Ripken, *Methods of Beam Optics*, AIP Conference Proceedings **184**, Physics of Particle Accelerators, 758, 1989
- [103] H. Wiedemann, *Particle Accelerators*, New York, Springer Verlag, 1993
- [104] M. Wong, K.G. Budge, J.S. Peery, A.C. Robinson, *Object-Oriented Numerics: A Paradigm for Numerical Object-Oriented Programming*, Computers in Physics, Vol 7., No. 6, 655-663, 1993
- [105] D. Zwillinger, *Handbook of Differential Equations*, Boston, Academic Press, Inc., 1989

—

—

—

2

1

—

■

•

•

•